The Development of Acoustofluidic Devices Using Printed Circuit Boards

Roman Mikhaylov

A thesis submitted for the degree of Doctor of Philosophy

Cardiff University

June 2023

ABSTRACT

Acoustofluidic devices utilise acoustophoretic forces to actuate fluids and particles and have attracted increasing interest in biomedical research, due to their label-free and biocompatible nature. They have demonstrated the ability to precisely manipulate particles and cells by creating acoustic forces that are proportional to the size, shape, and density of the particles and cells. These devices have demonstrated the ability to manipulate cells with considerable accuracy and sensitivity, in applications such as cell patterning, separation and concentration, and even demonstrated their capability to be applied in stimulation and transfection applications. One of the most prominent acoustofluidic devices for separation and manipulation based applications are the surface acoustic wave (SAW) devices. Conventional SAW based devices are manufactured by using the photolithography technique and require high-end cleanroom facilities, which results in devices that are not reconfigurable and not very accessible. In this thesis, a new PCB based fabrication technique for making SAW based devices is introduced as an alternative to the conventional method. This technique patterns interdigital transducers (IDTs) on a printed circuit board (PCB) to create PCB IDTs, which are mechanically clamped onto a piezoelectric substrate to form a PCB based SAW device. The PCB -SAW device removes the need for cleanroom facilities, which results in a device made via a widely accessible manufacturing technique that is reconfigurable. Additionally, this technique offers having the capability to couple the PCB IDTs with different piezoelectric substrates without the need of re-manufacturing. Herein, the PCB SAW device demonstrates its capability to generate SAW to pattern particles and cells with 128° Y-cut $LiNbO_3$ piezoelectric substrate using a standing SAW (SSAW), similarly to the conventionally manufactured SAW devices. The same device also demonstrated its capability to quickly couple with ZnO based piezoelectric substrate and generate SAWs. This thesis then explores the capability of different PCB substrates to generate SAWs and to develop a portable and compact acoustofluidic device made from widely accessible components, including its microchannel. Finally, the PCB based SAW technique is applied to develop a device for particle actuation, to study experimentally the actuation of different sized particles and at different microchannel configurations under flow conditions, to demonstrate its capability to potentially be applied for separation-based applications.

Contents

Publication list

- **Mikhaylov, R**., Wu, F., Wang, H., Clayton, A., Sun, C., Xie, Z., Liang, D., Dong, Y., Yuan, F., Moschou, D., Wu, Z., Shen, M.H., Yang, J., Fu, Y., Yang, Z., Burton, C., Errington, R.J., Wiltshire, M., Yang, X., 2020. Development and characterisation of acoustofluidic devices using detachable electrodes made from PCB. Lab Chip 20, 1807–1814. https://doi.org/10.1039/C9LC01192G
- **Mikhaylov, R**., Martin, M.S., Dumcius, P., Wang, H., Wu, F., Zhang, X., Akhimien, V., Sun, C., Clayton, A., Fu, Y., Ye, L., Dong, Z., Wu, Z., Yang, X., 2021. A reconfigurable and portable acoustofluidic system based on flexible printed circuit board for the manipulation of microspheres. J. Micromech. Microeng. 31, 074003. https://doi.org/10.1088/1361-6439/ac0515
- Sun, C., Wu, F., Wallis, D.J., Shen, M.H., Yuan, F., Yang, J., Wu, J., Xie, Z., Liang, D., Wang, H., Tickle, **R., Mikhaylov**, R., Clayton, A., Zhou, Y., Wu, Z., Fu, Y., Xun, W., Yang, X., 2020. Gallium Nitride: A Versatile Compound Semiconductor as Novel Piezoelectric Film for Acoustic Tweezer in Manipulation of Cancer Cells. IEEE Transactions on Electron Devices 67, 3355–3361. https://doi.org/10.1109/TED.2020.3002498

List of Figures

List of Tables

Acknowledgements

I would like to express my sincere appreciation and gratitude to the individuals and organizations who have contributed to my research:

First and foremost, I am extremely grateful to the Engineering and Physical Sciences Research Council (EPSRC) from UK Research and Innovation (UKRI) for granting me a studentship that funded my research for 3.5 years. Without their generous support, undertaking this extensive endeavour would not have been possible.

I would like to extend my thanks to my supervisor, Dr. Xin Yang, for providing his support, encouragement, and valuable insights that propelled this research forward. I am also thankful to Dr. Chao Sun, Prof. Aled Clayton, Prof. Yongqing Fu, and Dr. Zhihua Xie for their invaluable assistance, guidance, and sharing their extensive knowledge and resources in their respective fields.

I would like to express my gratitude to Dr. Meng Cai and Dr. Jun Wei from IREGene, China, who offered me the opportunity to undertake a placement in their company, contributing to the further development of my research, and I am also deeply appreciative of their warm hospitality during my time there.

Furthermore, I want to acknowledge my colleagues, Dr. Fangda Wu, Hanlin Wang, Mercedes S. Martin, and Ziming Zeng, for their collaboration and collective efforts within our department. Their contributions have been instrumental in advancing our work.

Special thanks are due to Xiaoyan Zhang and Povilas Dumcius for their dedicated efforts in reviewing and enhancing the quality of this thesis, and their continuous support and invaluable friendship during my PhD. Your motivation and support helped me to arrive to this final step, and I am truly thankful for meeting you both.

While in my personal life I would like to thank Hannah Koufou, Phillipe and Calie Demougin, whose understanding and support played a pivotal role for me to achieve what I have. I honestly couldn’t have asked for better friends.

I am truly grateful to all those mentioned above and acknowledge their significant contributions to the completion of this research, in a direct or indirect manner.

Chapter 1

Acoustofluidics and Biomedicine

1.1. Introduction

Acoustofluidics is a multidisciplinary field that combines acoustics and microfluidics, and is a field that has a great prominence in applications involving the actuation and manipulation of fluids, particles, and cells (Rufo et al., 2022). This manipulation is made possible by the generation of sound waves and their ability to diffract into a fluid to generate time-averaged pressure fluctuations. These fluctuations are then utilised to actuate particles, cells, or fluids in a chaotic manner (e.g. mixing) (Zhao et al., 2021) or a precise manner (e.g. particle patterning) (Tian et al., 2019). This methodology of actuating particles, cells, or fluids using sound waves is known as acoustophoresis and is the fundamental phenomenon that drives the functionality of acoustofluidic devices in actuation based applications.

Acoustofluidic devices can actuate cells in a label-free and biocompatible manner by purely using the cells' mechanical properties (Bruus, 2011). As such, they have attracted great interest in actuation-based biomedical applications and have been applied in research fields such as tissue engineering (Deshmukh et al., 2022), cell manipulation (Guo et al., 2015), cell separation (Wu et al., 2017), cell concentration (Gu et al., 2021) and even applications such as cell stimulation (Ambattu et al., 2020). All the devices from the aforementioned applications strive to achieve a "Lab-on-a-Chip" configuration, which refers to small and easy-to-use devices capable of tackling challenging biomedical tasks.

While there are various setups for acoustofluidic devices, a common setup is the surface acoustic wave (SAW) based device. SAW based devices have been successfully applied to all the biomedical applications mentioned above, indicating both their capability and versatility. However, they are manufactured using photolithography (Ai et al., 2013; Li et al., 2014; Guo et al., 2015; Li et al., 2019), which is a process that requires high-end clean room facilities and is not widely available or accessible. The developed SAW device is also not reconfigurable, thus limiting the amount of experimentation that can be achieved with one device. These two factors might dissuade some from pursuing research in this field using SAW based devices. However, if a new fabrication method was created for SAW devices that is more widely available and accessible, and that allows the reconfiguration of the device, it could potentially lead to increased research and development in this field.

In this chapter, a thorough introduction will be presented on the working principles behind the acoustofluidic devices, their various applications and achievements in biomedicine,

their selection criteria for different applications, and their advantages over other competing techniques. The aim is to establish the need and advantages of these devices in research, to clearly stipulate that developing a new fabrication technique could greatly benefit this field by making these devices, SAW devices in particular, more accessible and hopefully driving more research and development in this area.

1.2. Foundation of acoustofluidics

To effectively utilise and build an acoustofluidic device, it is crucial to understand its fundamental mechanisms, one of which is acoustics or more precisely sound waves. According to the American National Standard (2013), acoustics is defined as the "Science of sound, including its production, transmission, and effects, including biological and psychological effects," while sound waves are defined as "Oscillations in pressure, stress, particle displacement, particle velocity, etc., propagated in a medium with internal forces (e.g., elastic or viscous), or the superposition of such propagated oscillations." From these definitions, it can be seen that any desired acoustic effects will be produced by and will be dependent on the sound waves.

1.2.1. Sound waves

In mathematical terminology, a sound wave propagating through a medium is described as cosine wave with following parameters (Long, 2014):

$$y(x,t) = A\cos(kx \pm \omega t \pm \phi) \tag{1}$$

$$k = \frac{2\pi}{\lambda} \tag{2}$$

$$\lambda = \frac{c}{f} \tag{3}$$

$$\omega = 2\pi f \tag{4}$$

$$f = \frac{1}{T} \tag{5}$$

where A, k, x, ω, t, ϕ, λ, c, f and T represent amplitude (Pa), wavenumber (rad/m), position (m), angular frequency (rad/s), time (s), phase (radians), wavelength (m), speed of sound (m/s), frequency (Hz) and period (s).

Eq. 1 can be plotted in either the space domain (x) or the time domain (t) to demonstrate how the wave looks during a specific time frame across a space domain or how the wave changes over time in a set space, respectively. For a simple demonstration, a sound wave is plotted, using eq. 1, and shown in Fig. 1.1a. The sound wave is plotted at an arbitrary time, t_1, in the space domain and illustrates the A and λ of the plotted wave. In Fig. 1.1a the effect of a phase shift (ϕ) is also demonstrated, where a positive ϕ is applied resulting with a wave lag of π/2. Fig. 1.1b is provided to clearly show how the wave changes in the space domain over different time intervals, t_1, t_2 and t_3 with $t_1 <$

$t_2 < t_3$. To illustrate this change, a section of the wave is highlighted to show how the wave propagates from left to right. It should be noted that if Fig. 1.1a was plotted in the time domain the X axis would change to "Time (s)", where then a full wave cycle instead of indicating λ would indicate T instead. A final important factor of the eq. 3 that should be pointed out, is that the wave's λ is dependent on the speed of sound of the medium that it propagates through, c.

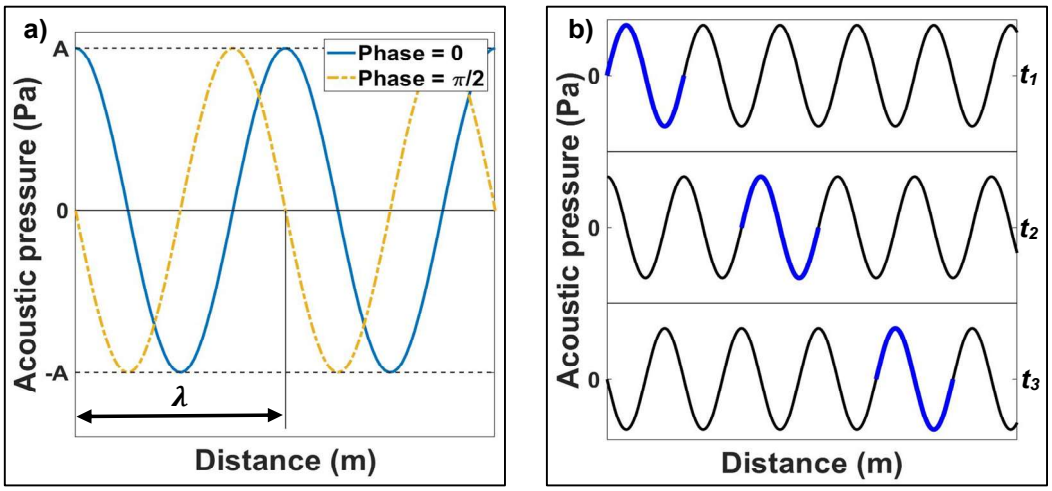

Figure 1.1. a) Sound wave plotted in the space domain at an arbitrary time, t_1. b) Demonstration of a sound wave in the space domain at different time intervals t_1, t_2 and t_3, with $t_1 < t_2 < t_3$. A segment of the wave has been highlighted to illustrate the propagation of the wave from left to right.

1.2.2. Superposition

Sound waves possess the characteristic of superposition which states: that when two waves propagate along the same plane, they can be combined into a single composite wave. As will be demonstrated later, this plays a major role in acoustophoretic applications where this principle is employed with identical counterpropagating waves to produce a standing wave. Figs. 1.2a and 1.2b demonstrate this concept, where two identical counterpropagating waves are shown individually and as a summative wave at different time frames, respectively. It should be noted that Fig.1.2 is primarily used to show the two most important stages of the waves' interaction, which are when the summative wave has a maximum (t_1, t_3 and t_5) and a minimum amplitude (t_2 and t_4). The maximum amplitude occurs when the two identical counterpropagating waves perfectly overlap with each other (Fig. 1.2a, t_1, t_3 and t_5), while the minimum is a result of when the waves are out of synch, which appear as if they have a phase shift of π (Fig. 1.2a, t_2 and t_4). During these two stages the resulting summative wave will have either the combined amplitude of the two waves or a zero amplitude, with the latter effect being possible only with identical counterpropagating waves. But one of the most important

properties of the resulting summative wave is that the resulting wave is a static wave. To illustrate this effect vertical dashed lines were added to both graphs to indicate set positions in space. In Fig. 1.2a, both the red wave (traveling to the right) and blue wave (traveling to the left) will initially have their have maximum amplitude peaks between the dashed lines (t_1), but as these waves continue traveling these peaks will intersect the dashed line (t_2) indicating their movement in space. But the summative wave resulting from this interaction, Fig. 1.2b, never crosses the dashed lines and its amplitude peaks are always between the dashed lines. This phenomenon of the summative wave that oscillates in time but whose peak amplitude profile does not move in space is referred to as a standing wave. This static property of the standing wave results in the characteristic that it has its maximum/ minimum amplitudes always at the same points, called anti-nodes, as well as points where there is zero amplitude, called nodes. The nodes of the summative wave in Fig. 1.2b are indicated by the red 'X' markers.

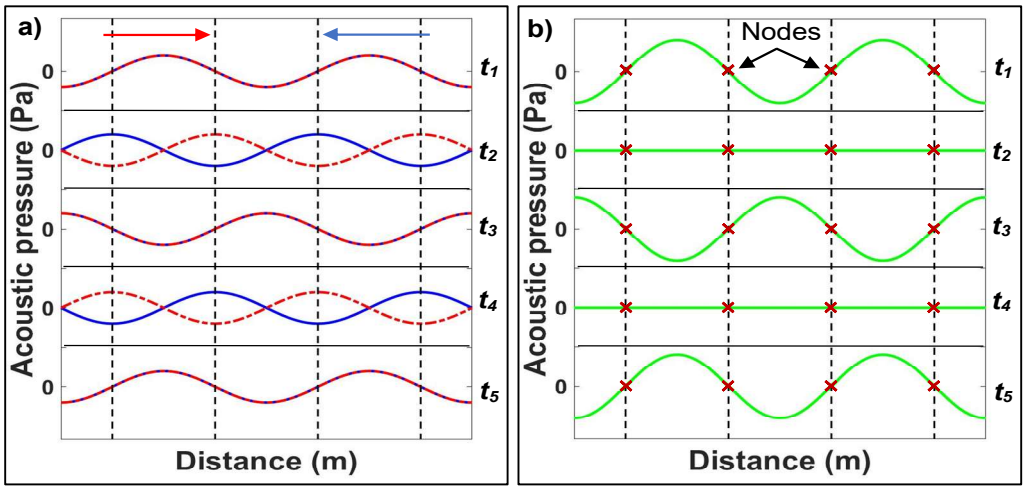

Figure 1.2. Two identical counterpropagating traveling waves plotted a) individually and b) as a summative wave (superposition) at different time frames (t_1, t_2, t_3, t_4 and t_5). The red 'X' markers on the superimposed wave indicate the nodes.

1.2.3. Types of sound waves

By establishing the general characteristics of the sound waves, the different categories and types of sound waves can now be discussed. The first and most straightforward categorisation of sound waves is based on the frequency/ wavelength of the wave. These are infrasound (< 20 Hz), audible (20 ≤ 20 kHz) and ultrasound (> 20kHz), with infrasound being below audible range and ultrasound above it. But while the characterisation based on frequency may be useful in other fields, in acoustofluidic the most common characterisation used for sound waves is of how a wave propagates through its hosting medium.

The method of propagation of sound waves through a medium typically falls into two broad categories: body waves and surface waves. Body waves are waves that deform the whole medium that they travel through and can either be primary or secondary waves (P- or S-waves) (Poisson, 1830). P-type body waves propagate parallelly with their oscillation and result with compression and expansion of the lattice of the medium that they propagate through. S-waves on the other hand propagate perpendicular to their oscillations and are commonly referred to as shear waves (Keith and Crampin, 1977). Body shear waves most commonly appear in solid materials, but they can also appear in liquids with very high viscosity (Greenwood and Bamberger, 2002). Body shear wave can have an amplitude in either the horizontal or the vertical axis (Jolly, 1956). It should also be noted that while in some fields the P- and S-waves connotations are still rather common, such as seismology (Zheng et al., 2022), in fields dealing with acoustics these two waves are more commonly referred to as longitudinal and transverse/ shear waves, respectively (Zhang *et al.*, 1772). Additionally, in acoustofluidics body waves are more commonly referred as bulk acoustic waves (BAWs) (Zhang, 2022). As such in this thesis the terms longitudinal BAW (L-BAW) and shear BAWs (S-BAWs) will be used when referring to these types of waves.

To demonstrate this concept more clearly, bulk waves and their resulting effects on a medium during propagation are illustrated in Fig. 1.3. Fig. 1.3a illustrates a medium and its lattice at rest, where no deformation is present resulting in a uniform lattice structure. Fig. 1.3b demonstrates the medium being subjected to a longitudinal wave propagating (dashed line) and oscillating (red arrow) along the X axis, which results in the compression and expansion of the medium's lattice. For the transverse/ shear waves their oscillations can be present either in the vertical (Z) or horizontal (Y) direction as shown in Figs. 1.3c and 1.3d, respectively. The vertical and horizontal oscillation are illustrated with blue and green arrows, respectively, and both waves propagate along the X axis (dashed line), resulting in their oscillations being perpendicular to their propagation.

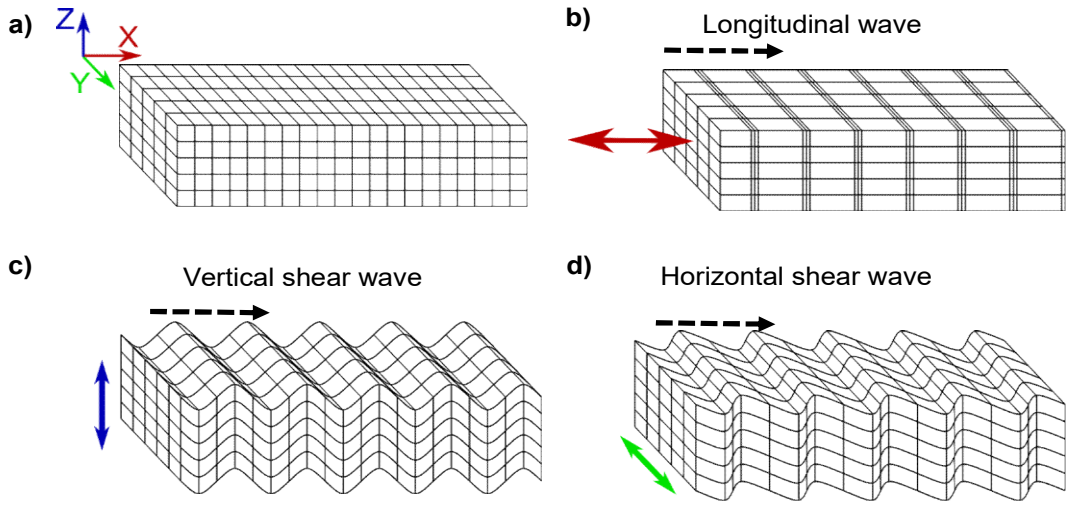

Figure 1.3. Different types of bulk waves propagating in a medium. a) The medium is at rest with no deformation present within its lattice. b) A longitudinal wave is applied to the medium, resulting in the compression and expansion of the lattice. The wave's oscillation and propagation are along the X axis and are shown by the red and dashed arrow, respectively. c) A vertical shear wave is applied to the medium, resulting in oscillations in the Z axis (Blue arrow) and propagation in the X axis (dashed arrow), while d) a horizontal shear wave results in oscillations in the Y axis (Green) and a propagation in the X axis (dashed arrow).

Surface waves, as the name suggests, are waves that propagate on the surface of the medium and are confined to its few top "layers" (Takeuchi and Saito, 1972). In acoustofluidics these waves are referred to as surface acoustic waves (SAWs) (Zhang, 2022) and the three most common types are Rayleigh waves, shear horizontal (SH) waves and Love waves. Rayleigh waves are named after Lord Rayleigh who first proposed them (Rayleigh, 1885), and these waves induce elliptical motion in the medium with the ellipses aligned perpendicular to the surface and parallel to the propagation direction. SH-SAWs are waves that propagate horizontally on the surface of the medium and have the unique properties of their propagation being much slower than the BAW's shear wave velocity and that they exhibit an upper cut-off frequency (Auld *et al.*, 1976). Figs. 1.4a and 1.4b demonstrate the propagation of a Rayleigh and SH wave in a medium, respectively. Love waves were discovered by Augustus Edward Hough Love (1911) and propagate in a very similar manner to SH-SAWs (Auld *et al.*, 1976). The main difference between SH-SAWs and Love waves is that the latter to be generated requires either a layered isotropic substrate (Auld *et al.*, 1976) or a waveguide (Steinem and Janshoff, 2005).

A final type of wave, that is worth mentioning, are Lamb waves (Lamb, 1917). Lamb waves are unique in the sense that while they cause the medium hosting them to fully

deform, they require that their hosting medium is thinner than the travelling wave's amplitude. As such it is hard to define them as either bulk or surface waves. Nonetheless, Lamb waves have been observed and used in acoustofluidic applications utilising thin films (Tao et al., 2019). Lamb waves have two modes of propagation, asymmetrical and symmetrical, shown in Figs. 1.4c and 1.4d, respectively. In the asymmetrical mode the wave's propagation and lattice deformation appears similar to a vertical S-BAW, if the medium of the latter was a few layers thick. The asymmetrical mode results in the mirrored expansion and contraction of the medium on the top and bottom surface while still propagating along the X axis.

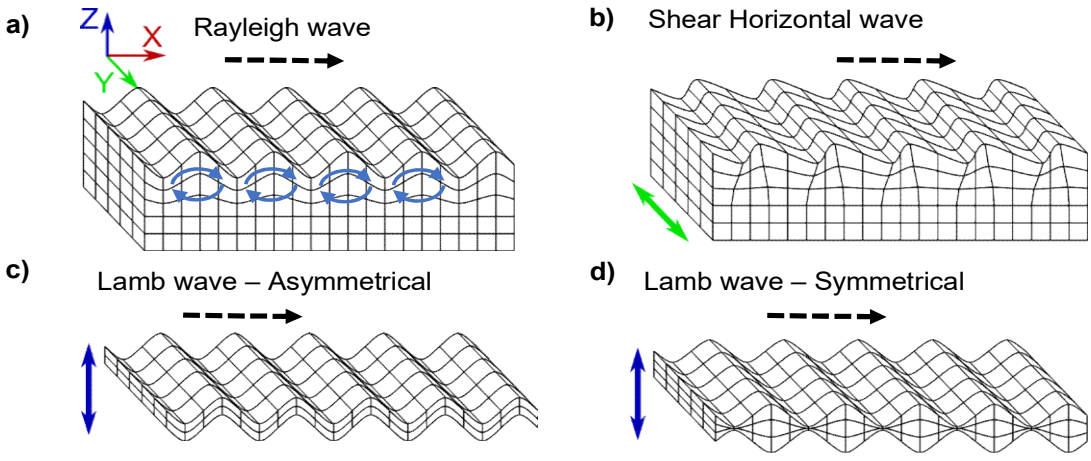

Figure 1.4. Different types of SAWs and Lamb waves. a) A Rayleigh wave propagating in the medium along the X axis, dashed arrow, resulting in elliptical oscillations (blue arrows) at the surface of the medium, with components both in the Z and X axes. b) Shear horizontal waves propagating in the X axis, dashed arow, with oscillations in the Y axis (green arrows). c) An asymmetrical and d) symmetrical Lamb wave oscillating in the Z axis (blue arrow) within a thin medium while propagating along the X axis, dashed arrow.

1.2.4. Acoustophoresis

Acoustophoresis refers to the phenomena where sound waves ("acousto") are used to induce some sort of actuation ("phoresis"). In acoustofluidics, this phenomenon is used to move or pattern particles or cells inside a bounded or unbounded fluidic medium in a precise manner. In this section an overview will be provided of how particles actuation is achieved within a microchannel, which is one of the most prominent setups to utilise this phenomenon with. It should be noted that the theory behind the acoustofluidics is vast and can be considered a field of study on its own. As such herein only the most essential equations and hypothesis will be provided to establish a basic theoretical foundation of acoustophoresis.

The primary governing equation that should be stated is the continuity equation, which expresses the conservation of mass (Pedlosky, 1987). For compressible fluids the continuity equation is written as:

$$\partial_t \rho = -\boldsymbol{\nabla} \cdot (\rho v) \tag{6}$$

where ρ and v are the fluid density (kg/m^3) and fluid velocity (m/s), respectively. The change of the mass momentum of the fluid over time is described as $\partial_t \rho$, with ∂_t being the time derivative. The differential operator nabla ($\boldsymbol{\nabla}$) is used to describe the change in three-dimensional space.

The second governing equation is the Navier-Stokes equation which, in simple terms, describes the motion of viscous fluids. The equation bears the names of Claude-Louis Navier, a French engineer and physicist, and George Gabriel Stokes, an Anglo-Irish physicist and mathematician. The equation's development took place over a span of several decades, beginning with Navier in 1822 and progressing through Stokes between 1842 and 1850. In acoustofluidics, a common assumption, for when this equation is used, is that at a given temperature the dynamic viscosity and viscosity ratio coefficient can be taken as constants (Bruus, 2011). Additionally, in acoustofluidics the external forces term ($\rho \boldsymbol{g}$) is ignored, giving rise to the following equation:

$$\rho[\partial_t \boldsymbol{v} + (\boldsymbol{v} \cdot \boldsymbol{\nabla})\boldsymbol{v}] = -\boldsymbol{\nabla} p + \eta \boldsymbol{\nabla}^2 \boldsymbol{v} + \beta \eta \boldsymbol{\nabla}(\boldsymbol{\nabla} \cdot \boldsymbol{v}) \tag{7}$$

where p, η, and β are the pressure (Pa), dynamic viscosity of the fluid (Pa·s) and the viscosity ratio. Eqs. 6, and 7 are the primary equations used to derive the motion of fluids under the influence of sound waves. But eq. 7 is a partial differentiational equation and is notoriously difficult to solve. As such to solve this equation, for acoustofluidic applications, the perturbation theory is used, with the postulate that the pressure can be expressed in terms of density as (Bruus, 2012):

$$p = p(\rho) \tag{8}$$

Additionally, to avoid the heat transfer equation the study case is considered isothermal. In perturbation theory the acoustic wave is let to be expressed as tiny perturbations that affect density, pressure and velocity of a quiescent fluid, written as (Bruus, 2012):

$$\rho = \rho_0 + \rho_1 + \rho_2 \tag{9}$$

$$p = p_0 + c_s^2 \rho_1 + p_2 \tag{10}$$

$$\boldsymbol{v} = 0 + \boldsymbol{v}_1 + \boldsymbol{v}_2 \tag{11}$$

where c_s is the (isentropic) speed of sound (m/s). By using the first terms ($\rho_0 + \rho_1$) from the above equations the first order terms for eqs. 6 and 7 can be derived as (Bruus, 2012):

$$\partial_t \rho_1 = -\rho_0 \boldsymbol{\nabla} \cdot \boldsymbol{v_1} \tag{12}$$

$$\rho_0 \partial_t \boldsymbol{v_1} = -c_s^2 \boldsymbol{\nabla}\rho_1 + \eta \boldsymbol{\nabla}^2 \boldsymbol{v_1} + \beta\eta \boldsymbol{\nabla}(\boldsymbol{\nabla} \cdot \boldsymbol{v_1}) \quad (13)$$

But if the secondary orders are also used, a more accurate for description for eqs. 12 and 13 can be derived as (Bruus, 2012):

$$\rho_0 \boldsymbol{\nabla} \cdot \langle \boldsymbol{v_1} \rangle = -\boldsymbol{\nabla} \cdot \langle \rho_1 \boldsymbol{v_1} \rangle \quad (14)$$

$$\langle \rho_1 \partial_t \boldsymbol{v_1} \rangle + \rho_0 \langle (\boldsymbol{v_1} \cdot \boldsymbol{\nabla}) \boldsymbol{v_1} \rangle = +\eta \boldsymbol{\nabla}^2 \langle \boldsymbol{v_2} \rangle + \beta\eta \boldsymbol{\nabla}(\boldsymbol{\nabla} \cdot \langle \boldsymbol{v_2} \rangle) - \boldsymbol{\nabla} \langle p_2 \rangle \quad (15)$$

with the ⟨ ⟩ denotes the time average over a full oscillation period. The oscillation period can be found by assuming a time dependence harmonic for the fields and expressing them as (Bruus, 2012):

$$\rho_1 = \rho_1(\mathbf{r}) \mathrm{e}^{-\mathrm{i}\omega \mathrm{t}} \quad (16)$$

$$p_1 = p_1(\mathbf{r}) \mathrm{e}^{-\mathrm{i}\omega t} \quad (17)$$

$$\boldsymbol{v_1} = \boldsymbol{v_1}(\mathbf{r}) \mathrm{e}^{-\mathrm{i}\omega \mathrm{t}} \quad (18)$$

where $\omega = 2\pi f$ is the angular velocity frequency of the wave (rad/s). Eq. 15 is the most fundamental equation for acoustofluidics. In this equation the term $\langle \boldsymbol{v_2} \rangle$ determines the streaming velocity of the fluid, while $\langle p_2 \rangle$ gives rise to the acoustic radiation force. But it should be noted that eq. 15 is still extremely complex and the only way to solve is to provide appropriate boundary conditions and assumptions.

The first most common assumption is that the flow velocities in the fluid are much smaller than the sound waves and as such the fluid appears incompressible, which results in $\boldsymbol{\nabla} \cdot v = 0$, allowing a significant number of simplifications (Bruus, 2011). A second assumption is that the flow velocity in the channel is limited to laminar flow. This can be demonstrated by the Reynolds number:

$$Re = \frac{\rho L v}{\eta} \quad (19)$$

where L is the length scale (m). In a typical microfluidic channel these parameters would be $\frac{\rho}{\eta} = 10^{-6} \frac{m^2}{s}$, be $L \approx 10^{-4}\, m$ and be $v \approx 10^{-3} \frac{m}{s}$, which results in $Re \approx 0.1$, which is much smaller than 1. The final assumption used in acoustofluidics is that fluid is inviscid, as such the viscosity terms can be ignored. Using the following information then the two primary forces acting on spherical particles inside a fluid can be established, i.e. the acoustic radiation force and Stokes drag force.

To derive the acoustic radiation force a lot of new theories and derivation need to be introduced. But the discussion and derivation of these in detail is beyond the scope of this thesis and as such just a short summary of the assumptions will be just provided here. To derive the acoustic radiation force the assumption of inviscid flow is used, a velocity potential is introduced and the scatter theory is applied. These theories and derivation are described in full in “Acoustofluidics 7: The acoustic radiation force on small

particles" (Bruus, 2012). The resulting equation is the general acoustic radiation force in 1D plane:

$$F_R = 4\pi\Phi(\kappa^*, \rho^*)ka^3E_{ac}\sin(2k\mathrm{x}) \tag{20}$$

$$E_{ac} = \frac{p_a^2}{4\rho_0 c_o^2} \tag{21}$$

$$\Phi(\kappa^*, \rho^*) = \frac{1}{3}\left(\frac{5\rho^* - 2}{2\rho^* + 1} - \kappa^*\right) \tag{22}$$

$$\kappa^* = \frac{\kappa_p}{\kappa_0} \tag{23}$$

$$\rho^* = \frac{\rho_p}{\rho_0} \tag{24}$$

where Φ, p_a, a, E_{ac}, κ_p, κ_0, ρ_p and ρ_0 are the acoustophoretic contrast factor, acoustic pressure (Pa), radius of the particle (m), acoustic energy density (J/m^3), compressibility of the particle (Pa^{-1}), compressibility of the fluid (Pa^{-1}), density of the particle (kg/m^3) and density of the fluid (kg/m^3). It should be noted that this equation is applicable only when $\lambda \gg a$, which is often the case in acoustofluidics. One of the most important parameters is the Φ, which determines whether a particle will travel towards the node or anti-node of a standing wave. In acoustofluidic nodes and anti-nodes are commonly referred to as pressure nodes (PNs) and pressure anti-nodes (ANs). A negative and positive Φ indicate that the particles will travel towards the ANs and PNs, respectively. This concept is illustrated in Fig. 1.5, where spherical particles are under the influence of a standing SAW (SSAW). These particles will then travel to the PNs (sides of the microchannel) and AN (middle of the microchannel) when they have a positive (Fig. 1.5a) and negative (Fig. 1.5b) Φ, respectively. In the case of solid particles and most cells, their contrast factor is positive in most aqueous solutions, and as such they will move towards the pressure node (Liu and Lim, 2011).

The final equation to include is the Stokes drag force (Stokes, 1851), also referred in acoustofluidics as acoustic drag force. This equation is derived from the Navier-stokes equation and assuming that flow velocities, compressibility and body forces are negligible. This gives the following equation:

$$\boldsymbol{F}_{drag} = 6\pi\eta a(\boldsymbol{v} - \boldsymbol{v}_p) \tag{25}$$

where $\boldsymbol{v}$ and $\boldsymbol{v}_p$ are the fluid and particle velocity (m/s). Eq. 25 is commonly used by being equated to $\boldsymbol{F}_R$, giving rise to the following equation (Barnkob et al., 2018):

$$\boldsymbol{v}_p = \boldsymbol{v} + \frac{\boldsymbol{F}_R}{6\pi\eta a} \tag{26}$$

This equation is used to determine whether the particles motion will be dominated by either the $\boldsymbol{F}_R$ or $\boldsymbol{F}_{drag}$. Fig. 1.5c demonstrates the motion of the particles when $\boldsymbol{F}_{drag}$ is the dominant force. From eqs. 26 and 25, one can clearly see that the common

characteristic that both equation share is a. Typically, the point at which $\boldsymbol{F}_{drag}$ becomes dominant can be determined by the a of the particle, which is commonly referred to as the critical particle diameter. A study by Nama et al. (2015) demonstrated, through simulation, that a device operating at 6.65 MHz would exhibit a critical particle diameter of approximately 1 μm.

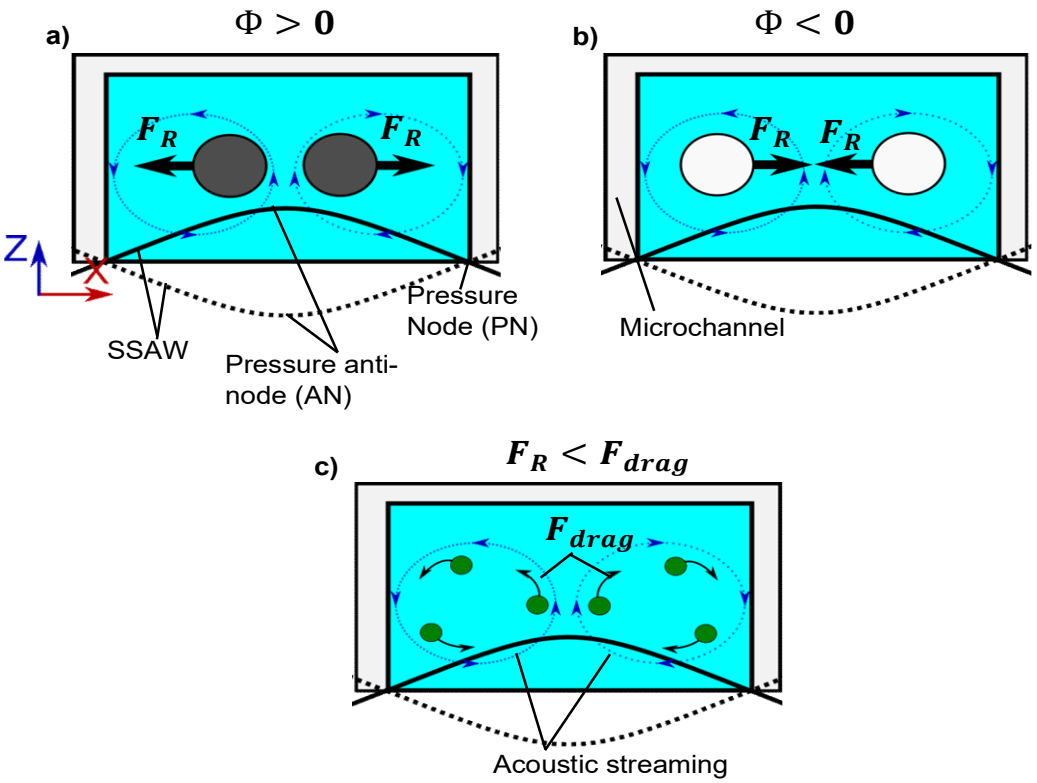

Figure 1.5. Particles within a microchannel actuated by a standing surface acoustic wave (SSAW). a) The actuation vector of particles is shown with a positive Φ and b) with a negative Φ. d) Particle trajectory when the acoustic drag force is the dominant force ($F_R < F_{drag}$).

In many applications that involve particle actuation, i.e. alignment and separation, $\boldsymbol{F}_{drag}$ is undesirable since it makes the movement of the particle unpredictable. While $\boldsymbol{F}_R$ makes the actuation of particles predictable and its intensity changes based on the particles' properties, such as size, density and compressibility, as can be seen from eq. 20. By utilising the $\boldsymbol{F}_R$ is how acoustofluidic devices achieve particle and cell separation and manipulation.

1.3. Acoustofluidic devices

In the preceding section, the theoretical aspects of particle actuation in acoustofluidic applications have been explored. In this section, the attention is shifted towards the development of devices that could achieve such phenomenon, specifically examining how the sound waves are generated and some of the setups that are employed in

acoustofluidic devices. However, to narrow the focus and provide a comprehensive analysis, the devices that meet two specific criteria will be discussed: 1) they are capable of actuating particles within a fluidic medium or microchannel, and 2) they utilise either L-BAWs or R-SAWs. Why these two wave types are selected is due to them being the most utilised waves for particle actuation, and why this is will be explained in detail in section 1.3.4.

1.3.1. Piezoelectricity and piezoelectric transducers

Piezoelectricity refers to a phenomenon where certain materials generate an electrical potential when subjected to mechanical pressure, a discovery first made by the Currie brothers (Curie and Curie, 1880). This phenomenon is also inversely related, meaning that if instead of mechanical pressure a voltage potential is applied across a piezoelectric material it will then generate mechanical distortion in response (Mason, 1981). In the realm of acoustofluidic devices, piezoelectric transducers are commonly utilised to generate sound waves. These transducers consist of a piezoelectric substrate and a conductive material that serves as one or more electrodes. By applying an alternating current (AC) to the electrode, the piezoelectric substrate is subjected to continuous alternating potential voltages and as a result undergoes continuous deformation, which produces continuous vibrations, i.e. sound waves (Mason, 1981).

One of the two most common types of piezoelectric transducers in acoustofluidics are BAW transducers and interdigital transducers (IDTs). BAW transducers refer to a setup where a piezoelectric substrate is sandwiched between two electrodes. These electrodes are then subjected to an AC which makes the whole piezoelectric substrate deform by either expanding or contracting based on the polarity. An example of a BAW transducer and its working mechanism is shown in Fig. 1.6a. IDTs also consist of electrodes, more specifically interdigital electrodes (IDEs), but in this case all the electrodes are patterned on top of the piezoelectric substrate. These electrodes are interchangeably connected to two different bus pads and this configuration forms an interdigital transducer (IDT), Fig. 1.6b. For the IDT the AC source is connected to the bus pads and each pair of IDEs is interchangeably charged positively and negatively, which creates localised expansions and compressions, respectively, on the surface of the substrate. The compressions and expansions result in a wave that can propagate along the surface of the piezoelectric substrate as SAW, which commonly is a Rayleigh SAW (R-SAW), Fig. 1.6c.

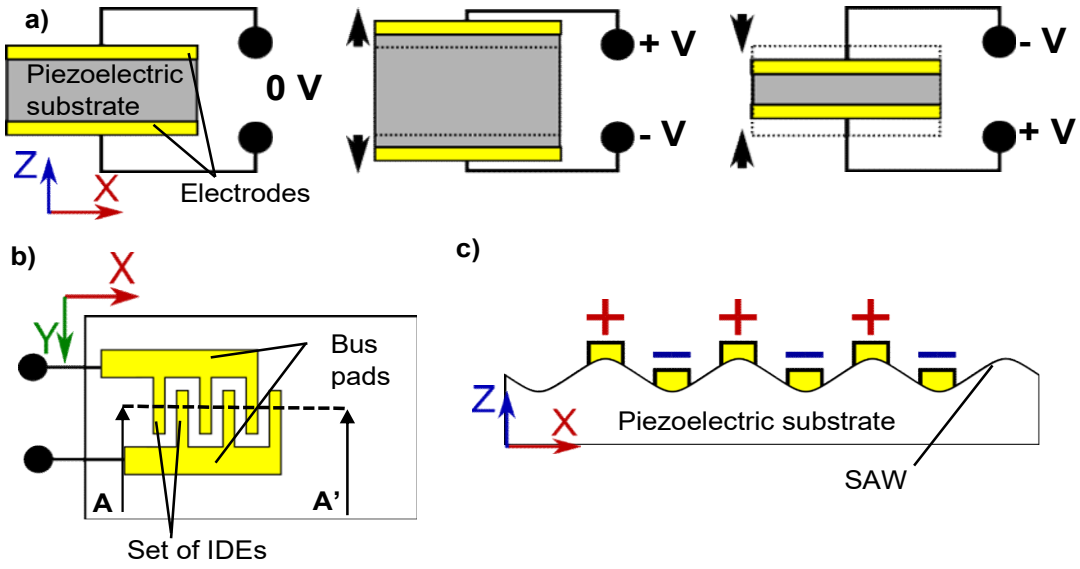

Figure 1.6. BAW transducer's and IDT's working mechanism. a) BAW transducer is shown at rest with no deformation (left), when a positive potential voltage is applied to the electrodes the piezoelectric substrate expands (middle) and compresses when the voltage is reversed (right). b) A conventional IDT consisting of sets of interdigital electrodes (IDEs) that are consecutively placed and connected to two distinct bus pads. c) The cross section (A-A') illustrates the resulting surface deformation effect when one of the bus pads has a positive potential voltage and the other has a negative potential voltage. The IDEs are then consecutively charged positively and negatively, resulting with local upwards (expansion) and downwards (compression) deformations on the piezoelectric substrate that generate a propagating SAW.

1.3.2. BAW-based acoustofluidic devices

It should be noted that BAW transducer have widespread use outside the acoustofluidic field (Kimura *et al.*, 2010). However, their ability to generate L-BAWs has made them particularly valuable in acoustofluidics. In essence, BAW based acoustofluidic devices employ a BAW transducer to induce a L-BAW wave into a fluidic medium, thereby achieving the acoustophoretic effects. A common setup for BAW devices implements a standing wave and a microchannel with a reflecting layer. This reflecting layer is incorporated into the microchannel by having the microchannel's top and bottom surface made out of a glass (Xu *et al.*, 2019) or by having the side walls be made out of silicon (Iranmanesh *et al.*, 2013). These materials have high acoustic impedance and as such are capable of reflecting the acoustic wave energy back into the microchannel, which will be covered in more detail in Chapter 2. Fig. 1.7a illustrates a BAW device with the BAW transducer bonded with epoxy underneath a microchannel with a glass roof and floor. The L-BAW, generated by the transducer, is coupled onto the bottom surface of the microchannel, using epoxy, and then diffracts into the microchannel fluid. Inside the

microchannel, when the wave interfaces with glass roof, it is reflected back by the roof and forms a standing wave (Xu et al., 2019). This standing wave can then be used to either trap or guide particles that pass through standing wave zone. A different setup, Fig. 1.7b, demonstrates an option to have a channel made of silicon and the BAW transducer bonded on the side of the channel (Van Assche et al., 2020). Both of these setups are used to generate a standing wave to either align particles or separated dissimilar particles. But even without a reflective surface and standing wave, BAW transducers can also be used to generate acoustic streaming when placed underneath a fluidic medium, as shown in Fig. 1.7c (Wu et al., 2022).

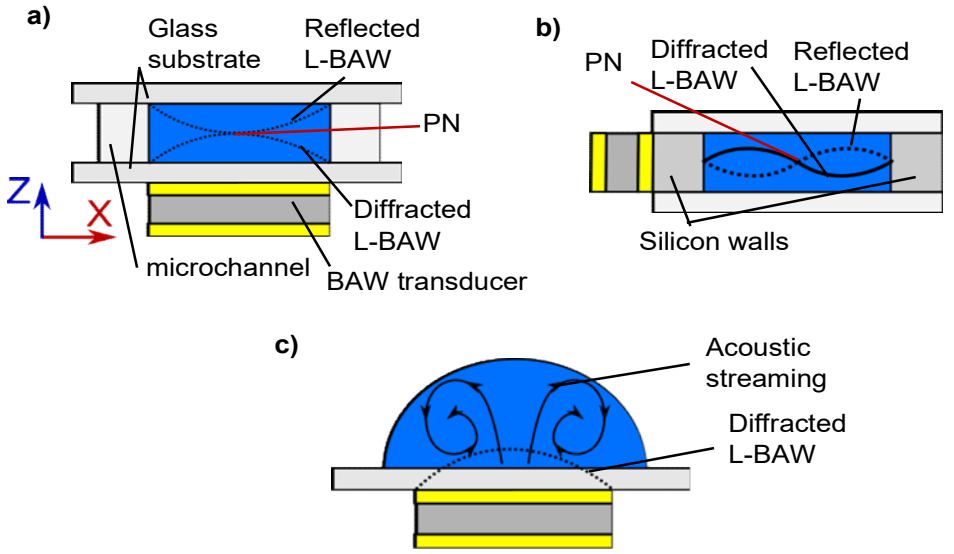

Figure 1.7. Different setups of BAW based acoustofluidic devices. a) The BAW transducer is bonded underneath a glass substrate with a microchannel sandwiched between two glass substrates. The generated L-BAW is coupled into the bottom of the microchannel, via the epoxy bonding layer, which then diffracts into the microchannel and the fluid. The diffracted wave is then reflected by the roof, which then forms a standing wave. b) The BAW transducer is placed on the microchannel's side wall. The walls of the channel are made of high acoustic impedance material (silicon) and reflect the diffracted L-BAW to form a standing wave. c) BAW transducer bonded underneath a glass substrate and a droplet is placed on top. The L-BAW diffracts into the droplet, generating acoustic streaming.

1.3.3. SAW based acoustofluidic devices

Similarly to BAW transducers, IDTs were already being used widely in the industry as SAW filters (Kirschner, 2010). However, their ability to generate SAWs also makes them well-suited for acoustofluidic applications. It should be stated while BAW transducers have also been used to generate SAWs (Huang et al., 2013), IDTs are by far the most common transducer used for this application. SAW devices that utilise IDTs can be broadly set into two major categories; SAW devices that utilise IDTs to generate a

traveling SAW (TSAW) or standing SAW (SSAW). Additionally, this section will mostly focus on Rayleigh SAWs (R-SAW) that are typically used for acoustophoretic applications.

When a R-SAW travels across a piezoelectric substrate it is perpendicular to the fluidic medium. Upon establishing contact with the fluid, the acoustic energy diffracts at an angle into the fluid. This angle is known as diffraction angle which can be calculated as follows (Wixforth et al., 2004):

$$\theta_R = \sin^{-1}\left(\frac{C_w}{C_{pz}}\right) \tag{27}$$

where C_w and C_{pz} are speed of sound in water (m/s) and piezoelectric substrate, respectively. This diffracted energy then translates as longitudinal waves resulting in acoustic streaming inside the fluid. The R-SAW then rapidly attenuates as it propagates along the substrate inside the fluid (Wixforth et al., 2004). This concept is illustrated in Fig. 1.8.

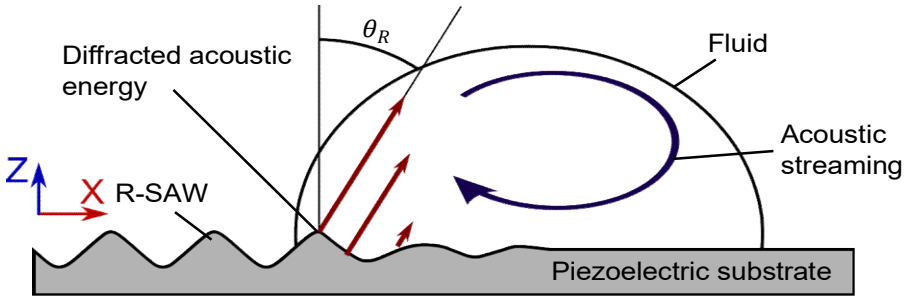

Figure 1.8. Diffraction of a R-SAW into a fluid. The R-SAW meets the fluid, diffracts into it at an angle θ_R and rapidly attenuates after the initial interaction. The diffracted energy disturbs the steady state of the fluid and generates acoustic streaming inside the fluid.

The above concept is the main principle used with SAW based devices to actuate particles inside a droplet or actuate the droplet itself (Fu et al., 2017). In such applications, a single IDT on a piezoelectric substrate is used to induce the acoustic streaming inside the droplet, as shown in Fig. 1.9a. The droplet is placed on the centreline of the IDT, which results in two circulating vortexes being generated inside, due to the acoustic streaming. Alternatively, as shown in Fig. 1.9b, placing the droplet off the centreline of the IDT results in a spiralling acoustic streaming, which has the capability to focus particles in the centre of the droplet (Destgeer et al., 2016). It should be noted that while these setups utilise one IDT, a second IDTs can be implemented to enhance or duplicate the effect. In Fig. 1.9c two IDTs are used and placed at the centreline of the droplet. This results in four vortexes being generated (each IDT generates two) instead of two, which also increases the total streaming inside the droplet. It is worth noting that this method can also be applied when the droplet is placed off the

centreline of the IDT, by placing the second IDT at the top right edge again off the centreline of the droplet. This arrangement would result with an enhanced focusing effect (Wang et al., 2022).

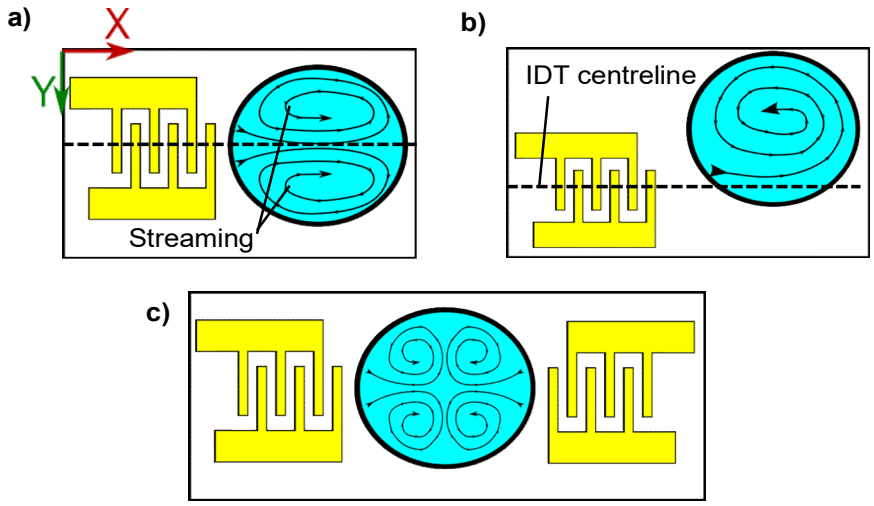

Figure 1.9. SAW based device for in-droplet particle manipulation. a) A droplet is positioned on the centreline of an IDT, resulting with two streaming vortexes within it. b) A droplet positioned off the centreline of the IDT, which results with a spiralling streaming vortex within it. c) Two identical IDTs are placed opposite each other to increase the total acoustic streaming effect. The droplet is placed between the two IDTs on their centreline, resulting in four streaming vortexes with each IDT generating two.

Another capability of SAW devices for droplet application is to actuate the physical droplet at higher amplitudes. This effect can be translated to pumping the droplet and event jetting (Fu et al., 2017). This effect is usually undesired for particle manipulation inside the droplet and, as such, it limits the acoustic energy that can be applied. To overcome this, the droplet can be held in place using with a boundary, that could either be a ring (Wang et al., 2022) or an open (no roof) rectangular microchannel (Ambattu et al., 2020).

Apart from droplet and open microchannels, SAW devices have also been used with microchannels utilising both R-TSAW and R-SSAW. These microchannels are commonly made from soft (acoustically leaky) material, such as polydimethylsiloxane (PDMS). Since soft materials are used, instead of a reflective material, SAW devices typically implement a second IDT to generate a SSAW. The implementation of the second IDT also offers the advantage that the PN of the SSAW can be moved by offsetting the phase (ϕ) of a wave generated by one of the IDTs (Mikhaylov et al., 2020). This concept is illustrated in Fig. 1.10, where particles are initially suspended in a microchannel with no flow, shown in Fig. 1.10a. When both IDTs are activated, each generates a R-TSAW which superimpose and create a R-SSAW, Fig. 1.10b. The initial

R-SSAW that is created creates a pressure node in the middle of the microchannel and the particles within the R-SSAW zone are moved towards the PN track. But the position of this PN can be moved to a desired location by shifting the ϕ of the wave generated by IDT$_2$. In this conceptual case by making $\phi_{IDT2} = \pi$, it results in the shift of the PN, and the particles trapped within it, to the right, Fig. 1.10c.

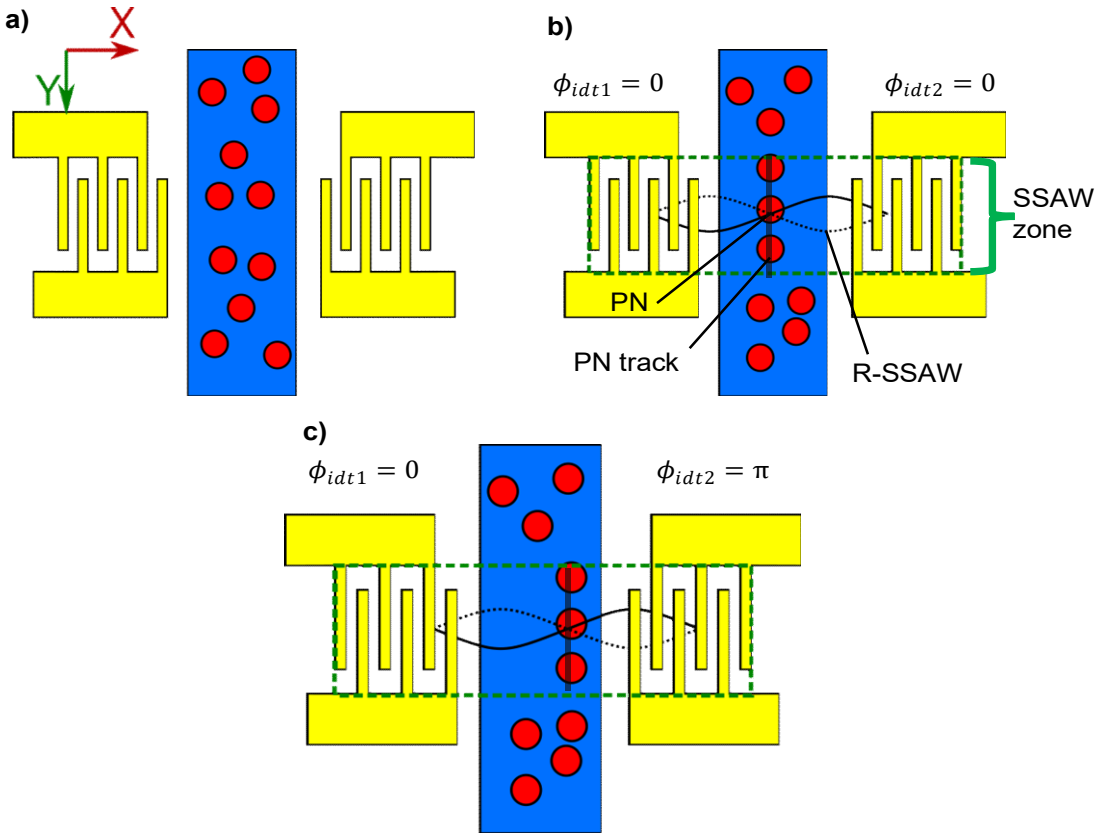

Figure 1.10. IDT based devices utilising R-SSAW for particle patterning. a) Particles are suspended inside a microchannel with no flow and no SAWs are present. b) Both IDTs are activated, each generating a R-TSAW which superimpose to create a R-SSAW. The particles within the SSAW zone are actuated and align on the PN track. c) The PN track can be moved by changing $\phi_{IDT2} = \pi$, which results in the PN shifting to the right. The particles in the figure have a positive Φ.

The aforementioned setup has been used in microchannels that implement flow in order to separate dissimilar particles based on their size (Ai *et al.*, 2013). An example of such a setup is shown in Fig. 1.11a, where a pair of IDTs is parallel to the microchannel creating a SSAW with a single PN in the middle of a three input-output microchannel. This single PN redirects the larger particles (red) that come from the side inputs, 1 and 3, to the middle of the microchannel towards output 5. It can be observed that while the F_R affects both types of particles the distance is not sufficient for the smaller particles (green) to be successfully actuated towards output 5, due to the smaller F_R that they

experience. This approach the limitation of the microchannel width being constrained to half the wavelength (λ) of the sound wave, to prevent the formation of multiple PNs. While this limitation can be mitigated by reducing the operating frequency, it also results in a reduction of the acoustic radiation force due to the decrease of k, see eq. 20.

A different approach to achieve separation has been to place the microchannel an angle at an angle against the pair of IDTs. This method has been termed as the tilted angled SSAW (taSSAW) (Li et al., 2015) and is shown in Fig. 1.11b. In this scenario the microchannel has two inputs and outputs and the formed SSAW forms PN tracks that are inclined. This inclined track then simply redirects particles from input 1 towards output 4. Here as well the green particles are affected by the F_R, but they are not redirected towards the output 4 because the distance is not sufficient for the particles to successfully migrate across. This technique has the advantages that width of the microchannel is no longer restricted by wave's λ (allowing the use of wider microchannels and higher operating frequencies), can create multiple tracks for the particles to travel (increases the number of particles that can be actuated) and can increase the length of the deflection path (increasing the possible separation resolution) (Ding et al., 2014).

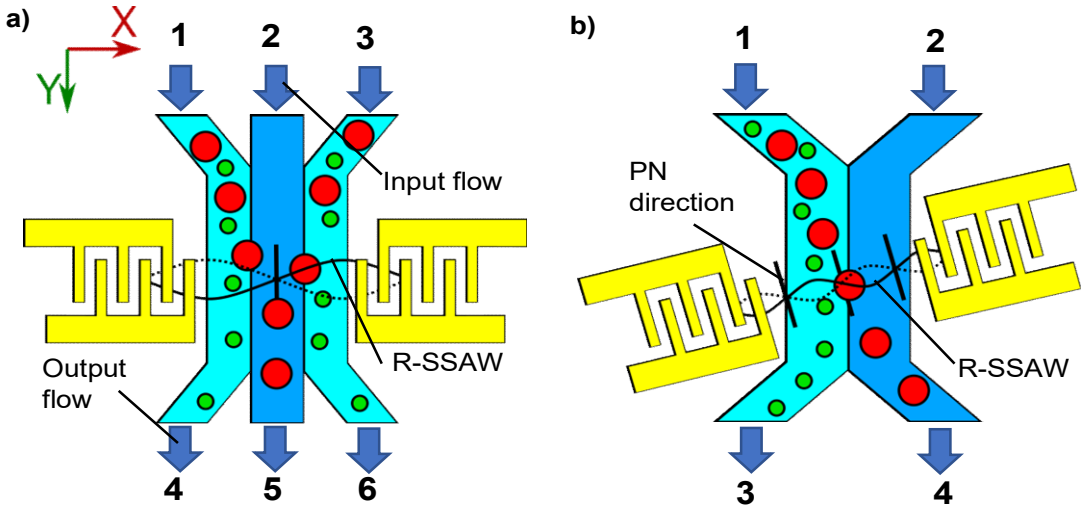

Figure 1.11. IDT based devices utilising R-SSAW for particle separation. a) Parallel IDTs creating a R-SSAW with a PN in the middle of the microchannel. Red particles entering from inputs 1 and 3 are redirected towards output 5. b) Microchannel placed at an angle against a pair of IDTs, creating the tilted angle SSAW (taSSAW) setup. The taSSAW setup generates PNs that are at an incline, resulting in a redirection path that actuates the red particles from input 1 towards output 4 at an angle. In both setups the red and green particles are affected by F_R, but the green particles do not develop sufficient velocity to successfully migrate over the given distance of the SSAW zone. The particles in the figure have a positive Φ.

Apart from R-SSAW, particle separation can also be achieved with a R-TSAW. But these setups tend to have higher frequencies compared to their SSAW counterparts in order

to compensate for the smaller acoustic energy amplitude (Destgeer et al., 2013). Furthermore, when applying a R-TSAW using an IDT with straight IDEs it can result in particle patterning in soft microchannels. This phenomenon arises from the Huygens-Fresnel principle, wherein the vibrations of the soft walls generate secondary waves that superimpose with the R-TSAW, resulting in the formation of an unintended R-SSAW (Devendran et al., 2017). This is undesirable since the wanted outcome is to achieve actuation similar to that of the taSSAW, where a deflection is created that pushes particles from one wall of the microchannel towards the other.

As such, to achieve the desired effect of deflecting the particles using only one IDT, typically a focused unidirectional SAW transducer (FUT) is used (Destgeer et al., 2013), which has also been referred to as FIDT (Li et al., 2019). The FUT design creates a focus region of R-TSAW which results in a highly localized beam. This beam creates two powerful steaming vortexes that that can push particles away from them. This effect is shown in Fig. 1.12a, where a FUT pushes particles from one side of the microchannel to the other. But apart from the FUT, another IDT design worth mentioning are slanted IDTs (H. Yatsuda *et al.*, 1990), shown in Fig. 1.12b. This design has a varied pitch along the IDT, by having slanted IDEs, which creates different operating frequencies along the IDT that create R-SAWs with different wavelengths. This gives the slanted IDT the capability to only stimulate a specific region along the IDT by choosing the required operating frequency, as shown in Fig. 1.12b.

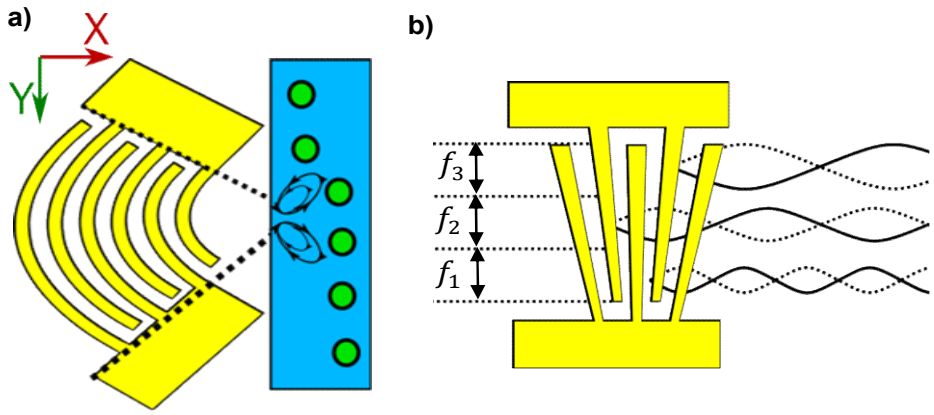

Figure 1.12. Different designs of IDTs. a) A focused IDT that incorporates a semi-circular design to create a highly focused R-TSAW. The highly focused R-TSAW can generate two streaming vortexes that can deflect incoming particles. b) Slanted IDT design where the IDEs have varying pitch along the Y. This creates the ability to stimulate specific regions along Y by choosing specific operating frequencies, where $f_1 > f_2 > f_3$, different region of the IDT along the Y axis.

1.3.4. L-BAW and R-SAW prominence

It should be noted that despite all the different types of waves, the sound waves used commonly in acoustofluidic actuation-based applications are L-BAWs, Rayleigh SAWs (R-SAWs) and Lamb waves. The main reason behind this is their wave type suitability for different acoustofluidic applications, with L-BAWs, R-SAWs and Lamb waves being more suitable for particle actuation (Ozcelik et al., 2022), while SH-BAWs, SH-SAWs and Love waves being most suited for bio sensing applications (Baumgartner and Westerhausen, 2023).

This is due to the amplitude (oscillation) direction of generated wave by the L-BAW, R-SAW and Lamb. From Figs. 1.3 and 1.4 it can be seen that these three waves' amplitude vector is directed outwards, towards a location where the fluidic medium or microchannel will be positioned at (refer Figs 1.7 and 1.9). This type of orientation results in most of the acoustic energy being diffracted into the fluidic medium (see Fig. 1.8), which is highly desirable for actuation based applications. This results in most of the acoustic energy being directed into the fluid and utilised to generate actuation, via acoustic streaming or via the acoustic radiation force. But for sensing application the aim is to maintain as much as possible of the wave's amplitude and transmit it to an opposing transducer to observe the changes on wave's signal (Baumgartner and Westerhausen, 2023). SH-BAWs and SH-SAWs have a large portion of their waves' amplitude within the material, and as such there will be less energy leakage and more signal preservation, which is what is needed for sensing applications (Baumgartner and Westerhausen, 2023). But even from these two waves, SH-BAWs and SH-SAWs, the latter tends to be preferred in sensing due to SH-SAWs having a higher sensitivity rate (Fu et al., 2017). But it should be noted that this could be an effect generated from the piezoelectric substrate that is used, quartz, and possibly not a direct short coming of the wave type itself (see section 2.2). Decreasing the energy loss in sensing applications can also be further improved by adding a waveguide, and thus creating Love waves. This will further decrease the power dissipation into the liquid and will create waves that are highly sensitive to physical changes, such as mass and viscosity, for better sensing in both gas and liquid environments (Rasouli et al., 2023).

From this point, one can observe why L-BAWs, R-SAWs and Lamb waves will be preferred for particles actuation. But from these three waves L-BAWs and R-SAWs still appear to be more commonly used, with SAWs devices being observed is many more application, as will be seen in section 1.4. This is potentially due to their versatile design nature (IDT pairs and various designs) and capability to be placed away from the microchannel/ fluidic medium (see Figs. 1.7 and 1.9). Lamb waves devices have the advantage of multiple usable acoustic modes and frequencies that can be excited within a single device (Hsu and Chao, 2021), but the payoff is a less efficient wave for fluidic actuation (Wang et al., 2021). Furthermore, the author speculates that having thin

substrates, needed for Lamb waves, would require careful handling, if made from fragile material. Also having the bottom side of the substrate vibrating could create the need for custom working holding, in comparison to a substrate that has an inert bottom surface. As such one can clearly see the advantages of L-BAWs and R-SAWs compared to other waves, at least in actuation based acoustofluidic applications, which is what this thesis is focusing on.

1.4. Acoustofluidic devices in biomedicine

As stated previously, acoustofluidic devices have been widely applied in the biomedical research due to their ability to provide a label free method to actuate cells, for manipulation or separation based applications. One of their greatest advantages is their biocompatible nature, which has been demonstrated both in BAW device and SAW devices, as will be discussed later. Below different applications in biomedicine utilising BAW or SAW devices will be briefly described to provide an overview of the versatility of these devices. Finally, the author will briefly discuss which are the most prominent applications of the acoustofluidic devices, and which fields he believes would be the most promising for the acoustofluidics devices to be implemented and developed for.

1.4.1. Patterning/ Manipulation

Cell patterning is one of the most common applications of acoustofluidic devices, offering a powerful tool for recreating tissue structures with the use of biomaterials such as hydrogels. SAW devices have emerged as a popular choice for these applications and researchers have utilised SAW devices to precisely pattern different cell types, to mimic arrangements found in specific tissues. For instance Deshmukh *et al.* (2022) used a SSAW to pattern myoblast cells into lines to mimic muscle tissue, while Naseer *et al.* (2017) used two slanted IDTs to align cardiac cells and build them into a 3D structure. Cell patterning techniques have extended beyond tissue mimicking and have been employed to create custom cell cultures with specific effects. Where, for example, Cohen *et al.*, (2020) patterned neuron cells into clusters, using both SAWs and BAWs, which then demonstrated an effect on their outgrowth directionality. Li *et al.*, (2014) demonstrated that by aligning cells within a microchannel, letting them deposit and adhere to the substrate, they could then offset the SSAW, introduce new cells, align them and let these newly introduced cells to deposit and adhere next to the first cell sample. With this method they created a monoculture of HeLa-HeLa (cervical cancer) cells and dimorphic culture of HeLa and HMVEC-d (Human Lung Microvascular Endothelial) cells, which allowed them to study their interactions. One of the most impressive applications of cell patterning has been demonstrated by Kang *et al.* (2018), where HUVEC/hADSC (human umbilical vein endothelial cells and stem cells) were patterned, co-culture and cured in a hydrogel into a 3D structure. This 3D structure was achieved with the help of

reflective top layer, made from glass, that allowed the formation of PNs in both XY and YZ direction. This engineered tissue was subsequently transplanted into mice, resulting in improved recovery of damaged tissue.

In addition to line patterning, a more advanced technique called 2D cluster patterning can be achieved by introducing a second pair of IDTs perpendicular to the first pair, i.e. having a pair of IDTs both in the X axis and Y axis. This approach offers unique advantages for applications such as single-cell analysis and the study of cell-cell interactions, since it can allow the formation of small cell clusters instead of lines, i.e. a grid. This precise single cell or an organism cluster formation can allow researcher to both better observe and study effects on the cells. Guo *et al.*, (2015) used this technique to create clusters of HEK 293T (Human embryonic kidney) cells and study the cell to cell interaction, of when these cells were patterned and allowed to adhere to the substrate and while they were held suspended using SSAWs. The patterning shape can also be made more complex by introducing more sets of IDTs around a microchannel, which was demonstrated by Tian *et al.*, (2019) with a decagon like shape of IDTs that operated at various frequencies. This device was able to achieve both cluster patterning and active cluster manipulation, such as rotation, shape switching and movement in X and Y.

1.4.2. Separation

The second most common application of acoustofluidic devices is the separation of cells based on their size and mechanical properties. But before this section can be discussed in detail certain key terminologies should be stated. These terminologies are separation efficiency and purity, with separation efficiency referring to how many of the target cells were successfully separated (i.e. ratio of target collected cells vs target wasted cells) and purity referring to the percentage of target cells compared to the untargeted cells at the collection ouput (ratio of unwanted cells against total cell number in the collected sample). It should be noted that separation efficiency has also been referred to as recovery rate in literature, but for here for consistency it will be kept as separation efficiency.

Most commonly SSAW devices are used for this application, with a parallel IDT setup being successfully used to separate Escherichia bacteria from peripheral blood mononuclear cells (PBMC) with 91.5% separation efficiency (Ai *et al.*, 2013). SSAW based devices can also be combined with other techniques, such as imaging analysis, and in a study by Nawaz *et al.*, (2020) a single cell channel was used to separate 3 different cell types. In this study, the SSAW was applied in a controlled manner, triggered by the image analysis software to selectively actuate the desired cells, where based on size and deformation, red blood cells (RBCs), lymphocytes and myeloid cells were separated with purities of 96.6%, 89.1%.and 94.7%, respectively.

The utilisation of SSAW devices for the separation of target cells, particularly circulating tumour cells (CTCs), has emerged as a prominent application in the field. CTCs originate from tumour cells and exhibit a larger size compared to normal cells. CTCs have been speculated as potential valuable biomarkers for cancer, even in the early stages of cancer (Wu et al., 2018). These cells can be used as a prognostic tool for cancer and due their larger size they have been a perfect candidate for acoustofluidic separation using a continuous SSAW. A noteworthy study conducted by Li *et al.*, (2015), demonstrated the successful separation of various types of CTCs from white blood cells (WBCs) using a tilted angled SSAW (taSSAW) device. The continuous application of SSAW allowed for the selective manipulation of CTCs based on their distinct mechanical properties, resulting in a separation efficiency exceeding 83% and a purity of 90%. This device setup was later optimised and its throughput was greatly increased by incorporating a PDMS-glass top hybrid channel, where the applied flowrate was able to be increased from 20 µL/min to 125 µL/min (Wu et al., 2018).

It is worth mentioning that R-TSAW devices have also been utilised for cell separation; however, these devices typically incorporate a labelling and a sensing system that controls the activation of focused unidirectional SAW transducers (FUTs) or focused interdigital transducers (FIDTs). This approach is necessary to mitigate the high streaming effects and elevated temperatures that can be generated during FUT/FIDT operation (Li et al., 2019). In a study, Li *et al.*, (2019) created a sheath less channel where fluorescence sensor was employed to activate the FUT and selectively push target cells towards the collection output. This design successfully achieved the separation between labelled and unlabelled populations of MCF-7 (breast cancer), MDA-231 (metastatic breast cancer) and hiPSC-CMs (human induced pluripotent stem cell derived cardiomyocyte) cell lines with a separation efficiency of 90% and purity of 100 %. These cells also demonstrated a minor drop in viability from the control (by ~4%) by utilising the pulsed technique, with MCF-7, MDA-231 and hiPSC-CMs still maintaining ~92%, ~92% and ~83% viability, respectively. Similar setups were used by Li and Ai, (2021) to separate live and fixed MCF-7 cells, achieving a purity of ~92%, and Zhong *et al.*, (2021) to separate live and dead PBMCs after thawing, achieving a purity of 90%.

Apart from cells separation, i.e. micro scale, SAW devices have been constantly pushed to the nanoscale manipulation, < 1 µm, due to the potential biomedical applications in this field. One such application lies with extracellular vehicles (EVs), an intercellular cargo released into the cellular environment and shown to be responsible for cell-cell communication as well as cell modification, such as cell mutation from a benign to a cancerous (Osaki and Okada, 2019). EVs tend to be grouped into two main categories, macrovesicles (150-1000 nm) and exosomes (30-100 nm), with their main difference being how they were produced by the cell, i.e. membrane shedding or endosomal

pathway, respectively (Colombo *et al.*, 2014). Exosomes have attracted huge interest due to their ability to act biomarker for cancer (Verma et al., 2015) and their potential for various therapeutic applications (Lener et al., 2015). As it can be observed the size difference between cells, 10-20 μm, and EVs is quite noticeable, and this naturally makes them a perfect candidate for SAW based separation.

The current successful exosome separations, with a microchannel, have all been achieved via a two stage taSSAW. This was firstly used by Wu *et al.*, (2017) to separate exosomes from whole blood, where the first stage (20 MHz) was used to separate EVs from whole blood cell elements, while the second stage used a higher frequency (40 MHz) and divided those EVs into two different subpopulations: vesicles and exosomes. To confirm the efficacy of exosome separation, the two EV subpopulations were subjected to analysis using western blotting and exosome-specific markers. The results demonstrated that the majority of exosomes were present in the collected exosome subpopulation. This device was subsequently utilised for various applications where it separated exosomes from plasma to be used as an early diagnosis indicator for brain injury (Wang et al., 2020) and saliva from multiple patients to determine whether they had cancer (Wang et al., 2020).

In contrast to their SAW counterparts, BAW devices have been less commonly employed for separation applications. Xu *et al.,* (2019) used a BAW transducer of 8 MHz and, with the assistance of 6 μm particles, enhanced the trapping force at the developed PNs to trap and hold sperm cells. This sperms cells were trapped, then the microchannel was depleting of the sample, and then these sperms were released and flushed through a different output for recovery. While Olm *et al.*, (2019) used two BAW transducer (5 and 2 MHz) to pre-align and separate neuroblastoma cells (NBCs) from peripheral blood progenitor cells (PBPCs). The best separation results showed that the two cells could be separated with a separation efficiency of 40-70% and >90% for the NBCs and PBPCs, respectively. It should be noted that BAW devices often modify the acoustic impedance of the liquid to enhance the separation of specific cells. This method was used by Chen *et al.,* (2016) where a channel made of stainless steel sheets and a BAW transducer (225-237 kHz) was used to separate platelets from RBCs/ WBCs with the assistance of a medium modified with dextrose. In this study, they achieved a platelet serration efficiency of 80% and purity of 88% with a flowrate of 10 mL/min and of 86% at a flowrate of 5 mL/min. Similarly Karthick *et al.*, (2018) used iodixanol to separate MDA-MB-231 and HeLa CTCs from PBPCs, using a 1.805 MHz BAW transducer, with a separation efficiency of 86% and 88%, respectively. A BAW transducer, using the same technique was also used by Van Assche *et al.*, (2020) to separate bacteria from blood lysis debris.

1.4.3. Concentration

While concentration of particles using a surface acoustic wave (SAW) offset and a droplet has been demonstrated, this method often requires precise fine-tuning and accurate positioning of the droplet (Destgeer et al., 2016). To provide a more reliable and efficient approach for particle concentration, alternative designs have been developed. One such method was demonstrated by Liu *et al.* (2020), where BAW transducers with a hole in their centre were bonded underneath the wells of a multi-well plate and successfully concentrated two type of cancer cells (HeLa and MCF7) in the middle of the transducer. Following the same philosophy, Zhang *et al.* (2021) developed a spiral circular IDT to concentrate particles in the centre of it, while also integrating a syringe underneath the droplet to extract the concentrated sample.

Similarly to separation, concentration of nano particles has also been challenging in this area. But this road block was overcome by Gu *et al.*, (2021) who used a SAW device with two set of slanted IDTs and PDMS ring. The slanted IDTs allowed the application of a fine-tuned SAW offset, without having to move the droplet, and using two IDTs increased the torque for faster concentration. The incorporation of a PDMS ring helped to hold the sample in the same position as well as to stop the actuation of the droplet at higher powers. Using this setup they managed to successfully concentrate exosomes and the same setup was later used by Wang *et al.*, (2022) to load and encapsulate exosomes into porous silica nanoparticles for drug delivery applications.

1.4.4. Stimulation/ Transfection

Cell stimulation is an expanding area within acoustofluidics, driven by the ability of high-frequency acoustic energy to promote or enhance specific cell behaviours. One study exposed bull sperm cells to R-SSAW and demonstrated an increase in their mobility (Gai et al., 2022). Brugger *et al.* (2020), demonstrated the improvement of wound healing properties with MDCK-II (Madin-Darby canine kidney) cells, where the acoustic energy would enhance the migration of neighbouring cells resulting in faster closure of an open wound. This enhanced migration, for wound healing applications, was also demonstrated by Imashiro *et al.* (2021), where it was demonstrated that fibroblast cell migration increased along the direction of the propagating wave. Finally, Sun *et al.* (2022) demonstrated with a T-RSAW the accelerated differentiation and maturation of neurons cells derived from human embryonic stem cells (hESCs).

Apart from increasing cells characteristics, acoustic energy can also be used to either increase cell permeability for higher cargo uptake, i.e. transfection, or increase the secretion of valuable cargos. Guo *et al.* (2021) generated L-BAWs, using a thin film bulk GHz resonator, that were able to controllably deform cells and increase cell membrane permeability of HeLa cells. The increased permeability and uptake was demonstrated by the acoustically exposed cells being mixed with fluorescence molecules, where the acoustically exposed cells showed a stronger fluorescence signal within the cell than the

control. The permeability and uptake increase was further demonstrated by Ramesan *et al.*, (2021), where a high FUT was used to increase the siRNA permeability of Jurkat and HuT 78 cells (T cells). In this study the cells exposed to acoustic treatment showed a similar uptake efficiency as the nucleofection, a conventional method of transfection, while also maintaining a high cell viability of 91%. Using a similar setup Kim *et al.*, (2022) initially attempted to stimulate NK-92 (Natural killer) immune cells to increase their cytotoxicity. While they were successful when compared against the control, the results were less significant against the positive control, which utilised an antigen. Although the acoustic stimulation was not as effective at purely stimulating the cells, it was then used to successfully increase the uptake of the antigen, when compared against a sample with the antigen and no acoustic energy. This application of acoustofluidic devices helping with antigen uptake has also been demonstrated again with Jurkat T-cells, using a BAW transducer, by Centner *et al.*, (2021), where, with the assistance of microbubbles, they increased the T-cell uptake of calcein. The same device was then used to demonstrate T-cell calcein uptake between a static and continuous flow system acoustic system. In this study the flow-based acoustic system improved the uptake speed of cells from 45 s to 2 s (Centner et al., 2023). This increased uptake of was also demonstrated by Belling *et al.*, (2020) with Jurkat cells, PBMCs (peripheral blood mononuclear cells) and $CD34^+$ HSPCs (umbilical cord blood $CD34^+$ hematopoietic stem and progenitor cells) by also using a BAW transducer. Finally, apart from the uptake results, Ambattu *et al.* (2020) demonstrated the increase segregation of exosomes in A549 and U87-MG (mammalian cancer) cells with the use of a SAW device.

1.4.5. Cell viability

One of the strongest points of the acoustofluidic devices is their biocompatible nature, as such herein a section is introduced to briefly discuss this. A thorough investigation of the effect of acoustic pressure on cell viability was conducted by Ohlin *et al.*, (2015), where it was demonstrated with 2 MHz BAW device and A549 cells. Using this device the A549 cells were trapped and held under an acoustic pressure of 1 MPa, where it was shown that this force doesn't affect their viability, as long as the temperature is controlled. While Chen *et al.*, (2016) demonstrated that separating platelets from WBCs/ RBCs at 46 V_{pp} (Peak to peak), using a BAW device, didn't affect their viability more than that of the conventional centrifuge separating method.

On SAW devices it has been demonstrated that an IDT with a 23.9 MHz frequency under 40 V_{pp} will generate only 0.4 MPa of acoustic pressure via simulation (Chen et al., 2018) and as such at this energy they should be safe to operate. The cell viability of inflammatory cells has also been demonstrated by using a 19.54 MHz IDT actuated at 34 V_{pp}, with a total flowrate of 10 µL/min, where no decrease of viability was shown when compared to the control (Li et al., 2016). The IDTs viability has also been demonstrated

with 19.573 MHz device actuated at 38 dBm (~ 6.31 W) with flowrate of 20 µL/min using HeLa cells, where \gain the cell viability didn't show any significant reduction from the control (Li et al., 2015). All these results were demonstrated in separation applications, but the viability of cells has also been documented in transfection applications. Where using a FUT of 30 MHz at a power input of 10 V for 10 min Jurkat and HuT 78 cells still maintained a viability of >91% (Ramesan et al., 2021). While Belling *et al.*, (2020) using a 3.3 MHz BAW transducer actuated at 40 V and a flowrate of >65 µL/min showed of a Jurkat cell viability of ~77%. This study also demonstrated that the viability starts to drop when the voltage is increased to 60 V as well as when the flowrate is decreased.

One can see that a variety of units can be used to describe the performance of acoustofluidic device such as; acoustic pressure (MPa) or by the input power into the device in either volts peak-per-peak (V_{pp}), dBm or Watts (W). Acoustic pressure, while is the most correct method, is not often used for the simple reason that it is very difficult to measure since it requires either expensive equipment, such as a laser vibrometer, a PIV software, with a camera strong enough to run it, or to develop a custom procedure to evaluate the acoustic energy density. As such typically it is much easier to just specify the input power into the device, either in V_{pp}, dBm or W. This potentially demonstrates that acoustofluidics is still a young field of research and will potentially require some standardisation in the future to unify the field. But the above results at least give researchers an idea what type of power can be applied to these devices without drastically affecting the cell viability. In fact it appears that cell death introduced via acoustic means typically is introduced as a result of temperature rise or due to cavitation via microbubble bursting, referred as thermal and cavitation based ablation, respectively (Liao et al., 2024). Therefore, as least of now, it can be assumed that the power and the scale these devices currently operate at, their acoustic pressure would not be the main cause for cell viability degrease. But rather this decrease would most likely be caused by the secondary effects they create, such as heat.

1.4.6. In demand applications in biomedicine and microfluidics

In the above sections various biomedical applications have been discussed, but most certainly some applications would be more desired than others. But to answer this question as objectively as possible, one would need some type of a measurement to establish what is in demand in the biomedical research field. A potential measurement of the demand for research could be the number of publications that have been published for the specific applications. As such to establish which applications would be the most promising ones the author has selected various cell based applications and investigated how many publications they had in the timeframe of 2000-2023. The selected applications were "Cell Sorting", "Cell Stimulation", "Cell Transfection", "Cell Manipulation", "Cell Patterning" and "Concentrating cells". It is worth mentioning that cell

sorting is a more popular term than separation, but occasionally these terms are used interchangeably. This term is used to probe how desired separation related applications are since sorting is a type of a separation of itself. Additionally, it should be noted that “concentrating cells” was chosen instead of “Cell Concentration” due to the latter being commonly used in papers to describe the cell quantity of the sample that was used instead of the action of concentrating cells. As such a less accurate wording had to be used to capture the actual application, but this also will result in a less accurate representation of this application. Applications with cells were selected due to acoustofluidics having a great focus on the applications revolving around cells, as well as biomedicine itself having a lot of applications utilising cells. The specific keywords that were used to search each subject, such as “Microfluidics” and “Acoustofluidics” are shown in Appendix 1. It should also be noted that publication results highly depend on the appropriate wording selection and as such these results could potentially overestimate, underestimate or misrepresent an application if the correct wording was not used or their wording overlaps with other fields. As such the following figures can only offer an estimation of what potentially is in demand and are subject to personal interpretation. Nonetheless, the author will use the following figures to offer some of his personal interpretation assuming that the search results are somewhat trustworthy and accurate.

Fig. 1.13 shows the results for different cell related application and the number of publications they have. The green column demonstrates the results when no additional keyword was added, and the blue column shows the results when the keyword “Microfluidics” is included. From this figure it can be seen that the cell applications that have the most publishing are “Sorting”, “Stimulation” and “Transfection”, but for microfluidics the most popular applications would be “Sorting”, “Manipulation” and “Patterning”.

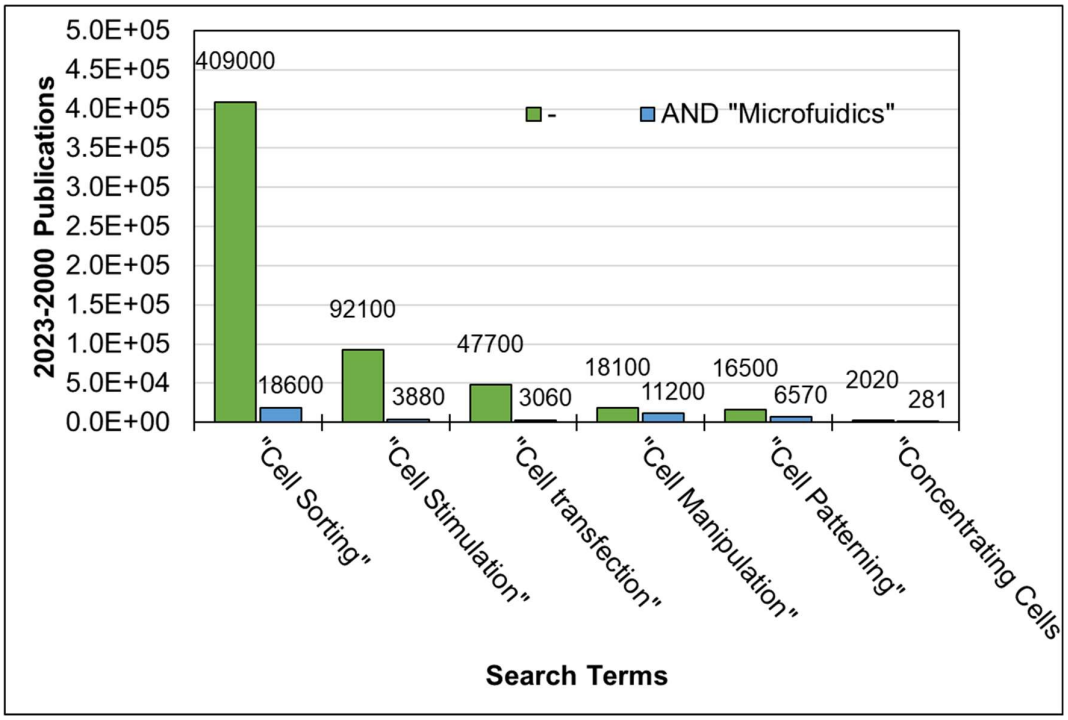

Figure 1.13. Publication results for various cell related applications between during the timeframe of 2000-2023. The green column shows the results for the applications with no additional keywords, while the blue column shows these applications while also including the keyword “Microfluidics”.

Before reaching any conclusion, it would be also interesting to explore from the point of acoustofluidics how much they correlate with the results shown in Fig. 1.13. Fig. 1.14 shows the results for when “microfluidics”, “acoustofluidics” and “microfluidics” AND “acoustofluidics” are included in the search term. In this Fig. 1.14 two things can be observed, a) that the acoustofluidic publishing follows a similar trend with the results of microfluidics and b) that most of the acoustolfuidics applications are related directly or indirectly to “microfluidics”. The second claim is backed by the fact adding the word microfluidics to acoustofluidics barely reduces the number of publications present, which then establishes that there is strong correlation between the two. Based on these results it can be clearly seen that the most popular application is cell sorting. But in regards what is the next most prominent, if microfluidics is consulted it would be “cell manipulation” but if pure cell based applications are consulted then “cell stimulation” would be the most prominent application.

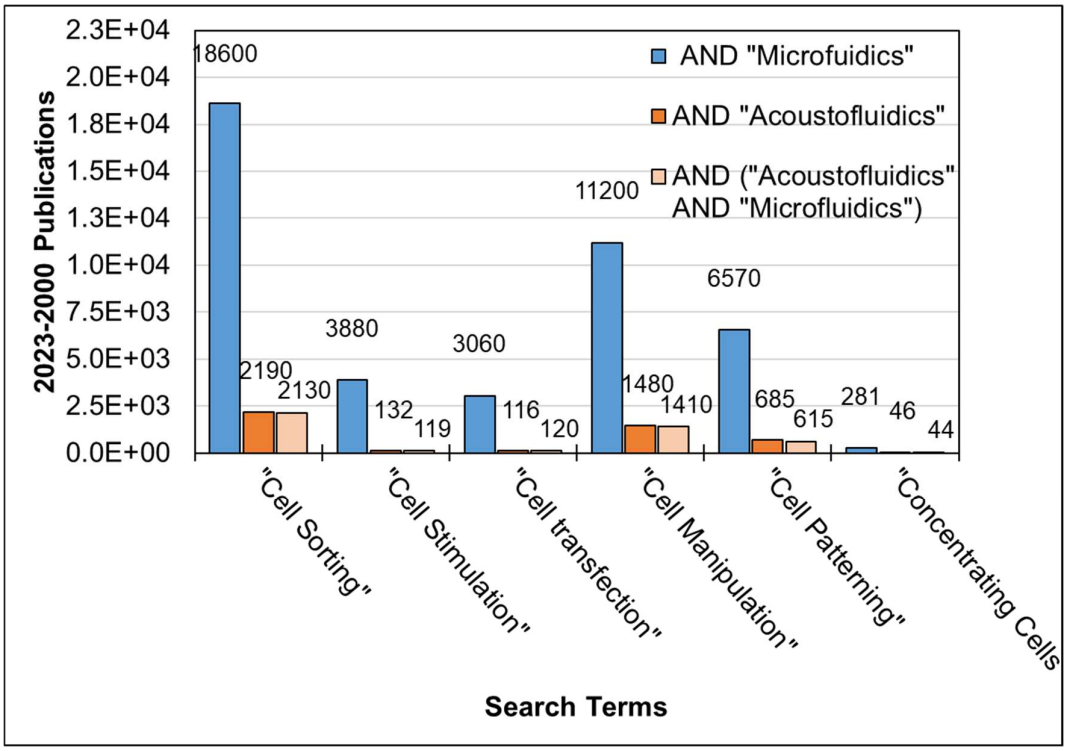

Figure 1.14 Publication for various cell based applications with the keywords “microfluidics”, “acoustofluidics” and (“microfluidics” AND “acoustofluidics”) included, represented by the blue, orange and light orange column, respectively.

By using the above results, the author can then provide some of his own speculations on which applications are the most promising applications for acoustofluidics to be applied and developed for. First, it is chosen to put more emphasis on the results shown in Fig. 1.13, without the inclusion of microfluidics. This choice is made to highlight promising research applications and to speculate what is desired overall in the biomedical field, without being limited by the current paradigm in acoustofluidics and microfluidics. The next step then is to determine, which applications would be the most suitable for acoustofluidics to be applied on, which will be based on the current available literature. In his own opinion, the author speculates that the most promising applications would be cell sorting/ separation and cell transfection, since in both of these applications acoustofluidic devices have demonstrated promising results.

The large amount of research done cell sorting could potentially be explained by the multitude of research fields requiring the sorting/ separation of cells, such as cancer diagnostics (He et al., 2020), therapeutics (Schriebl et al., 2010) and cell biology studies (Mattanovich and Borth, 2006). For this field, acoustofluidic devices have already demonstrated their capability of separating cells with a plethora of examples of their successful application, see section 1.4.3. But from section 1.4.3, it can be seen that acoustofluidic devices currently place a large focus on cancer diagnostics applications,

with most separation applications utilising some sort of cancer cell (such as HeLa and MCF-7). But acoustofluidic separation can also be useful for other applications such as HIV diagnosis and treatment (Cheng et al., 2007) and malaria diagnosis and treatment (Gascoyne et al., 2002). While in the case of cell therapy, the separation of neuronal cells can be potentially used in applications such as cell replacement therapy for neurodegenerative disorders such as Parkinson's disease and Alzheimer's (Korecka et al., 2007) by separating STEM cells from heterogeneous samples (Zhu and Murthy, 2013). Therefore, it can be observed that acoustofluidics separation, while currently focused on cancer diagnostic, has the possibility to be applied to a variety of fields and trialled in where there is a need for effective separation techniques.

While cell transfection's popularity could also be explained due to the rise in the recent years of cell-based therapy, in particular Stem (Zakrzewski et al., 2019) and T-cells (Sadelain et al., 2017). In cell-based therapy both of these play a very important role, with STEM cells having the capability to be applied in diseases where it is required to have transplantable tissues and organs such as; macular degenerations (Sun et al., 2017), strokes (Liu, 2013), osteoarthritis (Gangji et al., 2011), neurodegenerative diseases (Pramanik et al., 2017), and diabetes (Shahjalal et al., 2018). While T-Cells play a pivotal role in cancer therapy using CAR T-cells, where the cell are modified via to obtain their desired properties via viral vectors, i.e. bacteria or viruses. Viral vectors although effective have the limitation of safety issues, high manufacturing cost and vector capacity constraints, and it has been speculated that non-viral delivering techniques can address these issues and help scaling up their production (Raes et al., 2021). Acoustofluidic transfection is a non-viral transfection, i.e. it delivers molecules and cargo directly to the cells without requiring viral based vectors, and as such it has the potential to be applied in the field of CAR -T cells engineering. But apart from T-cells, it also has been shown capable of transfecting STEM cells, thus showing potential in both applications, see section 1.4.5.

For the second most prominent application one will wonder why cell transfection was chosen over cell stimulation. The reason is that while acoustofluidic cell stimulation has been shown in promoting neural STEM cell differentiation and improving wound healing, it is hard to say if a desired cell stimulation can always be achieved. This example was shown with the Jurkat T-cells, where while stimulation was not possible the same device had no issue of improving the uptake of antigen of cells (Kim *et al.*, 2022). This then potentially hints that transfection is a more suitable application for acoustofluidic devices. Additionally, a main reason why that transfection is chosen over something like manipulation, is that transfection based devices have the great advantage of typically utilising a setup that is much simpler than both the manipulation/ pattering and sorting/ separation devices. First, transfection devices typically don't require flow or a complex

microchannel, the microchannels used are typically a “well” type microchannel that can be easily manufactured due to their simple geometry. Additionally, they can use only one transducer, to generate acoustic streaming, and don’t have to precisely align or actuate particles. These devices just need to provide sufficient acoustic energy to initiate the transfection of the cells. This simplicity in both setups and operation then gives them the advantage of very easy development and implementation when compared to other acoustofluidic applications. As such transfection devices have both proven their capability in literature, but also have the capability to be easily applied to various applications.

But it should be noted that even though these two sorting/ separation and transfection are the most prominent application, selected by the author, the criteria of their successful operation are very different. Separation uses heterogeneous cell samples and attempts to separate them by actuating them based on their mechanical properties, while cell transfection uses relatively homogeneous samples and attempts to apply sufficient acoustic energy to permit cargo uptake. Therefore, even though both of these applications utilise acoustophoretic forces, the criterion for their successful application varies drastically. Due to these differences, it would be difficult to accurately cover or perform both of these applications. This thesis scope is mainly focused on demonstrating a new fabrication technique for SAW devices. As such while cell transfection is another a promising field for the acoustofluidic devices to be applied in, this thesis will primarily focus on demonstrating the new fabrication techniques by initially showing their manipulation/ pattering capability and then actuation capabilities. These two fields share a similarity in their successful applications, i.e. actuation of particles in a pre-determined manner, and these two applications are still quite popular for microfluidic based acoustofluidic applications, as can be seen in Fig. 1.14.

1.5. Acoustofluidics and other separation techniques

While acoustofluidics is a prominent technique in cell separation, other competing techniques exist in the field of microfluidics. These techniques can be separated into two broad categories, passive and active separation techniques. Some of the passive methods are deterministic later displacement (DLD), inertia and filtration (Zhang et al., 2021), while some of the active separation methodologies are dielectrophoresis (DEP), optical tweezers (Ots), magnetophoresis and acoustofluidics (Bhagat et al., 2010). In thia section these techniques will be briefly discussed to demonstrate the working principle behind each technique as well as some of the short comings that they have when compared against acoustofluidics. It should be noted that separation was chosen as the primary application of comparison due to its high demand and variety of competing technologies in this field.

1.5.1. DLD, inertia and filtration

Deterministic lateral displacement (DLD) in a technique that creates a microchannel that has a series of periodically arranged obstacles inside the main channel, which are designed based on the particle's sizes and their flow characteristics in a laminar flow. The design is made in a way that based on the size of particles, the particles of certain size would be redirected to different flow streamlines and as such end up in different outputs downstream (McGrath et al., 2014). This type of device has been used to successfully separate MCF-7 and MDAMB231 from peripheral blood cells using 2 ml/min flowrate with 99% and 80% separation efficiency, respectively (Liu et al., 2013).

Inertia based separation utilises the existence of a velocity gradient to separate particles. In short, in laminar flow particles are pushed forward by the fluid, with the flowing liquid having a parabolic profile. This profile will slowly then push particles away from the centre of the microchannel and towards the microchannel walls. But when the particles are close to the channel wall, the side walls will produce a force on the particle that keeps the particle away from the wall. The position of the particles along the channel will depend heavily on particle diameter, indicating the possibility of separations based on differential migration. But in straight channels, the particles will have multiple equilibrium positions, and the equilibrium positions of particles of different sizes are very similar (Xu et al., 2021). To overcome this issue curved inertial microchannels have been developed to introduce a secondary rotational flow caused by inertia of the fluid itself, called Dean flow. This adds a centrifugal force into the microchannel making the fluid to tend to move towards the outer wall. In this type of microchannel larger particles will gather closer to the inner wall, inner radius of the microchannel, while smaller particles will be located near the centre, thus giving the capability to achieve separation (Xu et al., 2021). The curved inertia microchannel has been successfully used to separate SH-SY5Y cells from C6 glioma cells with more than 80% separation efficiency at a 3 mL/min flowrate (Kuntaegowdanahalli et al., 2009), and in another case MCF-7 cells were successfully separated from peripheral blood cells with 100% separation efficiency at a 1 mL/min flowrate (Burke et al., 2014)

Finally, the filtration methodology relies on the introduction of pores/ pathways of a specified size to separate particles based on their size, i.e. filtering. One example of this application was capable of separating WBC from RBC using 3 μm porous membrane with ~ 100 % separation efficiency using a flowrate of 37.5 μL/min (Cheng et al., 2016).

While these techniques implement somewhat different techniques they, perhaps unsurprisingly, share similar disadvantages. In the sense that these techniques increase the complexity of the channel design and required careful design considerations to achieve the desired separation of the pre-selected particle size. Furthermore, once the channel has been designed it cannot be modified and can only separate particles based

on the selected critical diameter size, which holds true for DLD (McGrath et al., 2014), inertia (Xu et al., 2021) and filtration based channels, with the addition that the final also can suffer from clogging issues (Dalili et al., 2019)

1.5.2. Dielectrophoresis (DEP)

DEP is a technique that actuates neutrally charged particles, in contrast to electrophoresis that actuates charged particles. Electrophoresis requires particles to either have a different charge to be separated or to have been labelled in order to achieve this differentiation, but its actuation speed is very slow and this methodology is restricted by the amount of power that can be inputted in order to not create any undesired effects such as electrolysis (Kwon and Oh, 2018). In contrast, DEP relies on the medium having an electric polarity while the cells remain neutral, which then could be used to actuate particles based on the polarity difference between the cells and the medium (Chen et al., 2015). DEP device were shown capable to separate MG-63 cells from erythrocytes with a separation efficiency of 83% (Ling et al., 2012). The disadvantage of DEP is that it requires a dielectric medium in order to actuate the particles. The medium is also preferred to be of low conductivity, since a higher conductivity medium will create higher heating effects, but unfortunately most biological mediums have high electric conductivity (Kwon and Oh, 2018). Finally, the design of DEP electrode is critical and tends to have to be incorporated very close or inside the channel, which increases complexity of the design (Chen et al., 2015).

1.5.3. Optical tweezers (OTs)

OTs utilise light waves to create a focal point in order to actuate the particles. The motion of particles will depend on various conditions such as the size of particles compared to the wavelength as well as the shape of the particle. Due to the complex nature of this actuation there are different simulations models that can be used establish the movement of the particles (Pesce et al., 2020). But in short, the lasers are focused into a focal point which then creates a “trap” for the particles, similarly to the nodes in acoustofluidic devices. OTs have been used to separate hESC cells with fluorescent marker from unmarked ones, using a single cell actuation with a 90% separation efficiency and 90% purity (Wang et al., 2011). One disadvantage of OTs is that due the small size of the focal trap, they are typically implemented for single cells manipulation and struggle with large throughput. Additionally, due to the high intensity laser used in this application the cells tend to suffer from photodamage (Keloth et al., 2018)

1.5.4. Magnetophoresis

Magnetophoresis utilises magnets to create a magnetic repulsion or attraction force to actuate particles. The magnetic properties of cells are naturally either weak or non-existent, as such these devices typically magnetically label the cells or increase the magnetic properties of the medium, using mediums such as paramagnetic salts (Su et

al., 2021). Both these methods have been used to successfully separate cells, with paramagnetic salts being used to separate label-free U937 cells from RBCs with >90% purity (Shen et al., 2012) and magnetic nanoparticles being used to separate macrophages from monocytes with a purity >88% and separation efficiency >60% (Robert et al., 2011). While magnetophoresis has demonstrated its capability of separation, it suffers from a similar issue as DEP. To enhance the magnetic force either a paramagnetic medium must be introduced or cells should be magnetically labelled. This then makes the need to either label the cells, or restricts the mediums that could be used for the cell separation (Su et al., 2021).

1.5.5. Advantages of acoustofluidics

As such one can see that acoustofluidics offers unique advantages compared to other methodologies. When compared to passive technologies the user has the capability to use relatively simple channel design and transducer to generate adjustable actuation of particles based on their properties, to modify its actuation based on the sample used. Also, in the case of DLD and filtration, having a simple channel geometry that has no “barrier” or “pores” inside the channel makes it less prone to cloggage. While in active applications acoustofluidic has the capability of label free manipulation without needing to utilise specialised mediums or label the cells, which gives acoustofluidic advantage over techniques such as DEP and magnetophoresis. But it should be noted that the even though acoustofluidic can be used with most liquid mediums, the medium used will affect the actuation capability of the acoustofluidic devices, see eq. 22. While their capability to actuate a large number of particles in a biocompatible manner gives acoustofluidics an advantage in separation applications over techniques such as OTs, as long as there is sufficient cooling. As such one clearly see the advantages the acoustofluidics has to offer to biomedical application, at least in separation. It should be noted, it is chosen here to only focus on separation, to give a realistic comparison between the competing technologies for a specific application. In different applications these advantages and disadvantages may change, but to explore all these applications is beyond the scope of this thesis. As such, this brief overview is given to make the reader aware of these competing technologies and the advantages of acoustofluidic devices, while onwards focusing on the development of an alternative fabrication technique for the SAW based devices.

1.6. Research objectives

By exploring the capabilities of acoustofluidic devices, their potential significance in the future for biomedical applications becomes evident. But it is worth noting that while both BAW and SAW device have demonstrated their capability in separation and manipulation, SAW devices appear to be more versatile and commonly used in the

aforementioned applications. But the current manufacturing process for SAW devices requires high-end facilities, posing limitations to their accessibility and reconfigurability. Additionally, as it will be shown in Chapter 2, SAW devices, despite various piezoelectric substrate existing, most commonly utilise a few specific substrates. This is due to certain substrates having superior properties compared to others, and due the IDTs being permanently bonded to the substrates. Thus, making it is a risky investment to experiment with other substrates due to the potential negative results. As such if a new fabrication based method was established that makes the development of SAW devices more accessible as well as permitting the creation of IDTs that can be relatively easily coupled and de-coupled from piezoelectric substrates this could drive more research and room for experimentation in the field with SAW devices. Therefore, this thesis aims to accomplish the following objectives:

- Establish the current manufacturing techniques for BAW and SAW actuation based acoustofluidic devices, thus further establishing the advantages of SAW based devices and the limitation of the current manufacturing technique.
- Introduce the printing circuit board (PCB) manufacturing method, its advantages as well as why it would be a good alternative manufacturing for IDTs used in acoustofluidics.
- Manufacture the PCB based IDTs to fabricate a PCB IDT based SAW device, characterise it and compare it against the conventional device. Then, demonstrate its acoustofluidic actuation capabilities with particles (polystyrene microspheres) and cells, as well as its capability to couple with different piezoelectric substrates without the need of remanufacturing.
- Build upon the PCB based SAW device methodology by experimenting with different PCB substrates and develop any adjacent components required for the SAW device, such as the microchannel, using the most accessible means possible and off the shelve components to further capitalise on its accessible and reconfigurable nature.
- Develop a PCB SAW device to experimentally study the actuation and behaviour of particles based on their size and on microchannel orientations under continuous flow, to demonstrate its potential capability to be utilised for acoustofluidic based separation applications.

Through accomplishing these objectives, this thesis aims to advance the field of acoustofluidics by providing a more accessible and reconfigurable fabrication method for SAW devices. This new methodology could then broader the participation in this research field by enabling the reconfiguration of SAW device, fast prototyping, quick coupling of IDTs with different piezoelectric substrates and experimental based optimization for SAW based acoustofluidic devices. As well as the capability to quickly

explore different wave modes that can be generated on piezoelectric substrates by rotating the PCB IDTs, to suit different applications (Dumčius *et al.*, 2023).

Chapter 2

Manufacturing of Acoustofluidic Devices

2.1. Introduction

Among the introduced devices, SAW devices are some of the most frequently used devices in the field. For the separation and patterning applications this can be attributed, in part, to the capability of SSAW based device to utilise two IDTs to precisely manipulate the position of the PNs and the versatility in designing different IDTs on the substrate. But the ability to design different types of IDTs comes inherently from the high-end manufacturing procedure used as well as the careful selection of the available piezoelectric substrate that can be used. This chapter aims to provide a concise overview of different piezoelectric materials and explain the selection criteria for the manufacturing of piezoelectric transducers. Additionally, it will delve into the manufacturing processes of both BAW transducers and IDTs to shed light on why SAW devices exhibit such design versatility during their manufacturing.

However, it is important to note that while both BAW and SAW devices require various manufacturing procedures and the use of high-end equipment, BAW devices are generally considered more accessible compared to SAW devices. In light of this, herein an alternative method is introduced that utilizes interdigital transducers (IDTs) on a printed circuit board (PCB) to create a new fabrication process specifically for SAW devices. The primary objective of this fabrication process is to enhance the accessibility of manufacturing SAW devices and enable reconfigurable capabilities. In this chapter, the progression and optimization of this technique for acoustofluidic applications is briefly mentioned. However, the subsequent chapters will provide a comprehensive description and detailed discussion of this innovative fabrication method, covering its development, refinement, and its acoustofluidic capabilities. Furthermore, in this chapter the manufacturing of microchannels is also discussed in order to provide a comprehensive overview of the manufacturing procedures involved in producing acoustofluidic devices. This inclusion provides the necessary groundwork to address all the manufacturing processes of the components required for an acoustofluidic device, while also highlighting the different manufacturing techniques employed and their respective purposes.

2.2. Piezoelectric materials

Piezoelectric materials have many properties but three are most important for acoustofluidic devices: the coupling coefficient (K_{eff}), speed of sound velocity in the

substrate (c_s) and overall crystal structure. The coupling coefficient quantifies the efficiency of converting electrical energy into mechanical deformation, while the speed of sound aids in the designing actuators that possess the desired wavelength or operating frequency (Kirschner, 2010). The overall crystal structure refers to both to the crystal unit cell structure (Lynch *et al.*, 2017) and the crystal orientation (i.e. the cut) (Shur, 2017). Both these parameters are very important for how the material deforms, but the latter one appears to be more important in regards to the wave type it can generate (Shur, 2017).

A quick summary of these three properties is presented in Fig. 2.1. In Fig. 2.1a two piezoelectric substrates with identical IDEs are used to generate R-SAW. But substrate 2 has a larger K_{eff} which results with a R-SAW with a larger amplitude at the same power input (P_{in}). Similarly, Fig. 2.1b has two piezoelectrical substrates with identical IDEs, where the only difference is that substrate two has a larger c_s. This results with substrate 2 having a smaller R-SAW λ than substrate 1. Finally, Fig. 2.1c demonstrates that effect on the overall crystal structure of the material on the deformation the material undergoes under the piezoelectric effect. In this figure two abstract types of crystals are shown, type A and type B, where type A deforms purely vertically whereas the type B deforms diagonally. One could easily imagine based on this figure that type A would most likely be used for the generation of longitudinal waves while type B would more likely be used for the generation of transverse/ shear waves.

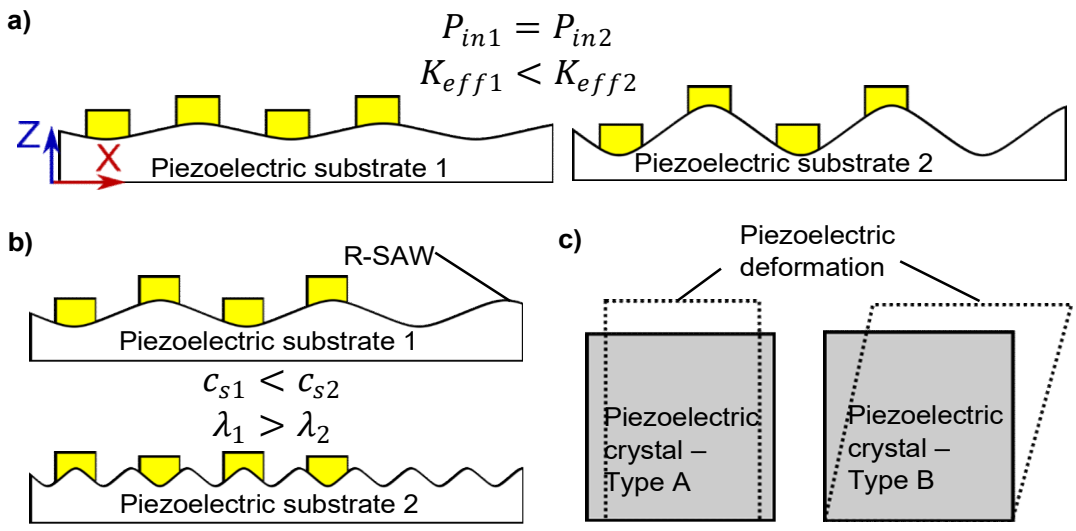

Figure 2.1. Piezoelectric substrates with different acoustofluidic related characteristics. a) Effect of the coupling coefficient (K_{eff}) on the amplitude of the generated R-SAW. Both substrates have the identical IDEs, but substrate 2 has a larger K_{eff} resulting with a R-SAW with a larger amplitude for the same power input (P_{in}). b) Effect of sound wave velocity (c_s) of the piezoelectric substrate on the wavelength (λ) of a R-SAW. Both substrates have identical IDEs, but substrate 2 has a smaller R-SAW λ due to its larger c_s. c) Deformation of the overall crystal structure of the material based on its intrinsic properties, where type A deforms purely vertically whereas type B deforms diagonally.

2.2.1. Lead zirconate titanate (PZT)

PZT is a solid piezoelectric solution that is based of lead, zirconate and titanate (Pb(Zr,Ti)O_3, PZT) which is used to create solutions such as; $PbZrO_3$ and $PbTiO_3$ (Kimura *et.al.*, 2010). It has the highest coupling coefficient (20-35) and a very high speed of sound (3900 m/s) (Fu et al., 2017), which lead to its wide applications in the market, despite of the environmental issues caused by the lead (Pb) (Kimura *et.al.*, 2010). PZT is mostly used to create ceramic substrates used in PZT transducers, which are also commonly used in BAWs devices to generate L-BAWs. Apart from being used in acoustofluidic applications, PZT transducer are manufactured in bulk and used to a large extend in industrial applications such as; inkjet actuation, fuel injection and buzzers. (Kimura *et al.*, 2010).

2.2.2. Quartz (SiO_2)

Quartz is a mono crystal piezoelectric material that can be found naturally in nature or artificially produced. While it has a relativly high speed of sound (3158 m/s), its coupling coefficient is lacking (0.16) (Uchino, 2010). 100% of piezoelectric devices use artificial quartz and are manufactured using a hydrothermal process in an autoclave. Quartz has been used in mobile communications, cellular phones, automotive applications and even medical instruments (Saigusa, 2010). Quartz has also been used to create S-BAWs (Fu

et al., 2017), but more commonly a ST cut quartz is used to create Love waves for sensing applications (Papadakis et al., 2013; Tsougeni et al., 2020).

2.2.3. Lithium niobate (LiNbO3)

$LiNbO_3$ are single crystal wafers that are manufactured using Czochralski's method for crystal growth (Shur, 2010). $LiNbO_3$ wafers are widely available commercially with a standardised manufacturing procedure and come in different cuts. Most commonly 128° Y-cut $LiNbO_3$, that generates R-SAWs, is used acoustofluidic applications, which has a very high coupling coefficient (5.6-11.3) and a speed of sound close to the PZT (3680-3980 m/s) (Fu et al., 2017). But different cuts of $LiNbO_3$ can also be used to create other types of waves such as a 36° Z-cut for longitudinal waves (L-BAWs) and a 163° x-cut for shear waves (Shur, 2010). It should be noted that different cuts will also have different properties, coefficient and speed of sound, but from all the cuts the one mostly used is the ones that generate R-SAW such as the 128° Y-cut (Baumgartner and Westerhausen, 2023).

2.2.4. Lithium Tantalate ($LiTaO_3$)

$LiTaO_3$ is a close relative of $LiNbO_3$, both are made using Czochralski's method for crystal growth and have similar characteristics (Shur, 2010). 36° YX cut $LiTaO_3$ has a coupling coefficient of 5-6.6 and a speed of sound of 4160-4420 m/s (Fu et al., 2017). Similarly to $LiNbO_3$, $LiTaO_3$ comes in different cuts that can be used to create different wave types (Shur, 2010). $LiTaO_3$ has been applied in communications for acoustic resonator filters of board bandwidth (Shur, 2010). While in acoustofluidics, 36° YX cut $LiTaO_3$ is commonly used to generate SH-SAWs for sensing applications (Brugger et al., 2021; H. Wu et al., 2015)

2.2.5. Gallium Nitride (GaN) and Zinc oxide (ZnO)

GaN and ZnO are materials that are typically grown on another material (i.e. a substrate) as a thin film and have gathered lots of interest in recent years. GaN is a crystal semiconductor material used primarily for light-emitting diodes (LEDs) and is typically grown on a sapphire (Al_2O_3) substrates using heteroepitaxy (Liu and Edgar, 2002). GaN on sapphire has a high speed of sound of 4130 m/s, but a low coupling factor of 0.13 (Fu et al., 2017). GaN has been demonstrated capable of creating SAWs and actuation of particles, where two IDTs on GaN were used to manipulate polystyrene microsphere particles (Sun et al., 2020).

Similarly, ZnO is a semiconductor material that can be grown using epitaxy on different substrates such as glass, sapphire and silicon (Özgür et al., 2005). Depending on the substrate ZnO material can have a speed of sound velocity of 3150-5000 m/s and a coupling factor of 0.64-1 (Uchino, 2010). A remarkable achievement of ZnO thin film devices has been to create a bendable acoustofluidic device (Wang et al., 2021), where

ZnO deposited on thin aluminium foils and sheets was bended to various angles and were used to actuate droplets across the bend substrate.

2.2.6. Summary of piezoelectric substrates

From the above, it can be seen that there are various piezoelectric substrates that can be used for acoustofluidics applications. Table 1 is provided to give a summary of these materials using substrates that are commonly seen for acoustofluidics applications. This table provides the coupling coefficient, speed of sound and types of waves that these substrates are commonly used to develop in acoustofluidic applications.

Table 1. Summary of various piezoelectric substrates used in acoustofluidic applications with their acoustic related properties, such as: coupling coefficient (K_{eff}^2), speed of sound (c_s) and wave type.

Piezoelectric substrate	Coupling coefficient, K_{eff}^2 (%)	Speed of sound, c_s (m/s)	Developed wave type
PZT	20-35	4500	L-BAW
ST Quartz	0.16	3158	Love waves
$LiNbO_3$ 128° Y-cut	5.6-11.3	3680-3980	R-SAW
$LiTaO_3$ 36° YX-cut	5-6.6	4160-4420	SH-SAW
GaN	0.13	4130	R-SAW
ZnO	0.64-1	3150-5000	R-SAW, Lamb waves

One can see that while there are various substrates their properties, certain substrates will be more suitable for certain applications. First, the substrates with the higher coupling coefficient such PZT, $LiNbO_3$ and $LiTaO_3$ will be the most preferred ones, especially for applications such as actuation where the requirement is that most of the acoustic energy is dissipated into the liquid to achieve the actuation. But from these three, two create waves most suitable for actuation, L-BAWs created by the PZT and R-SAW created by 128° Y-cut $LiNbO_3$. It should also be noted, while both $LiNbO_3$ and $LiTaO_3$ have different cuts that can achieve different wave types, the fact that these two most commonly are used to create R-SAWs and SH-SAWs, respectively, perhaps suggests that the substrates are most suitable for these wave types or that there are some drawbacks to different types of cuts in regard to their coupling coefficient and speed of sound. Nonetheless, as it stands with the current properties of the substrates that have been

presented in can be observed that why PZT and 128° Y-cut $LiNbO_3$ are so commonly seen in actuation based applications, such as manipulation/ patterning (Guo et al., 2015; Li et al., 2014; Naseer et al., 2017) and separation (Wang et al., 2020; Wu et al., 2018).

2.3. Piezoelectric transducers

While PZT and 128° Y-cut $LiNbO_3$ are both very capable substrates for actuation-based applications, the manufacturing process for their respectively transducers are vastly different. Both manufacturing process are quite complex, as will be seen below, but PZT transducer can readily be purchased from the market due to their excessive use on other industries. While 128° Y-cut $LiNbO_3$ substrate can also be readily purchased, to create an IDT on the substrate specialised cleanroom facilities are required.

2.3.1. PZT transducers

The two most common types of PZT transducer are single disk and multilayer, with the latter being more commonly used but the formed still being used in laboratory settings (Uchino, 2017). The multilayer PZT disk is made of multiple ceramic layers and have the advantage of high displacement, high reliability and low productions cost (Kimura *et al.*, 2010). It is hard to determine if acoustofluidics devices utilise more the former or the latter, but from the author's perspective it appears that the single disk is still more commonly used. The manufacturing procedure for both is quite similar and as such, and for simplicity, the manufacturing of the single disk will be described below. Fig. 2.2 demonstrated a real-life single disk PZT.

Figure 2.2. Real-life single disk PZT transducer.

A common manufacturing procedure for a PZT single disk is demonstrated in Fig. 2.3 (Nelson, 2010). (1) The first stage consists of the selection of high purity oxide materials (i.e. lead oxide, titanium oxide and zirconium oxide) and a range of dopants, which are then accurately weighted and (2) mixed (chemically or mechanically). (3) The mixture is then calcinated at 900-1000 °C, to produce a thermodynamically stable powder and to formulate the piezoelectric phase (Messing, 2021). After the calcination the mixture is relatively stable and is (4) milled (grain) to a fine powder, (5) granulated (with the aid of bonders) and (6) shaped via various manufacturing processes. It worth mentioning that while Fig. 2.3 demonstrates a wet granulation, dry granulation can also be implemented.

Similarly, herein shaping via a press mold is demonstrated, but they are other alternative shaping methods. (7) The burn out procedure is implemented at 500-600 ºC to remove any organic compounds that were introduced through the bonders, resulting with unwanted air gaps in the grain. (8) The ceramic structure is then sintered at a high temperature to allow the grain to form and diffuse into a uniform and dense, removing the air gaps, piezoelectric ceramic. (9) The ceramic then undergoes finishing machining procedures, one of which is lapping on a surface grinder to create the desired roughness. (10) In the termination procedure the metal layers are applied to the ceramic, to act as the electrodes. Typically, this is achieved by either the use of bonders and pressure, sputtering or a combination of the two. (11) The ceramic is poled using a strong electrical field, while the material is at elevated temperature. (12) This aligns the electric field domain in the material and leaves a remnant poling. Finally, the material is thoroughly characterised through inspection.

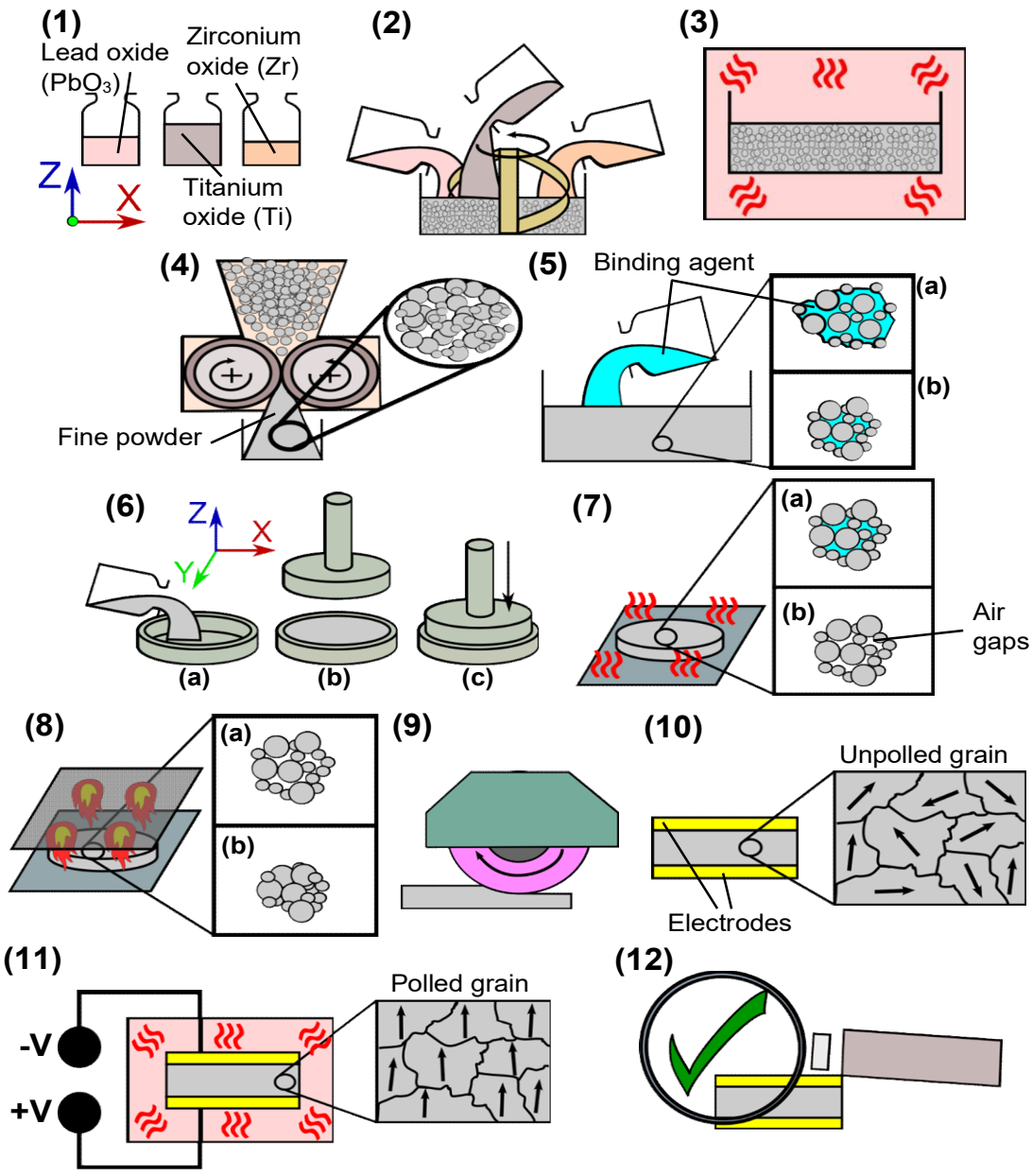

Figure 2.3. Manufacturing flowchart of a single disk PZT transducer. The flow chart describes the following procedures: (1) Selection of raw materials for the PZT manufacturing. (2) Mixing of raw material and the formation of the PZT powder. (3) Calcination of the PZT powder. (4) Grain milling of the PZT powder into a fine powder. (5) Granulation of the fine PZT powder. (6) Shaping of the PZT powder via a mechanical press and a mold. (7) Binder burn-out of the shaped PZT transducer. (8) Sintering of the PZT transducer. (9) Machining of the PZT transducer, specifically surface grinding. (10) Termination of the PZT transducer. (11) Polarisation of the PZT transducer. (12) Inspection of the PZT transducer.

As it can be seen, the manufacturing of the PZT transducer is not that simple and requires a lot of processing steps. But due to being widely used in various industries, it has been made widely available and cheap. A very important characteristic of the PZT

transducer is the thickness of the PZT ceramic, which, based on the speed of sound, determines the desired operating frequency. Thus, the desired thickness of the PZT ceramic can be described as (Zhou et al., 2011):

$$t = n\frac{c_S}{2f} \tag{27}$$

where n, c_S and f is the lowest resonant frequency (n=1), the speed of sound in the substrate (m/s) and operating frequency (Hz). While this parameter is not an issue at lower frequencies, at higher frequencies it becomes a crucial restricting factor. Since thin PZT ceramic are very hard to make, due to the inherent brittleness of ceramics (Lockwood et al., 1994) and the grain size of PZT being between 5-10 μm (Zhou et al., 2011). This is why there are no high frequency PZTs (>20 MHz) and thin film piezoelectric transducers are typically used for high frequency BAW devices (Guo et al., 2021). But thin piezoelectric transducers appear to not be that widely used in the general market and as such they do not share the lower price of their and accessibility of PZT transducer counterpart.

2.3.2. Cleanroom made IDTs

IDTs are manufactured on a piezoelectric substrate through the use of clean room facilities. The manufacturing procedure of an IDT involves 2 main processes; 1) photolithography and 2) metal deposition. In photolithography a layer of photoresist layer is applied onto a substrate, which can be either negative or positive. Positive photoresist will un-bond from the surface of substrate after being exposed to UV light, while the negative photoresist will bond to it (Vladimirsky, 1999) and each photoresist has its own advantages and disadvantages (XiaoMing Hu, 2015). Ai *et al.*, (2013) used positive photoresist for the development of their IDT on $LiNbO_3$, but if the manufacturing of IDTs for acoustofluidic application always involves the use of positive photoresist remains uncertain. Fig. 2.4 illustrates a real-life made clean room IDT.

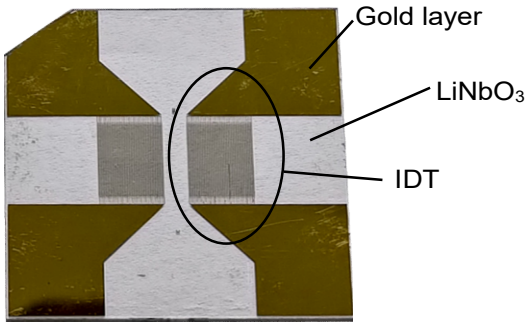

Figure 2.4. Real-life clen room made IDTs.

Fig. 2.5 illustrates the manufacturing procedure of an IDT on a piezoelectric substrate. (1) A piezoelectric substrate is first selected and then (2) it is spin coated with positive

photoresist. (3) A mask with the IDT pattern is then placed in the mask aligner, aligned on top of the substrate and exposed to UV light. (4) After the exposure, the substrate is developed and rinsed to remove the un-bonded photoresist. (5) A zoomed cross section of the middle of the substrate is shown, where an evaporator was used to deposit a thin layer of chromium (20 μm) on top the substrate, which was followed up by a layer of gold (100 μm). The chromium acts as bonding mechanism between the piezoelectric substrate and the gold, while the gold is deposited to act as an effective electrical conductor for electrical input power. (6) In the lift-off process, the substrate is left in acetone to remove the left-over photoresist, (7) leaving only the IDTs pattern on the substrate.

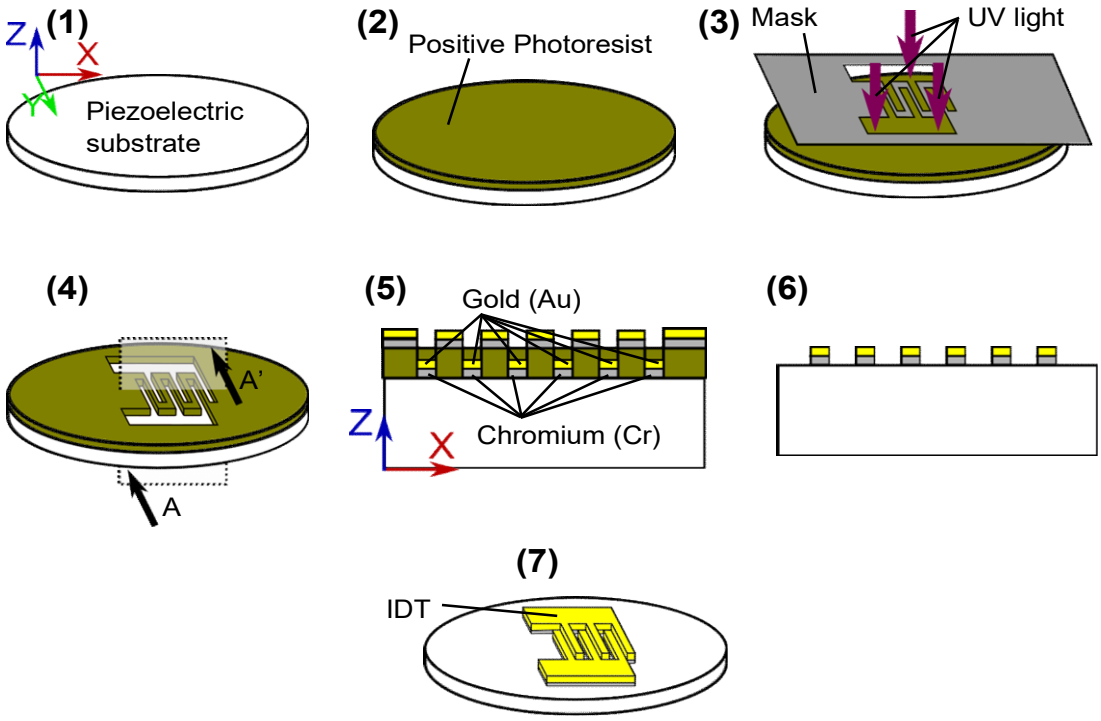

Figure 2.5. Manufacturing of IDTs on a piezoelectric substrate. (1) A piezoelectric substrate is selected and (2) spin coated with a positive photoresist. (3) The substate is then placed into a mask aligner, where a mask with the IDT pattern is aligned on top of the substrate and UV light is shone on top. (4) After UV exposure, the substrate is developed and washed to remove the unbonded photoresist. (5) A zoom cross section of the middle of the substrate shows the IDTs region after it underwent the metal evaporation procedure. During this procedure a thin layer (20 μm) of Chromium (Cr) and a layer (100 μm) of Gold (Au) have been deposited onto the substrate. (6) The substrate is then left in acetone to remove the rest of the photoresist, leaving only the Cr and Au on the wafer, which then leaves (7) only the finished IDT on the substrate.

For actuation based acoustofluidics applications, IDTs are typically manufactured on 128° Y-cut $LiNbO_3$ which is widely available and has the best piezoelectric characteristics

for the development of R-SAWs. Different piezoelectric substrates could also be used to develop IDTs on them using this method, but due to the manufacturing procedure and settling for a potentially less efficient device this is very rarely done. But it should be noted that while IDTs are used to create R-SAWs on $LiNbO_3$, conventional IDTs have also been used on ZnO, $LiTaO_3$ and ST Quartz to generate Lamb waves (Wang et al., 2021), SH-SAWs (Brugger et al., 2021) and Love waves (Zhang et al., 2016).

2.3.3. PZT transducers vs IDTs

From the manufacturing sections of both PZT transducers and IDTs it can be observed that both implement a significant array of equipment. PZT disks are used widely in the market and as such they are much easier and cheaper to acquire than their IDTs counterparts. Additionally, they have excellent resistance to temperature and are capable of creating large deformation and to handle large input power. But their general available shapes and wave mode capabilities are very limited, also making their implementations with a microchannel very limited. While IDT designs can be implemented in various shapes, can operate away from the microchannel, due to their wave type, and are capable of creating much larger frequencies than the PZT transducers. The limitation in frequency makes the PZT applications to also be not suitable in fields that require high frequencies, such as of nanomanipulation (Wu *et al.*, 2017) and cells stimulation (Ramesan et al., 2021). As such, it can be seen that the IDTs offer a great array of advantages and have driven a lot of development in the acoustofluidic field as such. But the requirement of specialised facilities is still a bottleneck, which limits their usage the ones that have access to them.

2.4. PCB IDTs

As stated above, the SAW devices requirement of specialised facilities is a potential limiting factor of the ease of access and used of these devices. Additionally, SAW devices cannot be easily repaired/ replaced or reconfigured, and if the IDTs are damaged or the substrate is damaged the whole device is rendered unusable and must be replaced. Thus, newcomers to this area might be dissuaded from using a SAW device due to these issues. These drawbacks have been identified by others, and alternative manufacturing techniques have been developed to attempt to bypass the need of clean room facilities with the aim to make SAW devices more accessible. One such attempt was done by Rezk *et al.*, (2014), who created IDTs using aluminium strips and demonstrated the creation of Lamb waves on $LiNbO_3$. This is technique is rather interesting, since it indicates that the $LiNbO_3$ and aluminium foils can create acoustic waves by simply being in contact with the substrate. Thus, if an IDT could be created with methodologies that are already standardised and widely available in the market, then it can be simply mechanically coupled to a piezoelectric substrate. As such here it

is proposed to offset the development of the IDTs to the PCB industry, which is both well standardised and available to the general market at a relatively cheap price. In this section a quick overview will be provided of the PCB industry, their manufacturing procedures and application in biomedicine. Then the current achieved fabricated and developed the PCB based SAW devices will be briefly introduced and further elaborated in the following chapters.

2.4.1. PCB

The PCB industry has a huge worldwide market that is expected to be worth 75 billion USD by 2026 (Mordor Intelligence). To put simply a PCB is a mechanical substrate that accommodates different electrical components on it. These electrical components are connected, via metal traces, in complex configurations called circuits. A PCB consists of four main components: the substrate, the copper layer, the solder mask and the silkscreen. The substrate acts as the assembly base and can be made of different materials but is usually made from epoxy fiberglass (FR4). The copper layer is the conductive material that is etched to form the traces of the circuit, while the solder mask is a thin film that is applied on the traces to stop the solder from spreading to them. It should be noted that in some designs only the board is solder masked while the copper layer is plated instead. Finally, silkscreen is a material that is placed on the PCB for labelling purposes. Fig. 2.6 illustrates three of these main components, the board, the traces and the solder mask.

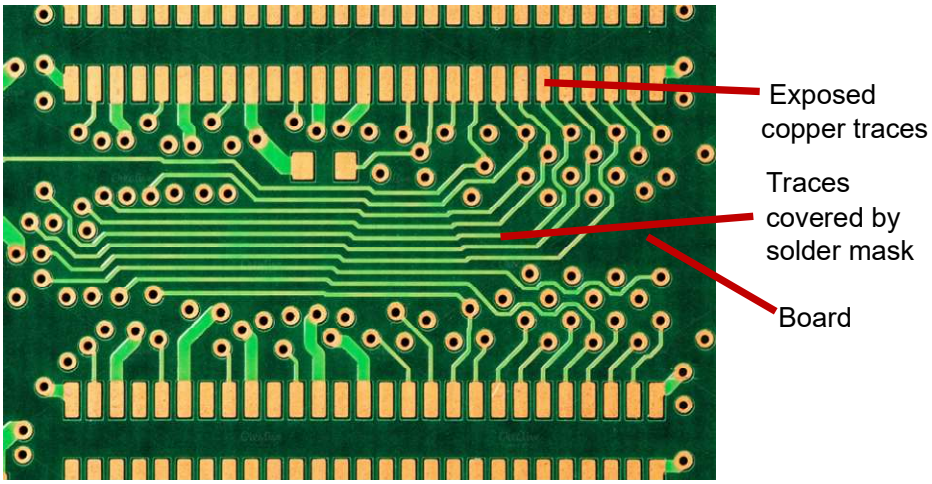

Figure 2.6. Real-life PCB. Image adapted from TechDiggersBlog.com.

A typical single layer PCB manufacturing procedure is shown in Fig. 2.7 (Millennium circuits limited). (1) The process starts with schematic design of the PCB being submitted by the designer to the manufacturing company. (2) Then the raw materials are selected, per designer's specification, where for a single layer PCB these typically are an FR4 board and a copper cladding. These two components are then bonded together and (3)

holes are drilled into the board at the specified locations and sizes. (4) The circuit schematic is then printed as a mask to be used after a photoresist has been applied to the board. (5) The copper layer of the PCB is spin coated with photoresist, (6) mask aligned, exposed to UV and (7) washed to remove any unbonded photoresist. (8) The copper is then etched to create the desired circuit tracing and is (9) resist stripped, i.e. any left-over photoresist is fully removed. The PCB then undergoes an automated optical inspection to confirm that it is up to specification and then the surface that is not covered in copper is (10) covered with a solder mask. Additionally, (11) if the design includes any labels or information on the PCB, a silkscreen is applied to present this information. (12) The PCB traces are then plated with a selected conductive material. One of the plating methodologies is immersion, which offers a variety of coating materials such as gold, silver and tin. (13) Finally, the PCB passes final inspection and is shipped out.

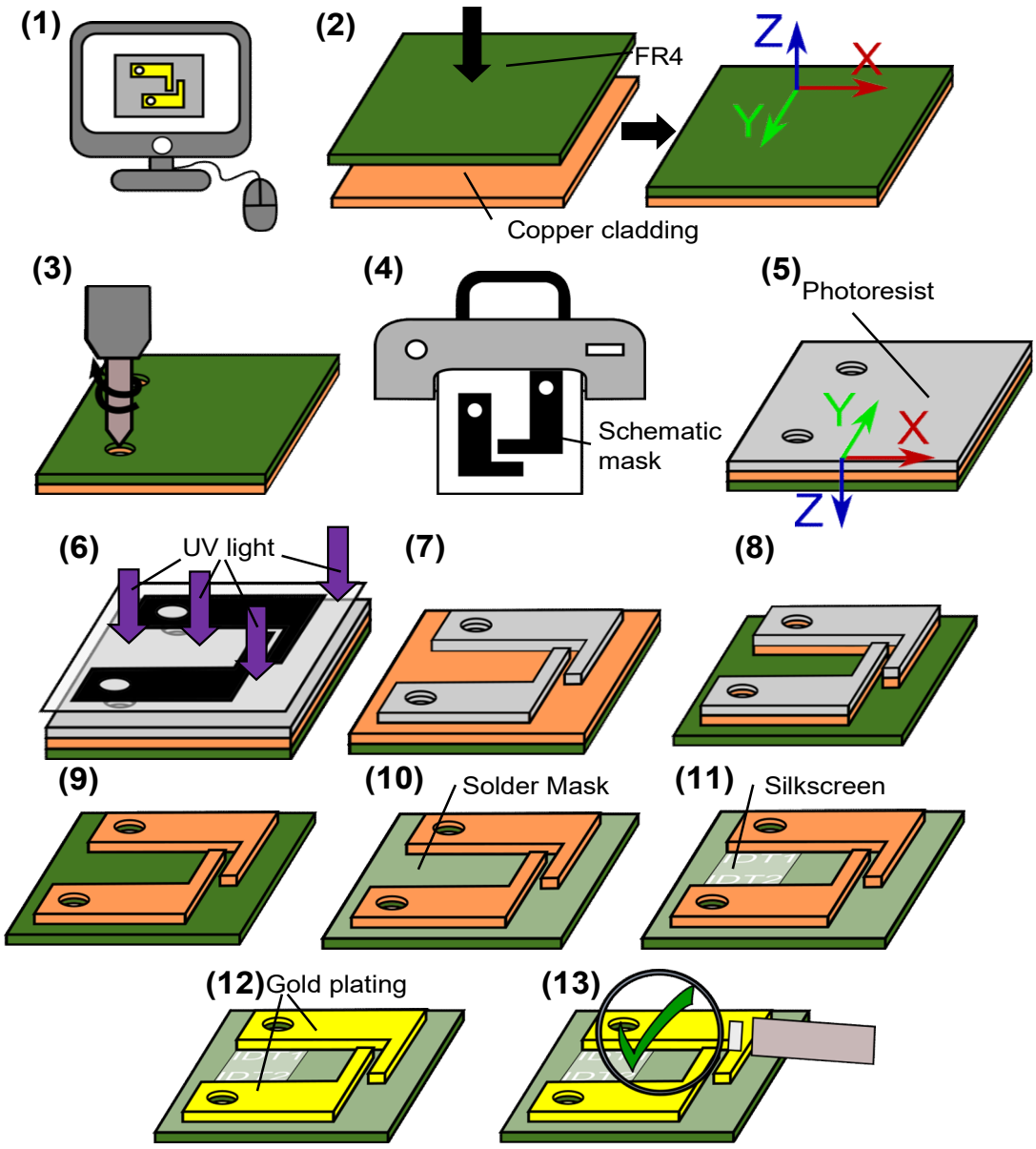

Figure 2.7. Manufacturing flowchart of a single layered PCB. (1) Design of the schematic. (2) Selection of raw materials for the board and traces of the PCB and their bonding. (3) PCB drilling. (4) Printing of the mask for the circuit schematic. (5) Application of the photoresist on the PCB. (6) Alignment of mask with PCB and application of UV light. (7) PCB after the washing of unbonded photoresists. (8) PCB after the etching procedure. (9) Removal of remaining photoresist. (10) Solder mask and (11) silkscreen addition. (12) Gold plating of the PCB traces. (13) Inspection of the PCB.

This type of manufacturing procedure for PCBs was reported to be able to easily achieve trace widths less than 0.005 in (127 μm), while the smallest practical range appears to be between 0.002-0.003 in (50-76 μm) (LaDou, 2006). This means that using a $LiNbO_3$ substrate a PCB IDTs that has a trace width of 50 μm can easily generate a 200 μm wavelength (~20 MHz on 128° Y-cut $LiNbO_3$). Apart from the conventional method, PCBs

can also be made in house using a pre bonded board with copper cladding, which are widely available in the market. As an example, a DYI CNC milling machine was built by Sathyakumar *et al.*, (2018), which etched away the copper material and created 200 μm wide straight traces and 100 μm wide irregular traces. Admittedly these trace sizes are not that impressive, but potentially a commercially available CNC etcher could create much smaller traces.

2.4.2. PCBs in biomedicine

PCBs have also been pushed in biomedicine as a tool to incorporated with “LOC” to create “Lab-on-PCB” solutions (Zhao *et al.*, 2020). Lab-on-PCB have been stated to have the advantages of 1) PCBs being flexible and able to be adjusted per demand, 2) able to integrate complex modules into a single PCB, 3) having a mature and standardised industry and 4) flexible substrate capabilities (Zhao *et al.*, 2020). Lab-on-PCB devices with custom PCB designs have been applied in application such as cell counting, viability testing, glucose and electrocyte detection, electrochemical analysis, immunoassay analysis and molecular analysis (Zhao et al., 2020). Apart from the general PCB designs, PCB with IDTs have also been previously developed, but instead for acoustofluidic applications the PCB IDTs were used for moisture sensing (Dean et al., 2012), water level measurements (Chetpattananondh et al., 2014), electro wetting (Jain et al., 2017), biosensing (Syaifudin et al., 2011) and even cell manipulation (Park et al., 2009).

2.4.3. PCB IDTs based SAW device

To test the PCB IDT fabricating concept for SAW device, initially PCB IDTs were developed on a FR4 board (Mikhaylov et al., 2020). As a substrate 128° Y-cut $LiNbO_3$ was chosen, due to the substrate’s excellent coupling coefficient as well as due to its large use in actuation-based applications . This would also give the capability of this new methodology to be compared against conventional SAW devices that have been widely used and characterised. The PCB IDTs were designed to generate a wavelength of 200 μm (~20 MHz) on 128° Y-cut $LiNbO_3$ and both IDTs were printed on a single board with a milled slot in the middle to permit the placement of a microchannel. The PCB IDTs were coupled with $LiNbO_3$ using a 3D printed clamp to create the PCB-SAW device. This bonding method had the consequence of a reduced coupling efficiency and to compensate for this matching network (MNs) were added to the assembly, which enhanced the electrical properties of the device and the coupling efficiency. The PCB-SAW device fabrication and assembly was thoroughly characterised and compared against a clean room (CR) made IDT. The tests indicated that the device operated less efficiently than the CR IDT, which was expected to the bonding mechanism implement in the PCB-SAW device. The device was then used to successfully stream particles inside a droplet and actuated particles and cells using R-SSAW inside a microchannel.

Finally, using the same setup the PCB-SAW was coupled with ZnO substrates to demonstrate its ability to couple with different piezoelectric substrates.

2.4.4. Flexible PCB IDTs (FPCB IDTs) based SAW devices

After the hard PCB IDTs, the ability of the PCB IDTs to generate R-SAW waves suing a flexible PCB substrate were investigated, in hopes to potentially to improve the contact and coupling between the IDEs and $LiNbO_3$. FPCB IDTs chips were manufactured with an identical geometry as the hard PCB IDTs (Sun et al., 2021). This setup also implemented MNs and a clamping mechanism of a much simpler design than the PCB-SAW one, which was done to illustrate that this device does not require intricate designs to remain functional. The electrical behaviour was studied for different chips and the device's frequency response under different environmental conditions. The SAW amplitude was also studied with and without MNs and its operation was then compared to that of the PCB-SAW, which demonstrated similar actuating capabilities with the FPCB IDTs having a slightly higher efficiency. Since the FPCB IDT chips has similar performance as the hard PCB IDTS, they were further investigated for SSAW applications. For the new setup, the FPCB IDTs chips were developed separated to address a clamping issue of the hard PCB SAW device. Apart from being used to create a SSAW, this setup was also developed to create a portable and reconfigurable FPCB-SAW device, which was dubbed as versatile acoustofluidic device (VAD) (Mikhaylov et al., 2021). The VAD had a DYI control unit developed capable of creating an input signal as well as to read the pressure that was applied on the FPCBs. A new assembly procedure was developed for the VAD using a vector network analyser (VNA), which assisted with the parallel alignment of two FPCB IDTs that were used to generate the SSAW. Furthermore, to make the manufacturing of SAW device even more accessible a new method to manufacture and bond PDMS microchannels at different orientations was developed. This device's manipulation capabilities were demonstrated by aligning particles parallelly and at tilted angles using the custom channel pressers and IDT rotation.

2.4.5. . High frequency PCB IDTs (hFPCB IDTs)

The final PCB-SAW device setup that will be discussed in this thesis are the high frequency FPCB IDTs (hFPCB IDTs) chips. These IDTs were designed with the aim to push the limits of the FPCBs by developing an FPCB with a pitch of 120 μm (~33 MHz on 128° Y-cut $LiNbO_3$) to be used for possible actuation of sub-micron particles. Apart from the sub-micron manipulation, this device's aim was to incorporate all the previously developed techniques to create a device that could be used to study and develop a PCB based SAW device for actuation, as a proof of concept of its potential to be applied for separation applications. To achieve this, the device incorporated a tilt-angle microchannel setup, a cooling system and a microfluidic pumping system. This device

was then used to experimentally study the actuation of 5 μm and 1 μm particles under different tilted-angle and demonstrated how to increase the actuation efficiency of the 5 μm particles by adjusting the flow rate of the sheath flows.

2.4.6. PCB IDTs advantages and limitations

In this thesis it will be demonstrates that the PCB IDTs offer a variety of advantages over the conventional photolithography IDT manufacturing technique. The demonstrated advantages are that the PCB IDTs provide an accessible manufacturing technique for SAW devices, which allows any user to quickly order a PCB with IDTs from the general market. The PCB can also be manufactured on different substrates, rigid or flexible, to suit the user's applications as well as different IDT design can be designed that can be used to quickly coupled/ decouple with different piezoelectric substrates. The same IDTs can be used to couple with different piezoelectric substrate to quickly and easily establish their acoustophoretic capabilities, without having to remanufacture the whole device. But apart from different substrates the PCB IDTS can also be used to explore the anisotropy of the substrates by placing the IDT on different orientation and exploring different wave modes that can be developed (Dumčius et al., 2023).

But it should be noted that the PCB IDTs also have limitations, with one being the size of the IDTs that can be manufactured on the PCB. The current conventional manufacturing technique can easily achieve a 50 μm IDE width and, in certain cases, a 30 μm width. But if a smaller IDE width is needed, a more specialised technique will be required, which also will result with a rise in cost. Furthermore, this technique requires the PCB IDTs to be clamped down as such the setup will be inherently more complex than the conventional device. Furthermore, due to the clamping mechanism there is a limit on how close the IDTs can be position to the microchannel, while the conventional IDTs can be placed very close to the internal channel, by having a PDMS roof (Wu et al., 2017b), or even directly underneath it (Tayebi et al., 2021). This will inevitably results with PCB IDT method always achieving a lesser acoustic energy density than the conventional IDT, due to the limit of how close they can be brought against the microchannel (Li et al., 2015). Additionally, due to the PCB IDTS relying on surface contact to transmit the electrical energy into the substrate, this will also inevitably result with a lower power efficiency than the conventional photolithography IDTs. This lower efficiency can be mitigated to an extend by implementing MN, though never reaching the efficiency of the conventional IDTs, but this also adds an extra step of complexity and design work.

2.5. Microchannels

A final component of acoustofluidic devices that must be discussed are the microchannels. Microchannels are a vital part of acoustofluidics devices and are almost

always included in biological application. Microchannels can be separated into 3 main types: acoustically leaky channels, high acoustic impedance channel or hybrid channels. Each channel type implements different manufacturing technique and certain channel types are used far more than others.

2.5.1. Acoustic impedance

Before proceeding it most important to define what acoustic impedance is to help demonstrate the difference between an acoustically leaky and high impedance microchannel. In more specific terms acoustic impedance is referred to as a term that roughly summarises the acoustic resistance and reactance of a material. Acoustic resistance absorbs and dissipates the acoustic energy, while reactance cyclically stores and releases the energy without dissipation (Kennelly and Kurokawa, 1921). The acoustic impedance of a material, also known as field or specific impedance, can be calculated using the following equation (Hiremath et al., 2021):

$$Z_o = c\rho \tag{28}$$

With Z_o being the acoustic impedance (Pa-s/m). Table 2 is provided below to indicate some of the acoustic impedances of various materials.

Table 2. Acoustic impedance of various materials. The speed of sound and density of water, glass and steel were taken from Engineeringtoolbox.com, while the PDMS properties were taken from *Nama et al. (2015)*.

Material	**Speed of sound, c, (m/s)**	**Density, ρ, (kg/m^3)**	**Acoustic impedance, Z_o, (Pa-s/m)**
Water (20 C)	1481	999	1.48E+6
PDMS	1100	1030	1.13E+6
Glass, pyrex	5640	2230	1.26E+7
Steel	5940	7850	4.66E+7

In acoustofluidic devices there is an interference layer between the liquid and microchannel material. If the acoustic impedance of these components is very similar the acoustic energy will leak from the fluidic medium into the microchannel, resulting with a loss of the acoustic energy i.e. an acoustically leaky microchannel. On the other hand if the acoustic impedance of the material is dissimilar it will lead to the acoustic energy being reflected back into the channel and improving the device's efficiency (Wu et al., 2018). This dissimilarity can be calculated as the reflection coefficient using the following equation:

$$R_{liqud-channel} = \left(\frac{Z_{channel}-Z_{liquid}}{Z_{chann}+Z_{liquid}}\right)^2 \quad (1)$$

With $Z_{channel}$ (Pa-s/m) and Z_{liquid} (Pa-s/m) referring to the acoustic impedance of the channel material and fluidic medium used, respectively. In the case of water and PDMS this would result with a value of 0.02, indicating that only 2 % of the acoustic energy is being reflected back into the microchannel. While with water and glass this value is increased to 0.62, i.e. 62% of the acoustic energy being reflected into the microchannel. As such one can clearly see why it would be beneficial to have a microchannel made from a material with a high acoustic impedance. It should be noted that the value range of the reflective coefficient that defines a microchannel as leaky is not precisely defined in literature, as well as this value depends on the fluidic medium that is being used in the microchannel. But fortunately, the materials summarised here are some of the most commonly used in acoustofluidics, and as such it is easy to define the PDMS as the acoustically leaky material while glass and steel as the high impedance material.

2.5.2. Acoustically leaky microchannels (PDMS)

Acoustically leaky channels are by far the most common microchannels and are typically made from PDMS. PDMS offers many advantages such as its low cost, fast and simple fabrication and high transparency that permits internal observation (Johnston et al., 2014). PDMS channel are almost exclusively made using soft lithography, which consists of creating a master mold using photolithography where the PDMS will be in poured and cured to create the internal geometry of the PDMMS microchannel (Xia and Whitesides, 1998). The master mold is made on top of a silicon wafer, due to its durability and good bonding properties (Xia and Whitesides, 1998), and the channel features are build up on it using specialised negative photoresist epoxy (SU-8). Fig. 2.8 illustrates the full manufacturing process of the silicon mold and the PDMS microchannel. (1) First a silicon wafer is selected and (2) spin coated with SU-8. (3) Then the wafer is placed into a mask aligner, where a mask is aligned on top of the coated wafer and exposed to UV. (4) The unexposed material is removed using acetone leaving only the master mold. (5) The master mold is then placed in container and a PDMS mixture is poured onto it. It should be noted that PDMS consists of an elastomer and hardener, and a typical PMDS mixture is made of a 1:10 (weight: weight) ratio of hardener and elastomer, respectively. After the PDMS components are mixed, they will naturally start to cure (ie solidify), which can be accelerated by exposing the mixture to heat. Most commonly, the master mold and PDMS are placed in an oven at 65 ^{o}C for an hour to cure, and after curing are left out to cool. (6) After curing and cooling, the PDMS is peeled from the silicon mold and (7) holes are punched on top of the channel to act as ports for any microfluidic (MCF) connectors. (8) To bond the channel to a substrate, at least with $LiNbO_3$, both components are placed into a plasma chamber and are plasma treated. After the treatment the PDMS is simply

pressed onto the substrate to bond them. This bonding method utilises the naturally occurring covalent bonds between the PDMS and some substrates, such as $LiNbO_3$, and strengthens them to create an almost permanent bond (Henniker Plasma, Ltd). It can be seen that the main components required to manufacture a PDMS channel are the master mold and the PDMS. This means as long as a master mold can be manufactured a PDMS channel can be created.

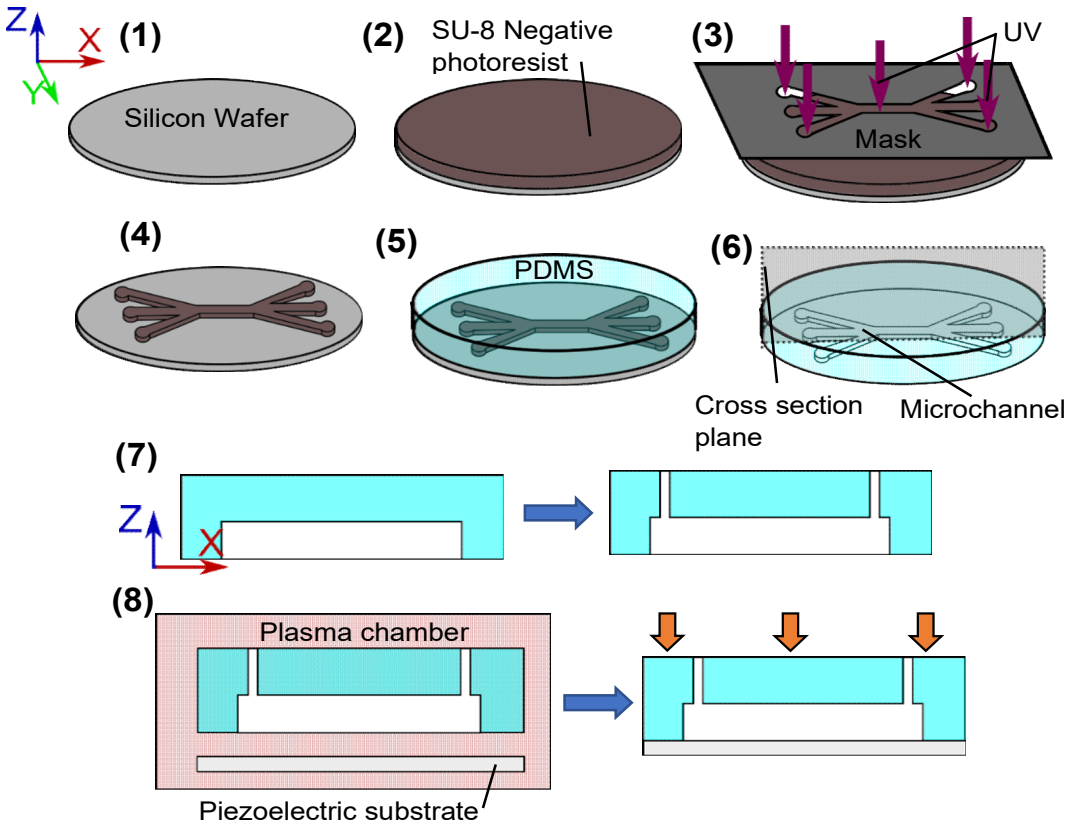

Figure 2.8. Soft lithography process of PDMS microchannel. 1) A silicon wafer acts as the base substrate and 2) is spin coated with SU-8 negative photoresist. 3) The mask, with the desired pattern, is aligned on top of the wafer and is exposed to UV, using a mask aligner. Acetone is then used to remove any unbonded photoresist, thus creating the 4) microchannel master mold. 5) The master mold is placed in a container and PDMS is poured onto it. 6) After curing the PDMS is removed from the mould and 7) holes are punched at the input locations of the microchannel for the MCF connectors. 8) The channel is then placed into a plasma chamber with the piezoelectric substrate and after the treatment the PDMS is pressed onto the substrate in order to bond the two.

One alternative methods of manufacturing a PDMS channel is by using a 3D printed master mold on a glass slide (Mikhaylov et al., 2021). This method allows to create a PMDS channel using off shelf components as long as the master mold is printed on a smooth surface. The smooth surface aspect is very important, since it helps maintain the PDMS channel's natural covalent bonding properties with the $LiNbO_3$. In fact, a PDMS

channel will slightly adhere and couple to a $LiNbO_3$ substrate after only a simple cleaning procedure with isopropanol alcohol (IPA). This is why a PDMS channel can also be bonded to $LiNbO_3$ with only mechanical pressure and without plasma treatment. This technique has been used to successfully create a microchannel for acoustofluidic applications without the requiring any cleanroom facilities (Mikhaylov et al., 2021). This procedure is explained in detail in Chapter 3.

2.5.3. High acoustic impedance microchannels

High impedance microchannel are far rarer than PDMS channels and are most commonly used in BAW devices due to their acoustically reflective properties. Channels with high acoustic impedance can be formed from any material that has a high acoustic impedance such as; steel sheets (Chen et al., 2016) or silicon/ glass slides (Iranmanesh et al., 2013). Most commonly dry etching (Laermer, 2016) is implement for their manufacture, which is used to etch either the channel into the material or the holes for MCF connectors. As with soft lithography, dry etching as well implements standard photolithography. But in the case of dry etching any material that is uncovered will be etched through during the etching procedure. Thus, the reader can imagine that the step 1-3 from Fig. 2.7 will be identical for dry etching. A silicon wafer is also typically used here, but in this case the material acts as the microchannel instead of the master mold. In Fig. 2.9, (1) A silicon wafer is shown, that has already been spin coated, UV cured and the unbonded photoresist was removed. The internal channel area is uncovered by the photoresist since the unexposed area will be etched in the etching chamber. (2) For this type of microchannel the etching is typically done all the way through. (3) After etching, the silicon wafer with the microchannel geomerty is sandwiched between two glass slides, with the top glass slide having input holes, to create the assembled channel (Iranmanesh et al., 2013).

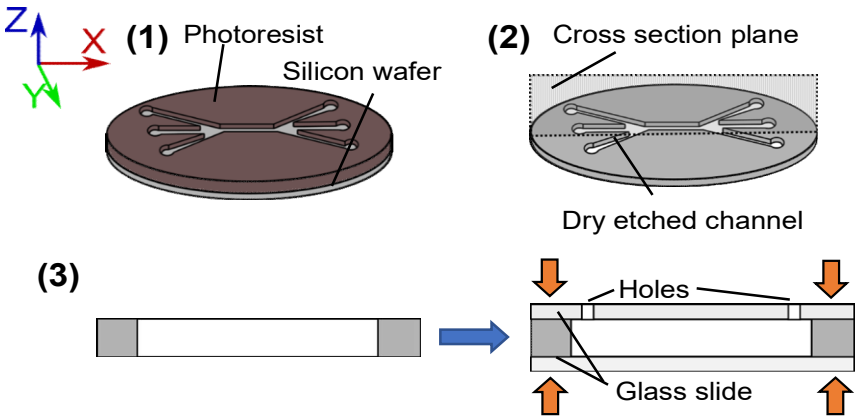

Figure 2.9. Manufacturing of a silicon etched microchannel. 1) The silicon wafer was spin coated and the unbonded photoresist has been removed, leaving the channel area uncovered. 2) The channel is etched through, and the rest of photoresist is removed. 3) The silicon wafer is sandwiched between two glass slides, with the top glass slide having holes for the microchannel's input/ output ports.

But dry etching is not always necessary, a high impedance channel can also with other methods. Chen *et al.* (2016) created a stainless steel microchannel using 75 µm stainless sheets which were laser cut, that were laminated and sealed together with epoxy, while Mao *et al.* (2017) used a rectangular capillary that was bonded with epoxy to the substrate, creating an artificial single input output "microchannel". But these two latter methodologies are not that commonly seen in literature.

2.5.4. Hybrid microchannels

A more recent microchannel trend have been the hybrid microchannels, which incorporate PDMS with a reflective layer such as; a PDMS/ glass slides (Xu et al., 2019; Wu et al., 2018) or PDMS/ hard PDMS thin film (Zhao *et al.*, 2020). While PDMS has its advantages, one major advantage of having higher impedance material added, i.e. hybrid channel, is that the reflective properties increase the acoustic force. This can be utilised to increase the critical particle diameter that the device can actuate or to increase the throughput of the channel (Barnkob *et al.*, 2012). One manufacturing method to create a hybrid microchannel is to have the PDMS sandwiched between two glass slides (Xu et al., 2019), while another is to create an internal glass roof inside the PDMS chamber. The latter is achieved by placing a cut glass slide on top of the master mold main channel feature before curing the PDMS. Thus, after curing and when the PDMS is removed it will result with the glass slide being impeded inside the PDMS. A final method to create a hybrid channel is to use specialised hard PDMS to create a thin film (13 µm) on which the PDMS channel can be placed on (Zhao *et al.*, 2020). All these configurations will result with an increased acoustic force inside the channel.

2.5.5. Prominence of PDMS

It can be observed, based on the last paragraph, that channels with high acoustic impedance seem to be the obvious choice for all acoustofluidic devices due to their acoustic enhancing properties. But in practice the channels made fully from high impedance material are rarely used for SAW devices. One reason is that these channels typically have a bottom layer, thus add an additional layer for SAW to penetrate before it reaches the fluid. Furthermore, a coupling layer will be required to bond these channels to the substrate, which will further increasing the diffraction of the wave as well as the travelling distance. But even if a microchannel made from high acoustic impedance material has no bottom layer, it would still be difficult to bond it to the piezoelectric substrate. This because it would still require a bonding layer, since a hard channel lacks both elasticity and the bonding attraction of the PDMS toward the substrate, such as $LiNbO_3$. As such the hybrid channels seem to be the most viable option to increase the acoustic impedance, specifically the PDMS channels with a hard PDMS film and a PDMS microchannel with an internal glass roof. But it should be noted that these channels add some manufacturing complexity, which might deter some. As such this could be why PDMS is still the most popular channel of choice. But it is possible that the paradigm might shift at some point in the future, at least for the applications that required the added acoustic energy such as separation.

Chapter 3

Methods and Materials

3.1. Introduction

This chapter contains all the methods and materials for the whole thesis, and it is divided into three sections. Section 3.2 discusses the development of the prototype PCB SAW device including the design, fabrication, and the experimental setups. Section 3.3 discusses the development and characterisation of the flexible PCB IDTs (FPCB IDTs) as well as the development of a versatile acoustofluidic device (VAD) using the FPCB IDTs. Section 3.4 discusses the development of high frequency FPCB IDTs (hFPCB IDTs) and its setup for the application of studying particle actuation inside the microchannel. It should be noted that all these devices used a 128° Y-cut $LiNbO_3$ substrate unless otherwise stated. This was done due to the advantageous piezoelectric properties of the substrate, especially the coupling coefficient, its smooth surface and its wide usage in the acoustofluidic field. 128° Y-cut $LiNbO_3$ has been demonstrated in both manipulation/ patterning (Guo et al., 2015; Li et al., 2014; Naseer et al., 2017) and separation applications (Wang et al., 2020; Wu et al., 2018), which then also provides solid examples of the devices' expected manipulation and actuation capabilities to compare the PCB fabrication technique with, if needed. This also helps to immediately prove the PCB-SAW devices capabilities on one of the most commonly used piezoelectric substrates for SAW devices.

3.2. PCB-SAW

This section is the methods and materials for the PCB-SAW device that is used in chapter 4. This section includes the designing procedure and characterisation of the PCB IDTs, the development and assembly of PCB-SAW device, its characterisation methodology, the methodology of the performed experiments using the device and the sample preparation.

3.2.1. Design procedure for PCB IDTs

A standard IDT and its main key features are shown in Fig. 3.1, which are specified as the pitch size, IDE length, IDE width, Bus-IDE gap and bus pad width.

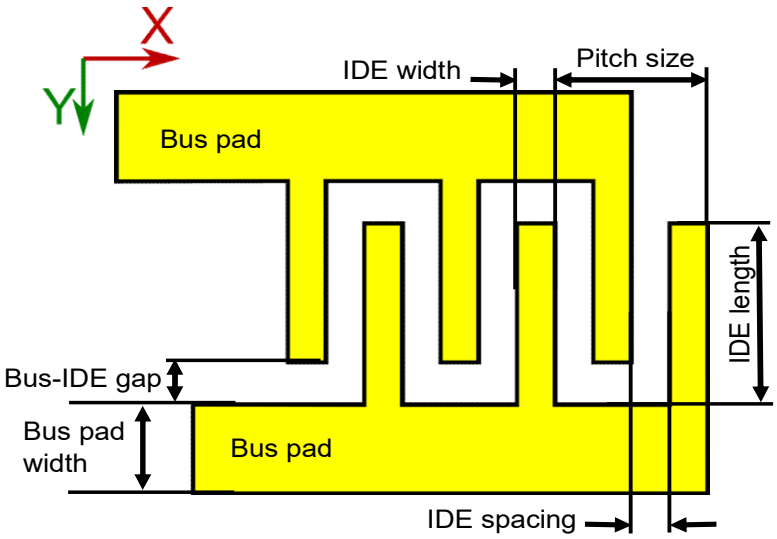

Figure 3.1. Key features/ dimensions of an IDT.

The pitch size is the most important parameter of the IDTs, and it governs its wavelength/ operating frequency. It has been previously stated that the pitch of the IDT is equal to the wavelength and as such eq. 6 can be rewritten to:

$$P = \frac{c_s}{f} \tag{29}$$

where P and f is the pitch of the IDT (m) and the operating frequency (Hz). This equation guides the user to design the pitch size of their IDTs based on the material they use, with respect to the desired wavelength/ operating frequency. It should be noted that in some literature the pitch size refers to $\frac{P}{2}$ and whether this is correct is up to debate. But to avoid confusion, in this thesis the author will continue applying P as described in eq. 29, which also results with $P = \lambda$ and therefore they can be used interchangeably. As such, a single pitch includes a pair of IDEs and IDE spacings, and it is standard practice to make these dimensions equal. Thus, the width of the IDEs can be calculated as follows:

$$w_{IDE} = \frac{P}{4} \tag{30}$$

Even though the w_{IDE} is typically ¼ of the pitch, it can be made wider or smaller. But the spacing between the IDEs will have to be adjusted accordingly to maintain the pitch size. Additionally, the designer of the IDTs must determine how many pairs of IDEs are required. It has been stated by Kirschner (2010) that the bandwidth of the frequency is defined by the pairs of the IDEs as:

$$BW = \frac{2f}{N} \tag{31}$$

where N is the number of pair of IDEs. Eq. 31 demonstrates that more pairs of IDEs result with a wider frequency bandwidth, and it provides a leeway around the operating frequency. This means that if a frequency is slightly offset from the operating frequency

used, the device can still remain operational. But apart from these general guidelines there are no further instructions on how to design an IDT for acoustofluidic applications. This then leaves the bus pad width and length, the bus-IDE gap, length of the IDEs and even pairs of IDEs to be arbitrary. To provide more guidelines the author has included some further comments on how to design an IDT in Appendix 3 based on his own developed experience.

The IDT feature that was the main driving force of design was the smallest pitch that could be reliably achieved by the hard (FR4) PCB manufacturing method, which was 200 μm giving which gives a finger width of 50 μm. This pitch would generate a frequency of ~19.9 MHz with a 128^{o} Y-cut $LiNbO_3$ substrate, a frequency that has been previously used in biomedical applications with SAW devices (Li et al., 2015). The IDT was designed to have 40 pairs of IDEs (i.e. 80 fingers), which would give it a theoretical bandwidth of 1 MHz. The PCB IDTs were designed using the Eagle software (Autodesk, US) and the design can be seen in Fig. 3.2a. The design was then converted to a GERBER file and was sent off to be manufactured externally (circuitfly.com). Fig. 3.2b illustrates the dimensions of the PCB IDTs and of its features, where the IDTs have a pitch size of 200 μm, IDE width of 50 μm, 40 pairs of IDEs (i.e 80 fingers), bus /IDE gap and IDE spacing of 50 μm, IDE length of 10 mm, bus pad width of 5 mm and bus pad length of ~43 mm. The PCB also contained additional features such as milled slots and drilled holes, with the middle slot added to allow the placement of a microchannel between the two IDTs. The remaining 3 slots on the PCB were added to help align the PCB with the flat reference edge of a 3-inch substrater at different orientations and the drilled holes were added to potentially hold the PCB at a set location using dowel pins. In the end, apart from the microchannel slot, the other features were not used, but nonetheless this illustrates the capability of the PCB industry to customise the PCB based on the designer’s preference.

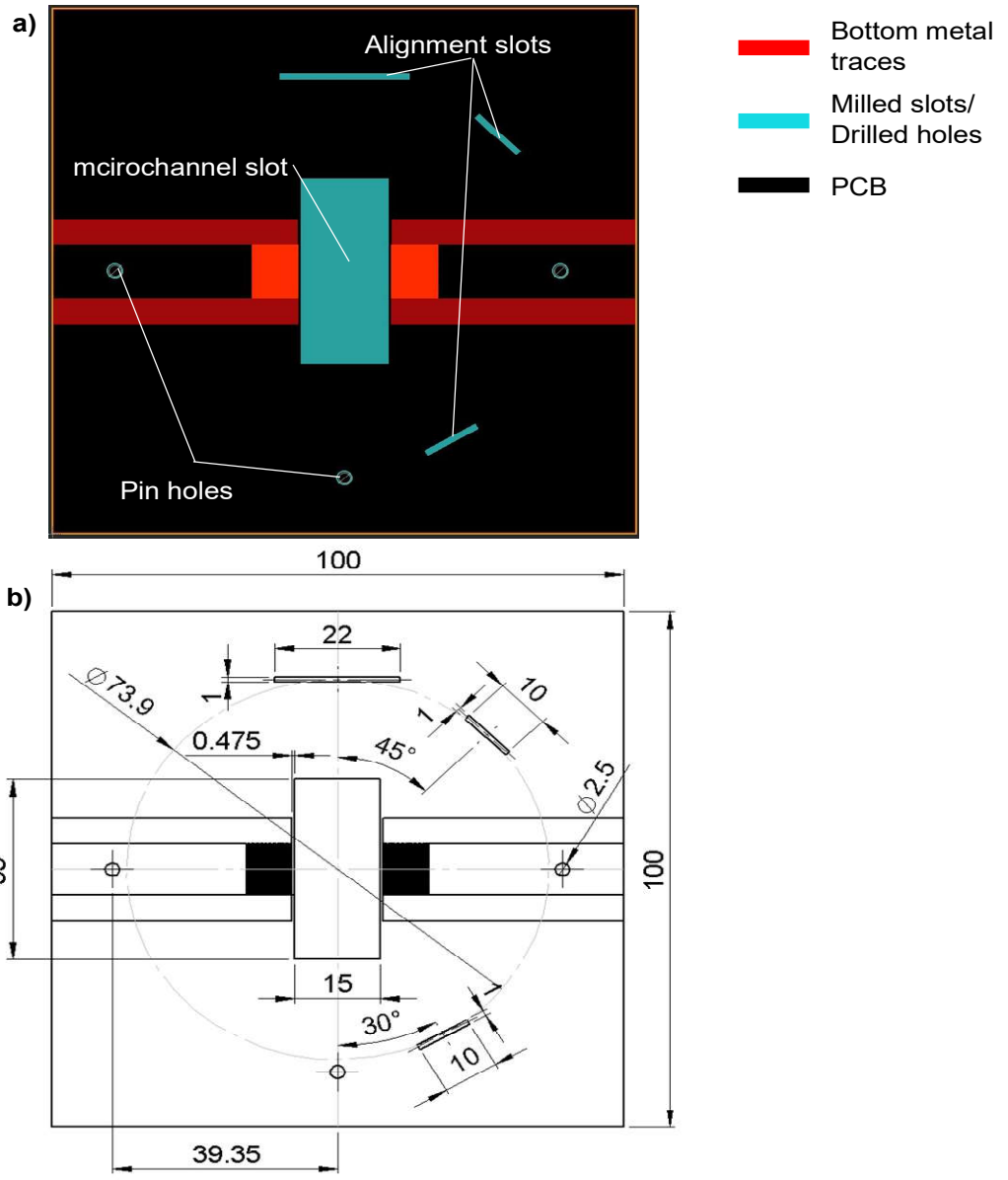

Figure 3.2. PCB IDT design. a) The Eagle design of the PCB IDT and b) the dimensions of the PCB IDT and its features.

3.2.2. IDEs characterisation

To establish the dimensional quality of the electrodes on the manufactured PCB, static images were taken of the IDEs using a microscope (KERN, Germany) with a 10x magnification. These static images were taken at nine different locations on nine different manufactured PCB IDTs, and a total of 161 measurement were obtained, for both the IDE width and spacing.

3.2.3. PCB-SAW jig development

To test the PCB IDTs and their capability to create a SAW device, a 3-inch 128° Y-cut $LiNbO_3$ substrate (PMOptics, USA) was selected. The fabrication of a PCB SAW device

is very simple and all that is required a clamping mechanism that presses the PCB IDTs onto the $LiNbO_3$ substrate. A schematic of a developed PCB SAW device is shown in Fig. 3.3a, and it consists of six main components: a base plate, a $LiNbO_3$ substrate, the PCB IDTs, a clamp, a pressure ring and a microchannel. From the base plate all the components are added on top and are held together using the four screws on the edges of the base plate. The pressure ring is added last during assembly and its function is to apply localised pressure on top of the IDE region, which results with the coupling of the IDEs and the $LiNbO_3$. Once a proper clamping force is established, RF signals can be applied to the IDTs which will generate counter-propagating SAWs on the $LiNbO_3$ and form a standing SAW (SSAW). Finally, a microchannel can be bonded in the middle of the $LiNbO_3$ substrate, if needed.

The manufacturing and design of the clamping mechanism is done internally using a 3D printer (Ultimaker 2+ extended, Netherlands). The components were all designed using SolidWorks (Autodesk, USA) and translated into g-code, for 3D printing, using Cura (Ultimaker, Netherlands). The components were printed using polylactic acid (PLA) (2.85 mm, Ultimaker) with the following settings: (1) Nozzle = 0.4 mm, (2) Top/ bottom layer thickness = 0.8 mm, (3) Top/ bottom printing line pattern = [0, 90]º, (4) Wall thickness = 1 mm, (5) Inflation pattern percentage = 35% and (6) Inflation line pattern = [0, 45, 90, 135]º. The only setting that was different per component was the printing line pattern, which was changed to concentric for circular features such as the pressure ring and the round holder. The round holder underwent an additional procedure, where it was polished using 1200 grit sandpaper to create a smooth surface for the $LiNbO_3$ to sit on and to avoid potential cracking due to an uneven/ rough surface when the pressure is applied. Additionally, to increase the rigidity and durability of the regions of the M5 threads, i.e. the holes on top of the localised pressers, stainless steel M5 thread repair inserts (RS PRO, UK) were added into those holes. An exploded view of all the components that compromise the PCB SAW device is presented in Fig. 3.3b and the real-life-assembled model is shown in Fig.3.3c.

Before the assembly, coaxial cables are soldered to the PCB IDTs' bus pads and both the $LiNbO_3$ and PCB IDTs are cleaned with IPA. Four M5 countersunk screws are pre bonded underneath the base plate using epoxy (Araldite, RS Pro). The base plate's circular incision has triangular extrusions while the round holder has triangular slots, which help align the components and stop the round holder from rotating. Both base plate and round holder have a rectangular though slot that acts as a window to permit light to pass through. The round holder is placed into the base plate, with its flat edge perpendicular to the X axis. The $LiNbO_3$ is positioned on top of the round holder, and its reference flat edge is coincidently aligned with the predesigned flat edge of the round holder. The PCB is then placed on top of the $LiNbO_3$, followed by the clamp being slotted

onto the screws and placed on top of the PCB. The internal width between the clamp's feet is made slightly larger (2 mm) than the PCB. This was done so the clamp doesn't latch to the PCB, but it was also kept small enough to help align the PCB and eliminate any potential rotation. The M5 nuts are then placed onto the four M5 screws, on the edges, and turned by a couple of threads, just keep the clamp on. The localised pressers are then inserted into the pressure ring and the pressure ring is threaded in until it slightly touches the top of the PCB. The four corner nuts are then tightened up and two M5 screws are inserted into the pressure ring, which permit the fine adjustment of the pressure on top of the IDEs. A microchannel is bonded in the middle of a $LiNbO_3$ substrate using plasma treatment, via an external supplier, and a secondary $LiNbO_3$ substrate is used when no microchannel is needed.

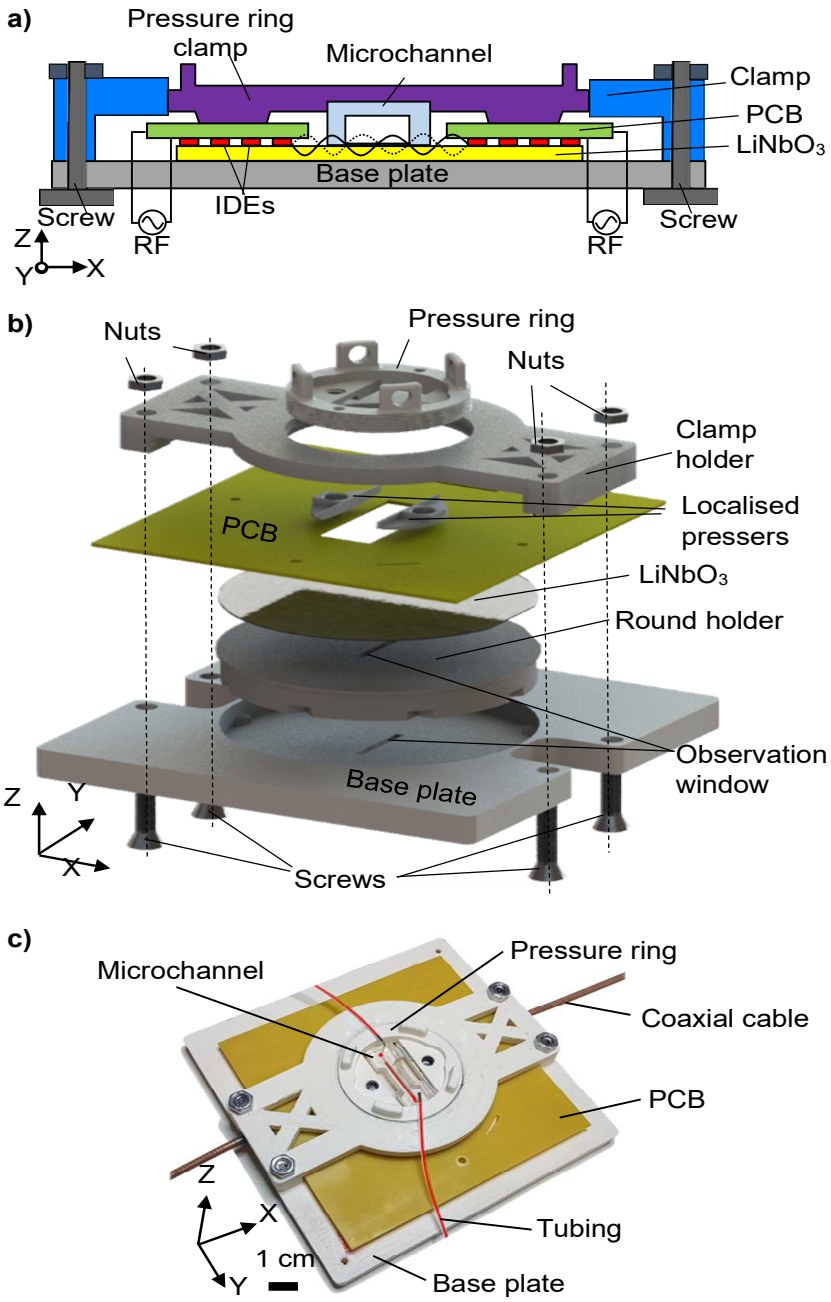

Figure 3.3. a) PCB SAW schematic consisting of a base plate, a $LiNbO_3$ substrate, the PCB IDTs, a pressure ring, a clamp and a microchannel. The clamping components are help together using M5 screws and nuts. b) PCB SAW device exploded view indicating all its components. c) Real-life assembled PCB SAW device.

3.2.4. Electrical characterisation of PCB SAW

The most common method of characterizing a piezoelectric device is by its electrical properties, or more specifically by its scattering parameters (S-parameters) which are measured using a vector network analyser (VNA, E5061B ENA, Keysight). The left and right IDTs form a two-port network, shown in Fig. 3.4a, which allows the VNA to measure

the following S-parameters: S_{11} – power reflection coefficient seen at the left IDT (Port 1), S_{21} – power transmission coefficient from the left to the right IDT (Port 1 to Port 2), S_{12} – power transmission coefficient from the right to the left IDT (Port 2 to Port 1), and S_{22} – power reflection coefficient seen at the right IDT (Port 2). As an example, a S_{11} of -12 dB indicates that most of the electrical power transmitted to the device is absorbed (~93%), while a S_{21} that approaches 0 would indicate that there are no transmission losses when the signal travels from one IDT to the other. Due to the contact between the PCB IDE and the $LiNbO_3$ being formed via mechanical clamping, the power reflections from both Port 1 and Port 2 are naturally very high. To counteract this, an impedance matching network (MN), shown in Fig. 3.4b, is developed for both the left and the right IDTs to bring their impedances close to 50 Ω and reduce reflections.

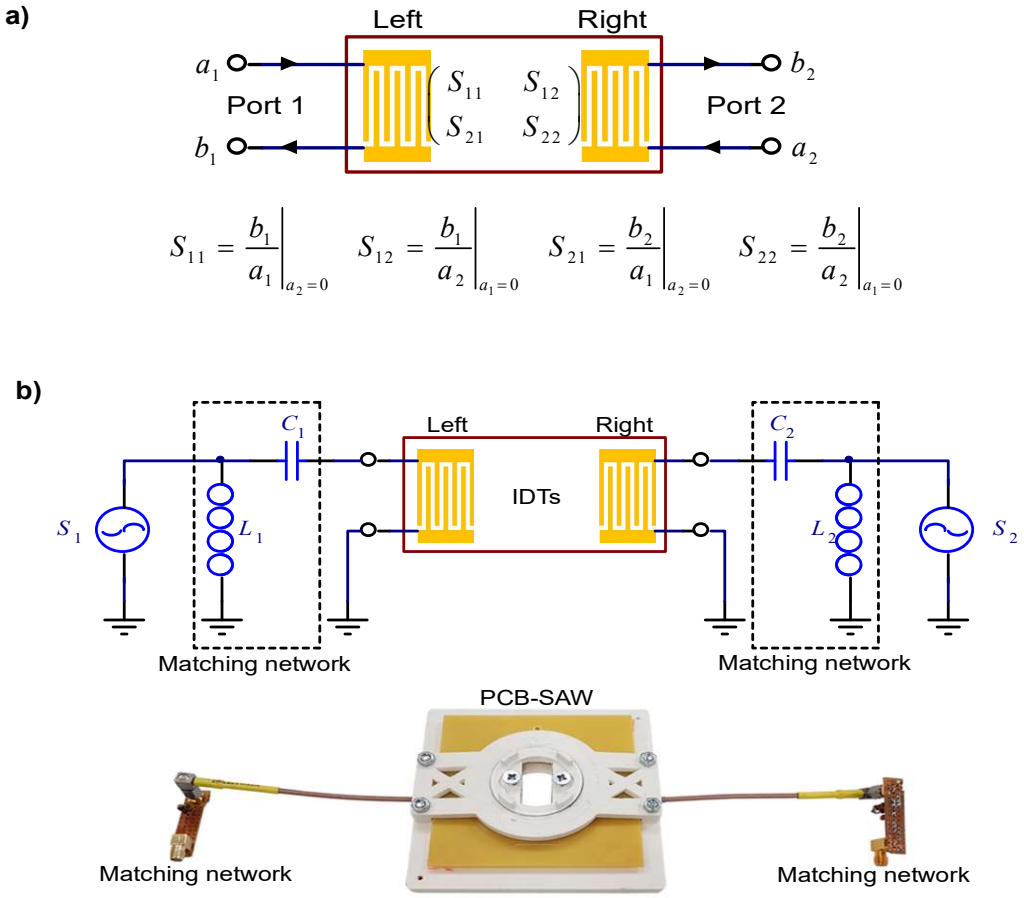

Figure 3.4. Electrical characterisation of the PCB-SAW device. a) Schematic and description of the *S*-parameters formed by the IDTs. b) Schematic (top) and real-life model (bottom) of MNs, where S, L and C represent the power source, the inductors (450 nH) and the capacitors (82 pF), respectively.

3.2.5. Electrical setup

The electrical setup that is used to power and monitor the inputted power into the PCB-SAW device is shown in Fig. 3.5. The setup consists of a signal generator (SG)

(RSDG5162, RS pro), a 6 W power amplifier (PA), a power coupler (ZFBDC20-62HP-S+, Mini circuit), two power meters (PM_F, PM_R) and a MN. This setup is identical for both the left and right IDT. The coupler and power meters are used to monitor the inputted (PM_F) and reflected power (PM_R).

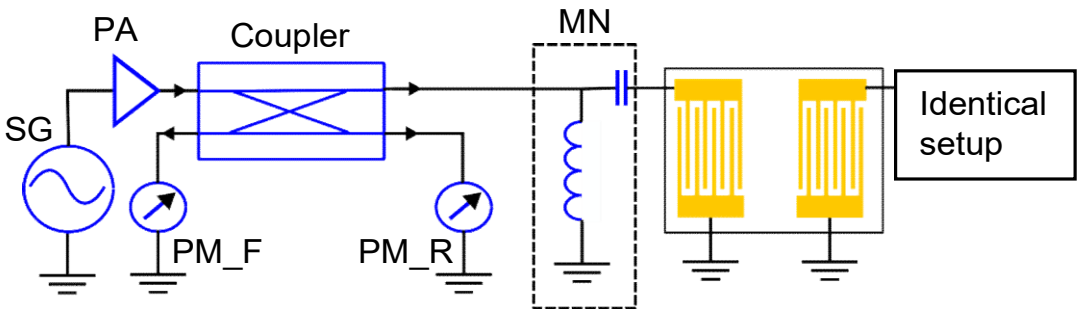

Figure 3.5. Electrical setup for PCB-SAW device, where SG, PA, PM_F and PM_R stand for signal generator, power amplifier, power meter incident and power meter reflected, respectively.

3.2.6. PCB-SAW droplet actuation

The mechanical clamping force, produced by the pressure ring and screws on top of the localised pressers, determines the contact quality (S_{11}) between the PCB and the $LiNbO_3$ substrate. A droplet actuation test is performed to investigate the relationship between the clamping force, R-SAW generation and S_{11} reading. To perform the tests a $LiNbO_3$ substrate was coated with a hydrophobic substance (CYTOP™, AGC Chemicals Europe), which was done by evenly distributing it across the $LiNbO_3$ substrate and letting it cure (Fu et al., 2017).

The clamping force between the $LiNbO_3$ substrate and the PCB IDEs was increased by adjusting the torque of the M5 screw on top of the localised presser. A digital torque screwdriver (5-50 cNm, Adema, Taiwan) with a digital display was used to apply and read the torque. The torque was converted to clamping force by using the formula $F = \frac{T}{cD}$, where F, c, D and T correspond to clamping force (N), coefficient of friction, screw diameter (m) and torque (Nm), respectively. The standard value of c for unlubricated steel is 0.2 and the minimal reading of the digital torque screwdriver was 0.05 Nm, which allowed a minimum reading of 50 N.

Under each measured torque, a 1 µL water droplet was pipetted onto the $LiNbO_3$ substrate 5 mm away from the first IDE. Then an input power of 1.26 W was applied to the PCB-SAW device to actuate the droplet. Although there was a slight location variance of droplet initial positions in each test, this should be insignificant as the SAW attenuation in the $LiNbO_3$ substrate is relatively small (Slobodnik *et al.*, 1970). But even though the

droplet was placed in nearly identical location before actuation, a variation in speed of droplet transportation can be observed on both the devices. It is hypothesised that this could have been caused by slightly uneven CYTOP coating, coating deterioration, slight contact angle variance, droplet volume variation, slight location variation or a combination of these factors. Therefore, the droplet actuation by the SAW was repeated 5 times before changing to another clamping force. A 60 fps camera was used to capture the droplet moving and a calibrated software Tracker (www.compadre.org/osp/) was applied off-line to analyse the droplet velocity for indicating the SAW amplitude. The droplet observation was performed under an inspection microscope with 2x magnification (Lynx Evo, Vision Engineering). The captured droplet videos were analysed frame by frame, using the leading edge of the droplet as the reference, to determine the displacement of the droplet. Any 2 consecutive frames could produce one velocity using the displacement multiplied by the framerate step time. Five consecutive frames after the droplet moved were used to get four velocities, which then were averaged to get the mean droplet velocity. The pixel size and the frame rate of the camera system were 10 μm and 60 fps, respectively, resulting in a velocity resolution of 0.6 mm/s, which was sufficient for capturing droplet movement.

To benchmark the performance of the PCB-SAW device with a SAW device made by standard photolithograph, a cleanroom made IDT (CR IDT) was manufactured, by a cleanroom technician in Cardiff University, on the identical type of $LiNbO_3$ substrate and had the identical geometry as the PCB-SAW device. The CR IDT was also coated with CYTOP™ and the same droplet actuation, with the same setup, were performed to characterise its actuating performance. For both the CR IDT and PCB-SAW device the droplet actuation tests were repeated three times to get an average velocity at various input powers.

3.2.7. Droplet streaming

To test whether the PCB-SAW device was indeed generating a R-TSAW capable of generating acoustophoretic effects within a liquid, a simple droplet setup was initially used to investigate this. A 3-4 μL glycerol droplet (3 mm in diameter) was pipetted onto the $LiNbO_3$ substrate and then 20 μm polystyrene microsphere particles (Sigma Aldrich) were pipetted directly into the glycerol droplet (concentration of ~18,000 particles/ μL). An input power of 0.2 W was used for each IDT to generate the R-SAWs. Glycerol was chosen as the medium instead of water because of its higher viscosity and lower evaporation rate. The reason why 20 μm particles were selected is that due to their large size they were easy to observe in the droplet under 2x times microscope magnification (Lynx Evo, Vision Engineering). The videos were recorded using a 60 fps camera.

3.2.8. PDMS microchannel fabrication

The microchannel used was fabricated using soft lithography and PDMS. The master mold was manufactured externally and had a microchannel pattern with width, length and height of 200 μm, 15 mm and 60 μm, respectively. The PDMS (Sylgard 184, Farnell UK) was mixed to 1:10 (weight: weight) ratio of hardener and elastomer, poured onto the master mold and left to cure on a hot plate at 65 ºC for 4 hours. After curing the PDMS was then left to cool and afterwards was peeled of the mold with the help of IPA. The PDMS input ports were then created using punching tools (Darwin Microfluidics, France). Initially a 1.25 mm hole diameter was punched halfway through the PMDS channel from the bottom side, where the microchannel internal geometry is located. The semi attached PDMS was then pinched and removed with tweezers and then a final hole diameter of 0.5 mm was punched straight down through the rest of the material. This two-stage operation was done in order to reduce the fluid velocity entering the chamber and thus potentially minimize the chance of leakage. During the punching, it was ensured that the puncher was not rotated when cutting into the PDMS, since that could rapture the surrounding PDMS. PTFE tubing with an internal and external diameter of 1/32'' and 1/16'' (Darwin Microfluidics, France), respectively, were used for the fluid handling with 23G stainless steel connectors inserted into the tubing and then into PDMS holes. The overall liquid sample was handled with a 5 mL SGE luer lock syringe (Hamilton Syringe) with a blunt end 23G needle to connect to the tubing. The syringe was actuated using a syringe pump (KDS LEGATO 78-8212C, Cole-Palmer).

3.2.9. Particles actuation simulation.

To study the distribution of acoustic pressure and predict particle trajectories, COMSOL Multiphysics® was used to compute the numerical results on the X-Z plane of the microchannel. The acoustofluidic model used was adopted from conventional SAW device modelling program (Barnkob et al., 2018; Nama et al., 2015) by the department's software engineer. The particle size used for the trajectory simulation was 10 μm.

3.2.10. Particle and cells preparation

To demonstrate the PCB-SAW device's capability in manipulating particles inside the microchannel, 10 μm polystyrene microspheres (Sigma-Aldrich) were mixed with a custom media at a volume ratio of 1:2.7. The custom media consisted of glycerol and phosphate-buffered saline (PBS) with a volume ratio of 1:4.4, which was made to prevent particle deposition. Before sample introduction, the microchannel was flushed with bovine serum albumin (BSA) solution (water:BSA = 100:1, mass ratio) for 20 min at a flow rate of 20 μL/min using a syringe pump. The input power in this experiment was 0.5 W and a microscope with 4x magnification was used (KERN, Germany) with a 60 fps camera to record the videos.

It should also be specified here that 10 μm particles were selected, due to it being a size that has been demonstrated to be possible to actuate via the acoustic radiation force

(Ding et al., 2014, 2012; Edthofer et al., 2023; Liu et al., 2019). This would ensure that they would not be affected by the acoustic drag force and only demonstrate the actuation generated the by acoustic radiation force (Ding et al., 2014). This size is also just large enough for the particle to be still distinguishable and observable under the microscope with 4x magnification. The author also speculates that the manipulation of these particles could then also indicate the possibility manipulating various cancer cells, due to a proven past example in literature (see Appendix 2). For the actuation images the particles were actuated by supplying ~0.5 W per IDT.

For the cell manipulation, the cells were cultured and obtained from the Tissue Microenvironment Group (TMEG) department of Cardiff University. In short, the human non-small-cell lung carcinoma (NSCLC) cell line- A549 (ATCC® CCL-185™) were obtained from the American Type Culture Collection (Virginia, USA) and were grown by a technician in Dulbecco's modified eagle media and supplemented with L-Glutamine (200 mM at 1:100 dilution, Gibco), Penicillin/Streptomycin (10,000 U/mL at 1:100 dilution, Gibco), and 10% foetal bovine serum (FBS) in 75-cm^3 cell culture flasks until their density reached 1×10^7 /mL. The cells were harvested by the technician from the plastic surface by trypsinisation, and then concentrated by centrifugation (3500 rpm, 5 min) to 2×10^7 /mL. The concentrated cells were then given to the author and used for the experiments. The input power was set ~1 W per IDT in the experiment and the collected videos were recorded using a microscope with 4x magnification and 60 fps camera.

3.2.11. Viability test procedure

There were three sample groups for viability test: (1) SAW-on Group, in which the NSCLC cells were continuously run through the PCB-SAW device for 5 minutes under the input power of ~1 W per IDT and flow rate of 20 µL/min. (2) SAW-off Group, in which the cells were running through the PCB-SAW device at the same flow rate and duration without applying SAW. (3) Control Group, in which the cells were kept in a tube on an ice bath for the same period of time.

Acridine orange (AO, 30 µg/mL) and di-amino-phenyl-indole (DAPI, 100 µg/mL) were mixed at the volume ratio of 3:10 to prepare an AO-DAPI solution for cell staining by a technician. For both SAW-on and SAW-off Group, 100 µL sample in total was collected after five minutes, and given to the technician, of which three 10 µL samples were taken out to mix with the AO-DAPI solution at the volume ratio of 5:1 to stain the cells. The three stained samples were then pipetted into three cell chambers on a cell counter slide for viability analysis using a cell counter (NucleoCounter® NC-3000™). The same amount of the sample was also taken for the Control Group. All the tests were repeated three times.

3.2.12. ZnO substrates

ZnO substrates were obtained externally and were used to demonstrate the capability of the PCB IDTs to couple with different piezoelectric substrates. Both substrates had a thin ZnO layer, with the difference that one had a silicon substrate and the other an aluminium sheet and both substrates were 1.5 mm thick. Both substrates were actuated using 50 W input power per IDT, but the ZnO-silicon substrate was actuated at 23.13 MHz while the ZnO-aluminium substrate was actuated at 9.75 MHz. Both were coated with CYTOP™, as in section 3.5.6, and had a 1 µL droplet applied on the substrate for the actuation. These tests were done preliminary and as such each substrate was assembled and actuated at the indicated S_{11} drop with no MNs using only a signal generator and a 50 W amplifier.

3.3. FPCB-SAW and VAD

This section describes all the methodologies for the chapter 5. This includes the development of the FPCBs IDTs which includes their geometry as well as the setup used to test them (Sun *et al.*, 2021*)*. This section also discusses the development of acoustofluidic device made fully from accessible components, termed as the versatile acoustofluidic device (VAD) and a new methodology of manufacturing PDMS microchannel's using 3D printing.

3.3.1. FPCB-SAW fabrication and setup

For the thorough characterisation of the FPCB IDTs, FPCB IDEs chips were designed and manufactured externally (circuitfly.com) by patterning interdigital electrodes (IDEs) made of metal bilayers (Au/Ni, 30 nm/2 µm) onto a 70-µm-thin polyester laminate. The IDEs on the FPCB consist of 40 pairs of 20-mm-long finger electrodes and coaxial cables were soldered to the bus pads of the FPCBs. Instead of 3D printed components this design integrated metal components to create both a more robust and simpler device. Fig. 3.6a shows both the FPCB IDEs chip design and the assembled real-life model of the FPCB-SAW device, while Fig. 3.6b illustrates the electrical setup and cross section schematic of the FPCB-SAW device. It can be observed that this device's clamping mechanism has been greatly simplified to a just an aluminium base place and an aluminium holder. The holder is held by two M3 screws at its far edges, which are also used to apply the clamping pressure to the FPCB IDEs. A silicone gel pad is integrated at the middle of the holder to evenly distribute the pressure and allow the FPCBs to freely deform and match their coupling surface. The only 3D printed component is the housing unit, which hosts the wires and MNs of the device. The electrical setup is identical to the PCB-SAW device.

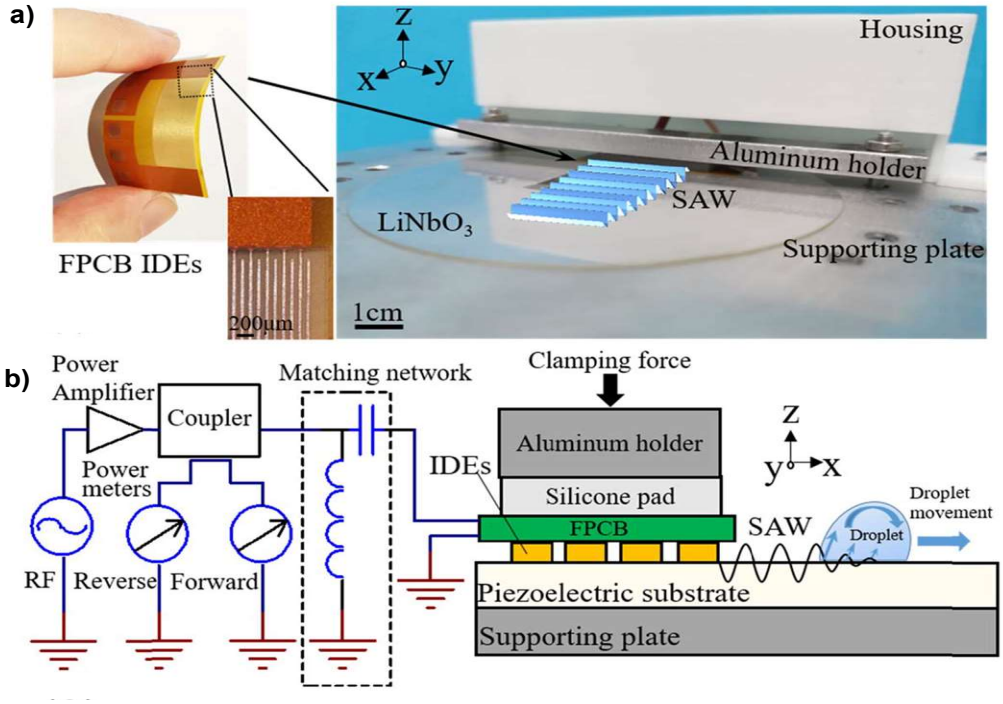

Figure 3.6. a) Photograph of the FPCB IDEs and the FPCB-SAW device consisting of an FPCB stacked on a $LiNbO_3$ substrate. b) Assembly diagram of the SAW generation on the FPCB-SAW device and its driving circuitry. Figure adapted from *Sun* et al., *2021*.

3.3.2. FPCB IDTs characterisation and experimental setups

The electrical characterisation was done using a vector network analyser (VNA, E5061B ENA, Keysight). The surface deformation characterisation, i.e. the characterisation of SAWs, was done the using a laser vibrometer (PSV-500-VH, Polytec, Germany). For the pressure tests the torque was applied onto a 3 mm screw with a digital torque screwdriver (5-50 cNm, Adema, Taiwan). For this test three repetitions were performed. For the droplet actuation the piezoelectric surface was coated with CYTOP (Asahi Glass Company Ltd., Japan) and 1 µL water droplet was pipetted onto the surface, near the IDT, similarly to the section 3.2.6. For the environmental tests the device was placed into a temperature-humidity chamber.

3.3.3. VAD components and assembly

The FPCB IDTs used were manufactured identically as the ones in the previous section, 3.3.1. They had the identical feature dimensions apart for the IDE length, which is 10 mm is this design. The FPCB IDTs used in this design are shown in Fig.3.7a. The VAD also has a very similar setup schematic as the previous devices, see section 3.2.5 and 3.3.1, but in this case the MNs have a value of 68 pF and 470 nH for the capacitor and inductor, respectively. This design also incorporates additional features, as shown in Fig. 3.7b, such as a fan, temperature sensors (T) and force sensitive resistors (FSR), which are operated via a compact control unit. The control unit was developed to increase the

portability of the acoustofluidic system and to facilitate on-demand use of the VAD and was designed by the department's electrical engineer. The control unit includes a waveform generator, a power amplifier, a microcontroller, sensors, a display, and a power supply. The schematic and the components of the control unit are illustrated in Fig. 3.7c.

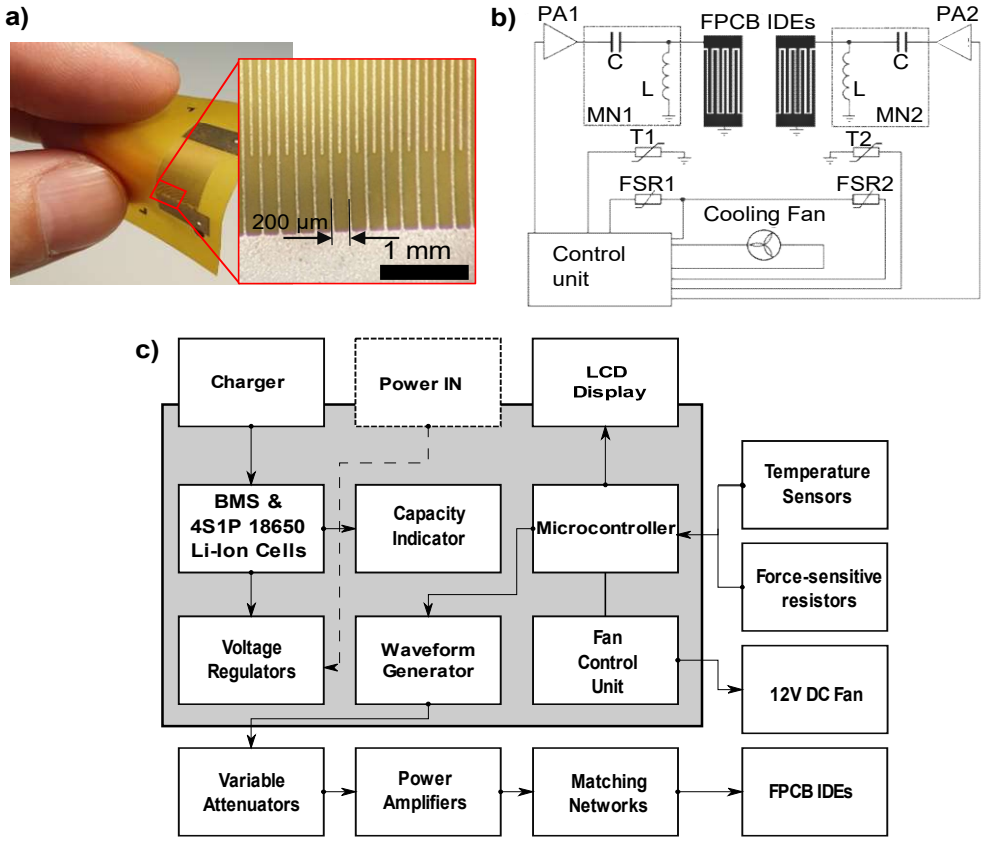

Figure 3.7. a) Real-life flexible printed circuit board (FPCB) pre-patterned with interdigital electrodes (IDEs) with a zoom inset of the IDEs. b) Schematic diagram of the Versatile Acoustofluidic Device (VAD) and a portable control unit, that can drive a cooling fan and provide radio frequency (RF) signals to drive the two IDTs. The RF signals are amplified by two 6 W power amplifiers (PA1 and PA2). Each IDT is connected to a matching network (MN1 and MN2) for impedance matching. The values of the capacitor (C) and inductor (L) are 68 pF and 470 nH, respectively. The sensing components include two temperature sensors (T1 and T2) and force-sensitive resistors (FSR1 and FSR2). c) Control unit block schematic.

As with the previous devices this device as well implements a clamping mechanism and localised pressers, with all the components being 3D printed using PLA with the settings stated in section 3.2.3. The reason why this device moves back to a 3D printed clamping system, instead of the simpler metallic presser (shown in Fig. 3.6), was to permit the creation of relatively complex structures and features using a relatively easy and accessible method. While these structures could be indeed created with metallic

materials using various machining processes or even metal 3D printing, they are less easy to use and more expensive in comparison to the desktop 3D printing.

The VAD components are shown in Fig. 3.8a which, going from the bottom to the top, are: the heatsink (supports the entire device and dissipates heat), the temperature sensors (measure the IDT temperature), the $LiNbO_3$ substrate (produces the SAWs), the FPCB IDTs (convert RF to SAWs), the silicone gel pads (evenly distribute the clamping force), the localised pressers (apply the clamping force), the force-sensitive resistors (FSRs) (measure the clamping force), the FSR roofs (holds and presses into the FSRs), the M5 screws (generate the local clamping force) and the main holders (holds the whole structure onto the heatsink). Before any assembly the heatsink was sanded using a P1200 grit sandpaper and the localised pressers had the silicone gel pads attached to them using epoxy (Araldite, RS Pro). As stated previously, the silicone gel pad are added to distribute the pressure evenly across the surface and allow local deformation. This is also why the silicon pads are added in the location where the FSR sits, to permit it to freely deform under the applied pressure and to provide the readings based on the deformation. The main clamps had also M5 thread repair inserts (RS PRO, UK) added into its M5 holes on top of the localised pressers. The last structure added to the VAD consisting of an acrylic presser and a microchannel presser, which is developed, via 3D printing, to press and hold down the microchannel between the two IDTs. Additionally, it should be noted that the bottom edges of the main holders were made to match the circumference of the 3-inch $LiNbO_3$, shown in 3.8b, and as such the $LiNbO_3$ and the rest of the components could be easily aligned to sit in their desired locations.

To assemble the VAD, the following procedure was followed: the FPCB IDTs, microchannel and $LiNbO_3$ substrate were thoroughly cleaned using isopropyl alcohol (IPA) and de-ionised (DI) water, dried using a compressed air duster and checked under the microscope to ensure that no fibres or dust particles were present on the parts before the final assembly. Initially, all the M5 threaded rods are placed into the heatsink, then the localised pressers (without the FSR) are assembled and placed into the main holders. Only one of the main holders is placed into the threaded rods and it is fully tightened down using M5 nuts. The $LiNbO_3$ is then placed on the heatsink, pushed against the bottom edge of the main holder and its flat edge is aligned to be parallel with the main holder. The second main holder is then added, checked to see that it sits on the heatsink and that it is in slight contact with the edge of the $LiNbO_3$. After the inspection the second main holder is also fastened down with M5 screws. The M5 screws sitting on the main holder on top of the localised pressers are then added, slightly threaded in and the FSR sensors are slotted inside the localised presser. The FPCB IDTs are then placed underneath the localised presser and clamped down by fastening the M5 screw on top of the main holder. A vector network analyser (VNA, E5061B ENA, Keysight) is used to

monitor the reflection coefficient (S_{11}) and to confirm when the IDEs are in contact with the $LiNbO_3$ and to determine when the optimal clamping force is achieved. The methodology for aligning the two FPCB IDTs chips is discussed in the section below.

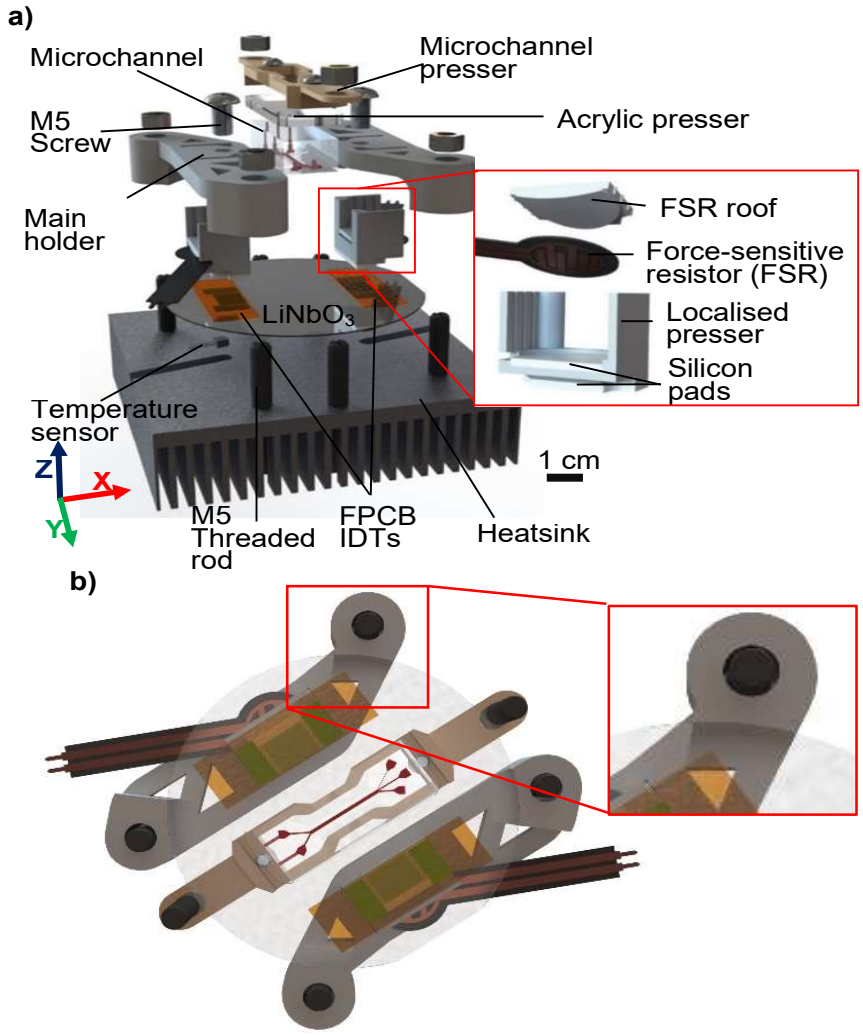

Figure 3.8. a) 3D exploded view of the VAD with an inset presenting the assembly and components of the localised pressers. b) Bottom view of the main holder edges' matching the $LiNbO_3$ circumference.

3.3.4. IDT alignment setup and analysis

Through brief preliminary assemblies of the VAD, one interesting phenomenon that was observed was that the devices insertion loss (S_{21}) would decrease (negative value increase) when the IDTs are intentionally misaligned and were not parallel. As such a theory was established that two IDTs chips with set locations could be aligned to be parallel using only the S_{21} reading and a VNA. To tests this, the procedure demonstrated in Fig. 3.9 was used, were by connecting two IDTs to the VNA as a two-port network one IDT becomes the receiver and the other the transmitter. The test keeps one of the IDTs

unmoved, as the receiving IDT, while rotating the other IDT, as the transmitting IDT. The S_{11} of the transmitting IDT is measured during this procedure to monitor how it changes with the rotation. Top view images of the transmitting IDT at different orientations were captured by an overhead camera, which were then analysed using a customised MATLAB code that extracted the angle between the two IDTs. Five reference angles, 17°, 11°, 6°, 2°, and 0°, were determined for the S_{21} readings, which were selected by finding the most observable change in the S_{21}.

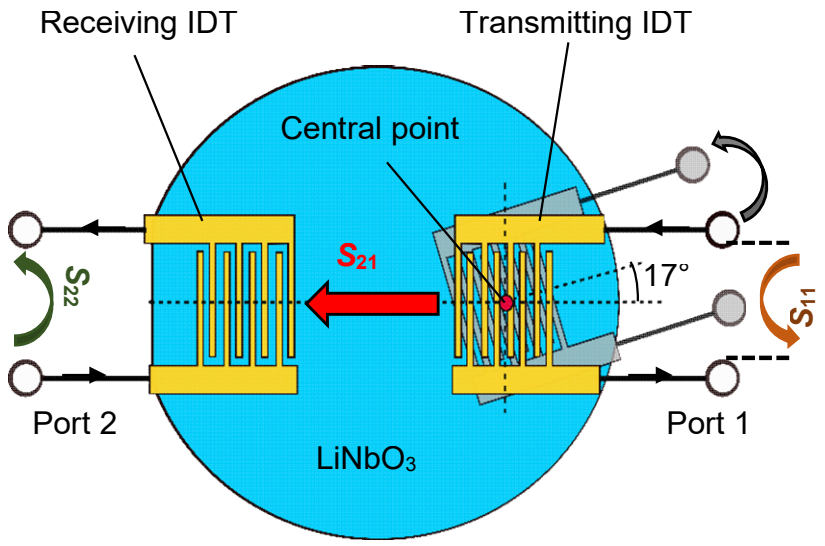

Figure 3.9. IDT rotation test for investigating the use of the vector network analyser (VNA) to register the alignment of the IDTs. The transmitting IDT being rotated around its central point, while the receiving IDT is held fixed.

3.3.5. 3D printing based microchannels

To eliminate the need of any clean room based manufacturing, 3D printed microchannel molds were created to replace the silicon based ones. The developed microchannels were also attached to the $LiNbO_3$ using mechanical clamping, by using a 3D printed microchannel presser, to eliminate the need of plasma treatment. These molds were developed using PLA, a 0.25 mm nozzle and 1 mm thick glass slides, using the setting and tools described in section 3.2.3. The development flow of the 3D printed moulds is illustrated in Fig. 3.10a where: (1) A glass slide (76 mm (W) × 26 mm (L)) is placed on the 3D printer table and held in place using masking tape. A compensatory offset is applied by using a "Z offset setting" plugin in the 3D printer software (Cura), which was selected based on the glass slide thickness. Using this software glass slides with various thicknesses can be used as the glass-bottom of the mold by adjusting the offset setting. The 3D printed mold, designed in SolidWorks, is then directly printed on the glass slide, (2) removed from the 3D printer table after completion and left to cool. Before proceeding further, the glass slide is inspected from underneath and from the sides to ensure that

the 3D printed structure is in full contact with the glass slide. (3) The glass-bottom 3D printed mould is then placed in a plastic petri dish and filled with PDMS (Sylgard 184, Farnell UK), which is prepared according to the manufacturer's protocol, see section 3.2.8. The dish is placed onto a hot plate (SD160, Colepalmer) at a temperature of 45 °C to cure for 24 hours, which is below the 60 °C melting temperature of the PLA. (4) The set PDMS is removed from the mold, (5) the outer perimeter of the channel is cut and (6) a premade acrylic presser, with the dimensions of 47 mm (L) × 15 mm (W) × 3 mm (H), is placed on top of the microchannel. (7) The microchannel is then bolted onto the pre-assembled VAD using the 3D printer microchannel presser (Fig. 3.10b). (8) The M5 nuts on the far edges of the microchannel presser are fastened until resistance is felt and (9) finally the M3 screws are screwed in to ensure even distribution of the pressing force. The walls of the microchannel presser (Fig. 3.10a, step 9) are created to prevent it from overbending. Two examples of the glass-bottom 3D printed moulds are shown in Fig. 3.10c, which represent a single input/outlet (top) and a 3-input/ 2-output microchannel structure (bottom).

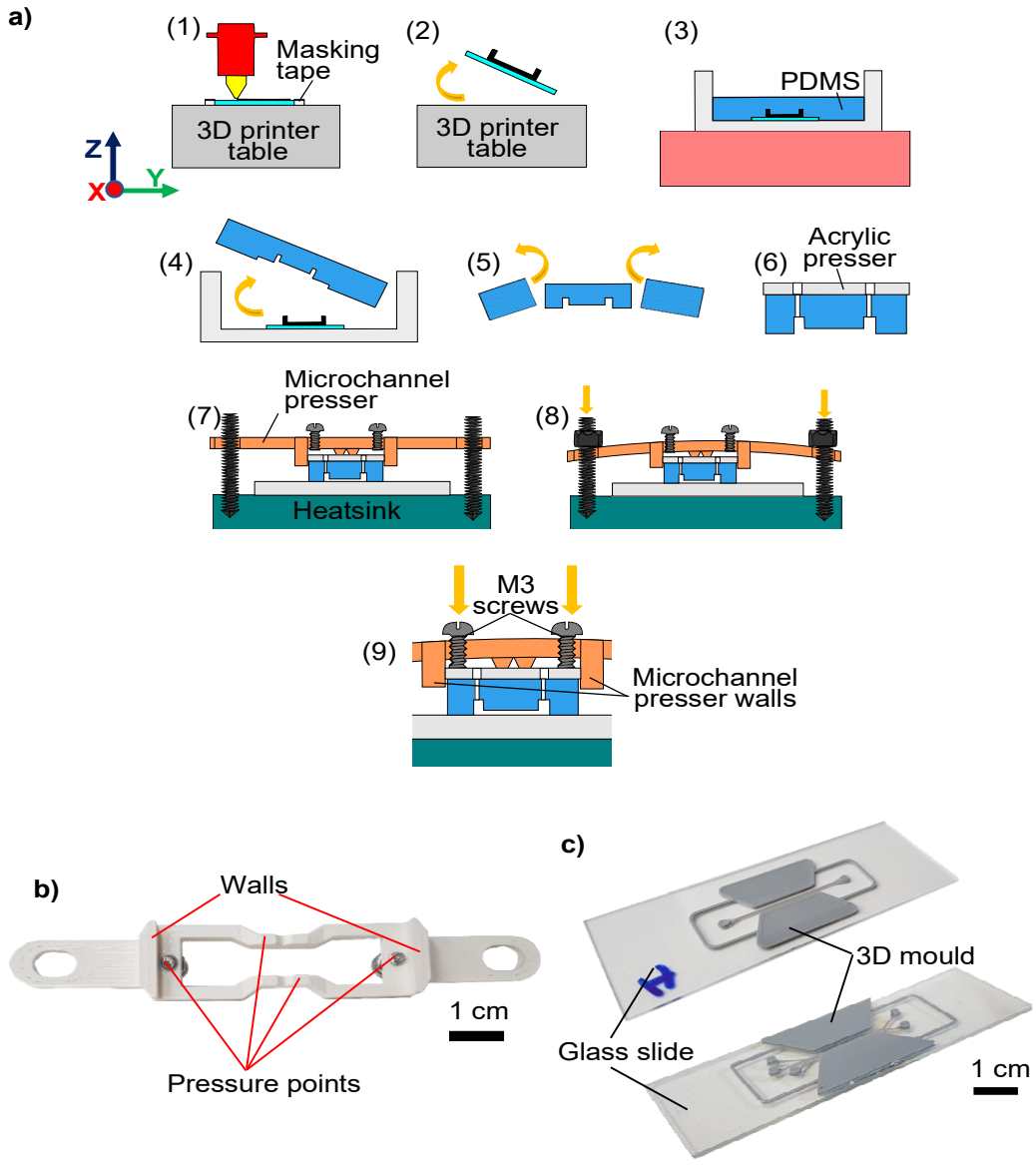

Figure 3.10. a) The development steps of a PDMS microchannel using the glass-bottom 3D printed mold method. (1) A glass slide is selected, placed in the centre of the printing bed and held down using a masking tape. A Z offset is applied to the 3D printer, to compensate for the glass slide height, and the microchannel mold is printed on the glass slide. (2) After printing is complete, the glass slide mold is left to cool. After cooling it is removed and checked that 3D printed microchannel is well adhered to the glass side. (3) The glass slide mold is then placed in a container, PDMS is poured to it and is left to cure under 45 °C. (4) After curing the PDMS is removed, (5) cut to an appropriate microchannel shape and (5) MCF input holes are punched into the microchannel and an acrylic with pre-drilled holes is aligned and placed on top of it. (7) The microchannel presser is placed on the microchannel and then both components are placed on the piezoelectric substrate. (8) The M5 nuts, at the edges of the presser are tighten and (9) The M3 screws are tighten until contact is felt. b) The microchannel presser with its the pressure points and walls highlighted. c) Real-life models of the glass-bottom 3D printed mold.

The smallest channel width and height that could be produced using this technique was 500 and 100 μm, respectively. To tests the dimensional quality of the 3D printed molds the width and height of these molds was measured by printing five molds. The width was measured using a calibrated microscope (KERN, Germany), while the height was measured by removing the PLA layer and measuring it using a micrometre (Mitutoyo, Japan). The 500 mold was printed with a single input and output port, but also an 800 μm wide mock mold was printed with 3 inputs and 2 outputs.

3.3.6. Coating and sample preparation

The microchannels were all coated with 1% (w/w) bovine serum albumin solution for 10 min and then flushed with DI water at a flowrate of 20 μL/min using a syringe pump. For the microsphere test, 10 μm polystyrene microspheres (Sigma Aldrich) were used and suspended in a 23% (v/v) glycerol and phosphate-buffered saline solution. The microsphere suspension was injected into the microchannels using a 2.5 mL syringe (Hamilton Syringes) and the particles alignment was collect using a microscope with 4x magnification.

3.3.7. Acoustic energy density

To characterise the performance of the VAD, via the particle actuation inside the channel, the acoustic energy density was chosen as the method of measurement. The acoustic energy density was calculated via a MATLAB from Barnkob *et al.*(2012), which was adapted by the department's software engineer for this purpose. To calculate the acoustic energy density videos were recorded of the particles in the microchannel prior and after their alignment using a microscope with 4x magnification and a 60 fps camera. Then image frames were extracted from captured videos and were analysed, via the MATLAB code, which took each frame and obtained its pixel intensity near the pressure node (PN) line. The last frame of each frame was used as the maximum intensity frame. The normalised intensity and the relative intensity of each frame were calculated and fit into an expression using a fitting parameter, which was done automatically by the MATLAB code.

3.4. High frequency FPCB IDTs (hFPCB IDTs)

This section describes all the methodologies used in chapter 6 for developing the hFPCB IDTs. In this section the fabrication of the hFPCB IDTs based SAW device is described, which incorporates active flow and a cooling system. The development of both the cooling system and flow system setups are described in this section. Finally, in this section the methodology used to study the particles actuation inside the microchannel and characterise their actuation efficiency is also discussed.

3.4.1. hFPCB IDTs development

The developed hFPCB IDT chip is shown in Fig. 3.11a, with a 4x zoom inset of the IDEs. The hFPCB IDTs had the following dimensions: IDEs length of 8.5 mm, bus-IDE gap of 0.5 mm and each hFPCB IDTs chip had a coaxial cable soldered to it. They were fabricated using a standard PCB manufacturing process by patterning two metal layers, nickel (2 µm thick) and gold (30 nm thick), onto a polyester film (70 µm thick) to form flexible IDEs (circuitfly.com). Additionally, MNs were also designed for the FPCB IDTs chips using a SMD inductor and capacitor of 330 nH and 110 pF, respectively. The resulting S_{11} readings are shown in Fig. 3.11b, when the hFPCB IDTs chips are assembled. It should be noted that the MN design procedure has not been discussed in detail, since it is not the centre of focus of this thesis. But for completion a detailed report on how to design a MN for a PCB IDT device is given in Appendix 4, using the hFPCB IDTs as the example.

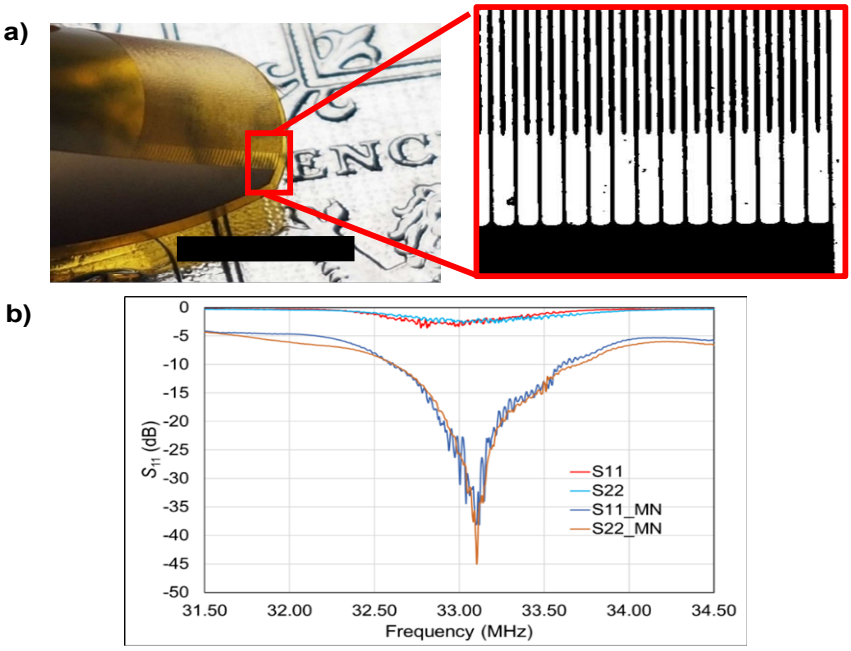

Figure 3.11. a) hFPCB IDT chip with an inset zoom of the IDEs. b) S_{11} reading of hFPCB IDTs chips with and without MNs. Scale bar is 5 mm.

3.4.2. hFPCB-SAW assembly

The clamping mechanism is very similar to the one in section 3.3.3, but for this device the components have been scaled down to accept a 2-inch $LiNbO_3$ substrate. Fig. 3.12a demonstrates the clamping mechanism of for hFPCB IDTs chips and the setup consists of a 2-inch $LiNbO_3$, a 1.5 mm thick aluminium plate, bridge style clamps with localised pressers, bus pad holders, bus pad washers, M5 screws, M5 nuts and M5 threaded rods. All the red coloured components from Fig. 3.12a were 3D printed using the setting stated in section 3.2.3. Pre-assembly all the components are thoroughly cleaned, as stated in section 3.3.3. The assembly process is almost identical to the one in section 3.3.3, which

included the clamps matching the circumference of the $LiNbO_3$, as shown in Fig. 3.12b. There are a few exceptions such as the FSRs not being used as well as a few additional steps. One of the additional steps is the adding of thermal grease underneath the $LiNbO_3$ before it being placed on the aluminium plate. Another is the bus pad holders and washers, which were created to hold the bus pads and the soldered wire on each hFPCB IDTs chip in a set location. The bus pads holders are designed to latch onto the chips' wires. The assembly procedure is already described in section 3.3.3, as such here only the additional steps after assembling the clamps with the $LiNbO_3$ on the aluminium plate will be discussed. When the first chip is to be inserted, the bus pad holder is first slotted onto the M5x10 rods, the chips' pads are then placed on top, the bus pad washer is then placed on top the IDTs bus pads and a M5 nut is threaded on to stop the washer, hFPCB IDT and holder from lifting off. The chip's IDEs are then aligned with the edge of the localised presser and slightly pressed down by screwing the M5 screw on top of the localised presser. The FPCB IDEs chip's S_{11} drop is checked using a VNA and the pressure is adjusted until the optimal drop is achieved. Then the M5 nut of the bus pad is tighten down. The same procedure is repeated for the second chip, but additionally the S_{21} reading is used to finely adjust its position, by rotating it, until the optimal S_{21} reading (highest peak) is achieved and then it is clamped down.

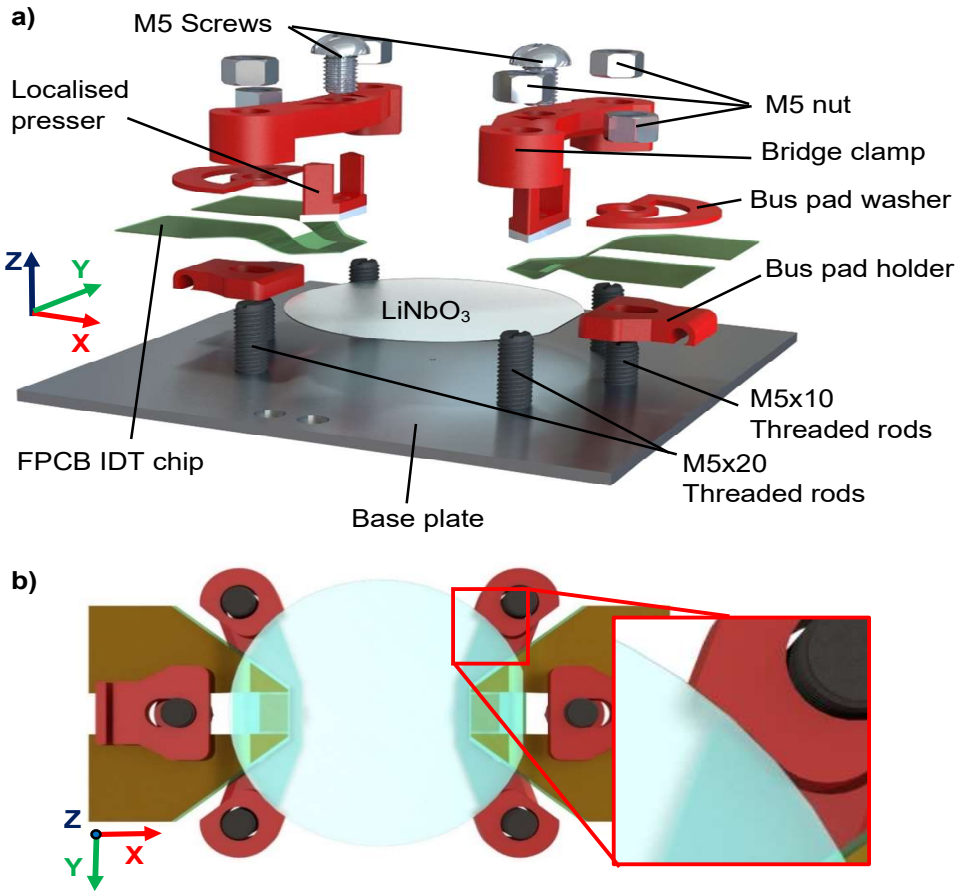

Figure 3.12. a) Exploded view of the hFPCB-SAW device. B) Bottom view of the hFPCB-SAW device demonstrating the matching surface of the bridge clamp's feet and 2-inch $LiNbO_3$, with an inset zoom showing the matching interference between the two components.

3.4.3. Microchannel development and assembly

The microchannel used in this study has 3 inputs 2 outputs, as shown in Fig. 3.13a. The microchannel has a main channel width of 800 µm, while the ports 1,2,3,4 and 5 have a width of 100, 300, 400, 400 and 400 µm, respectively. The main channel's length is ~17.8 mm and the external wall thickness is 1 mm at both sides. The overall external dimensions of the microchannel are approximately 39x15 mm and the silicon mold used has a feature height of 60 µm. This mold was designed using 2D CAD (Autodesk, USA) and was sent out to be manufactured externally. During the manufacturing of the PDMS microchannel custom mold features were also added into the PDMS to add some additional features to the microchannel design, shown in Fig. 3.13b. These mold features are the chamber inserts, with a 1 mm diameter and height, and the 3D printed roof inserts, with 2 mm in height. The chamber inserts where placed centrally on top of the silicon mold's microchannel ports, while the 3D printer roofs were placed 1 mm away from the external wall of the microchannel. These features where placed onto the silicon mold after the PDMS was poured into the mold before curing. The chamber inserts were

added to remove the use of the 1.25 mm PDMS puncher (see section 3.2.8), which was used to create an entry chamber by cutting halfway through the PDMS and then extracting this half-cut piece using tweezers. That extraction method could create small raptures on the surrounding PDMS, which potentially would result with the trapping of particles (i.e. sample loss) as well as potential damage in the microchannel on the input/ output region. With the inserts this issue is eliminated, and a smooth chamber surface is also achieved internally. The roof inserts are added to raise up the roof of PDMS and as such reduce the chance of the roof touching the substrate during the mechanical clamping of the microchannel. For the microfluidic inserts, 0.5 mm through holes are punched at the inputs and outputs, vertically for former and horizontally for the latter as shown in Fig. 3.13c. This punching procedure is implemented to allow easier fluid flow towards the output by implementing a potential passive flow design. Similarly, to the vertical punching, during the horizontal punching the puncher is pushed straight through with no rotation to avoid any potential rapturing of the PDMS.

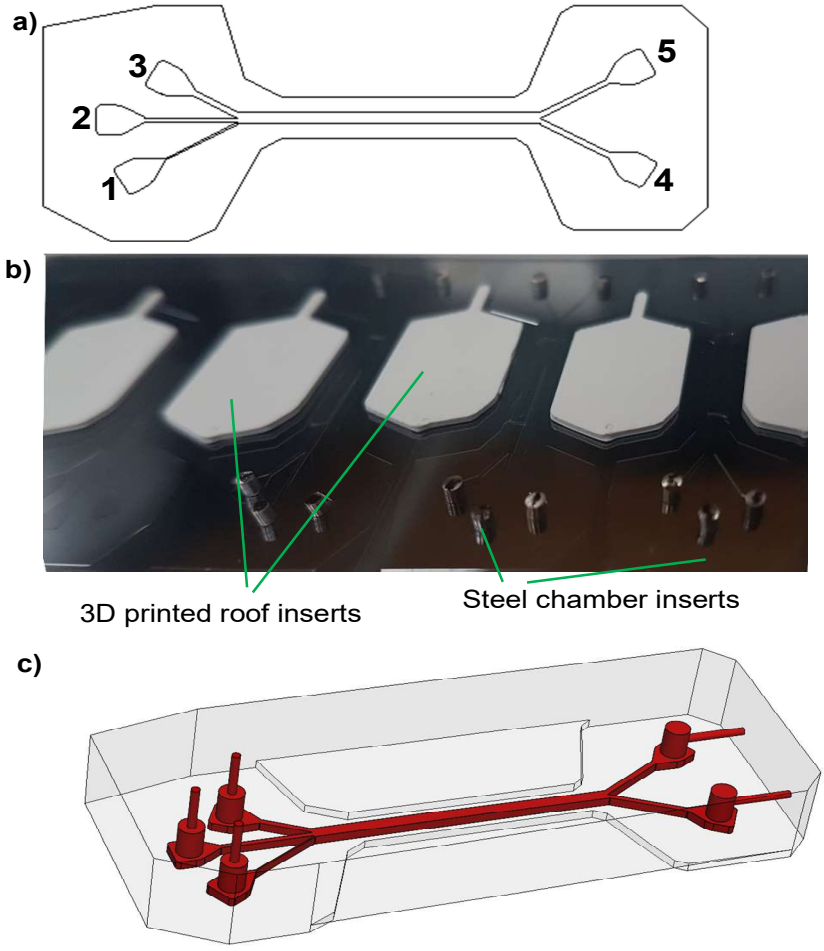

Figure 3.13. a) 2D drawing of the 3 input 2 output of the microchannel. b) 3D printed roof and chamber inserts on the silicon mold of the microchannel. c) PDMS channel geometry with holes punched for the MCF connectors.

To assemble and bond the microchannel, initially a 3 mm acrylic is cut with a width and length of 18 and 48 mm, respectively. Then three 2 mm holes are drilled into the acrylic to allow access to the input holes. The acrylic is then cleaned, aligned with the microchannel and the microchannel is pressed onto the acrylic. As with the $LiNbO_3$, the PDMS naturally adheres to the acrylic and remains weakly bonded with it. The microchannel presser is then placed on top of the acrylic and two M5x20 mm threaded rods are threaded into the based plate, as shown in Fig. 3.14a. The microchannel presser holes have been drilled perpendicular to ensure that the presser will be perpendicular to the clamping bridges. But since the presser is designed with a 5º inclination, when the presser and microchannel are placed into these holes it will result with 5º microchannel inclination, shown in Fig. 3.14b. The M5 nuts are then applied and synchronously tightened to ensure that the presser doesn't tilt and the pressure is evenly distributed. The pressure is applied until it is noticed that the roofs near the PDMS wall start to touch the $LiNbO_3$, made noticeable by the change of colour in that region under a 4x microscope magnification. The pressure is then released until the roofs no longer touch the substrate. Additionally, depending on which pair of holes is used on the aluminium plate, the microchannel could be aligned both at a 5º and 15º inclination, as shown in Fig. 3.14c.

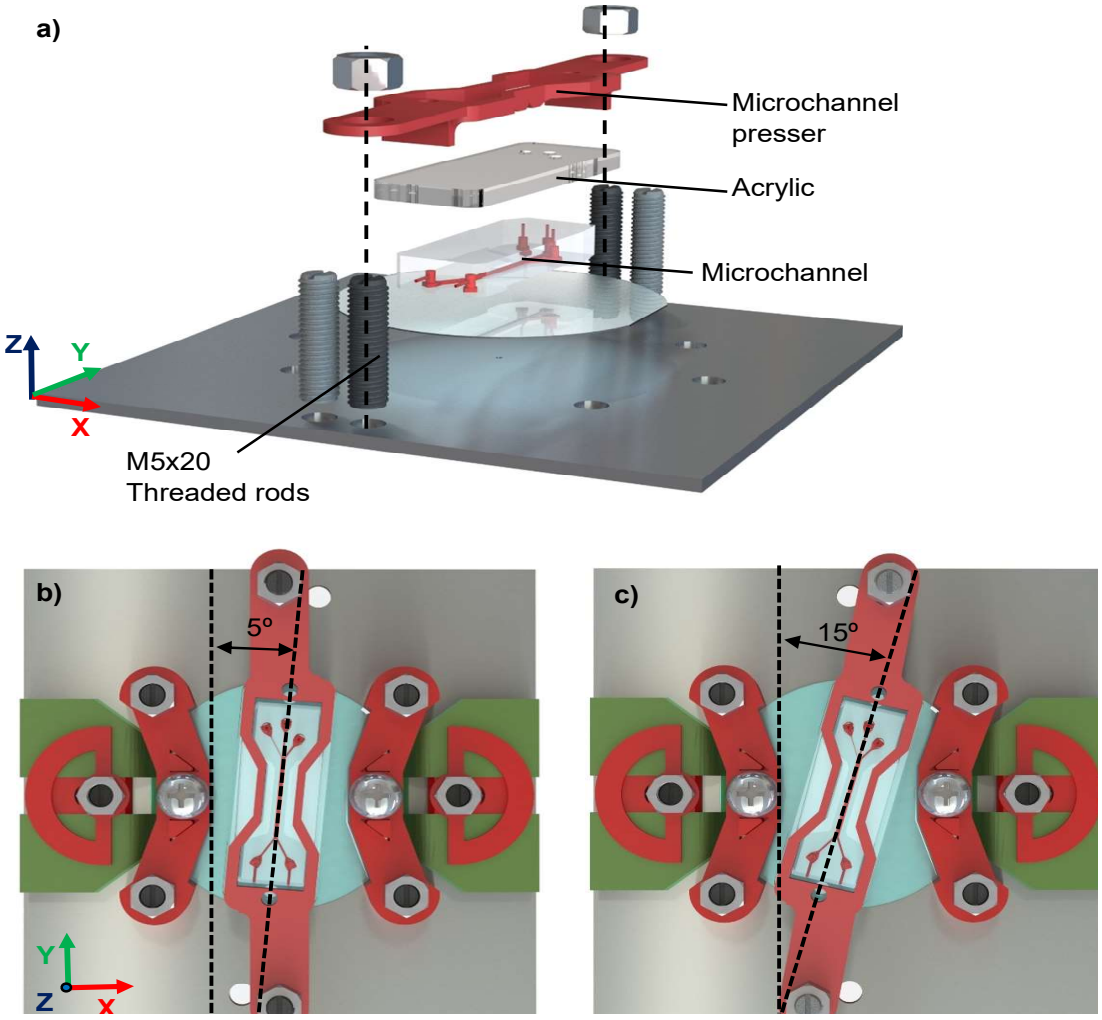

Figure 3.14. a) Assembly of the microchannel on the base plate and $LiNbO_3$ substrate. Top view of the hFPCB-SAW device assembly with the microchannel oriented at a b) 5º and c) 15º inclination.

3.4.4. Cooling system

During the generation of R-SAW, heating effects appear when a R-SAW wave diffracts into a viscous material (Han et al., 2021). To illustrate this the hFPCB-SAW device was assembled with a custom PDMS test “bone”, a thermometer (1314, RS Pro) with a K-type sensor and a heating camera (FLIR ETS320), shown in Fig. 3.15a. The PDMS “bone” has two circles at its ends with a 3.5 mm diameter connected via rectangle line with a width, height and length of 2, 1 and 9 mm, respectively. The rectangle width was selected to mimic the width of the microchannel. The heat camera was mainly used to observe the heating up effects around the PDMS, while K-Type sensor was used to measure the temperature rise at the region of interest (ROI). It should be noted that when no PDMS was placed between the IDTs, no temperature rise or change was observed. But if the PDMS “bone” was placed between the IDTs and the IDTs were turned on, a significant increase in temperature can be easily observed in the R-SSAW region, Fig.

3.15b. From the heat camera images it can be seen that only the PMDS “bone”, i.e. the viscous/ elastic material, heats up and only in the SSAW region, while the substrate temperature on the path of SSAW remains unchanged.

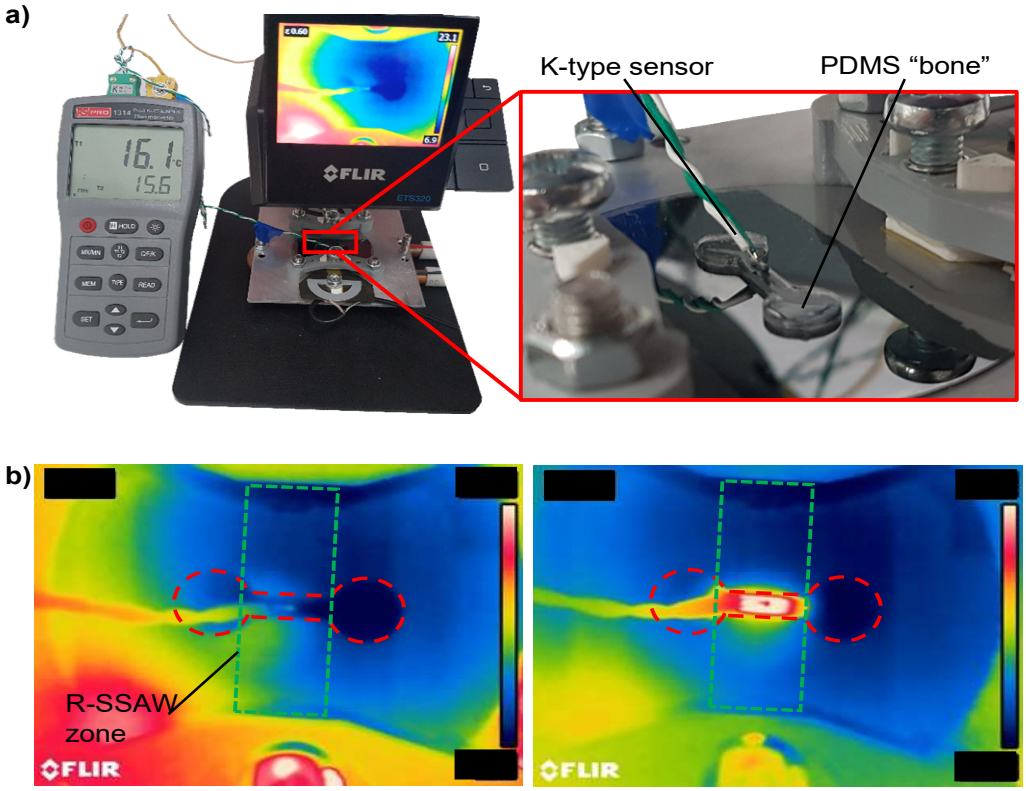

Figure 3.15. a) hFPCB-SAW device heat measurement setup with an inset demonstrating the PDMS “bone” used for the measurement. b) FLIR heat camera images of when the IDTs are off (left) and when they are on (right).

To mitigate these heating effects a cooling system has been built for the hFPCB-SAW device. The cooling system consists of 6 main components: a SAW cooling system, a water-cooling system, a pump, a water tank with a 3-way valve and a thermometer. The system setup is illustrated in Fig. 3.16a, where T, T_w, V, S-CS, W-CS and P represent the temperature sensor, the water tank, the valve, the SAW cooling system, the water-cooling system and the pump, respectively. The left side of the figure represents the system at rest, i.e. when the valve is “closed”, and in this configuration there is no water inside the pipelines and they are filled with air. While the right side represents the system when it is operational, where the valve switches from the top pipeline to the bottom pipeline of the tank, which then makes water to flow through the system and back to the tank. All the physical components, except the SAW cooling system (S-CS), are shown in Fig. 3.16b. The pump used is a gear pump (M42x30/I, KAG) which was power by 12V 2A power supply. The water tank was made in house using a 500 mL polythene wide neck bottle, which had holes drilled into it and plastic MCF connectors glued to it using

epoxy. The valve used is a 3-way plastic valve and C-Flex tubing (6424-12, Cole Palmer) was used to connect all the components. The water-cooling system is a pre-build commercial system that incorporated a cold liquid plate with two Peltiers and two fans.

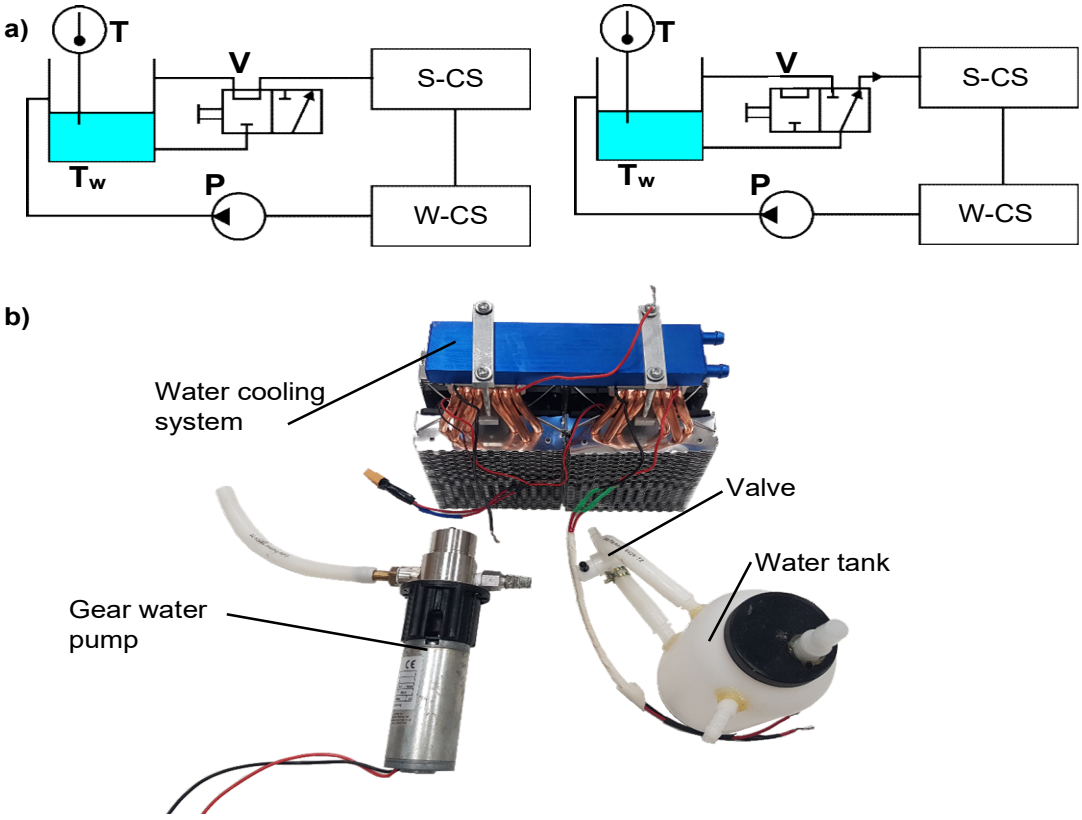

Figure 3.16. Cooling system setup with left side illustrating when the system is off and right side when the system is on. The system consists by the temperature sensor, the water tank, the valve, the SAW cooling system, the water-cooling system and the gear pump represented by the symbols T, T_w, V, S-CS, W-CS and P, respectively. b) Physical components of the cooling system are shown, which includes the W-CS, gear pump and water tank with a valve.

Unlike the above components the S-CS was integrated with the hFPCB-SAW device. It consists of a liquid cold plate and a Peltier (TEC1-12706). The liquid cold plate has a width, length and height of 47x47x14.5 mm, respectively, with a 40x40 mm slot milled in centre that is 3.7 mm deep to accept the Peltier. By implementing this design, the M5x20 treaded rods, used for the bridge clamps, are now being held by the cold plate and as such the base plate and bridge clamps slide on top of them. The exploded view of the components is shown in Fig. 3.17a, while the real-life fully assembled hFPCB-SAW device is shown in Fig. 3.17b.

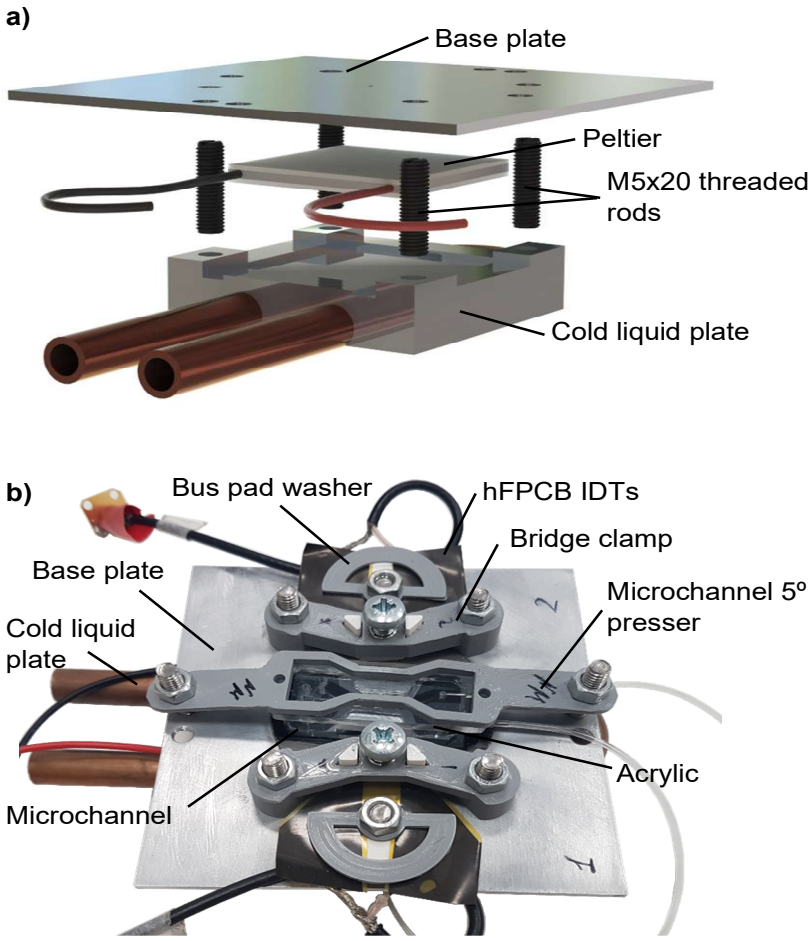

Figure 3.17. a) SAW cooling system (S-CS) components and assembly. b) Real-life model of the hFPCB-SAW device assembly on top of the S-CS.

The cooling system had multiple components that can be run at various settings. To make the system easier to operate it was decided that the water temperature would act as the main control setting of the cooling system. As such, the Peltiers were set at a constant voltage of 12 V, with the S-CS always on, while the W-CS would turn on and off depending on the water temperature. This setup proved to be the most easy and convenient to use and it created a relatively stable temperature.

Using the following setup, the cooling system was activated and was set to run under the water temperature of 15.9 ºC. To measure the heating effects the setup shown in Fig. 3.15 was used, where the IDEs were activated at different power inputs for 30s and after this period the temperature reading from the K-type thermometer on the PDMS “bone” was taken. After each measurement the PDMS “bone” was left to cool down to the temperature of the cold liquid plate, which was approximately 16 ºC, before increasing the input energy and repeating the same procedure for the next measurement. Three measurements were taken for each input power and the results are

shown in Fig. 3.18a. It can be seen that the heating up effect appears to scale linearly with the input power, and to confirm this a linear trendline is plotted which demonstrated a R^2 close to 1. It can be observed that even with the cooling system the heating effects were quite significant, reaching up to 100 ºC at 14 W of total input power (7 W per IDT). To investigate if this heat can be mitigated, the water temperature was set at three different levels, 15.9, 14.1 and 12.5 ºC. The results are plotted in Fig. 3.18b where it can be observed that when the temperature was reduced to 14.1 ºC (just by a couple degrees), it had little effect in mitigating the heating. But at 12.5 ºC a drastic decrease is observed, which also changed the slope of curve. Unfortunately, this result is due to condensation being built up on the surface of the $LiNbO_3$, shown in Fig. 3.18c, which created more viscous substance for the SAW to diffract into. The creation of condensation is in fact a detriment since it will both reduce the amplitude of the SAW and could also possibly short circuit the IDTs.

From these tests it is clear that it would be near impossible to eliminate the heating effects. If the device were to be actuated at around 4.5 W per IDT, at a water temperature of 15.9 ºC, it would result in a temperature of ~90 ºC. If the temperature was desired to be at 80 ºC it would mean that the initial water temperature would have to be reduced to ~5.9 ºC, which would create condensation on the device. Thus, a realistic cooling value is selected, which will allow the device to remain operational without creating a runoff heating effect and would also avoid the potential issue of condensation. As such the temperature of 15.9 ºC, for the water, was selected at a room temperature of ~24 ºC, since it is a value that would keep the device operational at high power but is also warm enough to avoid any condensation. Before proceeding it should be noted that even though Fig. 3.18a and 3.18b at 15.9 ºC have a similar starting water temperature, they have different trendlines in each graph. This could have been caused due to different environmental temperatures during the day of the experiment. This is why the measurements presented in Fig. 3.18b were all performed on the same day within a close time frame, to portrait the relationship between the heating up effects and the cooling temperature reliably.

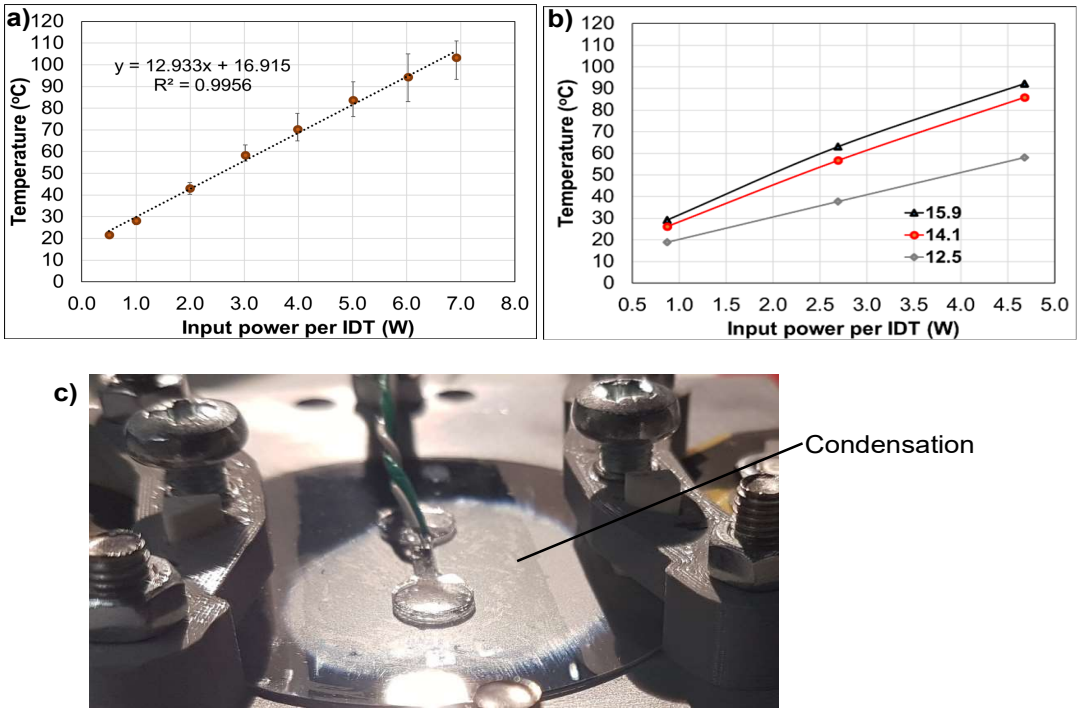

Figure 3.18. a) Thermometer temperature measurements at different power inputs per IDT at a water temperature of 15.9 ºC (n =3). Temperature measurement at a different input powers per IDT at a water temperature of 15.9, 14.1 and 12.5 ºC, with c) illustrating the condensation build on the substrate when the water temperature was set at 12.5 ºC.

3.4.5. Pumping system

It already has been established that the microchannel has 3 inputs and 2 outputs. This configuration will result with an internal flow as shown in Fig. 3.19, where the sample will enter from the input (input 2) and will have two tangent sheath flows (input 1 and 3). The larger sheath (sheath 2, input 3) will go directly to collection output (outlet 4), while the smaller sheath (sheath 1, input 1) will remain tangent with the input 2 and both will travel towards the waste output (output 5). The aim of the smaller sheath is to stop the particles from the dispersing and sticking to the channel wall as well as to force them to be placed somewhat in centre and near the flow of input 3. This positioning would allow for particles to easier migrate from the waste output to the collection output, by reducing the travel distance. The smaller sheath should preferably be as small as possible, and in the microchannel used for the experiments, sheath 1 was designed to be 1/4 of the output 5.

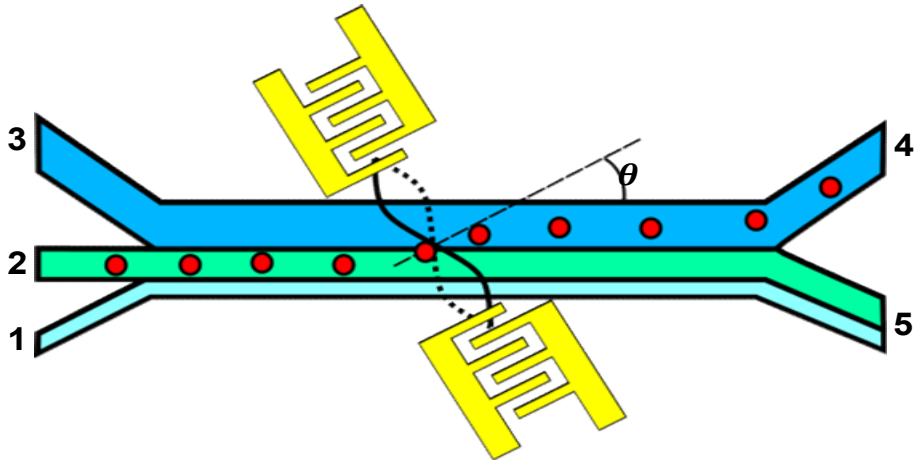

Figure 3.19. Microchannel flow setup and particle actuation using taSSAW.

The easiest way to establish a stable flow rate in this configuration is to have the flow rates of output 4 and 5 being equal. As such input's 3 flow rate should be equal to the output 4 and in turn the sum of the flow rates at the input 1 and 2 should be equal to the flow rate in input 3. To establish stable and reliable flow rates that would allow to investigate the transition and the flow of particles inside the microchannel, a pressure pump (Model 3-4, JUN-AIR) with a control unit (OB1 Mk3, ELVEFLOW) is utilised. The pumping setup is demonstrated in Fig. 3.20a, which consists of a pump (P), a control unit, pressurised fluid chambers, flow sensors (FS) (FS3D, ELVEFLOW), a microchannel and output chambers. The system operates as such: the pump builds up the necessary air pressure and supplies it to the control unit. The control unit then redistributes the air pressure to the closed fluid chamber, 15 mL Falcon Tubes, and builds up the pressure within them (pressurised chambers). This pressure can then be adjusted to initiate the fluid flow into the MCF tubing. Without the flow sensors the flow rate would be unknown and only the pressure supplied to the pressurised chambers would be known. But with the flow sensors the fluid flow can be both measured and controlled via the sensors to create a stable flow. Finally, the fluid travels into the channel and then out to its respective output tanks. The flow rates used in the tests were 1.4, 0.7 and 0.7 µL/min for inputs 3, 2 and 1, respectively. These flow rates were the default rate used for most tests, unless otherwise is stated. The 0.7 µL/min flowrate was chosen because it was the smallest flow rate that the system could reliably achieve.

One of the crucial aspects this system is the vertical positioning of each component to ensure that the potential flow is either targeted towards the output chambers or is at an equilibrium. A setup that complies with this shown in Fig. 3.20b, where the control unit is positioned the highest and the output chambers are positioned as low as possible. This positioning achieves an approximate equilibrium position, where if the pressure is at 0

bar it results in a flow that will either be towards the output or no flow at all, thus eliminating backflow. Another important aspect that this figure represents, is the submersion of the output tubing at the bottom of the output chambers. If this is not done the fluid flowing through the tubing would generate droplets which would grow and then fall due to gravity. This droplet generation will naturally create pressure oscillations and as such an unstable flow. By submerging the tubing this will result with the steady increase of pressure, due the increase of the fluid volume, which can be compensated by the control unit and flow sensors.

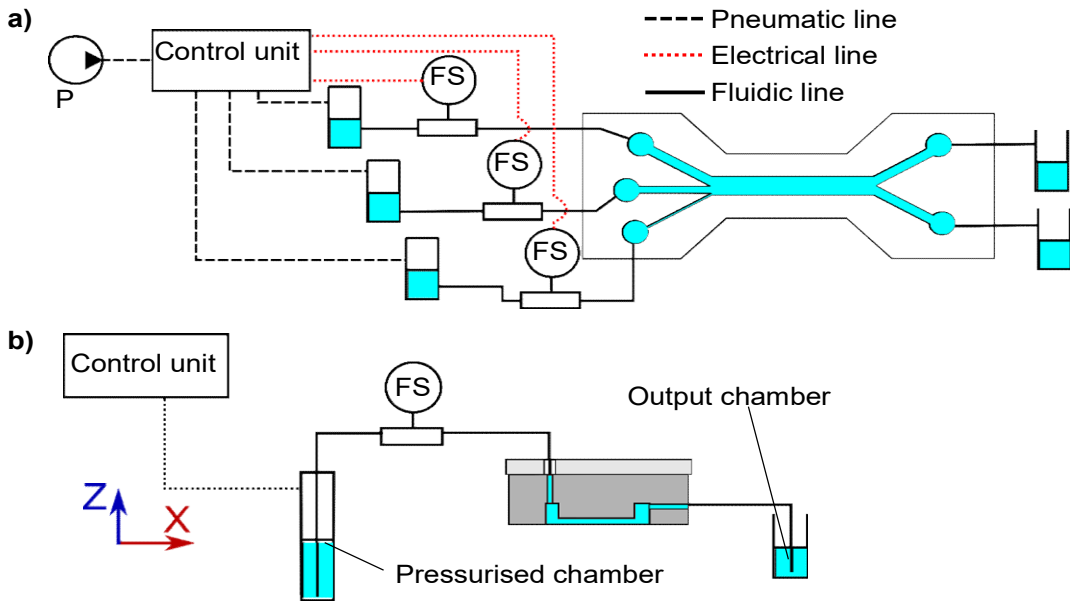

Figure 3.20. a) Fluid pumping system where P and FS represent pump and flow sensors, respectively. b) Vertical positioning of the components to mitigate/ reduce any possibility of backflow due to potential energy.

To create this vertical positioning for the components a custom raising jig was created to accommodate the whole hFPCB-SAW device setup, shown in Fig. 3.21a. This setup is assembled on top of a scissor jack to allow easy portability as well as height adjustment when placed under the microscope. The custom raising jig components are shown in Fig. 3.21b, which consist of an aluminium setup base plate, a 3D printed holder for the pressurised chambers and flow sensors, 3D printed output chamber bases and 3D printed custom microtube holders. In Fig. 3.21b an inset is also presented that demonstrated the components of the custom microtube holders (output chambers) which consists of a 3D printed threaded tube and cylinder holder, to accommodate a standard 1.5 mL microtube, and 3D printed custom microtube cap. These custom-holders were also designed to have the capability to adjust their vertical position through the threading of the one component into the other. This adjustment was needed to compensate for any slight pressure differences at the output lines of the microchannel, which are introduced

due to length differences of the MCF tubing used. Similarly, the cap was made to allow the tubing to be inserted and held in a repeatable and stable position.

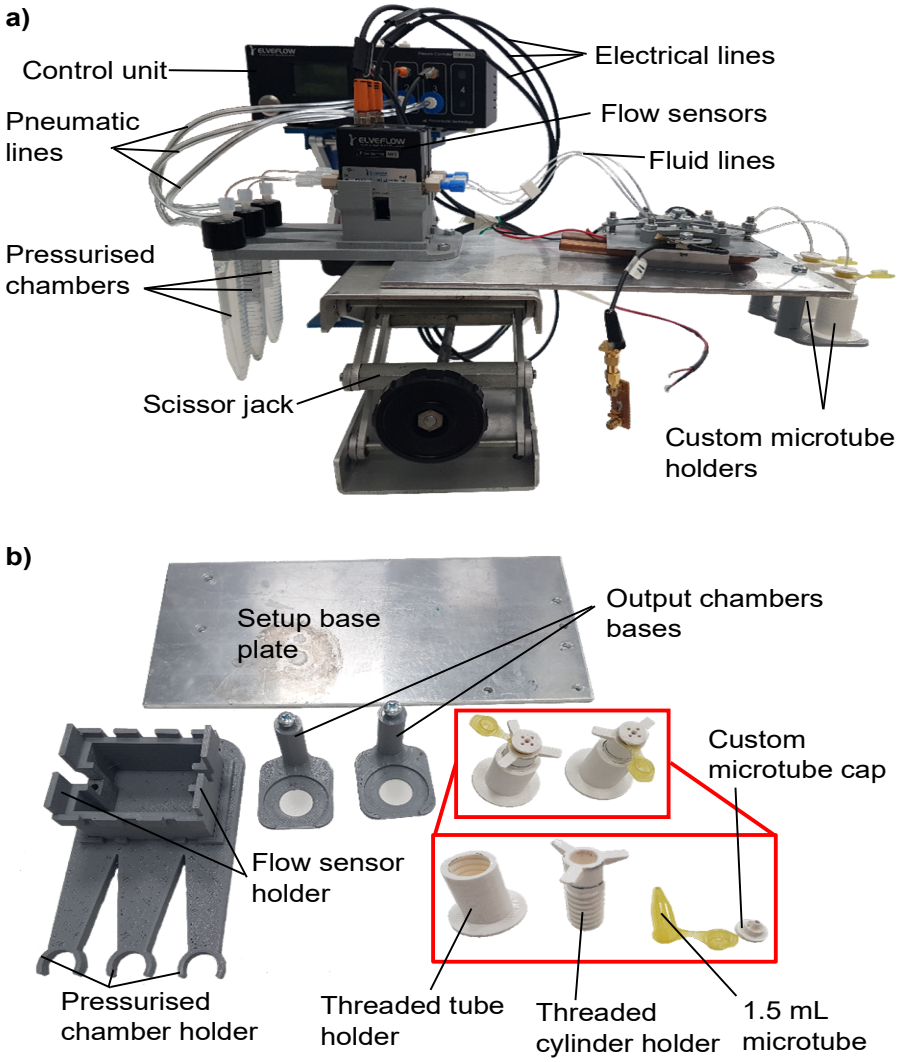

Figure 3.21. a) Custom raising jig with the pumping setup and assembled hPCB-SAW device on top of it. b) Components of the custom raising jig with an inset presenting the components used to create the custom microtube holders (output chambers).

3.4.6. Particle selection and preparation

The particle size was selected to attempt to explore the devices actuation capabilities with particle sizes smaller than 10 µm. The aim was to investigate whether the higher frequency device could successfully overcome the 1 µm diameter actuation limit, at which size particles start to get dominated by acoustic drag force (Nama et al. 2015). As such by using 5 µm particles the actuation capability would be characterised and optimised, demonstrating its capability with particles smaller than 10 µm. Then it would be attempted to be applied to 1 µm, and if successful the particle size would be incrementally reduced down towards sub-micron actuation. For this study 1 and 5 µm

polystyrene particles are used which are diluted in water in a 1:21.6 (v:v) and 1:540 (v:v) volume ratio, respectively. It should also be stated that in the figures in Chapter 6, the input power values refer to power per IDT unless otherwise is stated.

3.4.7. 5 µm particles separation analysis

To study the actuation of particles inside the microchannel, videos were recorded of the particle's actuation at the output region when the SSAW was off and on for 50 s. The electrical setup was identical to the setup in to section 3.2.5, with the difference that a 30 W power amplified was used (LZY-22+, Mini Circuits). The videos were recorded using a microscope (GXM series, GT Vision, UK) with 4x magnifying lens and a 60 fps camera. For the illuminance analysis studies to enhance the signal of the particles and remove the background noise a video editing software was used (DaVinci Resolve, USA) to adjust the recorded videos with the following video parameters; Contrast: 2 (1), Pivot: 1 (0.465), Mid/ Detail: 100 (0), Col Boost: -100 (0) and Hi /Light: 25 (0), with the parenthesis indicating the default value. The resulting video snapshots are shown in Figs. 3.23a and 3.23b, which illustrate how the adjusted videos settings affected the SSAW on snapshots from Figs. 6.2a and 6.2b in Chapter 6, respectively. After this modification the videos can provide a very distinct illuminance profile by using the Tracker software. The process involved the creation of a region of interest (ROI), the purple box, that run across the channel width and the box itself had a width (spread) of 50 a.u. In a perfect scenario the spread of the box would be as large as possible, but because this channel has been used multiple times some particles were trapped on the roof of the channel. These trapped particles are highlighted with yellow circles in the figure. The trapped particles can disrupt the illuminance reading, as such to avoid this an appropriate spread is selected and placed in a location free of trapped particles. The illuminance profiles of the region of interested (ROI) for the 5 and 15º microchannel inclinations are then shown in Fig. 3.23c and 3.23d, respectively. These graphs also include the segregation line to illustrate the clear distinction between the peaks formed in locations that lead towards the collection output and waste output. Additionally, the illuminance profiles of the unedited snapshots are also included to illustrate that the editing does not change the shape or location of the peaks, but only removes noise and enhances the signal from the particles.

These figures also show why the spread of ROI is important, in Fig. 3.23c all the illuminance peaks have a similar amplitude while the ones in Fig. 3.23d are drastically different. This is because the amplitude of the peak depends on how many 5 µm particles are present within the ROI in a specific time frame. As such this figure not only demonstrates the location of the travelling lines/ paths, but also the number of particles that are present within these lines at a given snapshot. Since the illuminance profile shows both the location and the number of particles, and only the particles generate an

illuminance peak, one can use this information to get an estimation of the percentage of particles that will travel to either the waste or collection output, termed here as actuation efficiency. This is achieved by calculating the total illuminance of the graph, then calculating the illuminance at the waste (0 – 401 μm) and collection (402-800 μm) output and diving each with the total illuminance to obtain the percentage of particles being actuated towards the collection output. The following equation can then be used to characterise the device's actuation efficiency percentage inside the channel:

$$eff_{act} = \left(\frac{ROI_c}{(ROI_w + ROI_c)}\right) * 100 \quad (32)$$

Where ROI_c and ROI_w refer to illuminance at the collection region (a.u.) and waste region (a.u.), respectively. This concept is illustrated in Fig. 3.23e and 3.23f where the total, waste and collection region illuminance are calculated from Figs. 3.23c and 3.23d, respectively, with the green column representing the actuation efficiency. This methodology is later used to develop data points that would represent the average particle actuation efficiencies at different input powers, shown in Fig. 6.3. In order to generate these data points ten frames were taken from the collected videos at a hundred frame intervals (100 fps) for each power input. Where the actuation efficiency for each frame was calculated to obtain the average actuation efficiency for each input power.

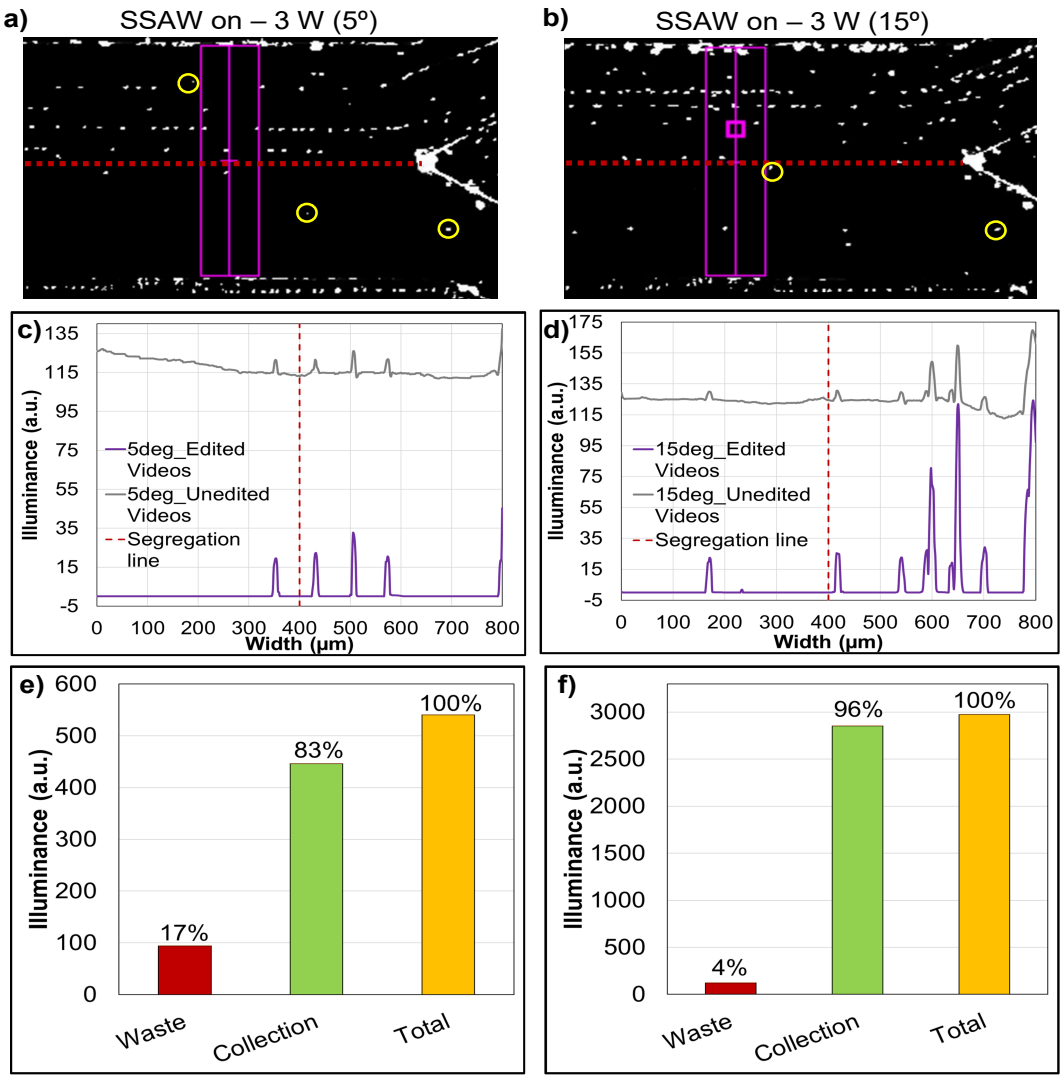

Figure 3.22. Edited video snapshots of the 5 µm particle actuation from Fig. 6.2 at the output region with the SAW on and the microchannel inclined at a) 5º and b) 15º. The red dotted line is a segregation line between the flows towards waste and collection output and the purple box indicates the region of interested (ROI). The ROI illuminance density profile from the snapshots is plotted for the c) 5º and d) 15º inclinations, containing both the pre-editing and edited snapshots illuminance profile. The edited snapshot illuminance profiles are then used to calculate the total illuminance at the ROI for the waste (0-401 µm) and collection (402-800 µm) region for the e) 5º and f) 15º inclination with an estimated actuation efficiency percentage of the particles in the ROI (green column).

3.4.8. 1 µm particle analysis

It should be noted that the analysis technique developed here was not able to be used for the 1 µm particles. This will be demonstrated in Chapter 6 by attempting to generate videos that have eliminated as much noise as possible, which had the following video settings; Contrast: 1.2 (1), Pivot: 1 (0.465), Mid/ Detail: 100 (0), Col Boost: -100 (0) and

Shadow: -100 (0), with the parenthesis indicating the default value. But this modification did little to improve the signal, see chapter 6. This was due to the particles not forming observable lines at the output, the tendency of the particles to spread across the microchannel, at the output region, and the weak signal that these particles were generating. This fault could be address in future iterations where fluorescence particles are used instead, which is discussed in more detail in chapter 6 and demonstrated in Appendix 5.

Chapter 4

PCB-SAW for Acoustofluidic Applications

4.1. Introduction

In this chapter the PCB-SAW device will be introduced. The design procedure of the IDTs, characterisation methodology and experimental setup of the PCB SAW device, have been all already discussed in chapter 3 in section 3.2. As such this chapter will focus on demonstrating that the PCB IDTs can be manufactured in a relative accurate and precise dimensional quality, which can be assembled into a PCB-SAW device that can be used for acoustophoretic applications such as droplet streaming and particle/ cell alignment inside a microchannel. Finally, this chapter will demonstrate that the same setup can also be used to couple the PCB IDTs with different piezoelectric substrates and achieve acoustophoretic effects.

4.2. PCB based SAW device characterisation

In this section the PCB-SAW device is thoroughly characterised to establish the stability of the device. First, the PCB IDE dimensional quality is established and then the PCB-SAW devices electrical characteristics using the *S*-parameters and the effects of implementing a MN. The device's *S*-parameters repeatability is also characterised by assembling and disassembling the device multiple times. Finally, the contact of the IDTs with $LiNbO_3$ is dependent on the pressure that is applied into M5 screw on top of the IDTs. As such this force is characterised by observing the device's *S*-parameters and resulting droplet speed velocity at a set power at different torque setting. The droplet actuation is also repeated on a CR IDT and compared to the PCB-SAW device at various input powers.

4.2.1. PCB IDE dimensional quality

Since this methodology heavily relies on the standards of the PCB industry it is important to evaluate how accurate and reliable the process is. The most important parameter is the pitch of the fingers since it will define the SAW's wavelength. The real-life model of the PCB IDTs can be seen in Fig. 4.1a. The IDEs are shown in Fig. 4.1b, which appear to be uniform and in good condition. The results are shown in Fig. 4.1c, where the IDE width and spacing were found to be 38.7±3.1 μm (average ± SD) and 61.1±3.0 μm (average ± SD), respectively, resulting in an average pitch of 199.6 μm.

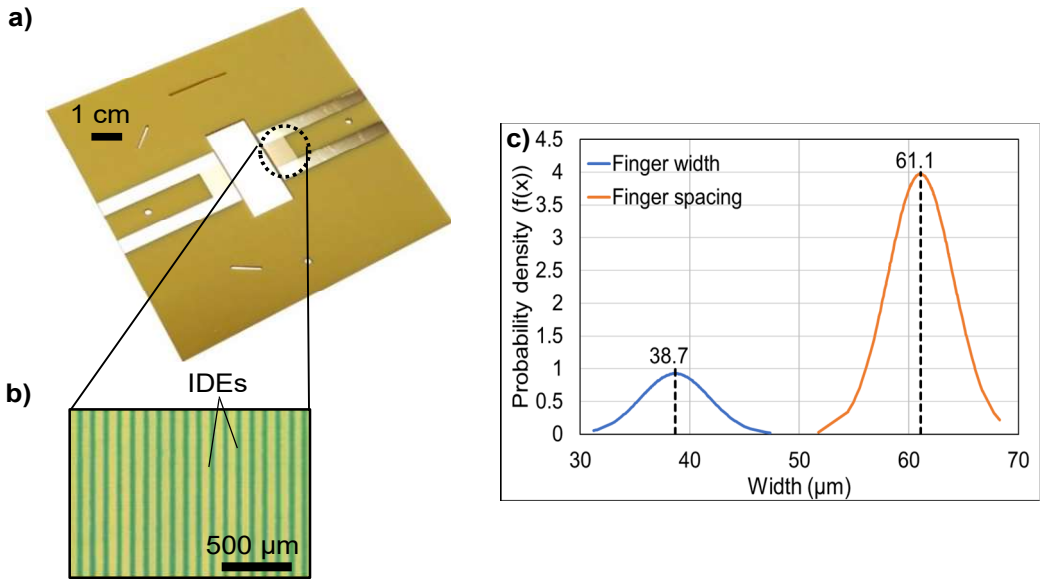

Figure 4.1. a) Real-life model of the PCB IDTs. b) A zoomed inset of the IDEs. c) Dimensional analysis of the IDE width and spacing (n = 161).

4.2.2. PCB-SAW Electrical characterisation

After confirming the dimensional quality of the PCB IDTs, they were used with 128 Y-cut $LiNbO_3$ to be assembled into the PCB-SAW device. Due to the coupling of these two components relying on surface contact of the PCB IDTs and the $LiNbO_3$, it would naturally result with weaker *S*-parameters. Thus, the next step was to characterise the device's electrical *S*-parameters and observe whether the implementation of MNs would offer any improvement by compensating for the imperfect bond (compared to photolithography) between the IDTs and $LiNbO_3$. Fig. 4.2a shows the measured S_{11} and S_{22} of the PCB-SAW device with and without MNs ('_MN' is the parameter with addition of the matching network in all figures). It can be observed that the reflection of device is -2.7 and -1.7 dB without MNs and is reduced to -18.4 dB and to -21.4 dB for S_{11} and S_{22}, respectively. Fig. 4.2b shows the Smith charts of both IDTs with and without MN, which indicates that the impedances of the two IDTs is significantly improved and approached 50 Ω with the MNs. The insertion loss of the PCB-SAW device, i.e. the transmission coefficients S_{12} and S_{21}, were also measured, shown in Fig. 4.2c, which also showed that the MNs improve power transmission from one IDT to the opposite one.

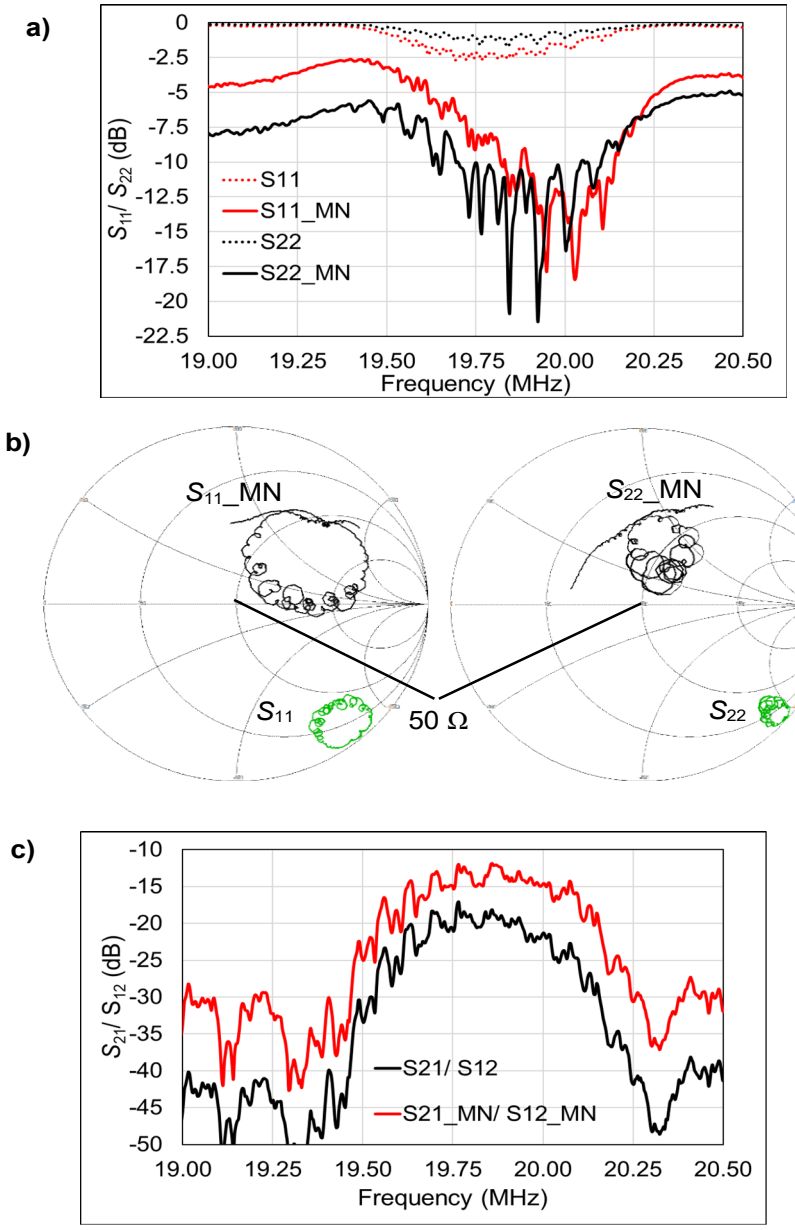

Figure 4.2. VNA readings of PCB-SAW device. a) Coefficient of reflection (S_{11}/S_{22}) with and without MN. b) Smith chart of the coefficient of reflection with and without MN, indicating the impedance approaching 50 Ω when MNs are implemented. c) Coefficient of transmission (S_{12}/S_{21}) with and without MN.

To test the stability and repeatability of the *S*-parameter of PCB-SAW assembly, the device was assembled and disassembled multiple times with and without MNs (n=23). The Rayleigh mode frequency data point for each assembly was selected at the point where the S_{11}/S_{22} was minimum or S_{12}/S_{21} was maximum for the respective measurements. The frequency measurements are shown in Fig. 4.3a, where the frequency readout from S_{11} and S_{22} indicated that the average frequencies shifted from 19.77±0.08 MHz (average ± SD) to 19.82±0.13 MHz and from 19.80±0.10 MHz to

19.89±0.11 MHz with the addition of a MN, respectively. While for S_{12} and S_{21} the average frequency shifted from 19.82±0.06 MHz (average ± SD) to 19.85±0.04 MHz. These frequency changes are most likely due to the additional inductance and capacitance introduced by the MNs. In general, the addition MNs slightly increased the average Rayleigh mode frequency but from the graph it can be observed that it was still well within the 1 MHz bandwidth boundary of the operating frequency. More importantly the average reflection coefficients were consistently reduced from -2.7 dB to -25.2 dB and from -2.4 dB to -27.8 dB for S_{11} and S_{22}, respectively, as shown in Fig. 4.3b. This improvement also appears with the transmission coefficients where they are both increased from -18.1 dB to -12.1 dB, shown in Fig. 4.3c.

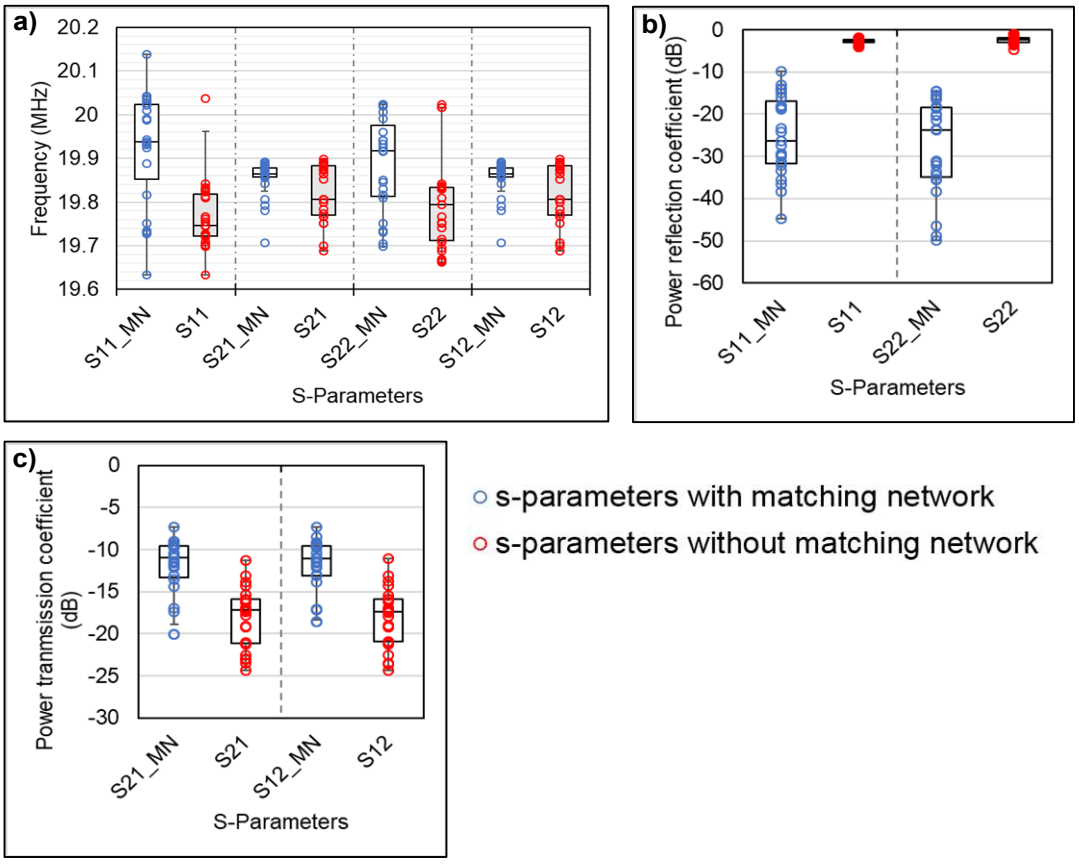

Figure 4.3. Box chart of *S*-parameter characterisation of the PCB-SAW device. (a) The readout of Rayleigh mode frequencies from S_{11}, S_{22}, S_{21} and S_{12} measurements with and without the MNs. (b) The reflection coefficients (S_{11}/S_{22}) of the PCB-SAW device with and without the MNs. (c) The transmission coefficients (S_{12}/S_{21}) of the PCB-SAW device with and without the MNs.

Frome these results it can be observed that the designed frequency (~19.9 MHz) is very close to the natural operating frequency of the device (19.77/ 19.8 MHz) and that the MNs while do offset the frequency still appear to be within the operating frequency bandwidth of the device. As such these initial tests have showed that the PCB-SAW

device has a consistent S_{11} drop with and without MNs, which falls very close to the designed operating frequency. Thus, demonstrating electrically that the coupling mechanism is working, and that the device should be capable of generating R-SAWs.

4.2.3. Characterisation via droplet actuation

During the electrical characterisation phase, at each assembly it was observed that the S_{11} drop would change based on how much torque was applied to the M5 on top of the localised pressers. This effect was investigated via droplet actuation to determine whether it influenced the generated R-SAW, where the amplitude of the generated R-SAW was characterised via the droplet velocity. Fig. 4.4a shows the |S11| and droplet velocity against the clamping force. Despite large variance of R-SAW amplitude indicated by the droplet velocity, the optimal clamping force of 50 N produced the minimum S_{11} of -46 dB and the maximum average droplet velocity of 24.4 mm/s. Further increase in the clamping force to the PCB-SAW device decreased both the |S11| and the SAW amplitude and its variance. The reduction of the droplet velocity at a higher clamping force could be a result of over compressing the piezoelectric material, which restricted its ability to deform and thus resulted in reduced SAW amplitudes and higher power reflection.

Once the optimal state of the PCB-SAW device was achieved, by applying the clamping force of 50 N, the S_{11} spectrum was compared with that of the CR IDT with the same specifications as shown in Fig. 4.4b. It can be observed that the minimum S_{11} for both the devices had a difference of ~0.21 MHz, which could be caused by the errors in the PCB manufacturing and the parasitic capacitance and inductance introduced by the MN circuits. Benchmarking the PCB-SAW device at the optimal state with the CR IDT in terms of actuating droplets under a range of input powers is shown in Fig. 4.4c. The CR IDT showed higher efficiency in converting the input power to SAW when compared with the PCB-SAW device. This is reasonable as the electrodes for the PCB-SAW device were mechanically clamped onto the piezoelectric substrate resulting in an imperfect signal coupling. This issue can be easily compensated by doubling input power to the PCB-SAW device. For example, operating the CR IDT at ~0.6 W drives the droplet velocity of 20 mm/s, which can be achieved by the PCB-SAW device working at ~1.2 W. It should be noted that the use of the MNs also improved the sensitivity of the S_{11} reading, which allowed to easily achieve an optimal clamping assembly by reading the real-time S_{11} spectrum. Thus, in subsequent assemblies the VNA was used to monitor the real-time S_{11} while fastening the screw to achieve the optimal clamping force.

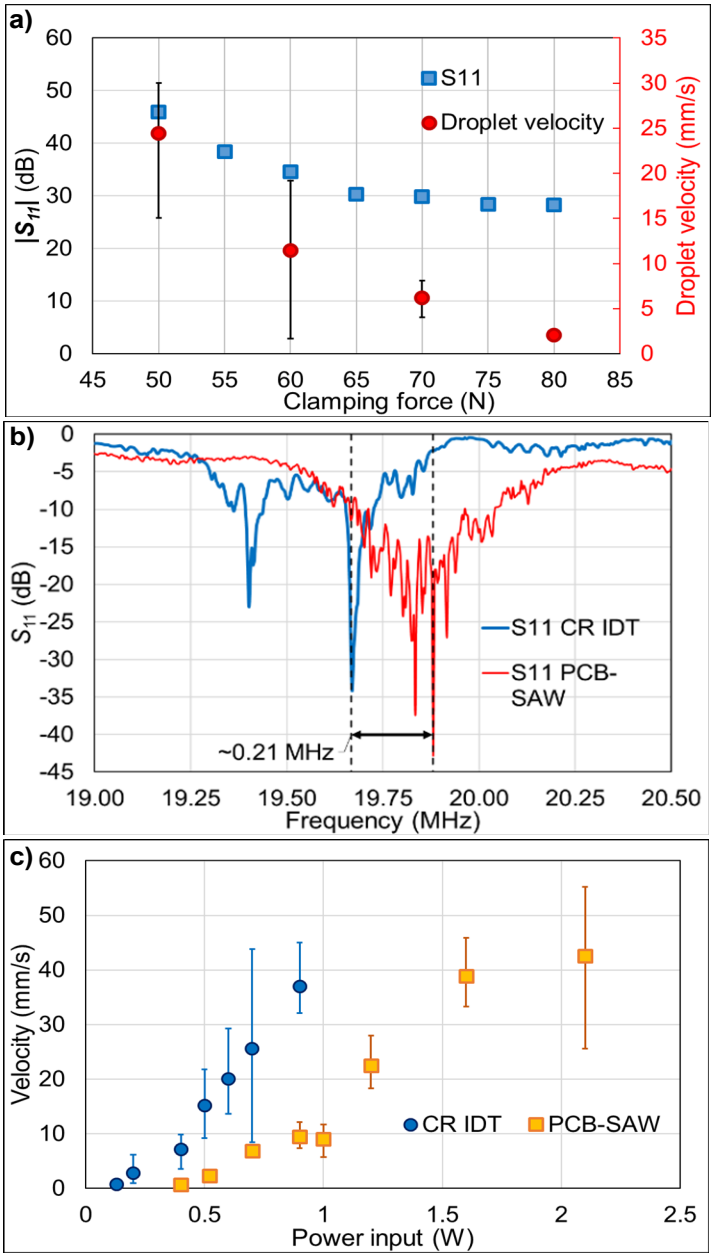

Figure 4.4. Characterisation of the PCB-SAW device and the comparison with the IDT made by photolithography in a cleanroom (CR IDT). a) Relationship between of the S_{11} and the droplet velocity and the clamping force applied to the device. The droplet tests were done by applying an input power of 1.26 W. b) Comparison between the S_{11} of the PCB-SAW device at 50 N and CR IDT, with the latter frequency being 19.67 MHz. c) Comparation between the droplet velocities, driven at different input powers in the PCB-SAW device and CR IDT.

4.3. PCB-SAW particle/cell manipulation

The PCB-SAW device demonstrated to be working very similar to a conventional IDT, in terms of frequency response and electrical properties, alas with less efficiency when compared to a conventional IDT. The PCB-SAW already demonstrated that it is capable

of generating acoustophoresis, at least in regard to droplet actuation. As such in this section the focus will be on its capability to actuate particles/ cells inside a fluidic medium and the effects it generates inside a fluidic medium.

4.3.1. Manipulation of microparticles

To demonstrate the PCB-SAW device's ability to create acoustophoretic effects that affect particles, a droplet sample containing polystyrene microspheres particles was placed at the centre between the two IDTs (Fig. 4.5a). When one of the IDTs was activated, a streaming pattern with two major vortices was observed (Fig. 4.5a), which was in good agreement with the pattern formed on conventional SAW devices (Fu et al., 2017). When both the IDTs were activated, a four-vortex streaming pattern was generated (Fig. 4.5c), which again agreed with that produced on conventional SAW devices. Thus, the above tests have successfully confirmed that the device creates a R-SAW with comparable acoustophoretic effects to a CR IDT inside a fluidic medium. However, to solidify the PCB-SAW capabilities, it is important to also demonstrate the acoustophoretic actuation of particles inside a microchannel. Prior to the microchannel experiments, simulations were created to predict the particle patterning based on established theories for R-SSAW actuation. These results then be used and compared to the experimental results.

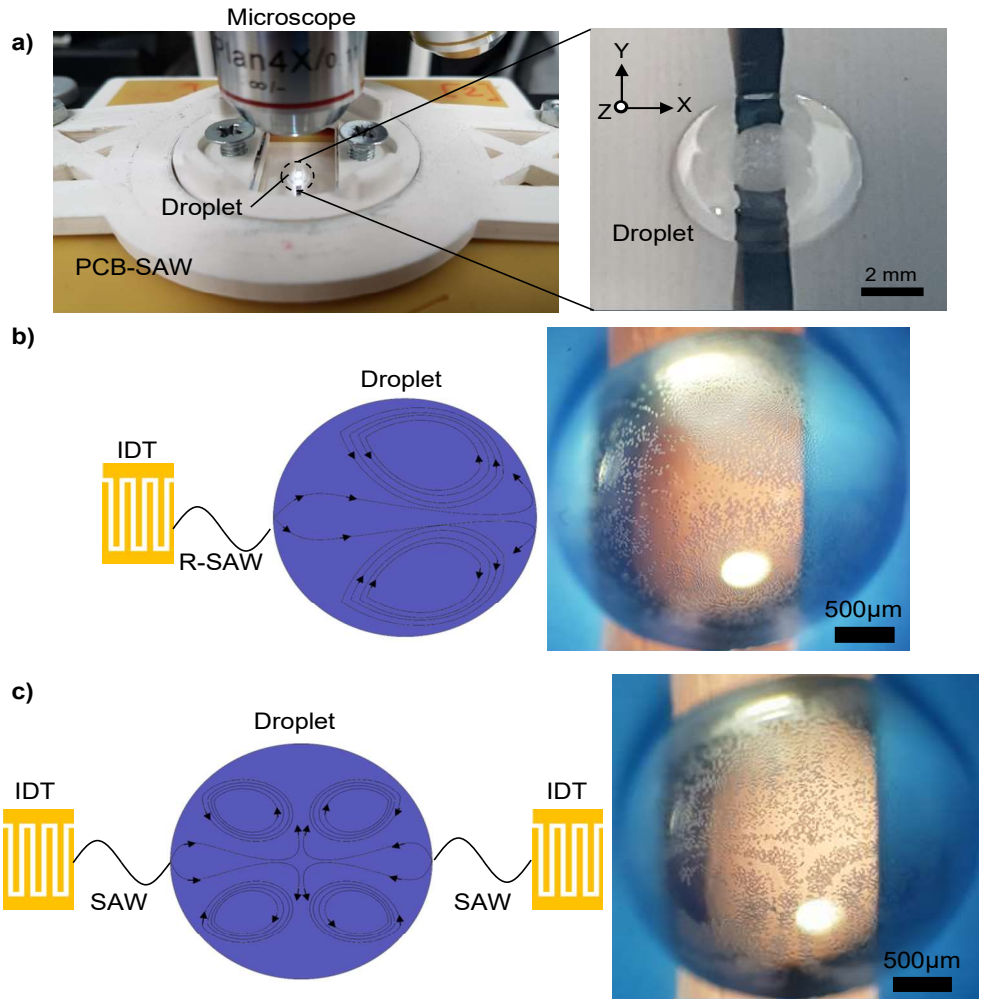

Figure 4.5. Testing of the PCB-SAW device using a droplet sample with particles. a) A droplet sample is placed at the centre of the PCB-SAW device, between the two IDTs, under a microscope. b) A representation of the expected two-vortex streaming pattern and the observed streaming pattern when one IDT is on. c) A representation of the expected four-vortex streaming pattern and the observed streaming pattern when both IDTs are on.

Figs. 4.6a and 4.6b show the distribution of the acoustic pressure when pressure node (PN) and pressure anti-node (AN) formed at the centre of the microchannel, respectively. The movement of the PN and AN is achieved by applying a 90º phase-shift to the SSAW, which in practice will be a 180º phase shift to the left or right for the R-SAW. Particle trajectories corresponding to both conditions are given in Figs. 4.6c and 4.6d, respectively. The first case indicates three particle aggregation traces (red dots in Fig. 4.6c) on the plane, two of which are close to the walls of the microchannel, while the second case indicates the creation of a more complex aggregation pattern.

It is worth discussing that the middle point (yellow dot) in Fig. 4.6d most likely will not appear in practical experiments. This is because that this point is assumed to be on the dead middle of the antinode and that the sum forces in X will be equal. In reality the sum

of forces will not be equal, i.e. ∑F_x≠0, and as such microparticles in the centre will tend to migrate towards the adjacent more stable PN locations (pointed by green and black arrows).

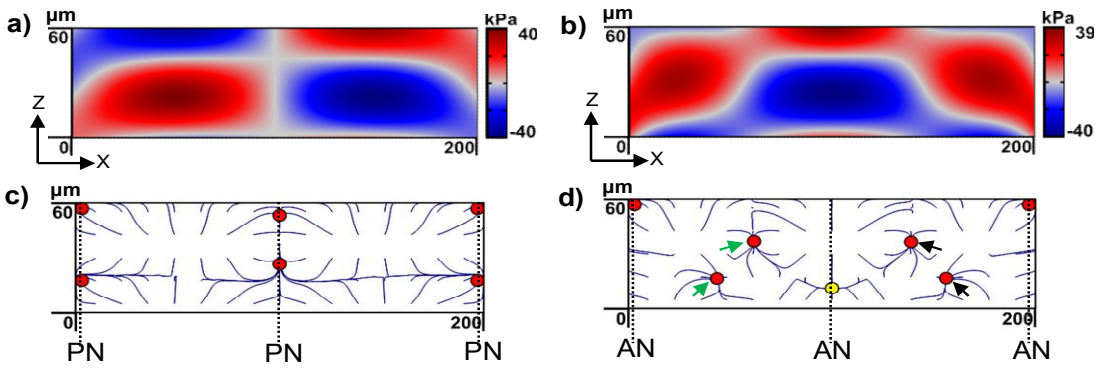

Figure 4.6. COMSOL Multiphysics® simulation of the PCB-SAW device. a) Acoustic pressure when the PN is located at the centre of the microchannel. b) Acoustic pressure when the AN is located at the centre of the microchannel. c) Particle trajectories for when the PN is located at the centre of the microchannel. d) Particle trajectories for when the AN is located at the centre of the microchannel.

The particle tests were conducted by using 10 μm polystyrene microsphere particles, with the particle sample being injected into the microchannel manually using a syringe. After an evenly dispersed pattern was formed within the microchannel (Fig. 4.7a), an RF signals with the same phase (Δφ=0°) were applied to both IDTs to produce SSAWs with the PNs located at the centre and near the two walls, resulting with the trapping the particles and formation of three aggregation traces, shown in Fig. 4.7b. By applying a 180° phase difference (Δφ=180°) to the RF signal driving one of the IDTs, ANs were formed at the centre and near the two walls, resulting in four particle traces, shown in Fig. 4.7c. It should be noted that in Fig. 4.7c the traces appear thicker, which is most likely the result of the 4 aggregation points in Fig. 4.7d (green and black arrows) either merging or being very close to each other. Regardless, these results show a very good agreement with the simulation results and that the PCB-SAW device can align particles identically to a conventional CR IDT device.

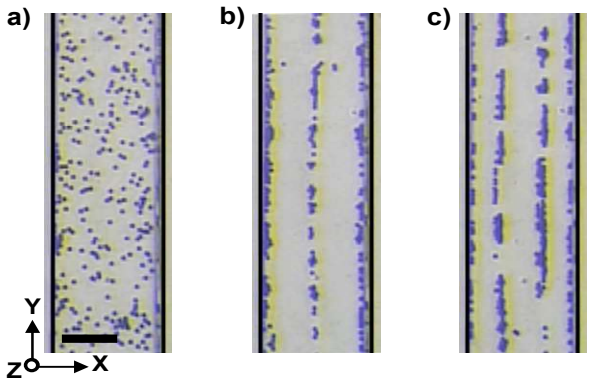

Figure 4.7. Particle patterning/ manipulation using the PCB-SAW device. a) Microscopic image of 10 µm polystyrene microsphere particles evenly distributed inside the microchannel before applying the SSAW. b) Microscopic image of three particle traces inside the microchannel when applying a SSAW with the PNs located at the centre and near two sides of the microchannel. c) Microscopic image of four particle traces inside the microchannel when applying a SSAW with the ANs located at the centre and near the two side walls of the microchannel. The scale bar is 100 µm.

4.3.2. Manipulation of cancer cells

As has been mentioned in the introduction one application that acoustofluidics are commonly applied is cell manipulation/ patterning. Here, NSCLCs are used to demonstrate that the PCB-SAW device can be applied in cell manipulation based applications. The NSCLCs used in this test had a size of 16±7.7 µm (average ± SD). The PCB-SAW device was filled with the NSCLCs sample (Fig. 4.8a) and the same actuation methodology as for the particles was repeated. When applying a RF signals with $\Delta\varphi=0°$ and $\Delta\varphi=180°$, to the two IDTs, it resulted in the formation of three-cell (Fig. 4.8b) and four-cell traces (Fig. 4.8c), respectively. The results demonstrated that the PCB-SAW device can be used as an acoustic tweezer to manipulate, and re-position cells controllably by changing the RF signal phase. Additionally, the ability of the PCB-SAW device in preserving the cell viability was tested using three sample groups, Control, SAW-off and SAW-on. The results are shown in Fig. 4.8d, denoting the viabilities of 98.2±0.8% (average ± SD), 97.6±1.2% and 96.9±0.6% for the Control, SAW-off and SAW-on group, respectively. The analysis of variance showed no significant differences among these three groups ($p = 0.166$).

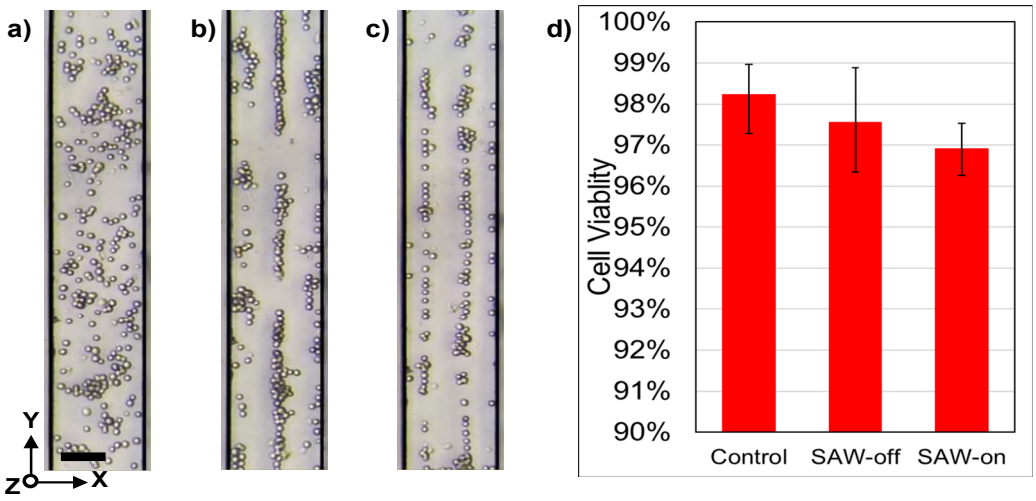

Figure 4.8. PCB-SAW patterning/ manipulation of NSCLCs. a) Microscopic image of NSCLCs evenly distributed inside the microchannel before applying the SSAW. b) Microscopic image of three cell traces inside the microchannel when applying the SSAW with the PNs located at the centre and near the two side walls of the microchannel. c) Microscopic image of four cell traces inside the microchannel when applying a SSAW with the ANs located at the centre and near the two side walls of the microchannel. The scale bar is 100 μm. d) Cell viability test for the Control, SAW-off and SAW-on Groups, no significant viability change was found (n = 3).

It should be noted that the NSCLCs required more power to be actuated into the PNs in comparison to the polystyrene particles despite being larger. The particles were actuated at ~0.5 W per IDT to achieve an almost instantaneous (<1 s) alignment on the PNs, while the NSCLCs needed a power input of ~1 W to achieve this almost instantaneous alignment (<1 s).This could be an effect caused either by the weaker acoustic contrast factor of cells compared to polystyrene particles (see Appendix 2), a result of the different medium that was used for the two actuations, with polystyrene particles using a mixture of glycerol and PBS while the cells being directly actuated in the cell culture medium, or a combination of both. Unfortunately, it is hard to speculate what was the cause here since the author doesn't have the data of the density and the speed of sound of either the culture media or NSCLCs to determine their acoustic contrast factor. Additionally, since the aim of this experiment was to simply provide a proof of concept for the capability of the PCB-SAW device to actuate particles and cells, there was not sufficient focus placed on developing experiments that would thoroughly characterise the dissimilarities in their actuations. But this result is consistent in the perspective that cells would require more power to be actuated when compared to polystyrene particles (see Appendix 2).

Nonetheless, in these tests it has been shown that the NSCLCs can be actuated. If it is also speculated that the 10 μm particles and the NSCLCs have somewhat similar to characteristics to other cancer cells, then this is a good indicator that other cancer cells can be actuated as well, such as MCF-7, HEPG2 and HT-29 (see Appendix 2).

Additionally, since the NSCLCs patterning was similar to the polystyrene particles, it is a good indicator that the NSCLCs have a positive contrast factor and as such it can be expected that most cells can be actuated by the PCB SAW device in a similar manner, assuming they are sufficiently large. It has also been shown that under the specified power the cells viability hasn't been significantly affect by this actuation. This signifies that not only the PCB SAW can actuate the cells but that it can also do so in biocompatible manner, proving that this technique can be used for biomedical applications with cells as the conventional SAW devices.

4.4. PCB-SAW with ZnO substrates

A concluding test of the PCB-SAW device's capabilities was to extend its coupling ability to different substrates. For these tests two ZnO substrates were used with one having ZnO deposited on a silicon substrate and the other on aluminium. Fig. 4.9a illustrated the actuation of a 1 µL water droplet across the ZnO-silicon substrate, while Fig.4.9b illustrate the actuation on a ZnO-aluminium substrate. Additionally, to demonstrate the PCB-SAW devices acoustophoretic capabilities on different substrate droplet pumping and merging were performed. Fig. 4.9c illustrates the pumping on a droplet towards a secondary droplet and their merging. This tests then proves that the PCB IDTs are not only capable of being coupled with $LiNbO_3$, but also other piezoelectric substrates to create SAWs. Thus, potentially giving researchers a technique that could allow them to build acoustofluidic devices using various piezoelectric substrates and test their acoustofluidic capabilities.

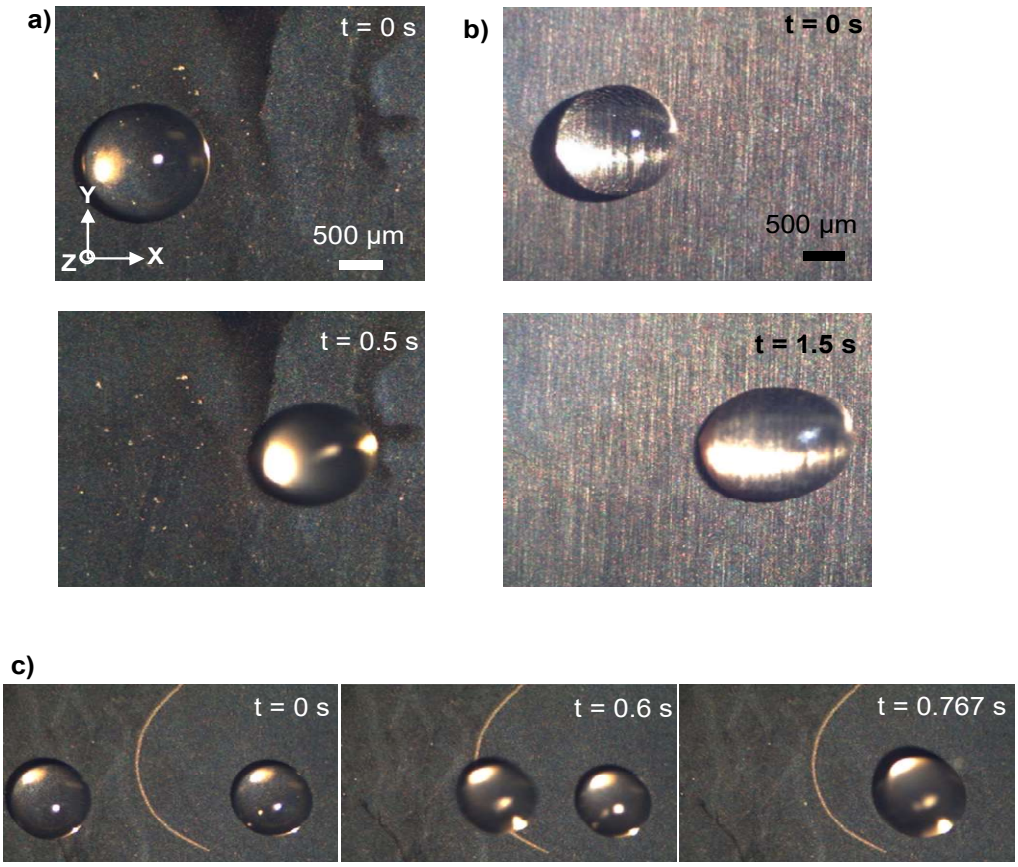

Figure 4.9. Droplet actuation on ZnO substrates using the PCB-SAW device. a) 1 µL droplet actuated across a ZnO-silicon substrate, b) 1 µL droplet actuated across a ZnO-aluminium substrate. c) Pumping and mixing of the droplets on the ZnO-silicon substrate.

4.5. Conclusion / Discussion

In conclusion, herein it was demonstrated that a PCB-SAW device can be developed using PCB IDTs. It was shown that by using a clamping mechanism that pushes the PCB IDEs onto a piezoelectric substrate one can achieve the generation of SAWs, which was demonstrated on both a $LiNbO_3$ substrate and ZnO based substrates. While the clamping "bonding" method will result with poor electrical properties, it was shown that this can be mitigated to an extend with the use of MN and appropriate pressure. However, even though the PCB-SAW can operate similarly as the clean room made IDT, it still was shown that it is a less efficient device when it comes to the conversion of electrical input power to R-SAW. Nonetheless this is to be expected and still the PCB-SAW device provides an accessible alternative of developing a SAW device using accessible means and the ability to both repair the device, by replacing broken components quick, as well as the ability to change substrates on demand. Finally, this device was used to demonstrate R-SSAW capabilities by aligning both polystyrene particles and NSCLC cells in a biocompatible manner.

Chapter 5

Flexible PCB IDTs

5.1. Introduction

An essential parameter of the PCB based SAW devices is to ensure that all the IDEs fingers are in contact with the substrate across their length and over different fingers. One hypothesis is that if the substrates is made of a hard material, it would be much harder to make all the finger be in contact if some defects exist. Some examples of these defects are present in Figs. 5.1a, 5.1b and 5.1c where an PCB board, made from FR4, is shown when it has IDEs with different height, a concave board and a rough piezoelectric substrate, respectively. While potentially the concave board design can be tackled with localised presser, by forcefully straightening the board, the other two issue are much harder to deal with. This is because of these defects are mostly in micron scale, meaning that the board will have to be very flexible and should be capable of local deformation in order to compensate for these defects.

An easy way of potentially addressing these issues, without vastly improving the manufacturing quality, would be to develop the IDEs on a board that could be locally deformed. Combining the flexible board as well as a material on top that could accommodate local deformation, such as rubber, would most likely improve the contact proximity of most IDEs to the piezoelectric substrate. This concept in illustrated in Figs. 5.1e and 5.1e where the IDEs manufactured on polyester board can come into contact with piezoelectric substrate even when they have a different finger height and are placed on rough substrate, respectively. But it should be noted that the rubber is important aspect of this equation since the localised presser are used and they are made of a hard material they will not be able to locally deform. As such a material that can be compressed and deform is vital to make this design work.

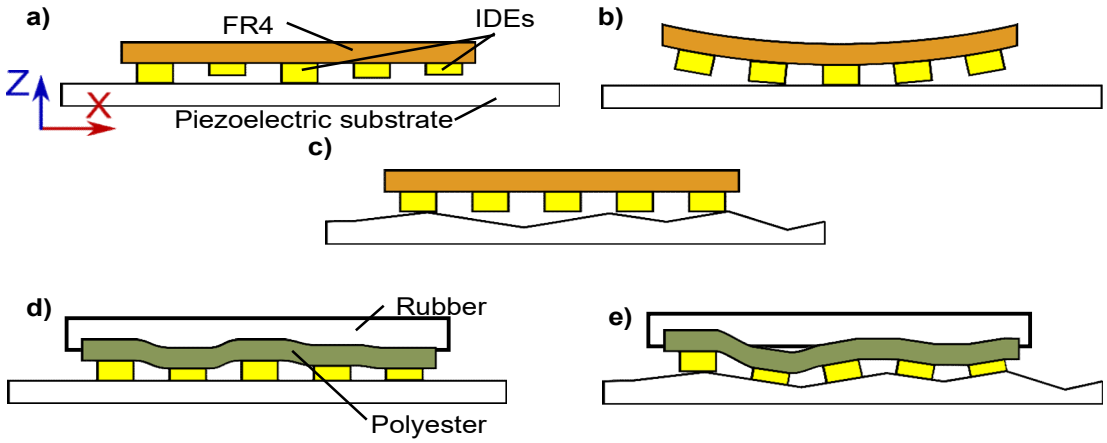

Figure 5.1. Coupling imperfection between hard (FR4) PCB IDEs and piezoelectric substrate when a) the IDEs have different height, b) the PCB board is concave and c) when the piezoelectric substrate has a rough surface. Flexible PCB IDES when d) the IDEs are of different height and e) IDEs are both of different height and placed on a rough piezoelectric surface.

As such in this section the development on FPCB IDTs will be explored in order to test whether the change in PCB substrates could benefit the device's efficiency. For this FPCB IDTs are created and characterised, in a similar manner as the PCB-SAW device to explore their potential. Additionally, while the PCB-SAW allowed the fabrication of the SAW device using relatively accessible means, there are still adjacent components that would require clean room facilities. Thus, a new device is developed using segregated FPCB chips, a DYI control unit, and a new methodology for manufacturing and bonding a microchannel into a piezoelectric substrate to create a device made by utilising means that are as accessible as possible.

5.2. Hard PCB vs flexible PCB (FPCB)

To test the hypothesis that the FPCB IDTs could result in a better data were obtained from a laser vibrometer (PSV-500-VH, Polytec, Germany) to compare the R-SAW generation using two board types; FR4 and polyester (i.e flexible board). For the FR4 board the PCB IDTs from chapter 4 were used, while for the flexible PCB IDT (FPCB IDT) an IDT patterned on a 70-μm-thin polyester laminate with an identical geometry was developed. The devices were assembled using the PCB-SAW device setup, with the only difference that for the FPCB IDTs a 1 mm silicone gel pad (Thermal Interference sheet, RS PRO) was added between the localised presser and the FPCB IDT. The obtained data for each are shown in Fig. 5.2, with the picture on the left indicating the results for the hard PCB and the right for FPCB IDTs. It should be noted that originally these data were not collected to compare the two, as such they show different modes of

actuation. The hard PCB-SAW device was actuated at 1.25 V per at each IDT, creating a R-SSAW, with the measurement taken in the middle of PCB-SAW at approximately 7.5 mm away from the IDTs. While the FPCB IDT was actuated at 1.5V, creating a R-TSAW, with the measurement being taken 2 mm away from the IDT. Both images illustrate the surface deformation of the measured region in Z and while not directly comparable, as such why units are omitted, they can be used to illuminate certain qualitive differences.

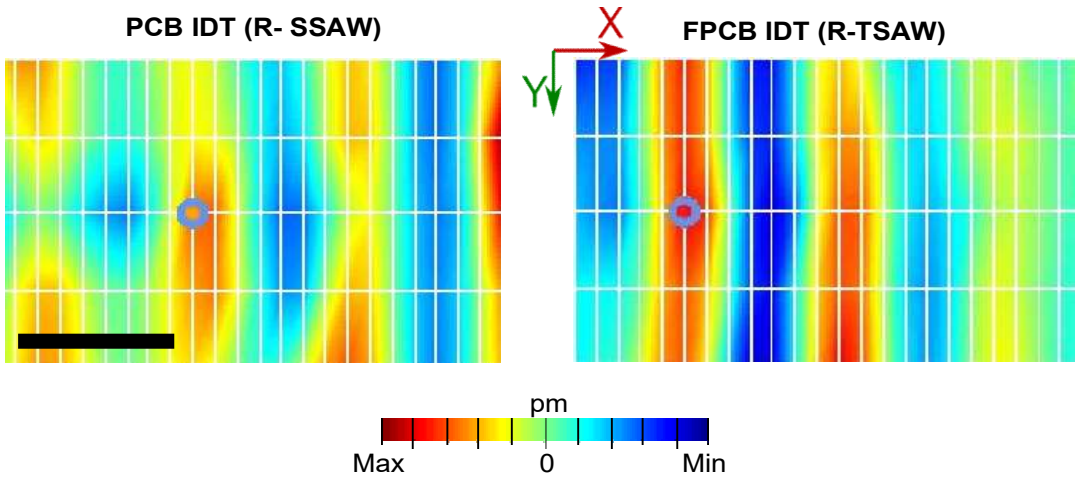

Figure 5.2. Surface deformation measurements on the $LiNbO_3$ when a) a R-SSAW is created, with the PCB IDTs being actuated at 1.5 V per IDT, and b) a R-TSAW is created, when the FPCB IDT is actuated at 1.5 V. Scale bar is 100 µm.

It can be observed that the PCB IDTs a create a SSAW that doesn't have straight and parallel lines, and even has gaps at certain regions. while the R-TSAW from the FPCB IDTs appears to be generating a more uniform deformation across the Y axis. This potentially is an indicator of a more uniform IDEs contact with the piezoelectric substrate, when using the FPCB IDTs. But this interpretation should be taken with caution since this comparison is not necessarily "apples to apples" per say. A R-SSAW might create a more complex deformation profile due to having a second IDT, where complexities may arise due to one of the IDTs not being in proper contact with the surface, waves being reflected after making contact with the second IDT and the generated waves not being identical due to slight manufacturing differences between the IDTs. Additionally, the measurement regions are in different locations in regard to the IDTs, which would normally not be an issue. But from the R-TSAW image a clear wave attenuation can be observed across the X axis, as such this also should be kept in mind since that may result with a rapidly degrading SAW deformation and thus non-uniformity.

As such, these data can only provide a hint on what is happening. Currently the only solid interpretation can be these: a) it is possible to create an uneven SAW field and b) the FPCB IDT SAW field appears more uniform, for whatever reason that might be. Even

if this is not strong evidence for FPCB IDTs being better than the hard PCB IDTs, it still creates an incentive to at least explore the capabilities of the FPCB IDTs.

5.3. FPCB-SAW

In this section a simple FPCB IDT has been created in order to evaluate its capabilities and to see if its comparable to the PCB IDTs (Sun et al., 2021). Herein, the setup was kept as simple as possible, see Fig. 3.6 in section 3.3.1, to also illustrate that a PCB based SAW devices does not necessarily require a complex setup in order to be created. As such the setup was simply a metal bar with a rubber pad and an aluminium plate. It should be noted that the development of the FPCB-SAW was led by Dr. Chao Sun (Sun et al., 2021).

5.3.1. Device Characterization

As with the PCB-SAW device, so with the FPCB-SAW it is important to electrically characterise it. Fig. 5.3a shows the amplitude and phase of the reflection coefficient S_{11} of the FPCB-SAW device with and without using the MN. A minimum S_{11} is identified at 19.654 MHz with the MN and the S_{11} is reduced from −7.29 to −47.12 dB. As with the PCB-SAW a frequency shift is introduced with the implementation of MNs, but in case of the FPCB-SAW it results with frequency reduction instead of an increase. The S_{11} drop and frequency shift of the device are also characterised against the clamping force, as shown in Fig. 5.3b, with 3 repeated measurement at each clamping force. The clamping force is increased by fastening of the two M3 screws on the sides of the pressers. An initial reduction of the S_{11} drop is observed with the increase of the clamping force and the S_{11} drop reaches a minimum at approximately 133 N. As with the PCB-SAW any further increase of force after the 133 N point results with the increase of the S_{11} value but additionally it can be seen that when different clamping forces are applied the optimal frequency of the device doesn't change drastically and remains relatively similar, unlike the S_{11} drop.

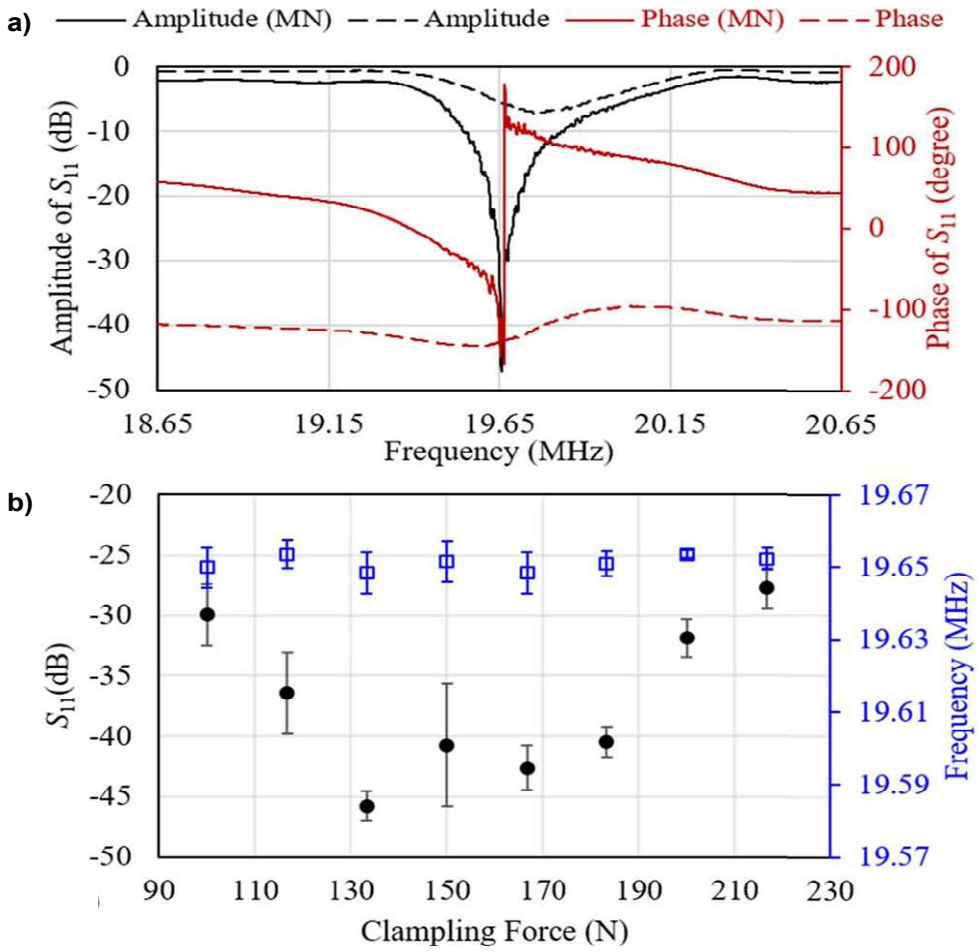

Figure 5.3. Characterization of the FPCB-SAW device. a) Amplitude and phase of the reflection coefficient S_{11} of the FPCB-SAW device with and without the MN. b) Relationship between the S_{11}/ the Rayleigh mode frequency and the clamping force. Figure adapted from *Sun* et al. *(2021)*.

It is noted that at 150 N a there is large increase in the error bars value, which may be a result of reaching a critical point at which the $LiNbO_3$ substrate starts to over compress, i.e. a transition point. As such the 133 N clamping force is selected as the assembly position, which is more stable and allows the maximum the S_{11} drop and assumingly surface deformation. Finally, it should be noted that even though the same tool was used as in the PCB-SAW study, due to the different screw sizes, clamping mechanism and implementation of the silicone rubber it is difficult to compare the results of the clamping force of the two devices. As such the comparison of the clamping force for the two devices is avoided.

To test the FPCB-SAW device's repeatability and reproducibility, five different FPCB IDEs chips were used to create five different FPCB-SAW devices. These devices were assembled and disassembled five times with and without MNs and characterised based on their frequency and S_{11} drop, as shown in Fig, 5.4. From Fig. 5.4a it can be observed

that the MNs consistently reduce the operating frequency of the devices as well as the frequency variation in four out of the five setups. But the implementation of MNs also creates quite distinct operating frequency across different setups, when compared to the operating frequencies without a MNs. This variation could be a result of the manufacturing differences between the FPCB IDEs being magnified by the MNs since the S_{11} drop gets drastically reduced across all devices, Fig. 5.4b. But this variation could also be present due to the different components that are used on the MNs, such inductors, capacitors, cable length and amount of solder used. Regardless, these variations are all very close to the Rayleigh mode frequency and consistently greatly reduce the S_{11} drop, thus improving the operation of the device.

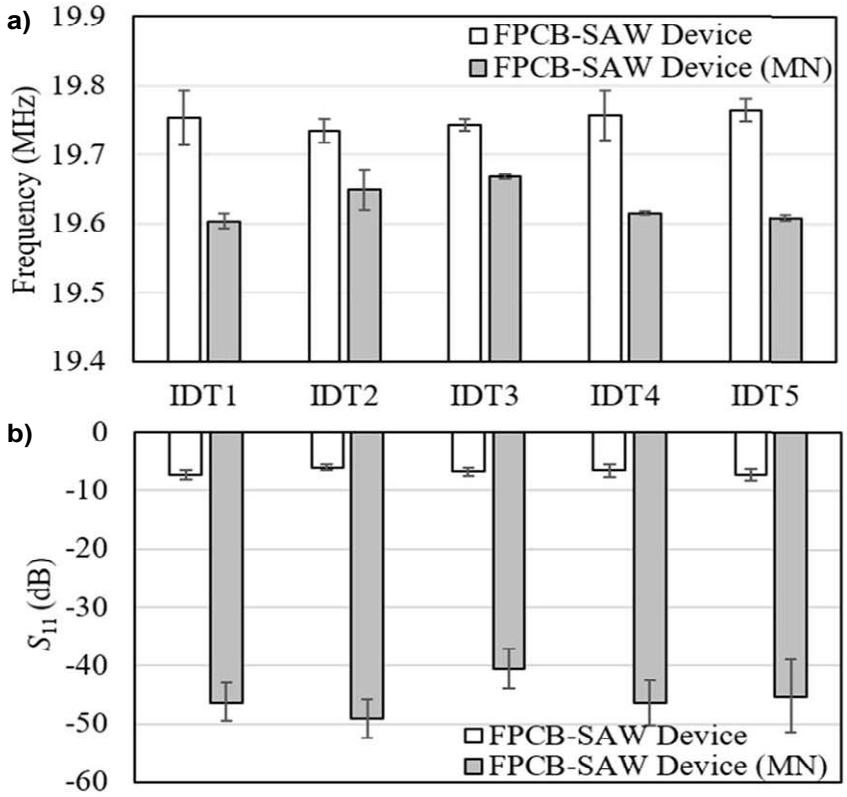

Figure 5.4. Reproducibility of the a) Rayleigh mode frequency and the b) minimum S_{11} drop of the reassemblies of the FPCB-SAW device with and without the MN. Figure adapted from *Sun* et al., *(2021)*.

5.3.2. Environmental effects

Another important aspect to study about FPCB-SAW devices, or rather SAW devices in general, are the environmental effects. For the FPCB-SAW device two environmental effects are studied, temperature and humidity, which is done by placing the device in a temperature-humidity chamber. The results of these effects and their variation on the frequency and S_{11} drop are shown in Fig. 5.5. Temperature has the most noticeable

effect and its increase results in shifting of operating frequency to a lower range and with an increase of S_{11}, as shown in Fig. 5.5a. While the relative humidity (RH) variation had little to no effect on the device's operational parameters, as shown in Fig. 5.5b.

This large effect of temperature on the FPCB-SAW device is rather interesting and there may be a few reasons why this is happening. One reason could be due to change in the materials properties, such as in conductivity, inductance, capacitance, speed of sound, piezoelectric properties and even a combination of these factors. The second reason could be the change in pressure due to thermal expansion. Since the device relies on pre-set pressure to create the optimal contact between the IDEs and the $LiNbO_3$, the thermal expansion of some components could result with the change of the pre-set pressure.

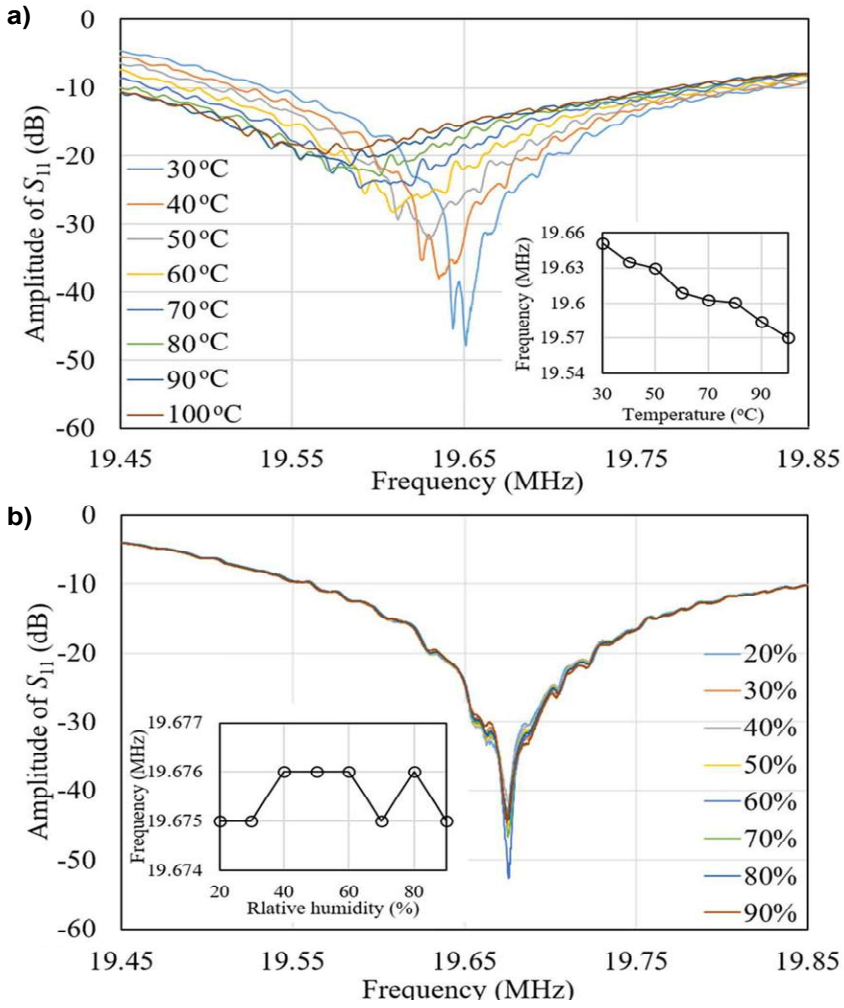

Figure 5.5. Temperature and humidity tests of the FPCB-SAW device. a) Amplitude of S_{11} changes with respect to the frequency over a temperature range of 30–100 ºC. The inset is the varying Rayleigh mode frequency versus the temperature. b) Amplitude of S_{11} changes with respect to the frequency over a RH range of 20%–90%. The inset is the Rayleigh frequency versus the RH. Figure adapted from *Sun* et al. *(2021)*.

5.3.3. SAW generation

The last part of this device's characterisation is the observation and quantification of the R-TSAWs. A laser vibrometer (PSV-500-VH, Polytec, Germany) was used to characterize the surface vibration patterns and quantify the amplitude of the T-RSAWs produced on the device. The maximum amplitudes of the surface vibration at various input powers with and without the MN were characterized. Three measurements were acquired for each input power and the results are shown in Fig. 5.6. Fig. 5.6a shows the visual results of the laser vibrometer reading of R-TSAW with no MN. It can be observed that a relatively uniform R-TSAW is developed by FPCB-SAW device that travels across the substrate and the R-TSAW wave's amplitude increases accordingly with the increase the input signal as well as with the implementation of the MN, as shown in Fig. 5.6b. This result is another indicator that the improvement of S_{11} drop results in the increased surface deformation and higher amplitude R-TSAW generation.

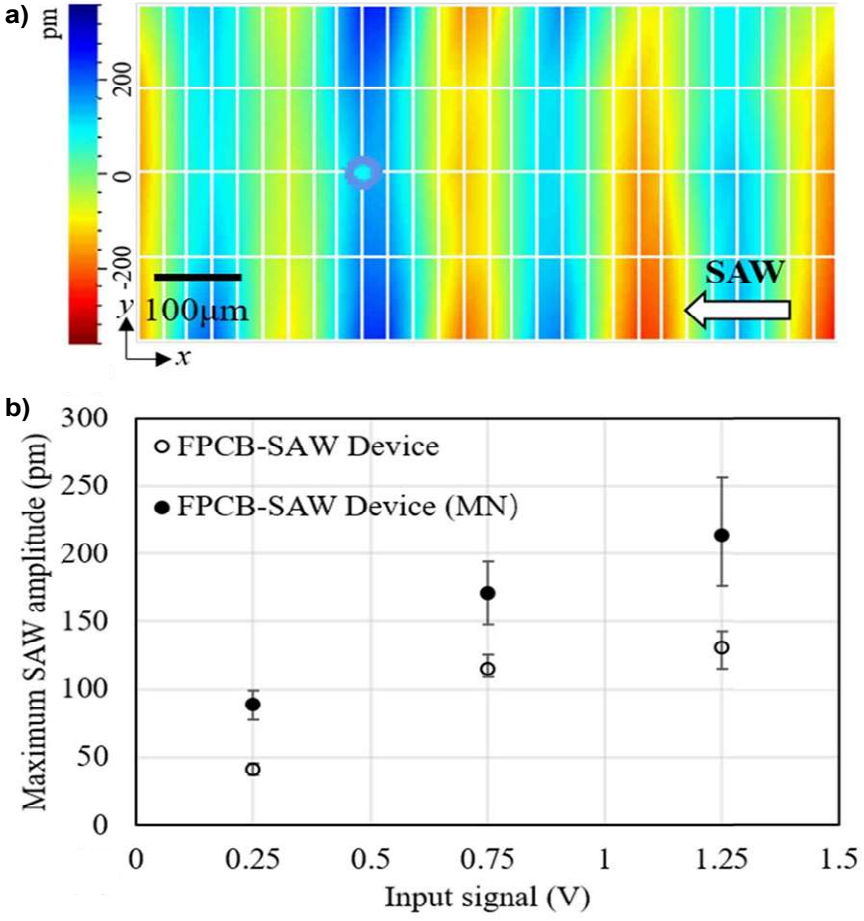

Figure 5.6. Surface vibration of the FPCB-SAW device. a) Vibration pattern of the SAW traveling on the surface at the input voltage of 1.25 V. b) Comparison of the maximum SAW amplitude of the FPCB-SAW device with and without the MN at a series of the input signals. Figure adapted from *Sun* et al., *(2021)*.

Finally, the same droplet actuation that was performed with PCB-SAW device was performed with this device as well, shown in Fig. 5.7. In Fig. 5.7a the actuation of a 1 μL droplet is demonstrated with the FPCB-SAW device using ~1.26 W of power. These actuation tests were then repeated 3 times for each power setting, and the results are shown in Fig. 5.7b. It can be observed that both the FPCB- and PCB-SAW have very similar actuation capabilities and as such, the FPCB IDEs can be a perfect alternative to the hard PCB IDEs.

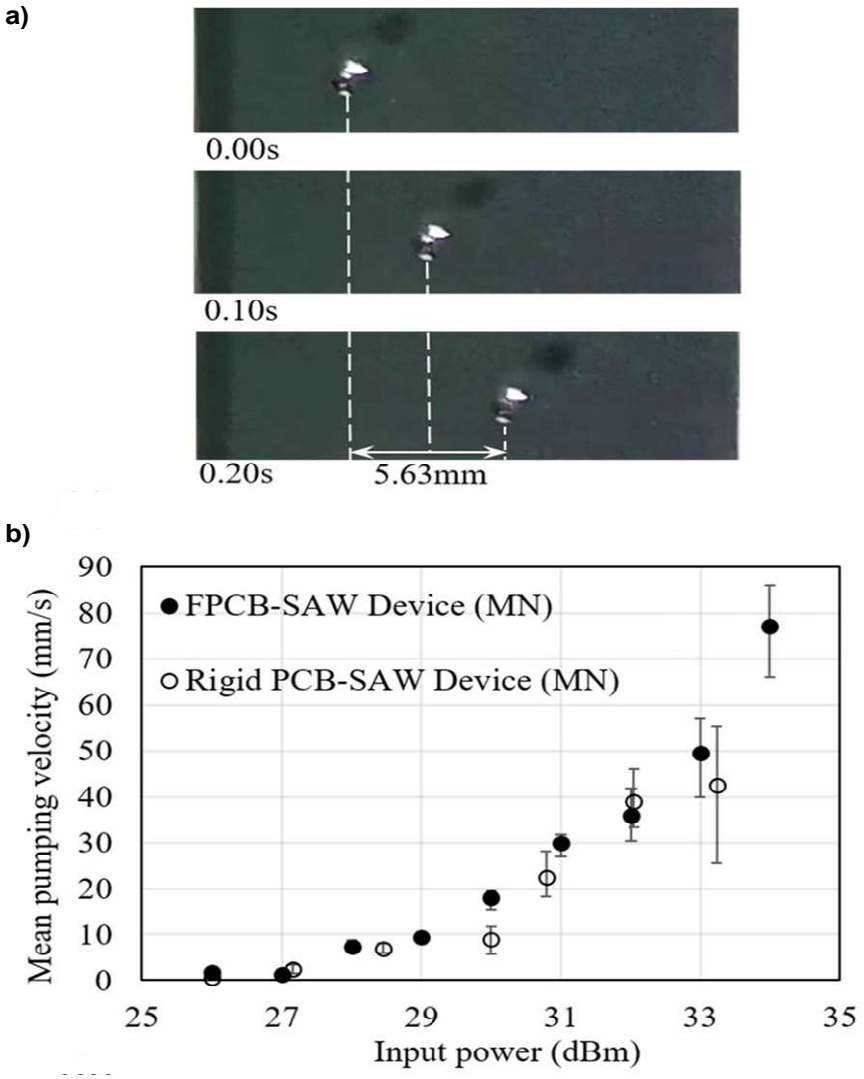

Figure 5.7. Droplet transportation on the FPCB-SAW device. a) Images of droplet transportation driven by the SAW at 31 dBm with the mean velocity of 29.79 mm/s. b) Comparison of the pumping velocity of a droplet between the FPCB-SAW device and the rigid PCB-SAW device at different input powers. Figure adapted from *Sun* et al.*, (2021*.

5.4. FPCB based versatile acoustofluidic device (VAD)

From the above tests it can be concluded that the FPCB IDTs can operate as good as the hard PCB IDTs, when it comes to the droplet actuation. As such it was decided, by the author, to carry on with the FPCB IDT design to test its capability for creating a FPCB-SAW device capable of particle manipulation. Instead of replicating the previous PCB-SAW device, the focus was on enhancing its capabilities by leveraging on the strengths of the existing design. The two main advantage of the PCB based SAW devices is their accessible means of fabrication and reconfigurable setup, but while the PCB IDTs and the substrate can be easily outsourced adjacent components like the microchannel still require high end facilities or equipment. Thus, the next challenge for SAW based PCB devices was to identify how much of that equipment could be mitigated/ replaced, while still creating a small and compact device that can be used for T-SAW and SSAW applications. The resulting device was dubbed as the versatile acoustofluidic device (VAD) and it implements two FPCB IDTs, a pair of 3D printed clamps and a DYI control unit. Additionally, with the VAD also a new manufacturing and bonding method for the microchannel was developed, which utilised a desktop 3D printer. The real-life model device is shown in Fig 5.8, with an inset that shows the assembled SAW device, with all its components, looks on top of the heatsink.

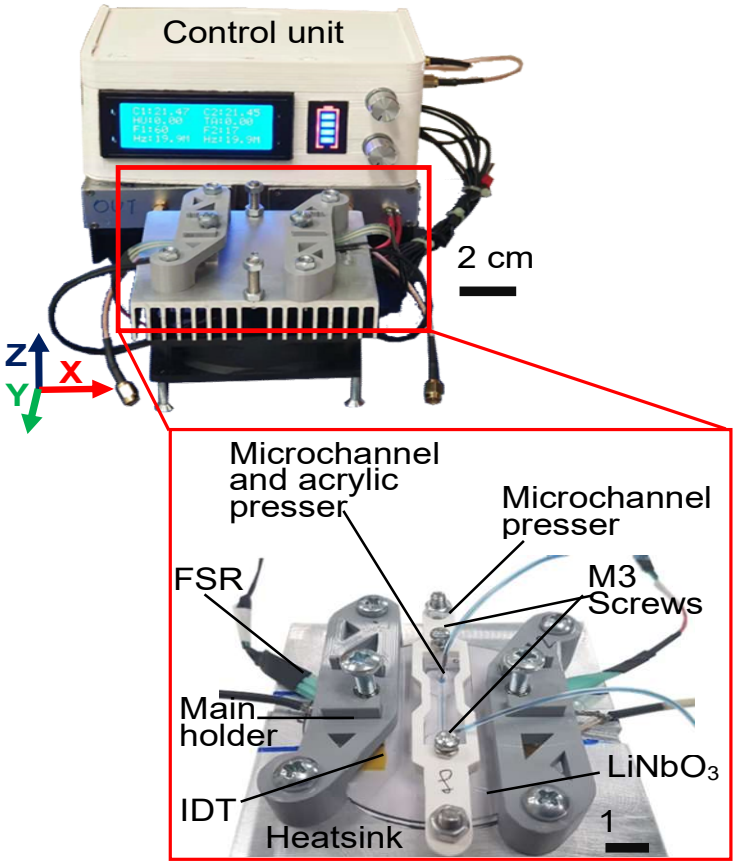

Figure 5.8. The portable control unit and the VAD with an inset demonstrating the real-life model of the assembled VAD on the heatsink, where FSR stand for force sensor resistor.

Before proceeding with the characterisation and functionality of the VAD, it is important to establish certain drawbacks of the PCB-SAW device. One drawback was the interconnectivity components on the left and right side via the FR4 PCB and the clamping mechanism. This interconnectivity created the following issue: due to the rigidity of the FR4 structure and clamping mechanism when pressure was adjusted in one side it would result with a change in pressure in the mirror side. As such it was difficult to easily balance and apply the appropriate pressure per each IDT and typically either a compromise would have to be selected between the two or a lot of time would be spent on balancing the pressure. The advantage of the flexible substrate is that easily solves this issue regarding the rigidity of the PCB, but if the hard PCB IDTs were manufactured as separate chips this would solve this issue as well. As such the FPCB IDTs were separated into two distinct chips to attempt to create a SSAW setup using distinct chips, which could also be implemented with hard PCB IDTs if required. The same philosophy was also implemented for the clamping mechanism, thus as to why the VAD has two distinct clamps instead of one.

5.4.1. IDT alignment

Since the FPCB IDTs were manufactured as distinct chips a methodology of aligning them parallelly to each other, for generation of SSAW, is required. Fortunately, it was observed that the S_{21} parameter could be used for that. To prove this concept on IDT was held statically while the second one was rotated and the resulting *S*-parameters at different orientations were recorded. The resulting *S*-parameters at different orientations are shown in Figs. 5.9a and 5.9b for the S_{21} and S_{11} reading, respectively. It can be observed that the 0° angle achieves the maximum S_{21} peak, which rabidly declines as soon as the parallelism of the IDTs is starting to be lost. This result then confirms that the S_{21} reading can be reliably used to establish the parallelism of the two IDTs. While rather surprisingly the S_{11} reading is much less sensitive to the change in angle. It indicates a very noticeable change only when it is rotated by 17°, where an observable frequency shift appears, and a rather faint indication at 11°, with a slight increase in S_{11}. This appears to indicate that even when the IDTs are not completely parallel to the $LiNbO_3$ flat edge some sort of SAW is still being manifested.

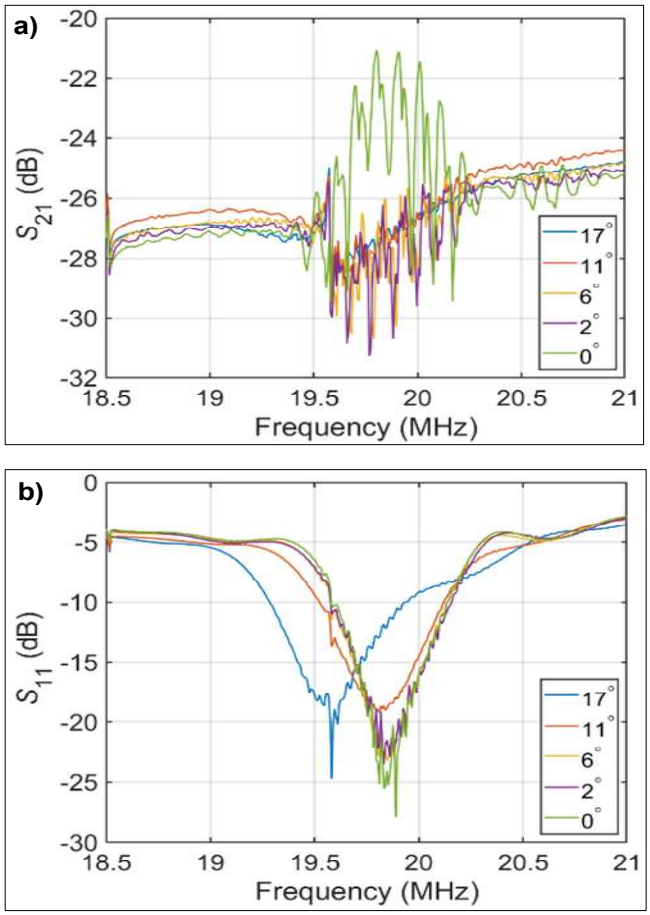

Figure 5.9. S-parameters of the VAD during the rotation of one IDT. a) Average insertion loss (S_{21}) for each different angle during the rotation. b) Average reflection coefficient (S_{11}) for each different angle during the rotation.

5.4.2. Microchannel manufacturing

|As stated in Methods and Materials, section 3.3.2, the microchannel mold was developed using 3D printing, which was designed to be 500 µm wide and 100 µm high. The resulting average height and width of the molds are shown to be (Fig. 5.10a) 102.8 ± 11.4 µm (Mean ± SD) and 451.4 ± 42.6 µm (Mean ± SD), respectively. The resulting 500 µm wide PDMS microchannel, that was used for the particles' tests, is shown in Fig. 5.10b. The microchannel was then bonded to $LiNbO_3$ using an acrylic and 3D printed presser and the bonding strength was tested with different flow rates. This bonding method achieved at a flow rate of up to 6 mL/min, which is considered as a high throughput flowrate for acoustofluidic devices (Chen et al., 2016).

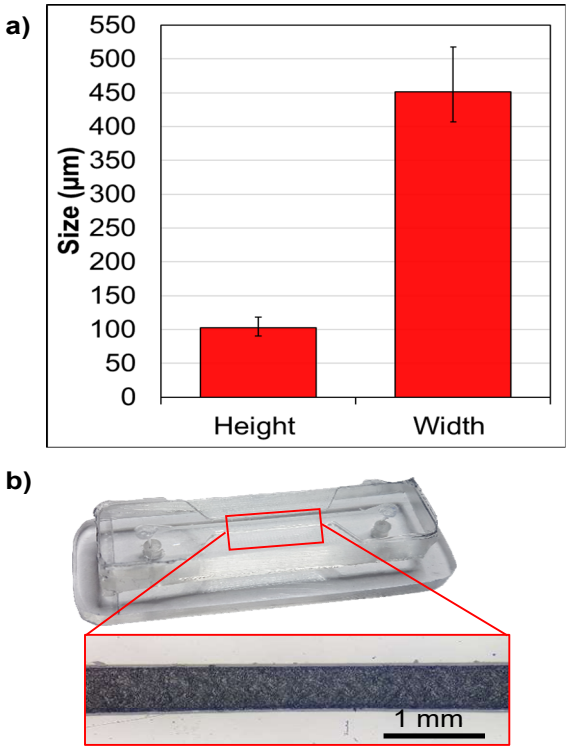

Figure 5.10. a) The 3D printed mold's average height and width of 102.8 ± 11.4 µm (Mean ± SD) and 451.4 ± 42.6 µm (Mean ± SD), respectively. b) Real-life model of a 500 µm wide microchannel sitting on top of the acrylic presser.

Following the promising results from the *S*-parameters, the next step was to investigate how this was reflected on the particle alignment. For this test 10 µm particles were injected into the microchannel, to mimic the PCB-SAW device, and were actuated at 19 dBm and using the established S_{21} readings to align one of the IDTs at 0°, ~6° and ~17° angle, shown in Figs. 5.11a, 5.11b and 5.11c, respectively. This resulted with the particles aligning into lines that have angles 0°, 2.5° and 6° against the channel wall. This is surprising since it demonstrates that even when one of the IDTs are misaligned, they can still be utilised to create tilt angle configuration without changing the channel

orientation in any way. But most importantly, this test proves that the S_{21} reading is a reliable indicator that can be used to establish parallelism of the IDTs, which will translate on the particle alignment within the microchannel.

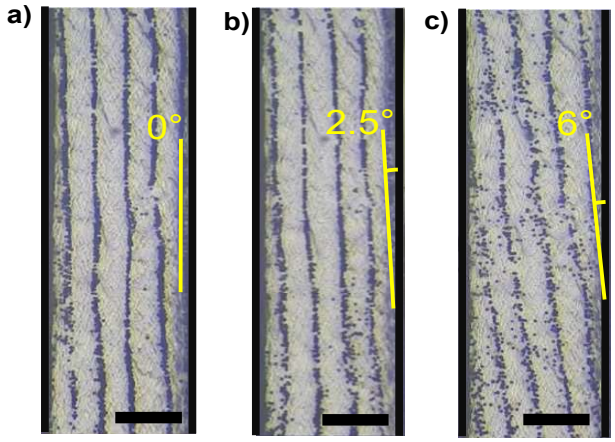

Figure 5.11. Microscope images showing the PN lines of 10 μm particles when one of the IDTs is rotated using the S_{21} reading to a a) 0°, b) ~6° and c) ~17° angle. The particles are aggregated on the PN lines exhibiting the angle against the wall of the microchannel. The scale bar is 200 μm.

5.4.3. Acoustic energy density analysis

While an input power demonstrates the power that is provided to the IDTs, this doesn't take into an account any losses that could happened during its travelling path as well as the internal losses of the system, i.e. the device's reflection coefficient potentially being higher at lower powers. On the other acoustic energy density considers only the power that was delivered into the channel, i.e. the acoustic pressure (see eq. 21). As such it a much more reliable method of characterizing a device performance since it relies directly on the actuation performance of the particles. This technique utilises the time the particles need to align on the pressure nodes to then calculate the acoustic pressure density. While this technique is similar to the droplet actuation it is far more accurate for the application of particle manipulation, since it directly characterises the actuation of the particles inside the microchannel. Finally, this measurement can also be used to decipher the acoustic pressure that the device develops and help the user to create more reliable simulation models using this experimental value.

The acoustic energy density of the VAD at 0° with an input power per IDT of 15, 20 and 27 dBm was calculated and the results are shown in Figs. 5.12a-5.12c, respectively. The initial results showed that the time required for 99% of microspheres to aggregate on the PN line, per respective input power, is ~1.9, ~0.6, and ~0.3 s. Since the preliminary tests appeared promising, these tests were repeated 3 times to obtain an average acoustic energy density for each input power, shown in Fig. 5.12d. These results illustrated that

the particles can be fully controlled by tuning the input power and the SAW amplitude changes with the power. This method then also provides an alternative way of characterising a SAW device by using only the microchannel and particles.

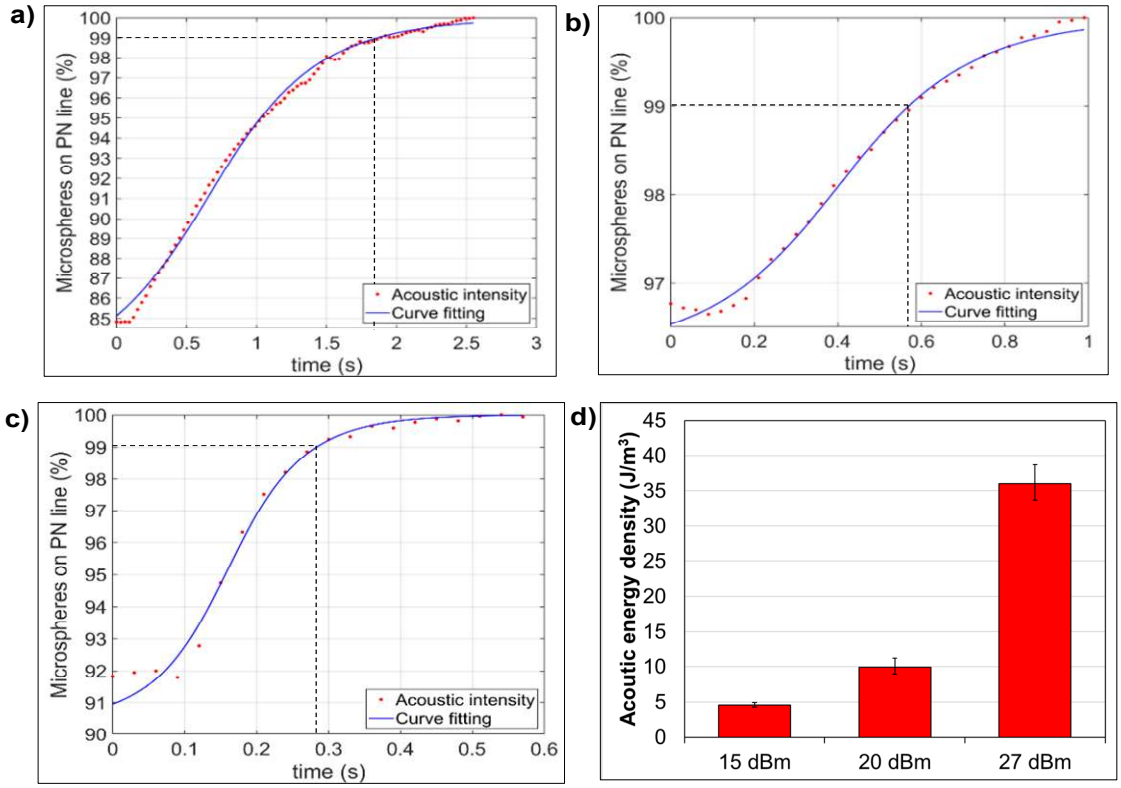

Figure 5.12. Acoustic energy density of the VAD with parallel IDTs. Under the input power of a) 15 dBm (~0.03 W), b) 20 dBm (~0.1 W), and c) 27 dBm (~0.5 W), the time for 99% of microspheres to reach the PN line is ~1.9, ~0.6, and ~0.3 sec, respectively. d) The average acoustic energy densities for the three input powers are 4.6, 9.9, and 36 J/m3, respectively (n = 3).

5.4.4. VAD visual alignment

One of the advantages of the VAD, more precisely the control unit, is the implementation of the FSRs. In short, the FSRs worked similarly as the torque screwdriver and provided a reliable reference point, in arbitrary units, on when the optimal pressure was applied. Using this tool one can reliably press down the IDTs without having to rely on the VNA reading. Thus, making the VAD device a much simpler device to use thanks to the control unit, since it could provide both the required RF signal and reference point of optimal pressure. But one thing that it could not inform the user was if the IDTs were aligned parallelly, as such it was interesting to test whether the IDTs could be visually aligned by the user without compromising its effectiveness.

This alignment was not done arbitrarily since the localised presser offered a flat edge and FPCB IDTs chips have also a front flat edge. As such these two edges can be used

as visual guides to attempt to make the components locally parallel to each other and, since the main holders are already parallel, by extension making the two opposites IDTs parallel. The FPCB IDTs chips were aligned visually 5 times, to obtain an average S_{21} reading, with was then plotted against the S_{21} achieved using the VNA, shown in Fig. 5.13a. From the graph it can be observed that the VNA guided alignment (blue curve) S_{21} peak is slightly larger to the visually guided alignments (orange curve), but still remarkably close to the S_{21} achieved using the VNA. Since Fig. 5.13a demonstrated such promising results, the next step was to characterise its acoustic energy density to compare the performance of the setup. For both the VNA and visually guided alignment 3 tests were performed at 17 dBm (~0.05 W) input power for each with average acoustic energy shown in Fig. 5.13b. Surprisingly the acoustic energy density is slightly higher in the visually guided assembly. It is speculated that this is most likely due to the distance between the opposing IDTs being reduced during the visual experiments. Since to visually align the IDTs the FPCB's edge is required to be exposed, this might have resulted with the FPCB IDTs chips to pushed further forward to expose more of the said front edge. As such the distance between the IDTs is reduced, resulting with a lesser wave attenuation (refer Fig. 5.2b), and as a result the acoustic energy density is increased. The microsphere aggregation image for the visually guided assembly is also shown in Fig. 5.13c, which achieves a similar pattern as that in the VNA guided assembly (Fig. 5.11a). Overall, this confirms that the assembling process of the VAD can be achieved by the visual alignment of the two IDTs without the use of the VNA.

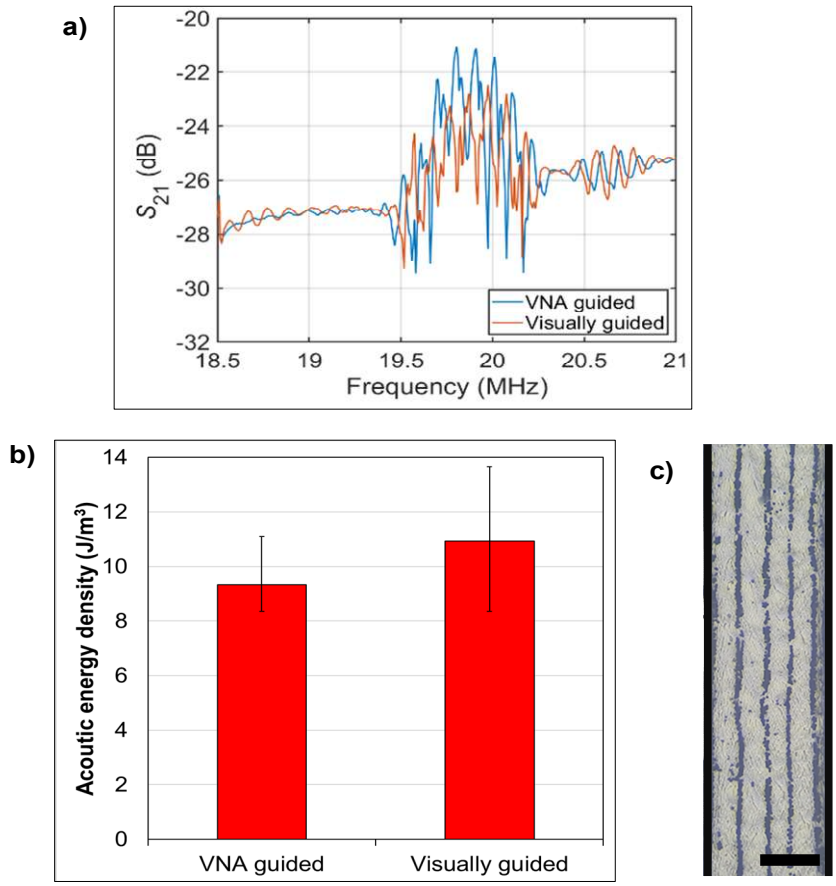

Figure 5.13. a) The S_{21} of the VAD assembled using the VNA and the visually guided assembly of the two IDTs (n = 5). b) Acoustic energy density of the VAD constructed by the two assembly methods, VNA and visually, with an acoustic energy of 9.3 ± 1.2 J/m3 (Mean ± SD) and 10.9 ± 2.7 J/m3 (Mean ± SD) at 17dBm (~0.05 W), respectively (n = 3). c) Particle aggregation on the PN lines of the VAD constructed by visually guided assembly (200 µm scale bar).

5.4.5. Rotating the Microchannel

While the rotation of one of IDTs has been demonstrated to be able to achieve a tilt angle alignment, this not the only method of achieving it. The unique bonding mechanism for the microchannel, utilised on the VAD, allows the possibility to alter the tilt angle by rotating the microchannel clamped to the VAD. For these tests new microchannel pressers are utilised that were designed to accommodate two different alignment angles of 15° and -5°, Fig. 5.14a. Additionally, for these tests a wider channel is used of 800 µm to clearly illustrate the tilt angle phenomena These pressers are utilised to clamp the microchannel and to create the respective inclinations for aggregating the particles using 17 dBm input power, as shown in Fig. 5.14b.

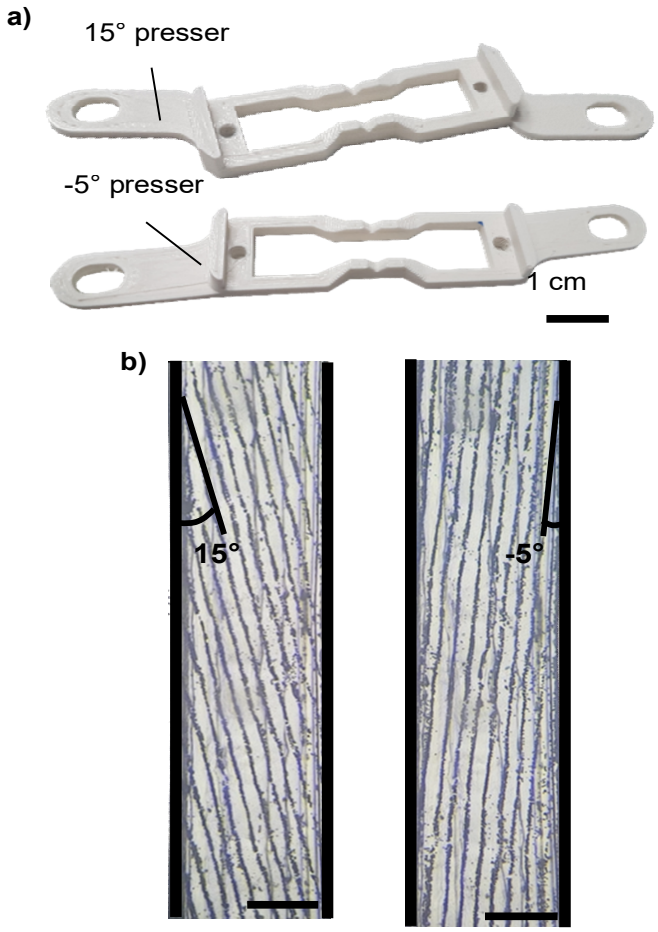

Figure 5.14. Rotating the microchannel to a set tilt-angle. a) 3D printed 15° and -5° microchannel pressers. b) Aggregated particles on the PN lines of 15° (left) and -5° (right) angles, in regard to the microchannel wall (450 µm scale bar).

From these tests it can be observed that the tilt angles can be achieved by either rotating the microchannel or the IDTs. But it should be noted that it might be preferable to rotate the microchannel as it will create a standard SSAW, while the tilting of IDTs will most likely result in a more complex wave superposition. If particles are statically aligned this may not pose a grave issue, but if the setup is utilised with flow for separation purposes this may result with complications. As such, the tilting of the IDT might be an attractive alternative but until this setup is further explored it is hard to determine how stable and predictable it can be.

5.4.6. Unutilised features

Before moving on from the VAD, the unutilised features of the control unit should be discussed. These unutilised features were the temperature sensors and the fan, i.e. the temperature related features. While these were implemented in the design and were in fact operational, when the temperature sensors were used, by being slotted underneath

the IDTs, they showed no increase in temperature during use. As such the use of the fan was not deemed necessary. But in hindsight this was not because there was no temperature increase, but rather because the temperature increase is not located underneath the IDEs and as such the temperature system was not exactly appropriate for the device.

5.5. Conclusion/ Discussion

In this chapter the PCB based SAW method was further explored by implementing a flexible PCB based IDTs. Through initial preliminary test the FPCB IDTs give hints that they might be able to create a more uniform SAW than their hard PCB counterpart, but this still requires a thorough investigation. Regardless, the FPCB-SAW device was developed and characterised, and it demonstrated its capability to achieve similar actuation results as the PCB-SAW device. Then the VAD was developed to fully capitalise on the PCB based fabrication strengths, which are the accessible means of fabricating a SAW device as well as the devices capability for reconfiguration. For this a DYI control unit and 3D printing based microchannel manufacturing and bonding mechanism were developed to ensure that the device was manufactures using the most accessible means. Through testing this device demonstrated its capability to create a R-SSAW as well as a tilt angle SSAW, via two different techniques. A capability that useful in the particle separation application where a high tilted-angle is optimal for the flow rate of 25 μL/min and a low tilted-angle is optimal for a flowrate of 50-125 μL/min (Li et al., 2015). Finally, the device's actuation capability was characterised and its ability to be assembled using nothing more than its primary components.

Chapter 6

High frequency FPCB IDTs

6.1. Introduction

The development of the VAD has demonstrated the FPCB-SAW device's various capabilities, but all these applications remain in the realm of static alignment. While these demonstrated applications might be useful in the realm of cell alignment and stimulation, the technique has yet to illustrate its potential in actuation/ separation based applications. Additionally, SSAW based devices for cell separation applications tend to operate within the 20 MHz threshold (Li et al., 2015), but in the sub-micron separation field they tend to be in the realm of 30-40 MHz (Wu *et al.*, 2017; Wang *et al.*, 2020). As such these following questions arise, 1) can this technique be utilised to develop a prototype device to study particle actuation, and demonstrate its potential for separation applications, and 2) can an FPCB-SAW device be developed with a frequency suitable for sub-micron actuation.

To demonstrate its capability of actuation for separation particles, the most promising way forward would be to develop a tilt angle SSAW (taSSAW) device that can redirect particles from one output port to another. The devices that utilise taSSAW have already demonstrated their capability in the separation based applications, see section 1.4.2, and it has been speculated that separation is one the most prominent applications for acoustofluidic devices. Thus, demonstrating the PCB fabrication's capability to actuate particles for separation application would verify that this technique is also suitable for these applications. This would then reinforce that a PBC fabrication technique is viable option to develop such devices and give researchers a more accessible way of fabricating such devices.

6.2. High frequency FPCB IDTs based SAW (hFPCB-SAW) device

To apply the FPCB IDTs for sub-micron manipulation the initial step is to manufacture IDTs that could actuate such particles. Wu et al., (2017) have shown that a 33 MHz frequency on $LiNbO_3$ can achieve sub-micron actuation. As such, for the new PCB based IDTs the wavelength of 120 µm was selected, which would theoretically generate a frequency of ~33.17 MHz on $LiNbO_3$. This pitch would also demonstrate that it is possible to develop finer traces (30 µm) on a PCB IDT. The next step was to select methodologies of the SAW device development that could be carried over from the previous studies. First, it is important to select the appropriate PCB substrate, which for the given pitch and IDE size were recommended to be manufactured on a FPCB. Furthermore, the VAD technique demonstrated its ability to reliably create a R-SSAW using two segregated

chips, as such this was also carried over to maintain the chip-based capabilities of the PCB based SAW devices. The clamping system from VAD was also demonstrated to be reliable and easy to use, and as such this technique is also carried over.

For the manufacturing of the microchannel it was decided to use a silicon mold channel. The 3D printing technique, while very convenient and easy to use, reduces the channel's transparency, has an irregular internal structure, and struggles with dimensions lower than 500 µm. All the aforementioned parameters are especially important for particle separation, with the transparency giving the ability to easily observe flowing/ moving particles, the structure is necessary for an even flowrate and the lower dimensions are required to design appropriately sized channel inputs and outputs. But while the 3D mold is not suitable for this application, the mechanical bonding method of the channel has proven to be quite effective and a convenient alternative to the plasma treatment bonding. This boding method also allows to change, quickly and easily, the angle of the microchannel. Lastly, while the DYI control unit is a very convenient setup to use, it hasn't been built to be capable of frequencies above 25 MHz, and as such is not carried over.

6.3. Actuation tests

By using the carried over techniques the hFPCB-SAW device was created to have a stable and controllable flow and the ability to mitigate heating effects, to an extent, see section 3.4. With these features the device could now be used to demonstrate its particle actuation capabilities and study the actuation behaviour of the particles. Additionally, instead of using this device to simply actuate particles, the ability of reconfiguring the microchannel is used in order to study the effects of different tilt angles, 5 º and 15º, as well as to optimise the actuation of said sizes. These tests are used to, hopefully, demonstrate that the PCB based methodology could be utilised for separation application, for both the development of a separation device or as tool to study and optimise SAW devices for separation based applications.

6.3.1. 5 µm particles actuation

Before the actuation of particles from one outlet to another can be studied, it is most important to check and establish that most of 5 µm particles can be aligned and actuated in the SSAW zone. This confirmation is performed for both angles, shown in Figs. 6.1a and 6.1b, where 5 µm particle are actuated in 5º inclination at 2 W input per IDT and 15º inclination at 5 W input power per IDT, respectively. From these figures it can be observed that most of 5 µm particles respond to the force and are being aligned and redirected upwards. Additionally, when the deflection angle is measured the resulting angles are 4 and 14º, which is very closed to the expected angles.

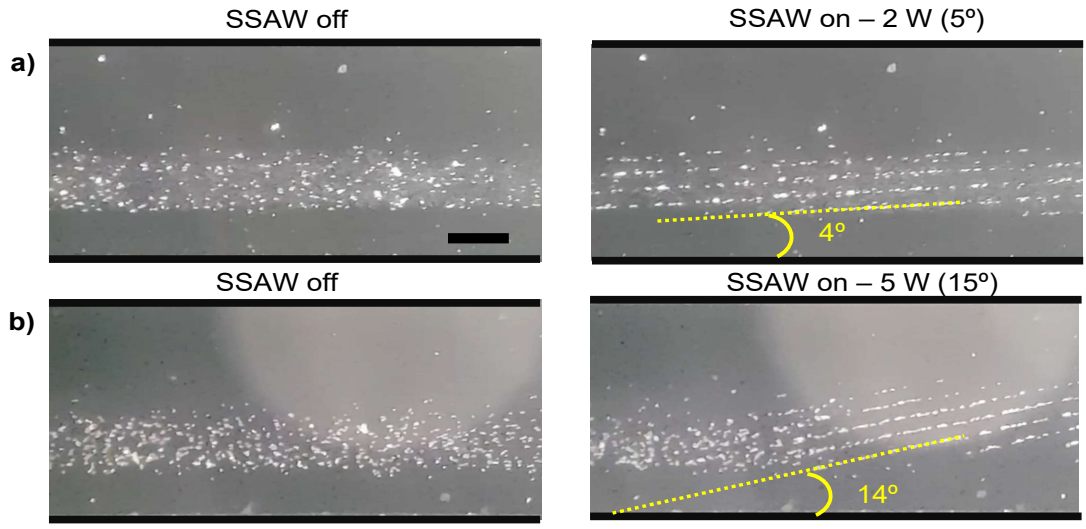

Figure 6.1. 5 µm particles in the SSAW zone with the SAW off (left) and on (right) in the microchannel inclined by a) 5º with 2 W input power per IDT and b) 15º with 5 W input power per IDT. Scale bar is 200 µm.

Since the 5 µm particle actuation at the SSAW zone showed promising results, their actuation at the output could then be studied. The resulting actuation of the particles at the output region is demonstrated in Figs. 6.2a and 6.2b, where a snapshot from the collected videos of the 5 and 15º actuation is shown, respectively, when the device is actuated at 3 W per IDT. These images show that particles are indeed actuated and displaced from the waste output (output 5, bottom) towards the collection output (output 4, top). Also, despite being actuated at an incline, the particles start to form travelling lines that are straight and tangent to the flow. Most of the particles will typically be secluded within those travelling lines and will travel as groups. This phenomenon is more clearly observed at a 5º actuation at a low power input (1 W) shown in Fig. 6.2c. In this figure the traveling lines can be clearly seen being formed both in the lower and upper region of the channel. It can also be observed that the flow at the middle of the channel splits, and particles that are below the midpoint will travel towards the waste output (orange arrows) while particles above towards the collection output (blue arrows). As such if an imaginary segregation line is drawn that indicates the boundary between the two flows (red dotted line) and the position of traveling lines one could know if the particles will be travelling towards the waste or collection output. As an example, if all the traveling lines were formed above the midpoint of the channel, then one could assume that at this power input all the particles that have been displaced from waste output toward the collection output. The formation of traveling lines is also demonstrated at low input power (2 W) for the 15º actuation, but unlikely the 5º actuation it can be observed that travelling lines/ paths are much more densely packed, Fig. 6.2d.

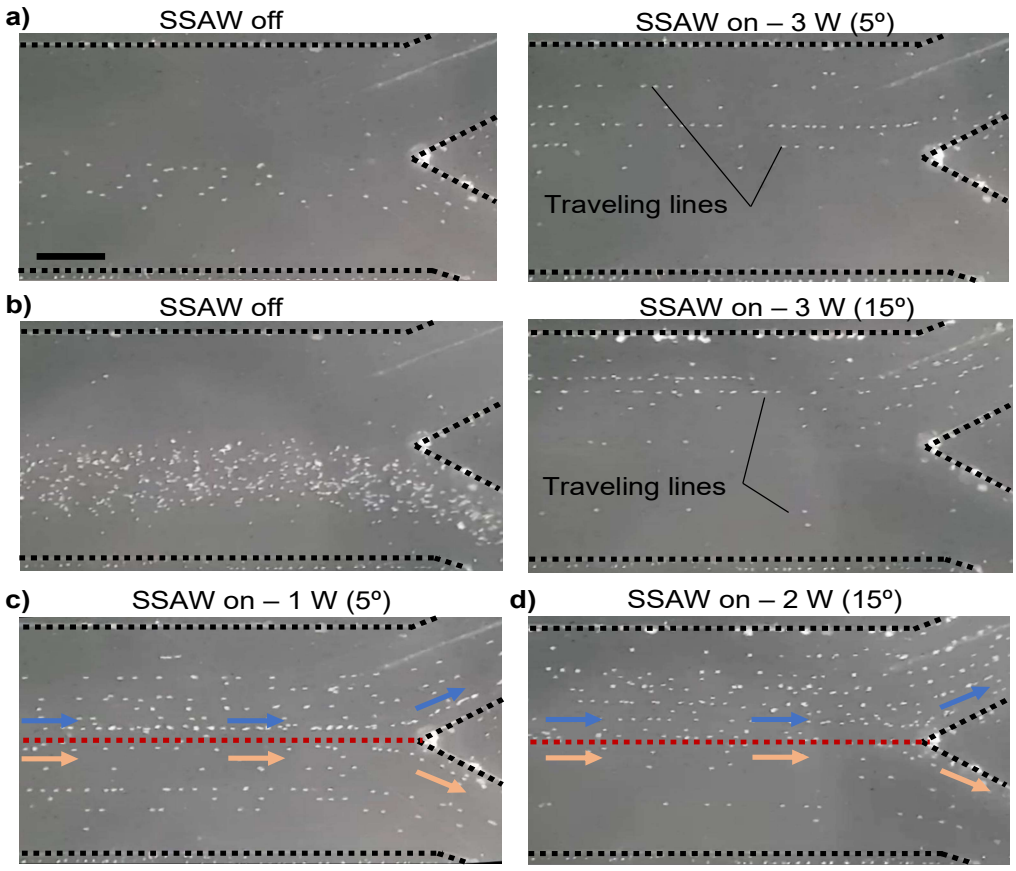

Figure 6.2. 5 µm particles at the output region with the SAW off (left) and on (right) with the microchannel inclined by a) 5º and b) 15º. Demonstrating the formation of traveling lines and their tangent propagation with flow at a low input power of c) 1 W for the 5º inclination and of d) 2 W for the 15º inclination (right). The blue arrows indicate the flow traveling towards the collection output (output 4), while the orange arrows indicate the travel towards the waste output (output 5). The red dotted line is a segregation line that illustrates the boundary between the two flows. Scale bar is 200 µm.

By establishing this phenomenon, the collected videos can then be edited to remove any background noise and used to create an illuminance density profile to help study the actuation of the particles, see section 3.4.6. Figs. 6.3a and 6.3b illustrate the illuminance density profiles of 5º and 15º inclination, respectively, at different input powers with the dotted line indicating the flow segregation line. It should be noted that each power's illuminance profiles have been offset by +100 a.u. to clearly distinguish each profile. In the case of 5º inclination the illuminance profiles indicate the creation of distinctly spaced and segregated traveling lines/ paths, where most particles are positioned at. By increasing the power, the particles start shifting towards the traveling lines closer to the collection wall (800 µm), resulting with almost all the particles being located at the collection region at the powers of 4 and 5 W. For the 15º inclination the traveling lines/paths are more chaotic and densely packed across most powers, which is most

likely a result of the more aggressive actuation angle. A higher actuation angle will result with a steeper particle traveling path, which in turn means that the particles will have to overcome higher fluid flow forces during actuation. This higher flow force pushes particles to travel with the flow and as such some particles “escape” the SSAW zone sooner, thus creating multiple traveling lines close to each other. But despite the different profile of the traveling paths for the 15º inclination, here as well most of the particles appear to be in the collection region at the powers of 4 and 5 W. These illuminance profiles can then be used to generate a graph to demonstrate the percentage of illuminance at the output 4 region. The resulting data are used to create Figs. 6.3c and 6.3d for the 5º and 15º inclination, respectively, where the average percentage of illuminance is shown for different input powers per IDT. From these graphs it can be observed that both inclinations can achieve almost 100% particles actuation efficiency towards the collection output at a high power, but the 5º appears to be the most effective actuation method since it can achieve a relatively amount of particle actuation towards the collection output even at lower input powers. But it should be noted that the 5º inclination has extremely large error bars between 3-4 W. This is due to the sample consistency running low at the designated powers, due to particle deposition in the sample tube. This then resulted with an increased illuminance intensity of the unseparated particles. Most likely if the sample was properly mixed the error bars would much smaller, as is the case at 5 W power input were this issue was mitigated. This consistency issue was mitigated in the 15º tests by remixing the sample tube and flushing the channel at a higher flow rate when the consistency was getting low. It should also be noted that 5 W separation percentage was omitted for 15º inclination, and the reason will be provided in the following paragraphs.

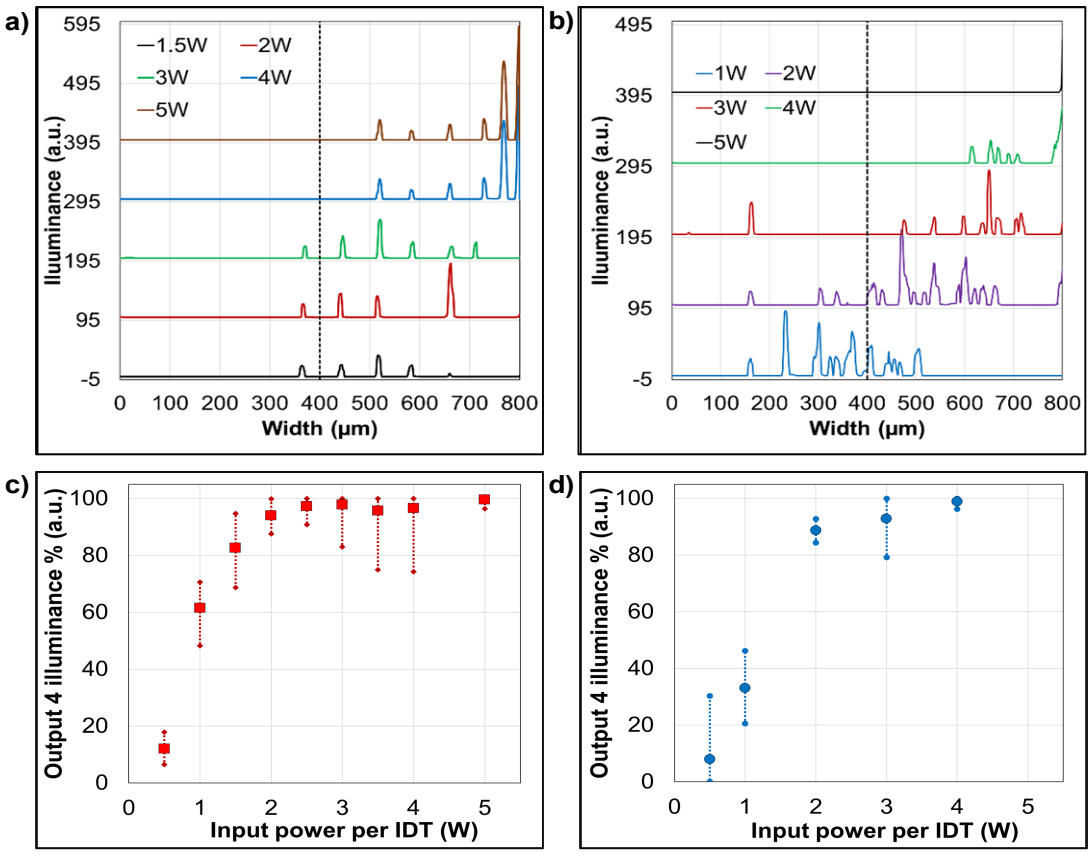

Figure 6.3. 5 μm particle actuation illuminance profiles at the output region of a) 5º and b) 15º channel inclination at different input powers per IDT. Each power profile is offset by 100 a.u. to clearly distinguish the profile for each input power. The dotted line is the flow segregation line. The average illuminance percentage with max/ min error bars at the collection region (401-800 μm) for the c) 5º and d) 15º inclination at different input powers (n=10).

But while the actuation efficiency appears to be nearly perfect at high powers, it can be observed that these figures still have error bars that indicate an imperfect actuation. The minimum actuation efficiency of 5º inclination at 5 W and 15º inclination of 4 W is approximately 96% for both. While this efficiency might be appropriate for certain applications, in an application that requires high specificity and has a low event rate, such as CTCs, this could be an unacceptable separation rate. This actuation efficiency decrease appears to be the result of single flowing (SF) particles that appear to flow independently or far away from the traveling paths. These particles are illustrated in Figs. 6.4a and 6.4b, where SF particles are indicated for the 5º inclination with 5 W per IDT and the 15º inclination with 4 W per IDT, respectively. It should also be noted that due to multiple use, the microchannel was contaminated with trapped particles on the microchannel roof. As such, to avoid their confusion with SF particles, the particles that are trapped on the PDMS are highlighted in yellow circles.

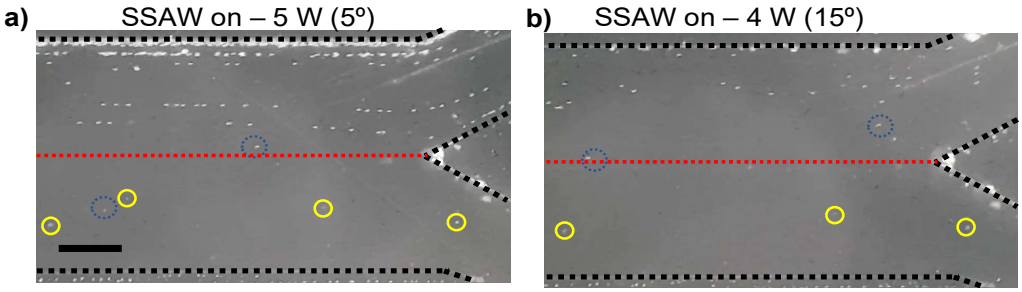

Figure 6.4. 5 μm single flowing (SF) particles (blue circles) in the a) 5º inclination at 5 W input power per IDT and b) 15º inclination at 4 W input power per IDT. The yellow circles indicate trapped particles on the microchannel, due to repeated use. Scale bar is 200 μm.

Apart from the SF particles, another issue is the sample loss/ retention at high input powers. This sample loss is most evident at 15º inclination and is the result of particles being pushed against the PDMS wall at the SSAW zone. This is presented in Fig. 6.5a, where the 15º with 5 W is illustrated with the SSAW on (left) and few second after it is turned off (right), ~5 s. It can be seen that when the SSAW is on almost no particle is flowing to the output region, but when the SSAW is turned off all these particles are released and flow through as lumps/ clusters. This is why the separation percentage of 15º inclination at 5 W is excluded in Fig. 6.3d, due to most particles being trapped in the SSAW region. This effect is also present when the power is 4 W and 3 W but is significantly reduced as the power is lowered, as is shown in Figs. 6.5b and 6.5c, respectively. This pushing effects also exist in the 5º inclination but because the angle is much less aggressive the particles are still able to flow while being against the wall and are seemingly rolling across. But this still remains an issue, since if the same principle is applied against cells they might adhere to the microchannel wall or rupture. As such to improve the actuation method there are two issues that are required to be resolved: a) the pushing of particles against the PDMS wall and b) the capturing of SF particles.

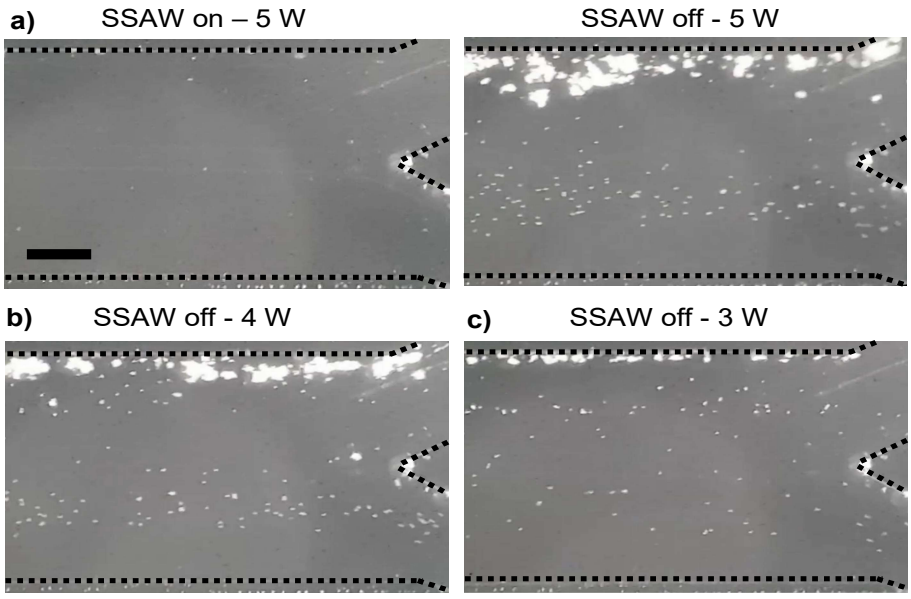

Figure 6.5. 5 µm particles at the output region at the 15º microchannel inclination. a) Output region under 5 W input power per IDT with SSAW on (left) and after few seconds (~5s) of it being turned off (right), illustrating the release of trapped particles. The release of particles is also shown for the input powers per IDT of b) 4 W and c) 3 W. Scale bar is 200 µm.

One of the advantages of having a 3-input microchannel setup, is that the sheath flows can be used to modulate the input/ sample flow. More precisely by adjusting both sheath flow rates one can change the width of input sample flow and bring its contents closer to the channel's centreline. This effect demonstrated in the Figs. 6.6a and 6.6b, where input region is observed for when the sheath 1 (input 1), input 2 and sheath 2 (input 3) flowrates are 0.7, 0.7 and 1.4 µL/min (default) and 9.8, 0.7 and 9.8 µL/min, respectively. Here it can be clearly observed that with a higher sheath flow rate, at both sheath 1 and 2, the sample width is greatly reduced, and the particles become densely packed closer to channel's centreline. Potentially, this modulation could resolve both the issue of SF particles, by bringing them closer to the segregation line, as well as stop particles from being pushed against the microchannel wall, by increasing the flow forces. But before proceeding with the actuation tests is important to characterise the resulting sample width at different sheath flow rates, which is achieved by recording videos at the input region and having them analysed with Tracker. To make this study easier, the sheath flow rates were equalised and increased by increments of 0.7 µL/min (i.e. the input flow rate) while the input 2 flowrate remained always as 0.7 µL/min. The sample width change at various sheath flow rates is then shown in Fig. 6.6c, where the blue points indicate when the sheaths 1 and 3 were equalised and the first point indicates the width at the default flow rate settings (i.e. 0.7, 0.7 and 1.4 µL/min). From this figure it can be observed that the sample width initially decreases drastically with the sheath flow rate increase,

but this reduction quickly stabilises, and further sample width decrease requires much larger sheath flow rates.

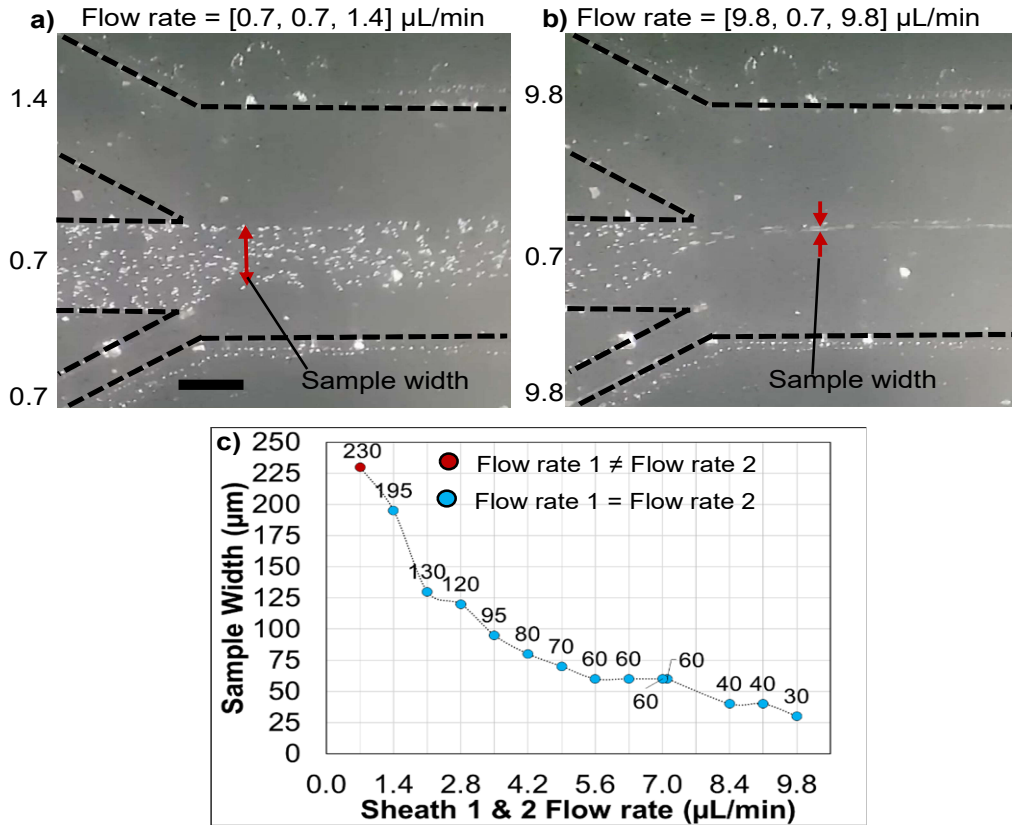

Figure 6.6. 5 µm particles flowing at the input region when the flow rates at the inputs 1, 2 and 3 are a) 0.7, 0.7 and 1.4 µL/min and b) 9.8, 0.7 and 9.8 µL/min, respectively. c) Graph presenting the width of the flowing sample at different flow rates. The X axis illustrates the flow rate at the sheath 1 and 2 which is equal everywhere except the first point. At the first point the flaw rate of sheath 1 and 2 is 0.7 and 1.4 µL/min, respectively. Scale bar is 200 µm.

From previous results it was observed that the 5 W actuation can achieve an almost perfect separation at the 5º inclination. As such, this input power and channel inclination would be used for the flow tests in order to see if the change in flow rate can eliminate both the SF particles and the particle actuation against the microchannel wall. But before proceeding another issue should be discussed, and this is the positioning of the segregation line. The segregation line would normally be positioned right in the middle of the channel when the pressure of both outputs is made equal, which is achieved by adjusting the position (height) of the output chambers held in the custom microtube holders. This has the effect of the particles flowing very close and hitting to the inner wall (green dotted line) of the waste outlet, as shown in Fig. 6.7a. While these particles would not normally flow to the collection port, due to the higher flow rate at sheath 2, if a slight

pressure imbalance appears after the actuation some of the sample may flow into the collection port.

To prevent this, a slight pressure imbalance can be introduced which will make a segment of the flow from sheath 2 to flow into the waste outlet. As result this would offset particles from the inner wall of the waste outlet, as shown in Fig. 6.7b, and prevent any accidental separation of the non-actuated particles. But this has also the consequence of shifting the segregation line upwards, as illustrated in Fig. 6.7c, where the original segregation line (yellow line) is shifted upwards by ~90 μm. This shift effectively reduces the collection region from 400 μm to 310 μm (490-800 μm). This shift remains present during the sheath flow increase, but at the initial flow increase this will result with a larger offset of 130 μm, as shown in Fig. 6.7d for the sheath flow rate of 2.1 μL/min. But when the sheath flow rate becomes high enough it is restored back to the original offset of 90 μm, as shown in Fig. 6.7e for the sheath flow rates of 5.8 μL/min. This variation of offset position from 90 to 130 μm is most likely introduced due to the initial increase of sheath 1 flowrate, which results with particles being slightly pushed upwards due to the unequal flowrate at outputs 4 and 5. But as the sheath flow rates keep increasing this flow rate imbalance starts to be negligible, due to the input 2 flowrate starting to have a lesser effect on the total flowrate.

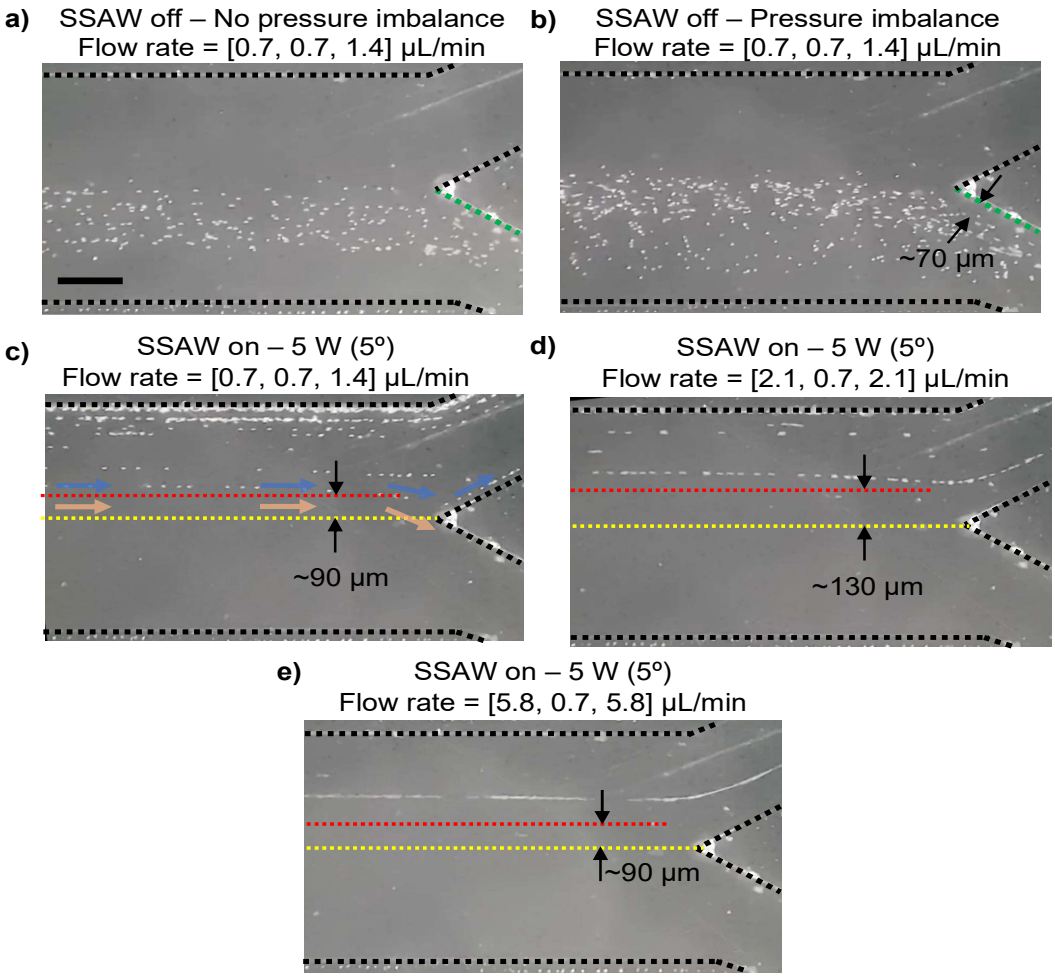

Figure 6.7. 5 µm particles at the output zone with a) no pressure imbalance and b) with a slight pressure imbalance, resulting with a 70 µm offset from the waste outlet inner wall (green dotted line). The pressure imbalance also results with an upwards shift of the flow segregation line shown for the flow rates of c) 0.7x0.7x1.4, where the original position of the line (yellow dotted line) is shifted upwards by ~90 µm (red dotted line). Due to the pressure imbalance this results with a segment of the sheath 2 flow flowing towards the waste outlet, as such reducing the area of the flow traveling to collection outlet (blue arrows) and increasing the one towards the waste outlet (orange arrows). This offset is also illustrated for the flow rates of d) 2.1x0.7x2.1 and e) 5.8x0.7x5.8 µL/min, where the initial increase of sheath flowrate increases the segregation line offset to ~130 µm but is restored back ~90 µm at a high enough sheath flow rates. Scale bar is 200 µm.

Having established the new particle collection region, the next step is to investigate if the 5 W 5º inclination actuation would still create an illuminance profile that indicates that most of the traveling lines are in within the collection region. These profiles are presented in Fig. 6.8 with focus on the 400-800 µm region of the channel. The reason why this region is highlighted is because at 5 W 5º inclination all the particles will be located here when SSAW is on, and since the segregation line has been offset upwards any un-

separated particles can be also detected within this region. Fig. 6.8a contains the illuminance profiles from top to bottom of 8.4, 7.7, 7 and 6.3 μL/min sheath flow rates, Fig. 6.8b contains the 5.6, 4.9, 4.2 and 3.5 μL/min sheath flow rates and Fig. 6.8c contains the 2.8, 2.1, 1.4 μL/min sheath flow rates and default flow rate. An offset of +300 a.u. has been added in each graph to allow the clear distinction between the different profiles. From these figures it can be observed that only at the flow rates of 1.4 and 2.1 (Fig. 6.8c) the separation boundary shifted to ~130 μm, while all the rest had a similar shift of ~90 μm. At the initial increase the separation seems to start to slightly deteriorate but then, perhaps surprisingly, improves at higher flow rates. Additionally, the increased flow rates also resulted with the transition lines to be pushed away from the microchannel wall while still remaining within the separation region. But after a certain point the increase of the flow rate will result with the traveling lines forming before the segregation line. Nonetheless the flowrates below the 7 μL/min flowrate form promising profiles for a more effective actuation method that can tackle one of the issues presented previously, that of the particles being pushed against the PDMS wall.

a)

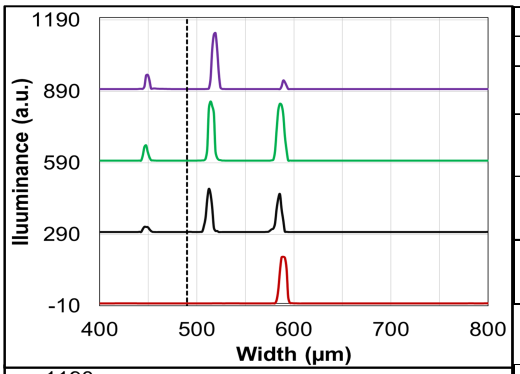

Flowrates (μL/min)		
Sheath1	Input 2	Sheath2
8.4	0.7	8.4
7.7	0.7	7.7
7	0.7	7
6.3	0.7	6.3

b)

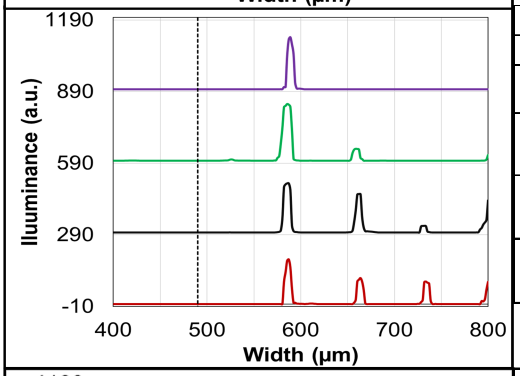

Flowrates (μL/min)		
Sheath1	Input 2	Sheath2
5.6	0.7	5.6
4.9	0.7	4.9
4.2	0.7	4.2
3.5	0.7	3.5

c)

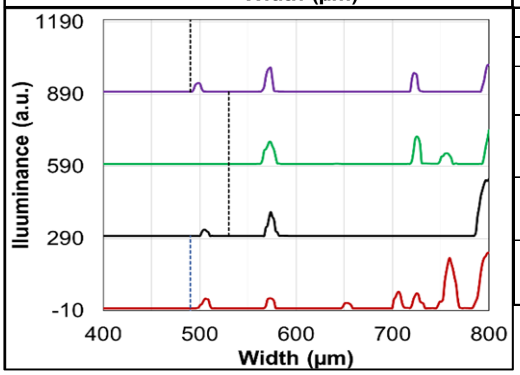

Flowrates (μL/min)		
Sheath1	Input 2	Sheath2
2.8	0.7	2.8
2.1	0.7	2.1
1.4	0.7	1.4
0.7	0.7	0.7

Figure 6.8. Illuminance profile of 5 μm particles in the 400-800 μm region actuated by 5 W per IDT at a 5º microchannel inclination.16 different sheath flow rates are presented with the a) presenting sheath flow rates between 8.4-6.3 μL/min, b) between 5.6-3.5 μL/min and c) between 2.8-1.4 μL/min and the default flow rate. The dotted line indicates the segregation line position at each flowrate.

But while the illuminance profiles give information about the location of the transition lines, they still do not detect the SF particles. The illuminance profiles give a good oversight of the general traveling profile of the overall particles, but this is still dependant on the time frame selection of the snapshots. Thus, in order to detect the SF particles, the actuation videos must be observed by the user, and the SF particles have to be observed and noted down manually. As such 30s of the actuation period were observed from each video, where the SF particles were counted and noted whether they were or were not separated, with the results illustrated in Fig. 6.9. From this figure it can be observed that SF particles are present and unseparated at the default flow rate and the

initial increase of sheath flowrate up to 2.1 µL/min. But as with the illuminance profile, the separation is improved at higher flow rates, possibly due to the sample width reduction and the segregation line being restored to its default position. With the higher flowrate also the total amount SF particles and the amount of unseparated SF particles starts to decrease, as can be seen at the 2.8 µL/min sheath flow rate. This reduction reaches its minimum at 3.5 µL/min and the total amount of SF particles remains low up until 4.9 µL/min. But when the flow rate reaches 5.6 µL/min the amount of SF particles drastically increases, but most of the particles still remain within the collection zone. This changes when the sheath flowrate is 6.3 µL/min where, even though the amount of SF particles remains similar to the 5.6 µL/min flow rate, half of these particles are no longer in the collection output zone.

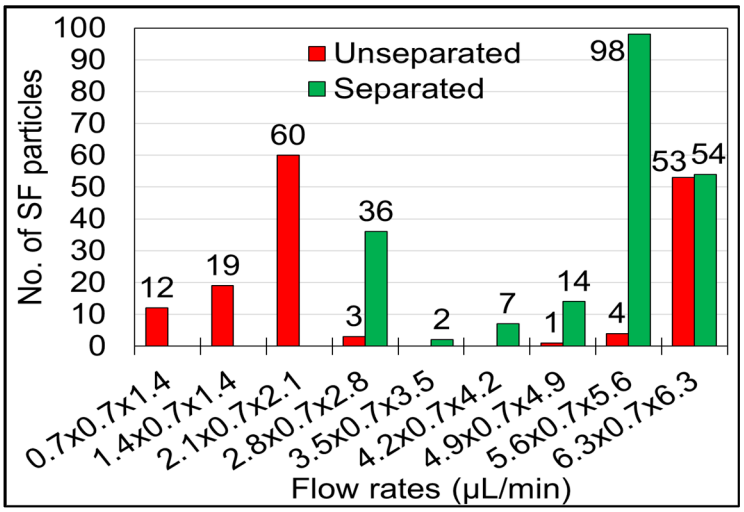

Figure 6.9. 5 µm SF particles at different flow rates with both separated and unseparated particles being shown. Separated indicating particles that have been actuated towards the collection output.

These results then indicated that the increase of the sheath flow rate could result with a higher actuation efficiency by actuating SF particles towards the collection output. Since the 5º inclination demonstrated such promising results, the same tests were also implemented for the 15º channel using the same settings. Initially it was important to observe if the higher flowrate compensated for the particles trapping in the SSAW zone and them being pushed against the microchannel wall. Figs. 6.10a, 6.10b and 6.10c illustrate the results of the particle release after 5 s for the flowrates of 1.4, 2.1 and 2.8 µL/min, respectively. As expected, the higher flowrate did prevent the trapping of the particles against the wall, with the flowrate of 2.8 µL/min eliminating the effect completely. Unfortunately, the increase of flowrate did not improve the particles separation as can be seen from the illuminance profiles in Fig. 6.10d. As soon as the flowrate exceeded

1.4 µL/min, the traveling lines/ paths started to form before the segregation line. In fact, the traveling paths started to be generated so far from the collection region that for these illuminance profiles the observation region had to be increase to 200-800 µm to illustrate the created lines/ paths. Furthermore, the segregation line for the 15º inclination is also initially shifted upwards by 140 µm, as with the 5º, but it remains shifted upwards until the 2.8 µL/min, then it is shifted to 110 µm at 3.5 µL/min and then restored to the default position at 4.2 µL/min. This lagging might be a results of higher flow disturbance being introduces at the more aggressive angle inclination.

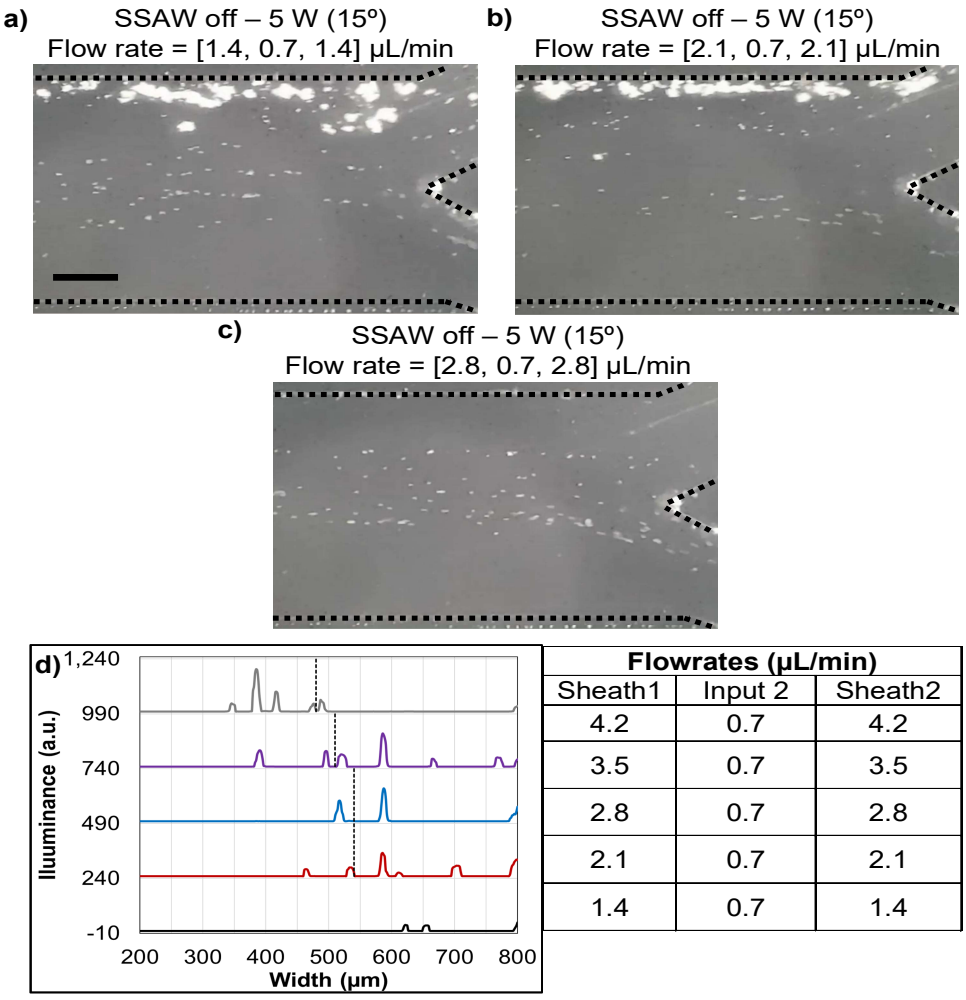

Flowrates (µL/min)		
Sheath1	Input 2	Sheath2
4.2	0.7	4.2
3.5	0.7	3.5
2.8	0.7	2.8
2.1	0.7	2.1
1.4	0.7	1.4

Figure 6.10. Images of flowing particles after the 5 s of the SSAW release at 15º inclination at the flow rates of a) 1.4x0.7x1.4 µL/min, b) 2.1x0.7x2.1 µL/min and c) 2.8x0.7x2.8 µL/min. c) Illuminance profile of particles in the region between 200-800 µm under different flowrate actuated by 5 W per IDT at a 15º microchannel inclination. The dotted line indicated the segregation line. 5 different sheath flow rates are presented for the sheath flow rates between 4.2-1.4 µL/min and the default flow rate. Scale bar is 200 µm.

6.3.2. 1 µm particles separation

While the device indicated promising results with 5 μm, it is also most important to investigate if this actuation limit can be pushed further down. Thus, the next step was to test whether the device is capable of actuating 1 μm polystyrene particles. As with the 5 μm, the tests start by observing the particles in the SSAW zone until a suitable actuation was observed, i.e. most of the particles were translated upwards. Figs. 6.11a, 6.11b, c, 6.11d, 6.11e and 6.11f demonstrate the actuation of particles at the input powers of 0.5, 1, 1.5, 2, 3 and 4 W, respectively. It can be observed that some particles start to be actuated upwards at 1W, but as soon as the power is increased these lines start to become fainter and eventually completely disappear at 2 W. Further increasing the power has the detrimental effect of spreading particles across the microchannel as indicated by Figs. 6.11e and 6.11f. Even though the effective actuation of 1 μm particles towards the collections output appears to be not feasible, by just observing the SSAW zone, this was also further confirmed by observing their behaviour at the output region. Figs. 6.11g and 6.11h illustrate the particle transition line under the influence of 1 W and 2 W, respectively. From these two figures it can be seen that the traveling lines/ paths are still being formed, but when the power is increased they tend to spread in both directions instead of shifting upwards towards the collection region. Additionally, If the videos were directly observed one would notice a faint “cloud” of particles travelling at the collection zone, which illustrates that some actuation efficiency is being achieved. Still this figure illustrates that a full actuation of 1 μm particles towards the collection output is not possible using this setup, since the increase of power will only result with the further spread of said particles in both directions. It should be noted that the particles here are aligned at ~7º which could be a result of the user not aligning the microchannel properly during assembly, and as such resulting with +2º offset.

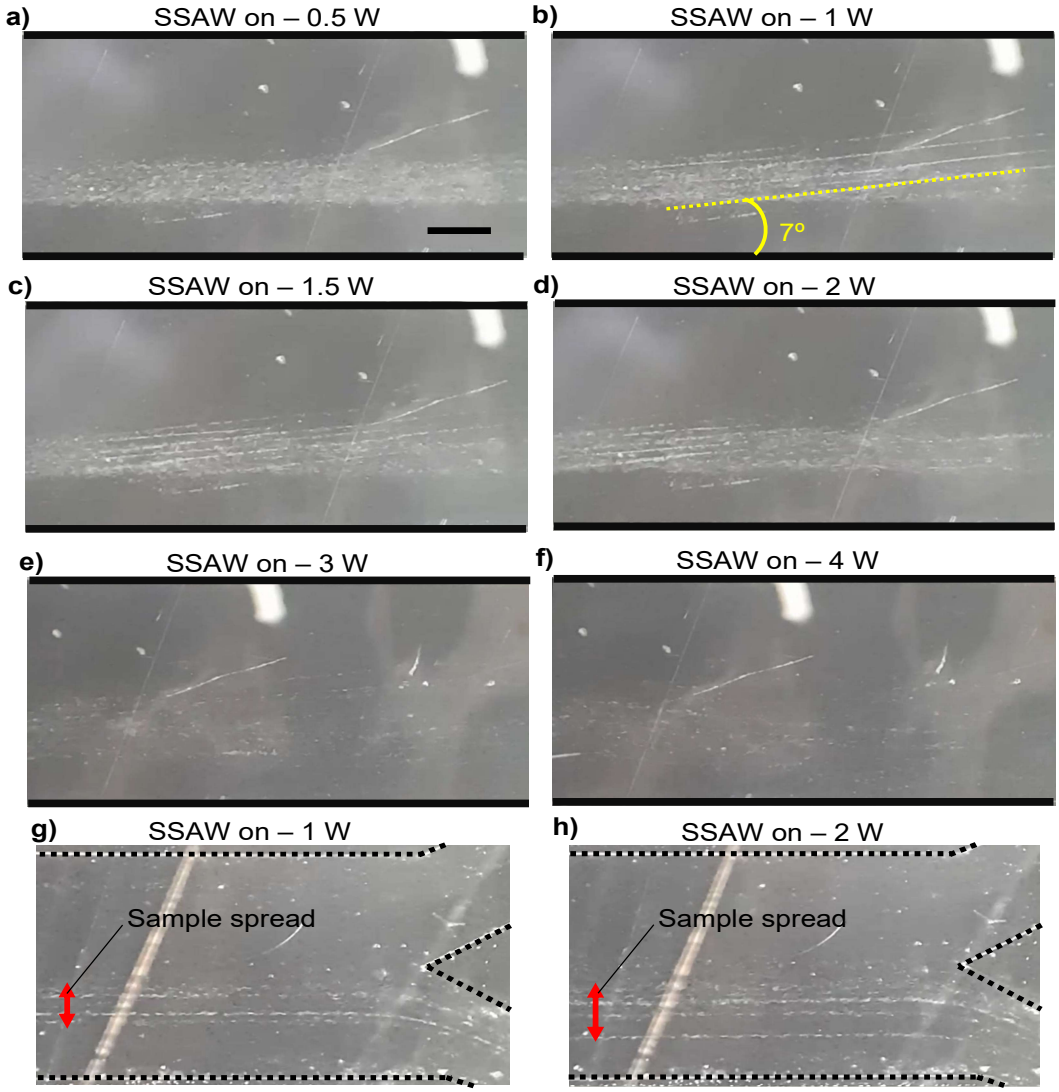

Figure 6.11. 1 μm particles in the SSAW zone actuated within a 5º microchannel inclination at an input power per IDT of a) 0.5, b) 1, c) 1.5, d) 2, e) 3 and f) 4 W. The created particle traveling lines at the output zone are shown at the input power per IDT of g) 1 and h) 2 W. Scale bar is 200 μm.

While the 5º inclination didn't have any promising results the actuation was also attempted with the 15º inclination, shown in Figs. 6.12. Fig. 6.12a, 6.12b, 6.12c, 6.12d, 6.12e, 6.12f and 6.12g illustrate the actuation of 1 μm particles at the SSAW zone under the input power of 1.5, 2, 2.5, 3, 3.5, 4 and 5W. As can be seen from the figure, while the actuated power was increased (to compensate for the more aggressive transition angle) the effects observed at the 5º inclination are also present here. Particles start forming traveling lines/ paths at 2.5 W which again start to degrade as the power keeps increasing. One can argue here the increased sheath flow rate tests should also be performed, but there was no point of doing this since the increased flowrate is only applicable when the actuation efficiency is aimed to be improved. If a relatively high

actuation efficiency cannot be achieved (>90%) at the default flow rate it will certainly will not be achieved at a higher sheath flow rate.

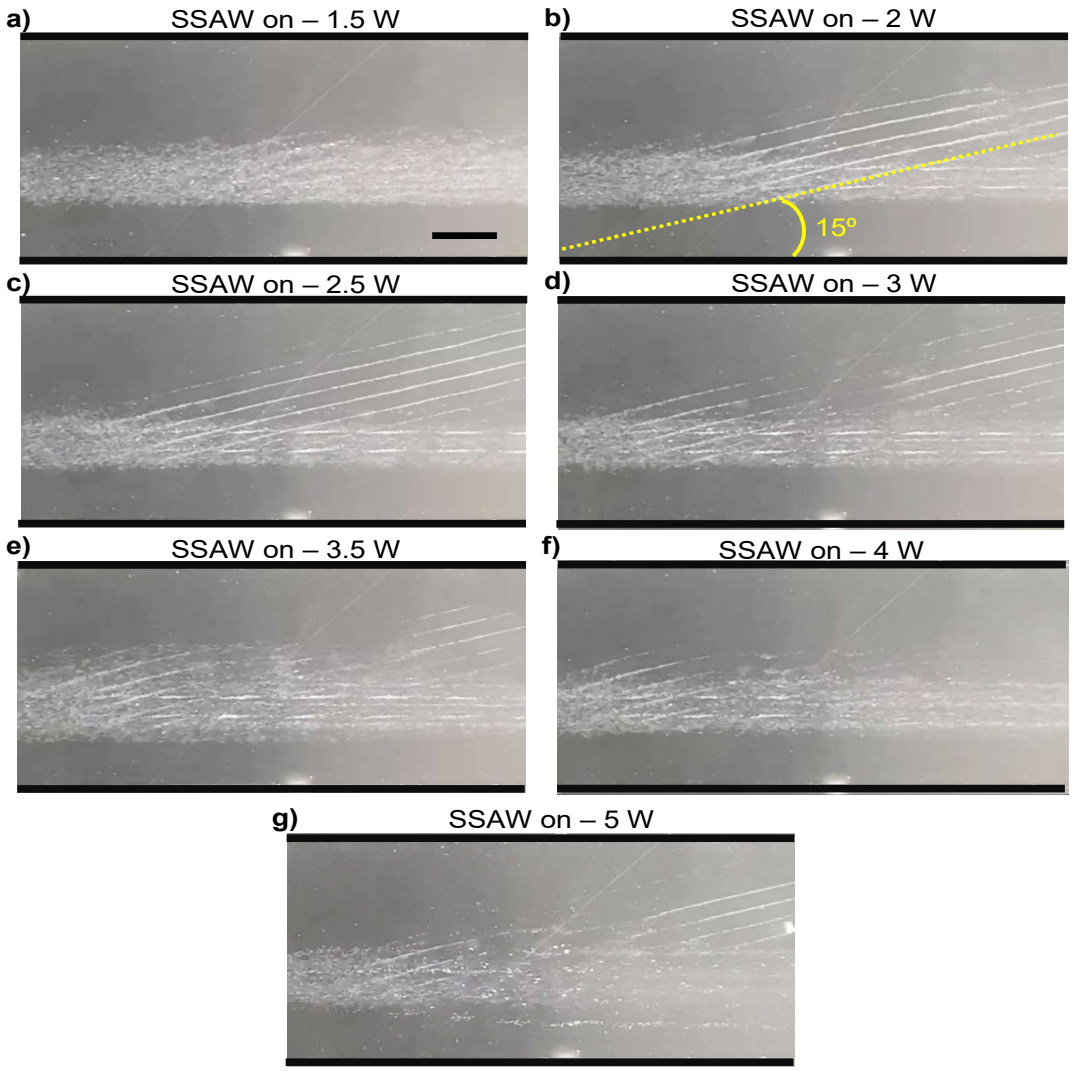

Figure 6.12. 1 µm particles in the SSAW zone actuated at a 15º microchannel inclination with an input power per IDT of a) 1.5, b) 2, c) 2.5, d) 3, e) 3.5, f) 4 and g) 5 W. Scale bar is 200 µm.

It should be noted that the actuation efficiency of the 1 µm cannot be characterised using the methodology used for the 5 µm particles. The reason is that while at the waste region some lines are being formed, most of the particles are spread across the channel at the output region. This makes the signal, i.e. illuminance, at the output region very weak and almost impossible to detect with the current methodology, especially with particles as small 1 µm. To illustrate this concept Fig. 6.13 is presented where its videos settings were edited to attempt to improve the signal quality. Figs. 6.13a and 6.13c demonstrated the actuation of the particles in the edited videos in the 5º inclined microchannel when the SSAW is off and on, respectively. While Figs. 6.13b and 6.13d demonstrate the

actuation of particles in the edited videos in the 15º inclined microchannel when the SSAW is off and on, respectively. The illuminance graph demonstrate the resulting illuminance profile pre and after editing for the 5º and 15º inclination, shown in Figs. 6.13e and 6.13f, respectively.

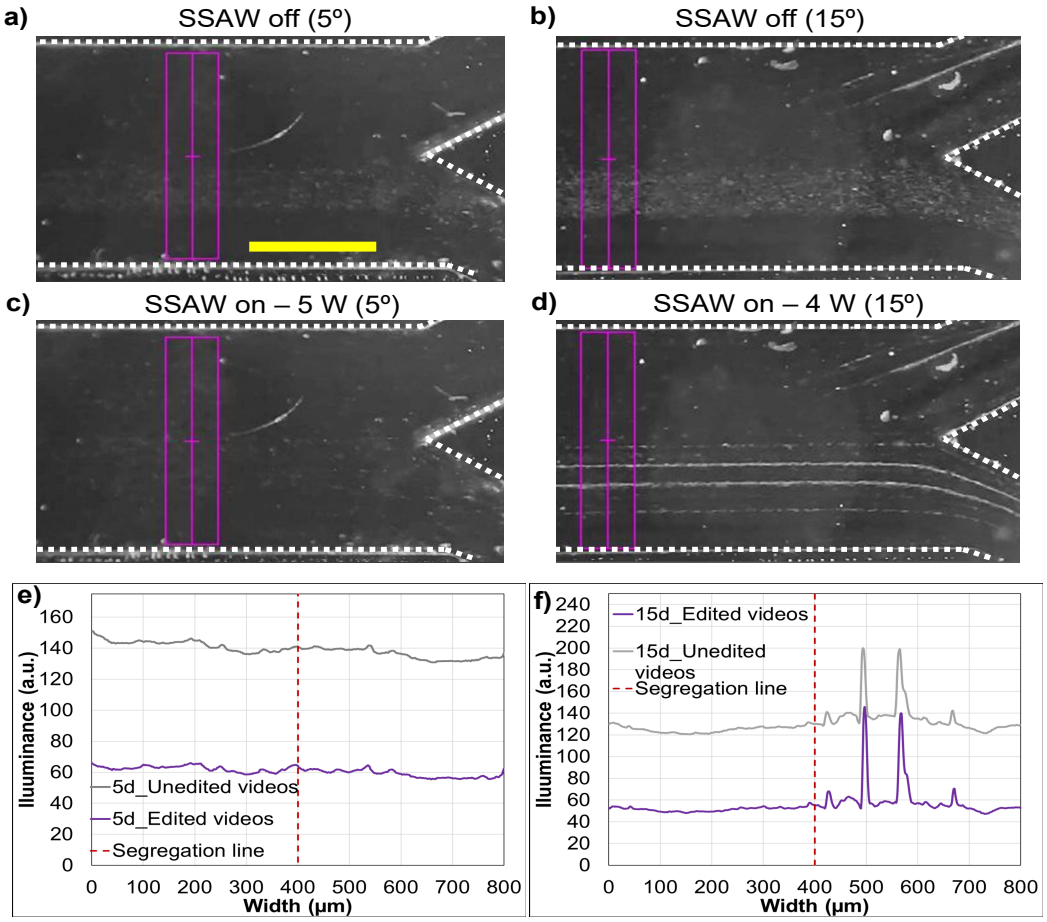

Figure 6.13. 1 µm particles actuation at the output region with edited videos, with the SSAW off at a) 5º and b) 15º inclination, and on with c) 5 W per IDT and d) 4 W per IDT. The illuminance profiles of the e) 5º and f) 15º inclination with the resulting signal from both the edited and unedited videos. Scale bar is 200 µm.

From the above, it can be observed that the signal is very weak, and the editing does not eliminate the noise completely. In the case of the 5º actuation it is almost impossible to separate the noise from the signal, reliably. But on the 15º actuation some traveling lines become apparent, as such one could then argue the methodology developed for the 5 µm particles could be applied here. But unfortunately, while this setup pickups the traveling lines, it is unable to pick up the particles that have been spread out. This is confirmed by the preliminary data that the author has on the actuation of sub-micron fluorescence particles in Appendix 5. There it is clearly illustrated why for sub-micron particles a fluorescence observation is required, which is mostly due to the spreading of

the particles but as well as the weak signal they generate. These results were chosen to be included in the appendix due to the slightly different setups used as well as due to a 9-month gap, due to Covid 19, between the results obtained in this section and the ones in the appendix.

6.4. Conclusion/ Discussion

In this section the observation and results of the above results will be quickly discussed to provide a summary of the achieved results and observed particles behaviour. As well as the advantages and limitation of the illuminance based analysis method.

6.4.1. Advantages and limitations of illuminance based analysis method

The methodology used in chapter to characterise the actuation performance of the device has the great advantage of observing the behaviour of the channel directly inside the channel. As has been shown with the 5 μm particles this allows the user to identify the behaviour of the particles and troubleshoot any identified issues to improve their actuation efficiency. Having the ability to observe particles allows the observation of elements such as single flowing particles and then gives the user the opportunity to eliminate their appearance. Additionally, this methodology allows to observe how different size of particles behave under the SSAW as was shown with 5 μm and 1 μm.

But while this methodology offers some advantages it also has a lot of limitations. As it was shown it relies on particles on forming streaming lines and creating lines that can be easily observed and the particles having a sufficiently strong signal to pick up. For larger particles (5 μm and above) this is not an issue since even single particles can be observed, if the magnification is sufficiently large. But for particles smaller than 5 μm, this methodology becomes unusable for both the actuation efficiency and the detection of SF due their spread and the low signal they generate. Thought it should be noted, that if fluorescent particles are used this issue could be easily resolved, as is shown in Appendix 5. But even then, only the overall actuation efficiency will be able to be characterised, since the detection of SF particle becomes unrealistic at that size. But even with the fluorescence particles, the setup needs to be carefully designed to eliminate any background noise since that will affect the reliability of the technique, see Appendix 5. The current methodology also relies on the frame rate of the camera to detect SF particles, as such a at higher flowrate in may be impossible to detect the particles if the framerate is not sufficiently high. If a mixed particles sample is used to study the efficiency of the device one would have to inevitable use different fluorescent particles in order to be able to study their separation efficiency. Since the current setup can only offer an insight on the actuation efficiency of homogenous samples, which might not translate well in mixed sample population where interparticle relationship are introduced, such as particles clashing. Finally, this technique should also be compared

with conventional analysis methods, i.e. output sample analysis, to see how accurately it reflects the actual actuation efficiency that was observed. The author doesn't believe that there would be any dissimilarities between the methodologies, but this should be confirmed.

6.4.2. 5 and 1 μm particle actuation performance and behaviour

Herein, the 5 μm particle these tests have demonstrated that that the default device setup can achieve an almost perfect actuation efficiency (~96%) of the 5 μm at both angles. But it was shown that at higher power the particles tend to be pushed against the microchannel side walls which could result with potential sample loss, especially in the case of the 15º inclination. Additionally, with the default flowrates occasional SF particles would not be actuated towards the collection output, reducing the devices actuation efficiency, and also potentially for cells this could damage their viability. To remedy these issues various flowrates for the sheaths were tested with the IDTs being actuated at 5 W. This resulted with the 5º inclination travelling lines being completely shifted away from the side walls, at the sheath flowrate of 4.2 μL/min while still achieving 93% actuation efficiency for SF particles. Unfortunately, the results were not as promising in the 15º actuation where the increase of flowrate, while managing to reduce the trapping of particles at the side walls, resulted with actuation efficiency starting to immediately drop. This in turn, potentially hints on the importance of having a methodology that allows the reconfiguration of a device, in order to experimentally study and optimise a device's actuation capabilities.

While the actuation efficiency of the 1 μm particles cannot be characterised, using the current videos and particles, their behaviour can be discussed since sub-micron particles in Appendix 5 have also demonstrated a similar behaviour. The author speculates that this different behaviour of 1 μm particles, compared to the 5 μm ones, is a result of 1 μm particles being more susceptible to the acoustic drag force (Nama et al., 2015). It has been observed that at higher powers the 1 μm particles actuation starts to become dominated by the acoustic drag force. As such instead of being aligned onto the traveling lines, they are more prone to be carried by the streaming vortexes created by liquid medium. A major question is why this effect is magnified at higher powers, since it was observed that at lower power some traveling lines are being formed. The author speculates that some secondary effects increase the acoustic drag force at higher powers, which in the author's opinion is the combination of the PDMS roof vibrating and the translation of particles in the Z axis, i.e. upwards and closer to the PDMS roof.

For the first effect, it is possible that the PDMS roof is vibrating and as such the power increase also increases this vibration, resulting in increased acoustic drag force and spreading of particles. The second effect that possibly takes place, is the hypothesis of the translation of particles in Z axis, where with the increase in the input power the

particles also translate upwards closer to the roof. It should be noted that it has been observed that at higher powers larger particles gets sometimes stuck at the top of the microchannel, making this theory very plausible. If then this translation is occurring it would result with particles being closer to the roof of the microchannel, which could either stop or slow their translation across the channel due to friction. But if the roof also experiences an effect similar to the wall induced vibrations of side walls, i.e. it is vibrating, this could also be a factor resulting in the spreading of the particles. Most likely, a combination of these two factors takes place, where particles are translated upwards, closer to the PDMS roof, and thus become more susceptible to roof vibrations.

It should be noted that 1 μm particles can be effectively actuated by introducing a hybrid PDMS microchannel, i.e. a microchannel incorporating a glass roof in the PDMS microchannel. The author has performed some preliminary tests using this setup, see Appendix 6, where the spreading of the particles was drastically reduced and the 1 μm particles started to behave similarly to the 5 μm particles. But while these tests showed that the actuation of 1 μm particles is possible it did not clarify, if the spreading of the particles was due to the PDMS roof vibrating, their translation in the Z axis or the combination of the two. Since the glass roof tackles both of these issues, by creating a surface where the particles could not adhere to and it eliminated the elastic property of the PDMS roof, i.e. its vibration. As such more tests are required in order to decouple these effects and clearly state what effect or if both have to be mitigated for the effective manipulation of particles that fall on the critical diameter of the device or below it.

One could also then ask why the 5 μm particles do not experience the same effect? The simplest answer is that they are above the critical size limit and the acoustic radiation force compensates for any detrimental effects. Tus, they experience a higher acoustic radiation force and are less susceptible to the acoustic drag force or/ and roof vibrations. While for any detrimental effects revolving around their upwards translation the simplest answer is that they do translate, but due to their size this effect is vastly mitigated. One mitigation is via the acoustic radiation force which compensates for any detrimental effects that the roof of the microchannel may create, such as friction. The second could be that due to their size 5 μm particles cannot be as effectively translated upwards as the 1 μm, as such even at higher powers they remain far enough from the roof to experience any of the aforementioned effects. But this is unlikely due the particles being observed to occasionally be stuck on the roof of the microchannel. Nonetheless, the above observations are the author’s speculations, and more experiments are needed in order to reach any concrete conclusion.

6.4.3. Conclusion

In this chapter a hFPCB-SAW device was developed for the application of studying particle actuation and proving its potential to be applied for separation applications. This

device implemented flow, cooling and different tilt angle actuations, which illustrated that the PCB fabrication method can be utilised to build a fully functional SAW device for actuating particles from one output to another. Furthermore, the hFPCB-SAW device was utilised to study the actuation of 5 μm by observing and analysing their distribution inside the microchannel at different actuation angles, where without any modifications the device was able to achieve actuation efficiencies of ~96% for both 5º and 15º microchannel inclination. The observation of the particle distribution allowed to study their behaviour inside the channel and identify different issues, such as SF particles and particles being trapped against the microchannel wall at the SAW zone. Which were then remedied and were able to be successfully used to improve the 5 μm actuation efficiency in the 5º actuation. While the hFPCB-SAW device was also utilised for 1 μm particle actuation, it was quickly observed that with the current setup it was not possible to achieve it yet due to their actuation behaviour being different to that of 5 μm particles. Additionally, the current analysis method is not suitable for particles as small as 1 μm due to them spreading out across the microchannel and not generating a sufficiently strong signal. But it was also stated that the analysis method could be used if fluorescence particles were used instead. The cause of the spreading of the 1 μm particles is speculated to be due to either the acoustic drag force becoming dominant (i.e. the device reached its critical particle diameter) or that the particles where translated upwards and were affected by the roof of the microchannel. But to confirm which of the above stands true more tests are required to be made, as such the actual cause of this remains inconclusive. Regardless, the hFPCB-SAW device was successfully utilised to study the actuation of particles and was used to optimise the actuation of 5 μm particles.

Thus, demonstrating that this device, if further developed, could not only be used to study the actuation of particles but also achieve a setup that could be used for biological separation applications. Since the actuation of 5 μm particles was achieved here it can be speculated that cells larger than the 5 μm particles (>10 μm) could be actuated using this device. But due to the variability of cells and the higher power required to actuate cells (see Appendix 2), as well as different fluidic mediums that could be used, the actuation efficiency of these cells would have to be confirmed. Nonetheless, the 5 μm particle actuation has highlighted some the potential issues that may appear during the cells actuation and how these challenges may be tackled. While for smaller particles actuation, 1 μm particles, it was observed that their actuation via acoustic radiation force is not yet possible to achieve. But it was highlighted that a hybrid PDMS channel could overcome this limitation. But most importantly this demonstrates that it is very important to have a setup that can be reconfigured to study the different actuations that can be achieved. With the PCB based methodology and the developed microchannel bonding method, it is then possible to be able to swap IDTs with IDTs of different frequencies or

design, change the microchannel or IDT orientation, change the microchannel design and change piezoelectric substrate to study experimentally the effects of these variables on the actuation of various particles or cells quickly and easily. Thus, enabling the user to be able to tailor a SAW device for a specific application without the need of remanufacturing.

Chapter 7

Conclusions and Future Work

7.1. Conclusion

In this thesis, the field of acoustofluidics was introduced as well as the founding principles and working mechanism of the acoustofluidic devices. The prime focus of this thesis was on the actuation capabilities of acoustofluidics devices and demonstrating, via literature review, their capability to be applied to various biomedical applications. It was also shown that SAW devices are very commonly seen in these applications. But while SAW devices are very prominent their manufacturing technique requires high end facilities and as such is not widely accessible. As well as once manufactured, the devices were non-modifiable, thus limiting the possible experimentation with these devices. As such herein a new fabrication technique that utilised PCBs based IDTs to create SAW devices, where a clamping system was used to push the IDTs onto a piezoelectric substrate. The aim of this technique was to make the SAW devices more accessible and reconfigurable, to create a technique suitable for prototyping purposes and research and development.

This thesis then has demonstrated:

- A new fabrication technique for SAW devices using PCB based IDTs, which utilised the PCB IDTs, a piezoelectric substrate, and a simple clamping device to create a PCB-SAW device.
- The developed PCB-SAW device was characterised and demonstrated that this it could create identical acoustofluidic effects to that of the conventionally manufactured SAW device, alas less efficiently, such as streaming of particles inside a droplet, particle and biocompatible cell manipulation/ pattering in a microchannel and its capability to quickly couple with different piezoelectric substrates and generate acoustophoretic effects.
- The creation of PCB IDTs on different substrates, such as FR4 and polyester laminate, was demonstrated and it was shown that both substrates have similar electrical and acoustophoretic capabilities.
- The FPCB IDTs then were used to create an acoustofluidic device using only accessible components and introduced a new manufacturing and bonding technique for the microchannel. A methodology to align parallelly the segregated FPCB IDT chips was demonstrated, and the device (VAD) was used to align particles parallelly and at a tilt angle by rotating one of the IDTs or by placing the microchannel at different orientations.

- Finally, high frequency PCB IDTs (hFPCB IDTs) were developed to demonstrate the possibility of the manufacturing of an IDT with a 120 μm pitch. The hFPCB IDTs were then subsequently used to develop the hFPCB-SAW device to study the actuation of particles under flow conditions and different microchannel orientations. The hFPCB-SAW system was utilised to optimise the actuation efficiency of the 5 μm particles and to study the actuation behaviour of 1 μm particles.

This then creates the following key scientific contributions:

- The development of a new fabrications techniques for SAW based devices for actuation based applications, that created identical acoustofluidic effects to the conventional device.
- The capability to create a reconfigurable SAW device, which gives the capability to quickly swap piezoelectric substrates and IDTs and change the IDT and microchannel orientation, to study different acoustofluidic effects without the need of remanufacturing the device.

In summary, herein a new fabrication methodology has been demonstrated for SAW devices using PCBs. This technique has been thoroughly characterised and shown to have the same acoustofluidic capabilities as conventional devices, while also demonstrating its reconfigurable nature and capability to modify the device to study different acoustophoretic effects. Thus, providing a new and accessible method for researcher to use to develop, study and optimise SAW devices for actuation and tailor them for their applications.

7.2. Future work

While the PCB-based method has been extensively explored in this thesis, there are still certain aspects that require further investigation. Here the author would provide some the future developments that the PCB methods could undertake.

7.2.1. IDTs designs and piezoelectric substrates

The first experiment would fall under the study of exploring different IDTs design that could be manufactured and how compatible they are with the PCB based methodology. Two of these IDT designs are the FUT are slanted IDT, which could then demonstrate the capability of this methodology to work with designs beyond the conventional IDT. Additionally, while herein the capability of the PCB IDTs to couple with different substrates was demonstrated, this was only done with ZnO substrates. As such it would be very interesting to tests how well this methodology would perform with other substrates and the advantages and disadvantages of using these substrates with the PCB methodology. This fabrication method could then also be used to create SH-SAW

and demonstrate the techniques capability to be utilised for sensing applications. Finally, this methodology could also permit the development of interesting configuration such as parallel IDTs, with a conventional IDT and a FUT, to experimentally explore the resulting effects the combination of these different wave modes and IDTs.

7.2.2. FPCB IDTs and hard PCB IDTs

While herein it has been speculated that FPCB IDTs may create a more uniform than the hard (FR4 based) PCB IDTs, this has not been tested thoroughly enough. As such it would be very beneficial for this technique to create a rigorous setup and compared the two techniques to reach a solid conclusion whether there are any advantages/ disadvantages between the two substrates. The most appropriate tool for this would be a laser vibrometer, since it would be able to characterise both the deformation and uniformity of the created wave. This study could also explore the profile of the different wave modes on $LiNbO_3$ that were observed when the IDTs was being rotated, as well as the resulting SSAW during parallel and rotating configuration of the IDTs.

7.2.3. Actuation of sub-micron particles

While herein the actuation of 5 μm particles has been demonstrated it would be interesting to see this methodology to be further developed for the actuation of sub-micron particles. While some preliminary tests were shown that this could be potentially achieved using hybrid channels, this needs to be further rectified by incorporating fluorescent particles and studying the actuation of these particles. Additionally, it would be interesting to understand why the 1 μm particles are being spread out during actuation. It has been speculated that this could be due the acoustic drag force becoming dominant at higher powers due to secondary effects such roof vibrations and the translation of particles in the Z axis. The way to decouple these two effects would be to create microchannels that have different channel heights. By implementation these microchannels and studying how the particles behave in them, it would clearly state if the microchannel roof and their upwards translation has any effect on them spreading out. Thus, helping researchers to understand and tackle the difficulties that arise at sub-micron actuations.

7.2.1. Separation studies of particles

While a device here has been implemented to study the actuation of homogenous particles, separation has not yet been demonstrated. As such by using particles above the critical diameter and characterising their actuation, one could then use these results to create a separation experiment. Additionally, it would be very interesting to see if the illuminance actuation efficiency could be developed into an automated program to study actuation of these particles more precisely, and to also have this technique compared with conventional analysis methods, i.e. output sample analysis, to see how accurately it reflects the actual actuation efficiency that was observed. As well as incorporating

different fluorescence particles to characterise the devices separation efficiency using the illuminance based analysis method.

Appendix

Appendix 1: Google Scholar keyword search methodology

In chapter 1, section 1.4.6, Fig. 1.13 and 1.14 represent publication data that was obtain from Google Scholar. For text clarity these figures included short abbreviation of the key search terms where necessary. To provide the full context of these search terms Table A1 is presented to establish the exact search terms that were used for each represented term.

Table A1. The table provides the key terms that are presented in the text for the publication number results in Figs. 1.13 and 1.14, and their corresponding exact search terms in the search engine.

Presented term	Exact search term
Cell sorting	“Cell sorting”
Cell stimulation	“Cell stimulation”
Cell transfection	“Cell transfection”
Cell manipulation	“Cell manipulation”
Cell patterning	“Cell patterning”
Concentrating cells	“Concentrating cells”
Microfluidics	("microfluidic" OR "microfluidics")
Acoustofluidics	("acoustofluidic" OR "acoustofluidics" OR "acoustophoresis" OR "acoustophoretic")

It should be noted that double quotations were used (“”) to ensure that the specific terms were found within the text. The “OR” argument is used to find either one of the specific terms used within a text. While the parentheses are used to specify another list of arguments for the search engine. For example, when “cell sorting” AND “microfluidics” is specified in the text, in the search engine this was written as: “Cell sorting” AND ("microfluidic" OR "microfluidics"). This then would require the search engine to find the term “cell sorting” and either the term “microfluidic” or “microfluidics” within the text to produce the link within the search results.

It should be also noted that the results numbers will depend on the internet connection speed and date of when the data were taken. To mitigate this to an extent, the author chose the dates 2023 as the cut-off, to ensure any new publications aren’t added and reduce the number variability. But a small variation may still be present when the same

kay terms are searched. As such the author must specify that the above terms were searched on the 07/04/2024, and some variation in the numbers may be present if attempted to replicate.

Appendix 2: Acoustofluidic properties of cells and polystyrene particles

The main parameters that are required to determine the acoustic properties of particles or cells, or more specifically their contrast factor, is their density and compressibility and that of the fluid they are actuated within. Thankfully, polystyrene particles seem to have a relatively consistent density and compressibility, with their average density and compressibility being 1050 kg/m^3 and 2.16 TPa^{-1}, respectively (Hartono et al., 2011). On the other hand, cells are more diverse, with various cancer cells such as MCF-7, HEPG2 and HT-29 having different densities, compressibility and size. Table A2 is created to quickly summarise these properties, indicating the mean size of the cells, density and compressibility. Table A2, also presents the calculated acoustic contrast factor of these cells in water, which was calculated using eq. 22 with the water properties used from the study by Nama et al., (2015). The MCF-7, HEPG2 and HT-29 compressibility and diameter taken from Hartono et al., (2011), while the MCF-7 diameter was taken from (Yang et al., 2016). The HEPG2 average diameter was calculated from the range provided by Arzumanian, et al., (2021) and the HT-29 was taken from Tahara et al., (2013).

Table A2. Size, density and compressibility polystyrene particles and various cancer cells. The water density and compressibility used to calculate the acoustic contrast factor is 997 kg/m^3 and 448 TPa^{-1} at 25 ^{o}C *(Nama et al., 2015)*.

Name	Diameter (μm)	Density (kg/m^3)	Compressibility (TPa^{-1})	Contrast factor in water
Polystyrene particles	5	1050	216 ± 0.18	0.19
MCF-7 Breast cancer cells	17.3 ± 1.0	1068	422 ±0.19	0.02
HEPG2 Liver cancer cells	15.5 (12-19)	1087	428 ±0.12	0.02
HT-29 colon cancer cell	16.6 ± 0.17	1077	402 ±0.16	0.06

A perhaps interesting fact is that most of the cells have a similarly small contrast factor despite their size, and that the polystyrene particles have an almost 10x larger acoustic contrast factor than some of the cancer cells. This begs the question if polystyrene particles can be representative of the cell's actuation. Fortunately, the acoustic contrast factor doesn't take in account the diameter of the particle used. As such if the particles and cells are aligned using the same microchannel and setup, then the ratio of acoustic

pressure that certain cells would need to experience in comparison to polystyrene particles in dissimilar fluids can be determined. This ratio can be calculated by ratioing the acoustic radiation force of the cells and particles:

$$r = \frac{F_{R\_cell}}{F_{R\_PP}} \tag{33}$$

$$r_p = \frac{p_{a_{cell}}}{p_{a_{PP}}} = \sqrt{\frac{\Phi_{\text{cell}} a_{cell}^3}{\Phi_{\text{PP}} a_{PP}^3} \frac{\rho_{01} c_{01}^2}{\rho_{02} c_{02}^2}} \tag{34}$$

with F_{R_cell} and F_{R_PP} being the acoustic radiation force of cells (N) and polystyrene particles (N). The above equation also assumes that both the particles and cells are also utilising different fluidic mediums. As such to find the ratio of the acoustic pressures (r_p) would require the following terms to be obtained: a_{PP}, a_{cell}, κ_{PP}, κ_{cell}, κ_{o1}, κ_{o2}, ρ_{PP}, ρ_{cell}, , ρ_{o1}, ρ_{o2}, c_{o1} and c_{o2}, which are the radius of the particles and cells (m), the compressibility of particles (Pa^{-1}), cells (Pa^{-1}), particle fluidic medium (Pa^{-1}) and cells fluidic medium (Pa^{-1}), density of particles (kg/m^3), cells (kg/m^3), particle fluidic medium (kg/m^3) and cell fluidic medium (kg/m^3) and speed of sound of particle fluidic medium (m/s) and cell fluidic medium (m/s). As one can observe, a plethora of information of the properties of both particles, cells and fluidic mediums would be required. But if the mediums are the same the equation can be simplified to:

$$r_p = \frac{p_{a_{cell}}}{p_{a_{PP}}} = \sqrt{\frac{\Phi_{\text{cell}} a_{cell}^3}{\Phi_{PP} a_{PP}^3}} \tag{35}$$

Which would then remove the requirement of the speed of sound property of the secondary fluid and would require only to know the density and compressibility of the fluid used. Using eq. 35 then the acoustic pressure ratio of that various cells would experience compared for polystyrene particles can be deciphered. If 10 μm particles are assumed to be used, and to have similar density and compressibility with 5 μm particles, and both cells and particles are actuated in water then the ratios would be 1.07, 0.92 and 1.2 for MCF-7, HEPG2 and HT-29, respectively. But it should be clearly stated that is not known how the acoustic pressure scales with the resulting actuation of particles. As an example, if particle A and B have a ratio of 2, would that mean that the particle B would need 2x the time to align at the pressure nodes, 3x or more, and how would that be reflected on the input power? This equation also doesn't consider the morphology of the cells, which may also create complications in the actuation performance. Additionally in reality, the cancer cells would always require more power to be actuated than 10 μm than particles. In a study Ding *et al.*, (2014) actuated both 10 μm particles and MCF-7 cells, and with simulation results the 10 μm particles required drastically different input powers to actuate. This then also suggests that eq. 35 is a very crude equation and doesn't consider the various complexities that may arise during cell actuation, in a way that simulation can. This also demonstrates that it is not very simple to obtain and

compare the actuation of cells and particles and a lot of thought and a careful experimental setup need to be designed for this purpose. But the example of this study also suggests that if the actuation of 10 μm particles is possible, it would also be possible to actuate larger cells such as MCF-7. Therefore, also making it possible to actuate cells such as HEPG2 and HT-29, and possibly cells with similar contrast factor and/ or size.

Appendix 3: PCB IDT design guidelines

While numerous have IDTs been designed in the field of acoustofluidics, it is noteworthy that comprehensive guidelines for the IDT design for acoustofluidics is not provided. Therefore, here the author aims to fill this gap by providing a set of guidelines that researchers could use when designing an IDT, specifically a PCB IDT.

IDE length

To design an optimal IDE length, first the trade-off between a longer and shorter length should be understood, as well as the applications it will be used for. For separation based applications, the biggest factor to consider is the area of the acoustic zone (Li et al., 2015), where a smaller area would result with a larger acoustic force. The smaller the IDE length the denser the acoustic energy will be. This can also be achieved by reducing the distance between two IDTs, which also results with a higher acoustic energy. If it is assumed that a shorter IDE length has a similar effect, then one should most definitely strive for the shorter length. But the length cannot be infinitely small, since if it is too small it may create an acoustic beam similar to a FUT which could create high streaming effects that could disrupt the laminar flow (Destgeer *et al.*, 2013; Collins *et al.*, 2016). To obtain a realistic length one can study past devices that demonstrated promising actuation results. By observing the FUT design by Destgeer *et al.*, (2014), it can be seen that an IDE length of ~400 μm can be used to effectively actuate particles, while creating a smooth trajectory of 200 μm across the channel. Therefore, a standard IDE with an identical length could be the best possible option if the channel is not too wide. But for tilt angle configurations it would be desirable for the generated SSAW to spam from one edge of the microchannel to the other, in order to create tracks that are long enough to displace particles from one edge to another. In the case of an 800 μm wide microchannel for a 5º and 15º inclination the required IDE length would be 803 and 828 μm, respectively. But practically, for PCB IDEs the minimal IDE length would have to be between 1 and 2 mm, to allow the creation of a localised pressers. While for applications such as cell stimulation or patterning the IDEs length is typically designed to cover the ROI of the microchannel where the particles will be simulated or patterned, but at the cost of acoustic energy density.

Bus pads width, length and bus-IDE gap

The bus pads tend to be much larger than the IDEs, which is often done under the impression that because the bus pad will be hosting the electrical power a greater area will avoid excessive heating effects. But in practice the IDTs do not appear to heat up that much and this still does not inform the designer on how big the bus pads should be. A more practical way of viewing this is that the bus pads should be large enough to avoid potential physical damage that would cause a broken section to disconnect a series of IDEs. In our group a 5 mm bus pad width is typically utilised, which is also sufficiently

large to host any wires or connectors during soldering. But this design can be altered to have the bus pad lines to be 2.5 mm with 5 mm circular end points. Thus, reducing the amount of metal used and the overall width of the bus pad.

The length of the bus pads on a hard (FR4) PCB should be at least 30 mm for a 3-inch wafer to keep the wire connectors away from the IDE region and to give the user enough leeway during the soldering of the connectors. But if the FPCB IDTs are utilized the bus pads length can be reduced and can be changed to the total width of the IDE region plus 15 mm, due to the ability of the FPCBs to bend and as such the underside hosting the wires can be bended and lifted upwards. Finally, the bus-IDE gap can be designed to be identical size of the IDE width, but if the designer wants to have more spacing between them (if potentially manufacturing issue arise) they can increase it by making it be equal to the pitch size.

IDEs pair number

The IDE pairs numbers on the PCB IDTs used in this thesis are 40, which gives an IDTs operating at 20 MHz a 1 MHz bandwidth. Typically, this bandwidth is more than enough, but under extreme conditions, for example where the temperature changes drastically (Sun et al., 2021), the designer might was to consider doubling the number of pairs. This will ensure that even if the operating frequency shifts the device will remain operational, but for normal applications the user can safely use 40 pairs (i.e. 80 fingers). But it should be stated while more fingers may result with a bigger bandwidth, this has not been experimentally confirmed by our group.

Appendix 4: Matching network (MN) design procedure

While the MN design procedure might appear straightforward, in actuality it involves a lot of trial and errors as well as pitfalls in regard to designing an appropriate MN. As such here a detailed guideline of how to properly design a MN for a PCB IDT is provided using the hFPCB IDTs as the example. To start off, it is most important to select the electrical components with parameters suitable for the application. While most ceramic capacitors are capable of handling high-power inputs, this is not the case for all inductors. Standard inductors will typically only remain functional at 0.1 W, which is a power input that is greatly exceeded for actuation based SAW applications. As such surface mount (SMD) power inductors are typically used when developing a MN such as SRP5020C-R33M SMDs (Farnell UK), which is used for the hFPCB IDTs MNs.

With the appropriate components, the actual design and fabrication of a MN for PCB IDTs consists mostly of trial and error. The first step is to obtain the impedance values at the operating frequency, which can be done using a VNA. These values then can be used to find the required capacitance and inductance MN values and the required layout via the use of either mathematical equations or an online source (http://leleivre.com/rf_lcmatch.html). Typically, the layout will be with either the capacitor in the main line and inductors connected to the ground, as shown in Fig. A4.1a, or the inverse, shown in in Fig. A4.1b. Additionally, the exact theoretical values will not match the available market values of capacitors and inductors, as such the layout can be selected on the available component values. The inductors and capacitors can also be set in either parallel or series to either reduce or increase their value. Additionally, a PCB breadboard can be used to assemble and connect the MN to the PCB IDTs to check which values will create an appropriate S_{11} drop (usually below -20 dB).

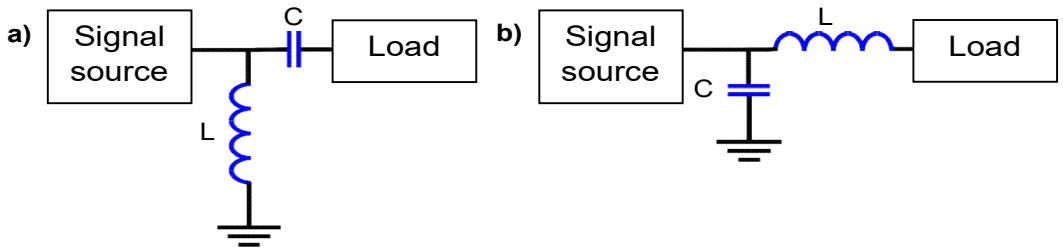

Figure A4.1. Different MN setups with a) illustrating a LC setup and b) a CL, where L and C refer to inductance and capacitance.

As an example, the S_{11} drop with no MN in Fig. 3.11b gives an impedance value of 26.96 – i67.974 Ω at 33 MHz. Using these values, the MNs values can be calculated and the layout based on these values can be selected. For the hPCB IDTs the inductor on the main line and capacitor to the ground gave the best values, i.e. values that were close to component values available in the market, with the values being 448 nH and 89.17 pF

for the inductor and capacitor, respectively. A series inductor setup was created to have a value of 430 nH (100 + 330) and a capacitor with the value of 100 pF was selected, but when assembled the resulting MN did not give the desired S_{11} drop and as such the values of the capacitor and inductors were tweaked up and down until the desired drop was achieved. Commonly this tweaking will be within the range of ± 100 nH and ± 50 pF from the theoretical values. For the case of the hFPCB IDTs the resulting values are 330 nH and 110 pF for the inductor and capacitor, respectively, giving the S_{11} drop shown in Fig. 3.11b.

It should also be stated that care should be taken on where S_{11} drop sits on the frequency spectrum, since certain MN values can give a very good S_{11} drop that is far away from the operating frequency. This concept is demonstrated in Fig. A4.2 where a MN is implemented (470 nH, 220 pF) that results in a very good S_{11} drop but an operating frequency far from the optimal frequency. If this new frequency is used the device will create little to no actuation and it will result with the MN components heating up very fast. As such the optimal frequency should always be referred to when designing a MN. But the frequency range should also be kept in mind, since most of the time the operational frequency will not perfectly match the one with MN. This is demonstrated by the second MN (330 nH, 100 pF) on the figure, which has an operation frequency that does not fall spot on the optimal frequency but is still within the operating range. While this MN is less optimal than the one used in the tests (330 nH, 110 pF), it still can be considered as an acceptable MN to use for the operation of a hFPCB-SAW device.

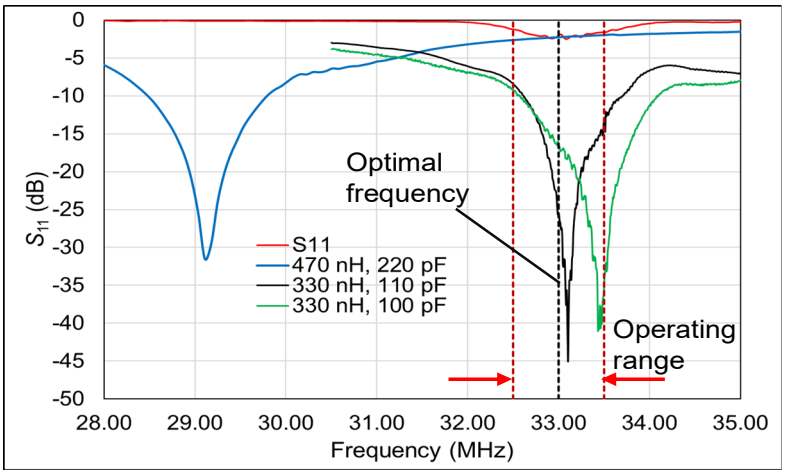

Figure A4.2. S_{11} reading of hFPCB IDTs with no MN and with three different MN designs. These designs illustrate a MN that is out of spec (470nH, 220 pF), close to the optimal frequency (330 nH, 110 pF) and within the operational range MN (330 nH, 100 pF).

Appendix 5: Fluorescent sub-micron particle actuation

In this section the author would provide the data that he had obtained during his EPRSC placement in IREGene, China, which was abruptly cut due to Covid19. This section was decided to be included in the appendix due to it utilising an earlier iteration of the device presented in chapter 6. Additionally, there was 9-month time lapse before these tests were able to be continued. As such to not disrupt the continuity of the main text these results are provided in the Appendix. As stated in chapter 6 the hFPCB-IDTs were initially developed to test if the PCB-method can be used to develop of actuating particles for separation applications. But additionally, it was also developed to see if it would be possible to use these higher frequency IDTs to actuate sub-micron particles. The results of these tests will be described below.

Methods and materials

The hFPCB-SAW device used in this section was identical to the one described in section 3.4. But the fluidic pumping system, cooling plate, microscope and power amplifier used in these tests were different. For the pumping system two syringe pumps were used with glass syringes (Hamilton, UK). The syringes sizes were 2.5, 2.5 and 5 mL which were used for the sample input (input 2), sheath 1 (input 1) and sheath 2 (input 3), refer figure 3.19. One of the syringe pumps was used to actuate the sample at a flowrate 2.5 µL/min, while the two sheath syringes were placed together at the second syringe pump and actuated at 2.5 µL/min. Due to the syringes volume ratio that would results with 5 mL syringe generating a flowrate of 5 µL/min. A fluorescence microscope was used with 60 fps camera to collect the videos of the particle actuation with 10x magnification lens. The cooling plate was a Chinese commercially available cooling plate with Peltier's and fans that was run at 12V and was set to keep the plate's temperature at 16 C. The power amplifiers were also purchased from the local Chinese market, which had a max amplification of ~4W and were suitable to be run up to the frequencies of 35 MHz.

The fluorescence particles used were 700 and 100 µm with green fluorescence and were mixed with DI water at a volume ratio of 1:4 (v:v). These particles were actuated by 15 s for each collected video. The collected videos were modified in a similar manner as described in section 3.4.7, where a video editing software (DaVinci Resolve, USA) was used to change the video setting to; Contrast: 1.4 (1), Pivot: 1 (0.465), Mid/ Detail: 100 (0), Col Boost: -100 (0) and Shadow: -100 (0), with the parenthesis indicating the default value.

Results

The resulting actuation of the particles is shown in Fig A5.1. In Fig. A5.1 the 100 nm particles are actuated under ~3.2 W per IDT in a 5º and 15º microchannel inclination, Fig. A5.1a and A5.1b, respectively, and the 700 nm in a 5º and 15º inclination, Fig. A5.1c

and A5.1d. respectively. From these images an interesting phenomenon is observed where the particles start to spread across both direction of the microchannel, which significantly more apparent with 5º degree actuations. Additionally, while a semblance of traveling lines can be observed, when compared to 5 µm particles actuation (see Fig. 6.2), sub-micron particles tend to be more spread out and not just stay on the travelling lines.

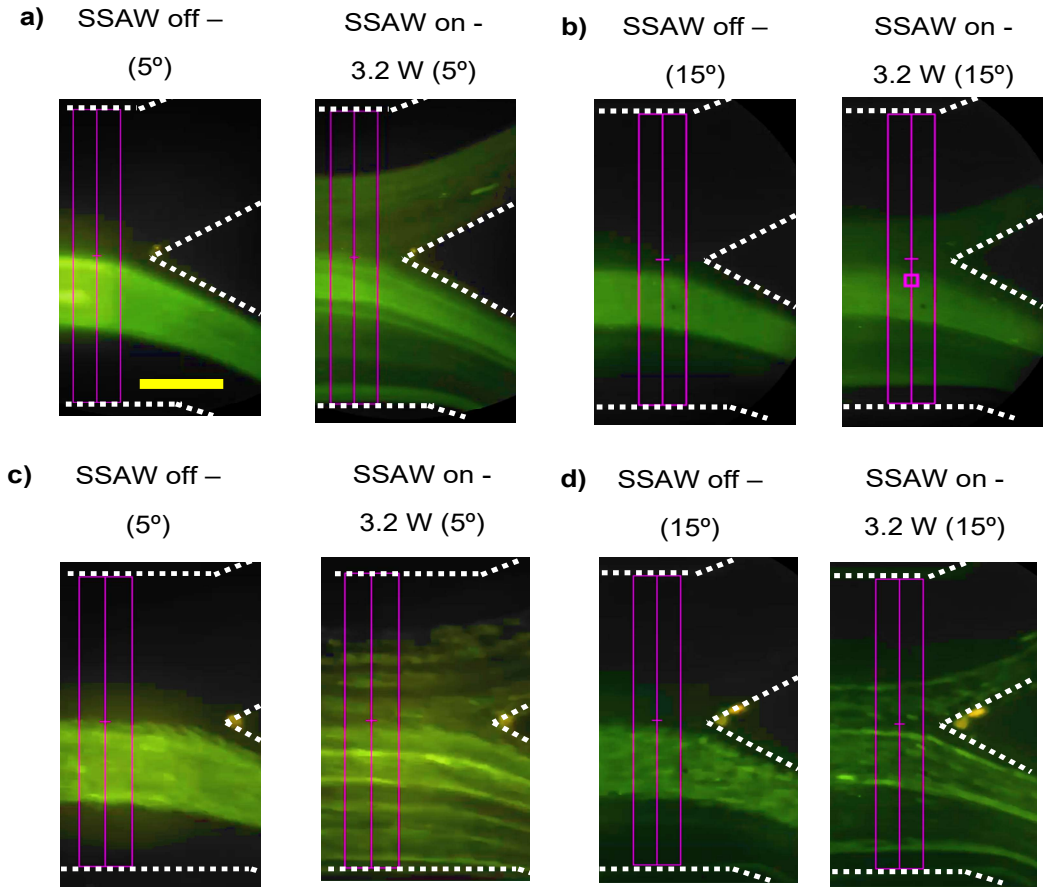

Figure A5.1. Snapshots of the sub-micron fluorescence particle actuation videos. The images demonstrate the particles distribution pre and during actuation, when the IDTs are supplied with 35 dBm (3.16 W) power per IDT. The actuation of both the 100 nm particles at a microchannel inclination of a) 5º and b) 15º and 700 nm at an inclination of c) 5º and d) 15º. Scale bar is 200 µm.

The collected videos were then used to generate the illuminance profiles of the particles' actuation at different input powers, Fig. A5.2. The actuation of 100 nm particles at different input power per IDT of 1, 2 and 3.16 W for the 5º inclination is shown in Figs. A5.2a, A5.2c and A5.2e, respectively, and 15º inclination in Figs. A5.2b, A5.2d and A5.2f, respectively. The dotted profile in the graphs shows the distribution of the particles before the SSAW was applied, and a straight segmented line is provided to illustrate the regions that lead towards the collection output (401-800 µm) and waste output (0-400 µm).

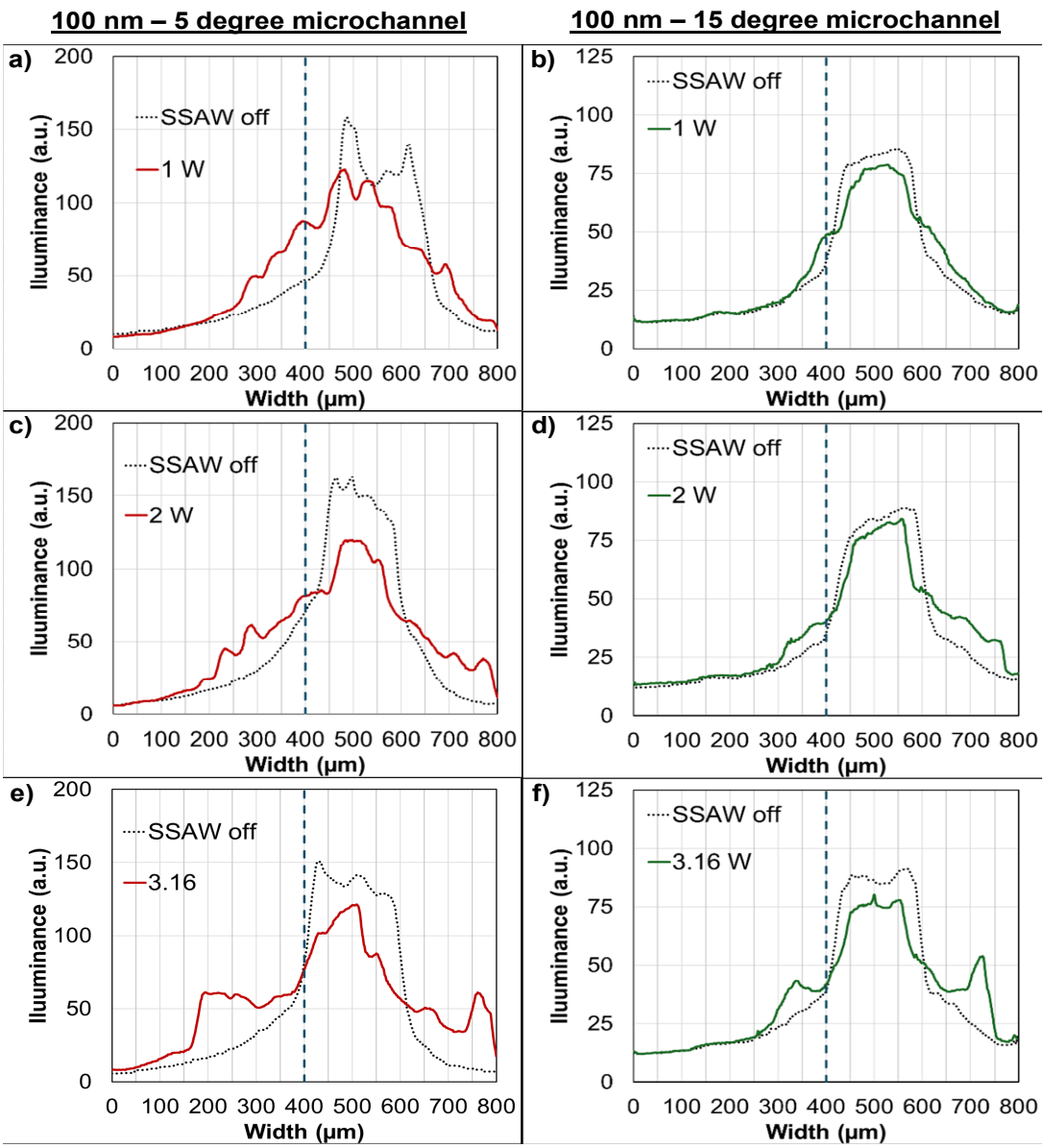

Figure A5.2. Illuminance profiles of 100 nm particle actuation at different power inputs. The figures on the left show the actuation in the 5º microchannel inclination at the input power of a) 1, c) 2 and e) 3.16 W, while the figures on the right show the actuation at the 15º inclination with the input power of b) 1, d) 2 and f) 3.16 W. The dotted profile shows the particle distribution of the particles pre actuation.

The same concept is demonstrated for the 700 nm in Fig. A5.3, with the input powers of 1, 2 and 3.16 W for the 5º inclination, Figs. A5.3a, A5.3c and A5.3e, respectively, and 15º inclination, Figs. A5.3b, A5.3d and A5.3f, respectively. From these figures it can be observed that the 5º channel results in a larger displacement of particles towards the collection output than 15º, reflecting the results also seen with 5 μm particles. But unfortunately, this larger actuation is reflected in both direction of the microchannel, again reflecting the issues observed with the 1 μm particle actuation.

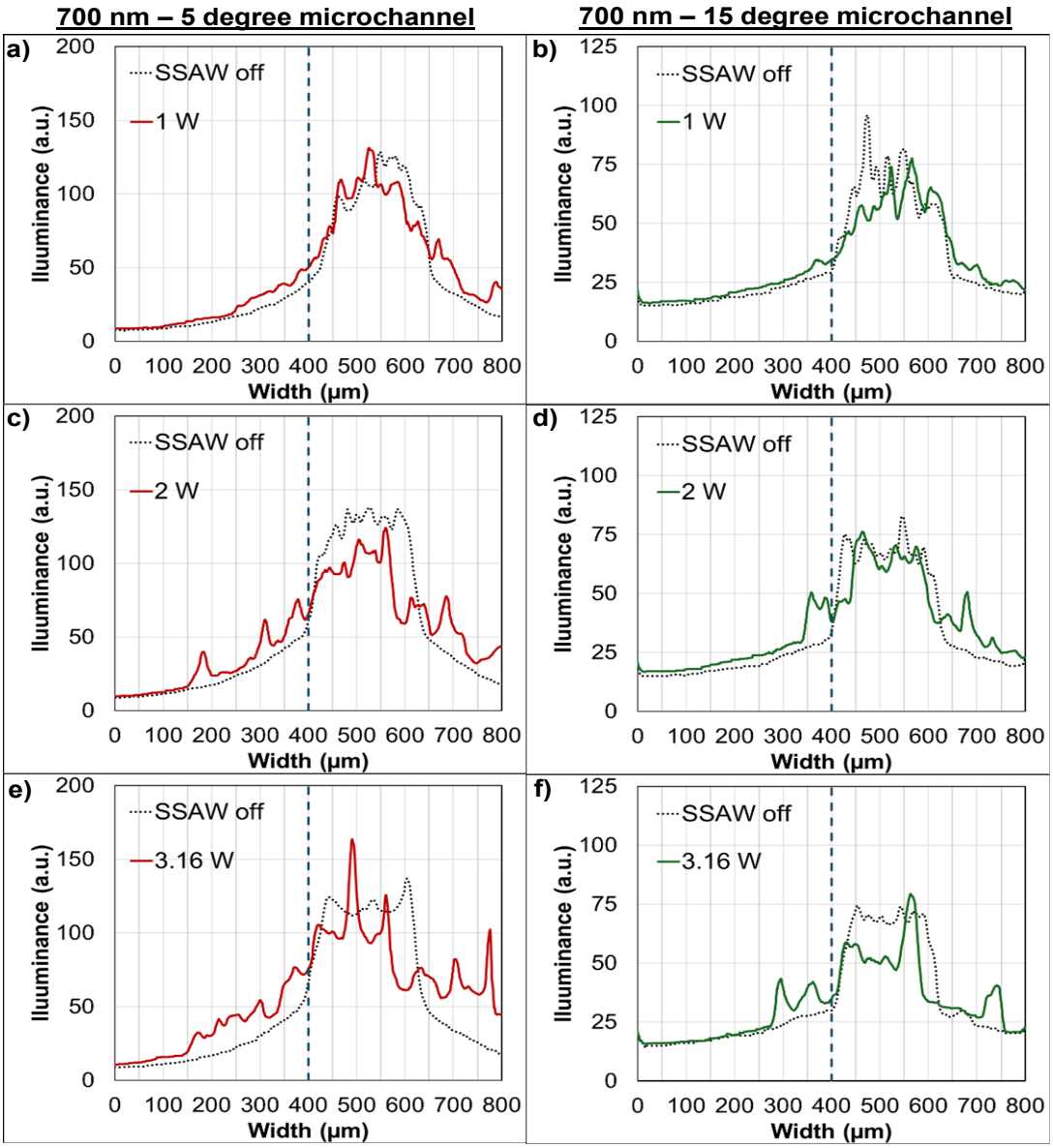

Figure A5.3. Illuminance profiles of 700 nm particle actuation at different power inputs. The figures on the left show the actuation in the 5º microchannel inclination at the input power of a) 1, c) 2 and e) 3.16 W, while the figures on the right show the actuation at the 15º inclination with the input power of b) 1, d) 2 and f) 3.16 W. The dotted profile shows the particle distribution of the particles pre actuation.

From the illuminance profiles one could then potentially reflect the percentage of illuminance at collection output (output 4), as described in section 6.3.1. But the current issue is that these videos still have noise within them, as can be seen from the illuminance profiles not being directly at zero and having an incline. This noise then will enhance the signal on some regions, thus creating a misrepresentation of the particles on the output 4 trajectory. As such, to eliminate as much noise as possible the author observed the videos and selected a signal cut-off point. While this would reduce the

noise, it could also have the adverse of removing some of the possible signal as well. But the author chose the more conservative approach, i.e. higher signal cut off to reduce the noise at the expense of losing some of the available signal, to obtain an estimation of the percentage of particles that have been actuated towards output 4. Table A3 is provided to illustrate the signal cut off for the actuation videos.

Table A3. Signal cut off of the illuminance signal of sub-micron particles actuations at different microchannel inclinations.

Size (nm)	Microchannel inclination (º)	Signal cut off point (a.u.)
100	5	35
100	5	30
700	15	25
700	15	25

Using the following cut off points Fig. A5.4 can be produced, where the illuminance percentage at output 4 was obtained by taking the average of 3 different frames from the actuation videos. Figs. A5.4a and A5.4b show that, similarly to the 5 μm particles results, 5º actuation appears to be more effective at translating the particles than the 15º actuation. But perhaps surprisingly, the 5º actuation is more effective at translating the 100 nm particles than 700 nm particles, while the opposite is true for the 15º actuation. This potentially then illustrates that for sub-micron particle actuation a higher channel inclination would be more preferrable, since although it would result with a less efficient translation of the particles it would also result with the unwanted spread of smaller particles in that streamline. But it should be noted that due to the signal noise cut out, this could potentially have played a role in these results. As such they should be carefully interpreted, and very likely future repetitions should be performed to verify these results. Another interesting observation is that at higher power inputs, the actuation efficiency barely improves, and in the case of 5º actuation it starts to plateau. While in the case of 5 μm particles this plateauing only started when an almost perfect actuation efficiency was achieved (<90 %). This early plateauing is not surprising and greatly highlights the issue of sub-micron particles spreading out in the microchannel, since this spreading will hinder the device of ever achieving an actuation efficiency above 50 %.

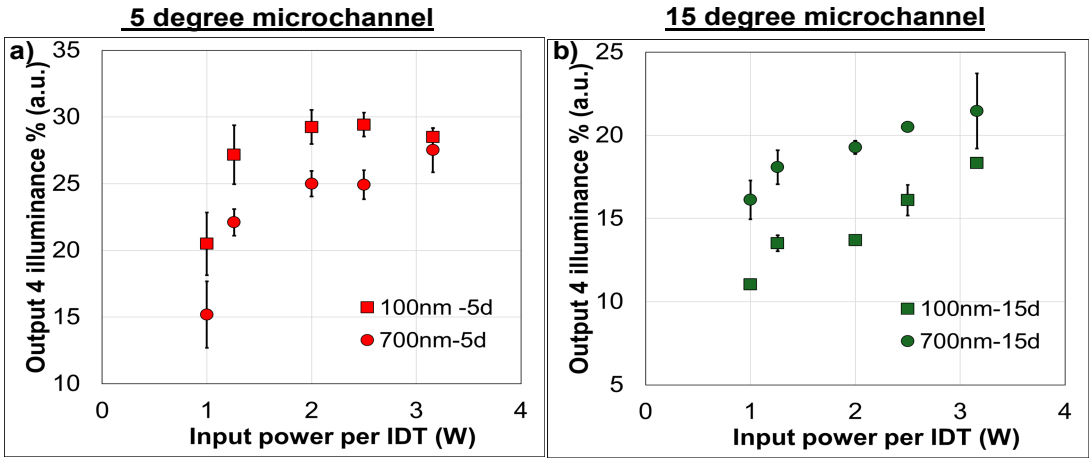

Figure A5.4. Illuminance percentage at output for the 100 and 700 nm particles at a) the 5º and b) 15º microchannel inclination. The data points show the average percentage of 3 frames with the error bars showing the standard deviation of the sample.

Conclusion

In this section two sizes of fluorescent sub-micron particles have been used to study their actuation behaviour using hFPCB IDTs and 5º and 15º microchannel inclination. It has been demonstrated that the particles under the critical diameter tend to spread within the microchannel instead of just being actuated towards the output direction. The reason of this particle spread is speculated in chapter 6, section 6.3.3. One interesting phenomenon that has been observed is that in the 5º actuation a larger percentage of the 100 nm particles than 700 nm particles is translated when compared to 15º degree actuation. This is the inverse for the 15º actuation, where a larger percentage of the 700 nm particles was translated when compared to 100 nm. This could potentially hints that a higher angle inclination would be more desired for sub-micron actuation, when attempting to remove larger particles from the sub-micron population. But it should be noted that these results should be repeated before any solid conclusion is reached.

Appendix 6: Hybrid channel tests

In this section the author will share his preliminary tests with a hybrid channel. The setup for this device was identical to the one in Chapter 6, with the only difference that the incorporated channel was a hybrid channel, i.e. a PDMS channel with a glass top roof. The channel was manufactured by following the steps identically to section 3.4.3, with the addition that after pouring the PDMS a cut glass slide was placed at the top of the microchannel before curing. The cut glass slide was 1.5 mm thick and was cut to an approximate width of the microchannel using rotary tool (Dremel 3000) with a diamond bit. The resulting channel is shown in Fig. A6.1a and a zoom inset of glass slide roof is shown.

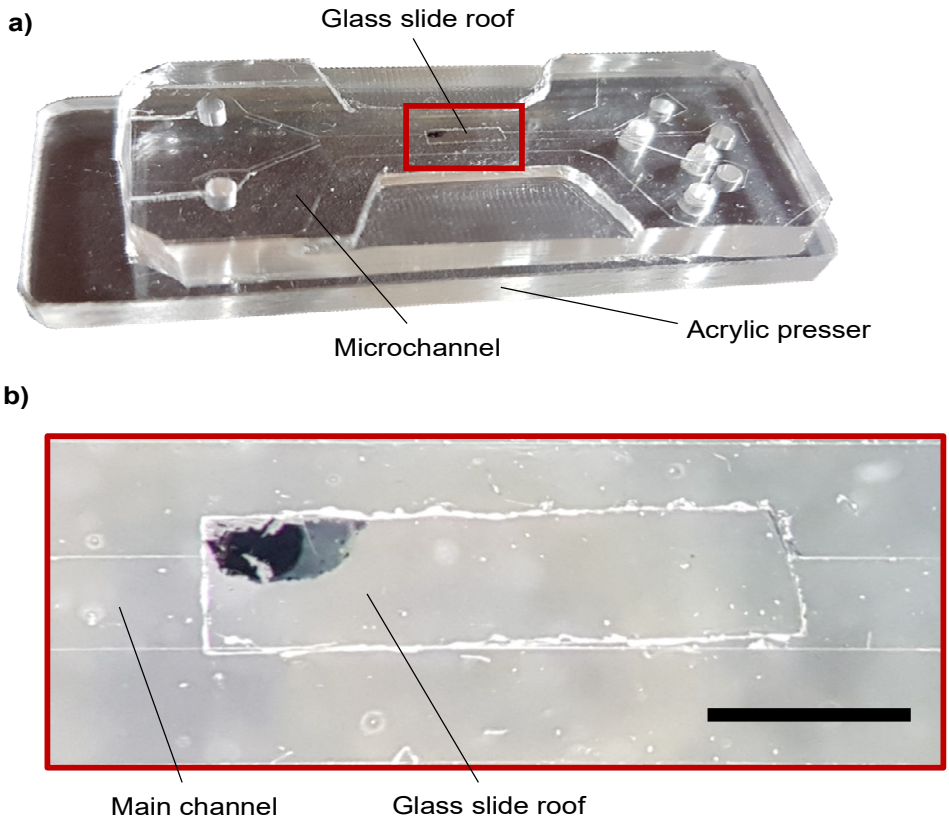

Figure A6.1. PDMS microchannel with glass roof. a) The manufactured hybrid channel on top of the acrylic presser with b) a zoom inset of the glass slide roof in the PDMS microchannel. The scale bar is 1.5 mm.

This microchannel was placed into 5º inclination and was injected with 1 µm particles to observe if the glass roof incorporation would assist with the actuation of the particles, the results are shown in Fig. A6.2. In Fig. A6.2a the particles can be seen in SSAW zone before and after the device is turned on. Perhaps surprisingly the patterning of the particles is different when compared to the patterning without a glass roof. This could be a result of the acoustic energy being reflected back, thus resulting in a different particle

configuration. But this could also be a result of potential manufacturing issues with the microchannel and placement of the glass roof. Nonetheless, this result seems promising since it demonstrates patterning and creation of traveling lines at 2 W, instead of particle spreading. As such, further actuation tests were performed at the output region with the SSAW off and activated under 2 and 3 W and shown in Figs. A6.2c, A6.2d and A6.2e, respectively. When the SSAW is turned on most of the particles are translated towards the collection output and do not seem to drastically spread out. The same actuations were performed within a simple PDMS microchannel, shown in Figs. A6.2f, A6.2g and A6.2h, with the SSAW off and activated under 2 and 3 W, respectively. In the pure PDMS microchannel the particles spread out, and their spreading increases with the power increase, which is indicated by lowest traveling line observable from the video snapshots. As such it can be clearly seen that incorporating a material with a high acoustic impedance benefits greatly the device in term of the actuation near the critical particle diameter of the device.

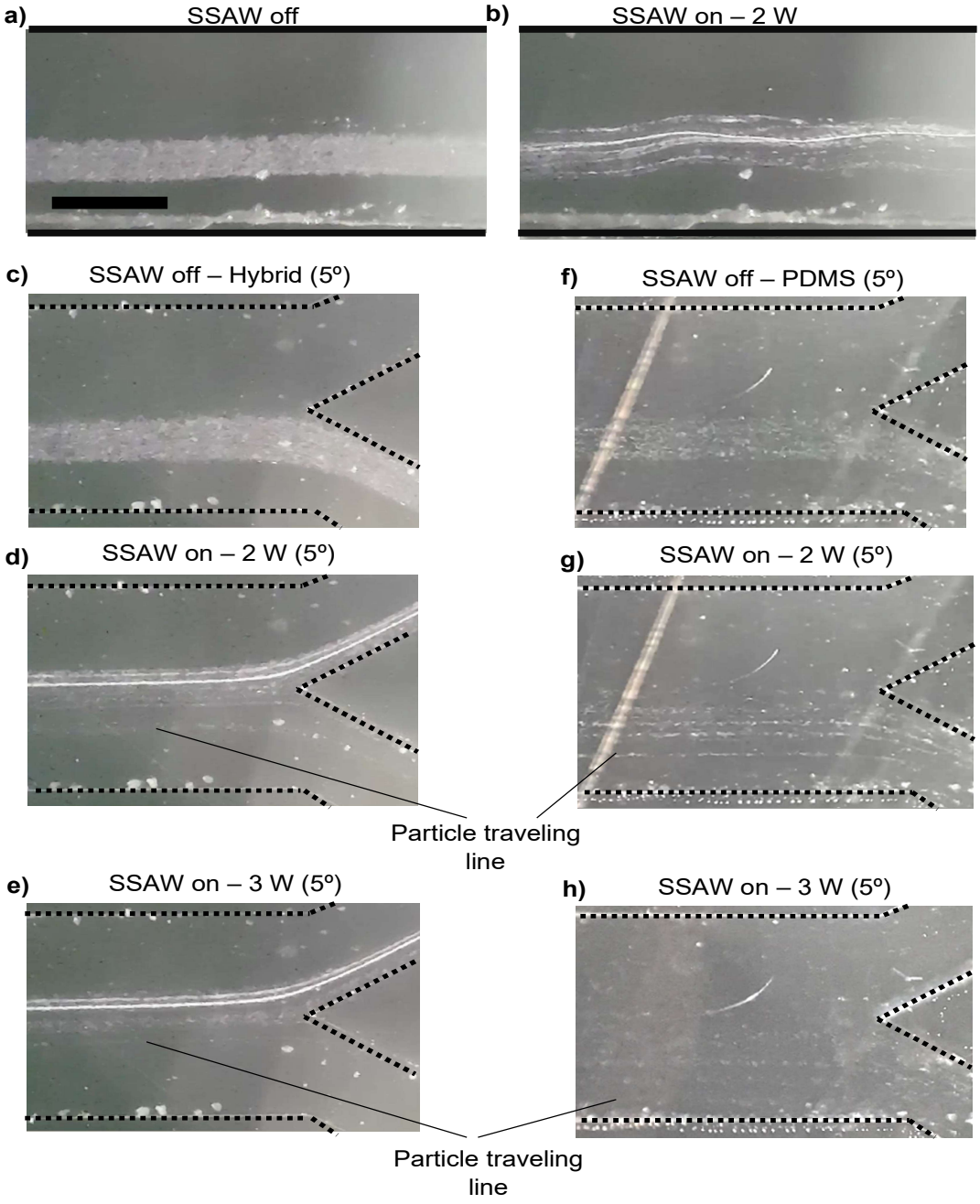

Figure A6.1. PDMS microchannel with a glass roof applied for 1 µm particle actuation at a 5º inclination. The actuation of particles in SAW zone is demonstrated when a) the SSAW is off and b) the SSAW is on with an input power of 2 W per IDT. The actuation at the output region is demonstrated when c) the SSAW is off, the SSAW is on with d) 2 W per IDT and e) 3 W per IDT. The actuation results of a non-hybrid PDMS channel are also shown at the output region when f) the SSAW is off, the SAW is on with an input power of g) 2 W per IDT and e) 3 W per IDT. Scale bar is 400 µm.

Conclusion

In this section, preliminary tests using a hybrid PDMS channel, i.e. PDMS microchannel with a glass roof, were performed. These tests indicated that the hybrid design does

indeed benefit the sub-micron actuation of the SAW device by reducing (perhaps even eliminating) the spread of the 1 μm particles and actuating the particles towards the collection output. But it should be noted, that due to using non fluorescence particles some of the traveling lines/ paths of the particles may not be detected. As such it is advisable to have these repeated with fluorescence particles to better establish the behaviour of sub-micron particles. Additionally, this microchannel could be a one-off and as such to confirm these results multiple hybrid microchannels should be created to observe if the shown effect is repeatable.

Bibliography

Ai, Y., Sanders, C.K., Marrone, B.L., 2013. Separation of Escherichia coli Bacteria from Peripheral Blood Mononuclear Cells Using Standing Surface Acoustic Waves. Anal. Chem. 85, 9126–9134. https://doi.org/10.1021/ac4017715

Ambattu, L.A., Ramesan, S., Dekiwadia, C., Hanssen, E., Li, H., Yeo, L.Y., 2020. High frequency acoustic cell stimulation promotes exosome generation regulated by a calcium-dependent mechanism. Commun Biol 3, 553. https://doi.org/10.1038/s42003-020-01277-6

Arzumanian, V.A., Kiseleva, O.I., Poverennaya, E.V., 2021. The Curious Case of the HepG2 Cell Line: 40 Years of Expertise. Int J Mol Sci. 22, 13135. https://doi.org/doi: 10.3390/ijms222313135

Auld, B., Gagnepain, J., Tan, M., 1976. Horizontal shear surface waves on corrugated surfaces. STANFORD UNIV CALIF EDWARD L GINZTON LAB.

Barnkob, R., Augustsson, P., Laurell, T., Bruus, H., 2012a. Acoustic radiation- and streaming-induced microparticle velocities determined by microparticle image velocimetry in an ultrasound symmetry plane. Phys. Rev. E 86, 056307. https://doi.org/10.1103/PhysRevE.86.056307

Barnkob, R., Iranmanesh, I., Wiklund, M., Bruus, H., 2012b. Measuring acoustic energy density in microchannel acoustophoresis using a simple and rapid light-intensity method. Lab on a Chip 12, 2337–2344. https://doi.org/10.1039/C2LC40120G

Barnkob, R., Nama, N., Ren, L., Huang, T.J., Costanzo, F., Kähler, C.J., 2018. Acoustically Driven Fluid and Particle Motion in Confined and Leaky Systems. Physical Review Applied 9. https://doi.org/10.1103/PhysRevApplied.9.014027

Baumgartner, K., Westerhausen, C., 2023. Recent advances of surface acoustic wave-based sensors for noninvasive cell analysis. Current Opinion in Biotechnology 79, 102879. https://doi.org/10.1016/j.copbio.2022.102879

Belling, J.N., Heidenreich, L.K., Tian, Z., Mendoza, A.M., Chiou, T.-T., Gong, Y., Chen, N.Y., Young, T.D., Wattanatorn, N., Park, J.H., Scarabelli, L., Chiang, N., Takahashi, J., Young, S.G., Stieg, A.Z., De Oliveira, S., Huang, T.J., Weiss, P.S., Jonas, S.J., 2020. Acoustofluidic sonoporation for gene delivery to human hematopoietic stem and progenitor cells. Proceedings of the National Academy of Sciences 117, 10976–10982. https://doi.org/10.1073/pnas.1917125117

Bhagat, A.A.S., Bow, H., Hou, H.W., Tan, S.J., Han, J., Lim, C.T., 2010. Microfluidics for cell separation. Medical and Biological Engineering and Computing 48, 999–1014. https://doi.org/10.1007/s11517-010-0611-4

Brugger, M.S., Baumgartner, K., Mauritz, S.C.F., Gerlach, S.C., Röder, F., Schlosser, C., Fluhrer, R., Wixforth, A., Westerhausen, C., 2020. Vibration enhanced cell growth induced by surface acoustic waves as in vitro wound-healing model. PNAS 117, 31603–31613. https://doi.org/10.1073/pnas.2005203117

Brugger, M.S., Schnitzler, L.G., Nieberle, T., Wixforth, A., Westerhausen, C., 2021. Shear-horizontal surface acoustic wave sensor for non-invasive monitoring of dynamic cell spreading and attachment in wound healing assays. Biosensors and Bioelectronics 173, 112807. https://doi.org/10.1016/j.bios.2020.112807

Bruus, H., 2012. Acoustofluidics 7: The acoustic radiation force on small particles. Lab on a Chip 12, 1014. https://doi.org/10.1039/c2lc21068a

Bruus, H., 2011. Acoustofluidics 1: Governing equations in microfluidics. Lab on a Chip 11, 3742. https://doi.org/10.1039/c1lc20658c

Burke, J.M., Zubajlo, R.E., Smela, E., White, I.M., 2014. High-throughput particle separation and concentration using spiral inertial filtration. Biomicrofluidics 8, 024105. https://doi.org/10.1063/1.4870399

Centner, C.S., Moore, J.T., Baxter, M.E., Long, Z.T., Miller, J.M., Kovatsenko, E.S., Xie, B., Menze, M.A., Berson, R.E., Bates, P.J., Yaddanapudi, K., Kopechek, J.A., 2021. Acoustofluidic-mediated molecular delivery to human T cells with a three-dimensional-printed flow chambera). The Journal of the Acoustical Society of America 150, 4534–4547. https://doi.org/10.1121/10.0009054

Centner, C.S., Moore, J.T., Baxter, M.E., Yaddanapudi, K., Bates, P.J., Kopechek, J.A., 2023. Comparison of Acoustofluidic and Static Systems for Ultrasound-Mediated Molecular Delivery to T Lymphocytes. Ultrasound in Medicine & Biology 49, 90–105. https://doi.org/10.1016/j.ultrasmedbio.2022.08.005

Chen, C., Zhang, S.P., Mao, Z., Nama, N., Gu, Y., Huang, P.-H., Jing, Y., Guo, X., Costanzo, F., Huang, T.J., 2018. Three-dimensional numerical simulation and experimental investigation of boundary-driven streaming in surface acoustic wave microfluidics. Lab Chip 18, 3645–3654. https://doi.org/10.1039/C8LC00589C

Chen, L., ZHENG, X.-L., HU, N., YANG, J., LUO, H.-Y., JIANG, F., LIAO, Y.-J., 2015. Research Progress on Microfluidic Chip of Cell Separation Based on Dielectrophoresis. Chinese Journal of Analytical Chemistry 43, 300–309. https://doi.org/10.1016/S1872-2040(15)60808-8

Chen, Y., Wu, M., Ren, L., Liu, J., Whitley, P.H., Wang, L., Huang, T.J., 2016. High-throughput acoustic separation of platelets from whole blood. Lab Chip 16, 3466–3472. https://doi.org/10.1039/C6LC00682E

Cheng, X., Irimia, D., Dixon, M., Sekine, K., Demirci, U., Zamir, L., Tompkins, R.G., Rodriguez, W., Toner, M., 2007. A microfluidic device for practical label-free CD4+ T cell counting of HIV-infected subjects. Lab Chip 7, 170–178. https://doi.org/10.1039/B612966H

Cheng, Y., Ye, X., Ma, Z., Xie, S., Wang, W., 2016. High-throughput and clogging-free microfluidic filtration platform for on-chip cell separation from undiluted whole blood. Biomicrofluidics 10, 014118. https://doi.org/10.1063/1.4941985

Chetpattananondh, K., Tapoanoi, T., Phukpattaranont, P., Jindapetch, N., 2014. A self-calibration water level measurement using an interdigital capacitive sensor. Sensors and Actuators A: Physical 209, 175–182. https://doi.org/10.1016/j.sna.2014.01.040

Cohen, S., Sazan, H., Kenigsberg, A., Schori, H., Piperno, S., Shpaisman, H., Shefi, O., 2020. Large-scale acoustic-driven neuronal patterning and directed outgrowth. Sci Rep 10, 4932. https://doi.org/10.1038/s41598-020-60748-2

Collins, D.J., Ma, Z., Ai, Y., 2016. Highly Localized Acoustic Streaming and Size-Selective Submicrometer Particle Concentration Using High Frequency Microscale Focused Acoustic Fields. Analytical Chemistry 88, 5513–5522. https://doi.org/10.1021/acs.analchem.6b01069

Colombo, M., Raposo, G., Théry, C., 2014. Biogenesis, Secretion, and Intercellular Interactions of Exosomes and Other Extracellular Vesicles. Annu. Rev. Cell Dev. Biol. 30, 255–289. https://doi.org/10.1146/annurev-cellbio-101512-122326

Curie, J., Curie, P., 1880. Développement, par pression, de l'électricité polaire dans les cristaux hémièdres à faces inclinées. Comptes rendus 91, 294–295.

Dalili, A., Samiei, E., Hoorfar, M., 2019. A review of sorting, separation and isolation of cells and microbeads for biomedical applications: microfluidic approaches. Analyst 144, 87–113. https://doi.org/10.1039/C8AN01061G

Dean, R.N., Rane, A.K., Baginski, M.E., Richard, J., Hartzog, Z., Elton, D.J., 2012. A Capacitive Fringing Field Sensor Design for Moisture Measurement Based on Printed Circuit Board Technology. IEEE Transactions on Instrumentation and Measurement 61, 1105–1112. https://doi.org/10.1109/TIM.2011.2173041

Deshmukh, D.V., Reichert, P., Zvick, J., Labouesse, C., Künzli, V., Dudaryeva, O., Bar-Nur, O., Tibbitt, M.W., Dual, J., 2022. Continuous Production of Acoustically Patterned Cells Within Hydrogel Fibers for Musculoskeletal Tissue Engineering. Advanced Functional Materials n/a, 2113038. https://doi.org/10.1002/adfm.202113038

Destgeer, G., Cho, H., Ha, B.H., Jung, J.H., Park, J., Sung, H.J., 2016. Acoustofluidic particle manipulation inside a sessile droplet: four distinct regimes of particle concentration. Lab Chip 16, 660–667. https://doi.org/10.1039/C5LC01104C

Destgeer, G., Ha, B.H., Jung, J.H., Sung, H.J., 2014. Submicron separation of microspheres via travelling surface acoustic waves. Lab Chip 14, 4665–4672. https://doi.org/10.1039/C4LC00868E

Destgeer, G., Lee, K.H., Jung, J.H., Alazzam, A., Sung, H.J., 2013. Continuous separation of particles in a PDMS microfluidic channel via travelling surface acoustic waves (TSAW). Lab Chip 13, 4210–4216. https://doi.org/10.1039/C3LC50451D

Devendran, C., Collins, D.J., Ai, Y., Neild, A., 2017. Huygens-Fresnel Acoustic Interference and the Development of Robust Time-Averaged Patterns from Traveling Surface Acoustic Waves. Phys. Rev. Lett. 118, 154501. https://doi.org/10.1103/PhysRevLett.118.154501

Ding, X., Lin, S.-C.S., Lapsley, M.I., Li, S., Guo, X., Chan, C.Y.K., Chiang, I.-K., Wang, L., McCoy, J.P., Huang, T.J., 2012. Standing surface acoustic wave (SSAW) based multichannel cell sorting. Lab Chip 12, 4228–4231. https://doi.org/10.1039/c2lc40751e

Ding, X., Peng, Z., Lin, S.-C.S., Geri, M., Li, S., Li, P., Chen, Y., Dao, M., Suresh, S., Huang, T.J., 2014. Cell separation using tilted-angle standing surface acoustic waves. PNAS 111, 12992–12997. https://doi.org/10.1073/pnas.1413325111

Dumčius, P., Mikhaylov, R., Zhang, X., Bareford, M., Stringer, M., Errington, R., Sun, C., Gonzalez, E., Krukovski, T., Falcon-Perez, J.M., Liang, D., Fu, Y.-Q., Clayton, A., Yang, X., 2023. Dual-Wave Acoustofluidic Centrifuge for Ultrafast Concentration of Nanoparticles and Extracellular Vesicles. Small 19, 2300390. https://doi.org/10.1002/smll.202300390

Edthofer, A., Novotny, J., Lenshof, A., Laurell, T., Baasch, T., 2023. Acoustofluidic Properties of Polystyrene Microparticles. Anal. Chem. 95, 10346–10352. https://doi.org/10.1021/acs.analchem.3c01156

Fu, Y.Q., Luo, J.K., Nguyen, N.T., Walton, A.J., Flewitt, A.J., Zu, X.T., Li, Y., McHale, G., Matthews, A., Iborra, E., Du, H., Milne, W.I., 2017. Advances in piezoelectric thin films for acoustic biosensors, acoustofluidics and lab-on-chip applications. Progress in Materials Science 89, 31–91. https://doi.org/10.1016/j.pmatsci.2017.04.006

Gai, J., Dervisevic, E., Devendran, C., Cadarso, V.J., O'Bryan, M.K., Nosrati, R., Neild, A., 2022. High-Frequency Ultrasound Boosts Bull and Human Sperm Motility. Advanced Science n/a, 2104362. https://doi.org/10.1002/advs.202104362

Gangji, V., De Maertelaer, V., Hauzeur, J.-P., 2011. Autologous bone marrow cell implantation in the treatment of non-traumatic osteonecrosis of the femoral head: Five year follow-up of a prospective controlled study. Bone 49, 1005–1009. https://doi.org/10.1016/j.bone.2011.07.032

Gascoyne, P., Mahidol, C., Ruchirawat, M., Satayavivad, J., Watcharasit, P., Becker, F.F., 2002. Microsample preparation by dielectrophoresis: isolation of malaria. Lab Chip 2, 70–75. https://doi.org/10.1039/B110990C

Greenwood, M.S., Bamberger, J.A., 2002. Measurement of viscosity and shear wave velocity of a liquid or slurry for on-line process control. Ultrasonics 39, 623–630. https://doi.org/10.1016/S0041-624X(02)00372-4

Gu, Y., Chen, C., Mao, Z., Bachman, H., Becker, R., Rufo, J., Wang, Z., Zhang, P., Mai, J., Yang, S., Zhang, J., Zhao, S., Ouyang, Y., Wong, D.T.W., Sadovsky, Y., Huang, T.J., 2021. Acoustofluidic centrifuge for nanoparticle enrichment and separation. Science Advances 7, eabc0467. https://doi.org/10.1126/sciadv.abc0467

Guo, F., Li, P., French, J.B., Mao, Z., Zhao, H., Li, S., Nama, N., Fick, J.R., Benkovic, S.J., Huang, T.J., 2015. Controlling cell–cell interactions using surface acoustic waves. PNAS 112, 43–48. https://doi.org/10.1073/pnas.1422068112

Guo, X., Sun, M., Yang, Y., Xu, H., Liu, J., He, S., Wang, Y., Xu, L., Pang, W., Duan, X., 2021. Controllable Cell Deformation Using Acoustic Streaming for Membrane Permeability Modulation. Advanced Science 8, 2002489. https://doi.org/10.1002/advs.202002489

H. Wu, H. Zu, Q. -M. Wang, G. Zhao, J. H. -C. Wang, 2015. Monitoring the adhesion process of tendon stem cells using shear-horizontal surface acoustic wave sensors, in: 2015 Joint Conference of the IEEE International Frequency Control Symposium & the European Frequency and Time Forum. Presented at the 2015 Joint Conference of the IEEE International Frequency Control Symposium & the European Frequency and Time Forum, pp. 310–315. https://doi.org/10.1109/FCS.2015.7138849

H. Yatsuda, Y. Takeuchi, S. Yoshikawa, 1990. New design techniques for SAW filters using slanted-finger IDTs, in: IEEE Symposium on Ultrasonics. Presented at the IEEE Symposium on Ultrasonics, pp. 61–66 vol.1. https://doi.org/10.1109/ULTSYM.1990.171327

Han, J., Yang, F., Hu, H., Huang, Q., Lei, Y., Li, M., 2021. Thermal Control Design and Packaging for Surface Acoustic Wave Devices in Acoustofluidics. IEEE Transactions on Ultrasonics, Ferroelectrics, and Frequency Control 1–1. https://doi.org/10.1109/TUFFC.2021.3101248

Hartono, D., Liu, Y., Tan, P.L., Then, X.Y.S., Yung, L.-Y.L., Lim, K.-M., 2011. On-chip measurements of cell compressibility via acoustic radiation. Lab Chip 11, 4072–4080. https://doi.org/10.1039/C1LC20687G

He, Z., Chen, Z., Tan, M., Elingarami, S., Liu, Y., Li, T., Deng, Y., He, N., Li, S., Fu, J., Li, W., 2020. A review on methods for diagnosis of breast cancer cells and tissues. Cell Proliferation 53, e12822. https://doi.org/10.1111/cpr.12822

Hiremath, N., Kumar, V., Motahari, N., Shukla, D., 2021. An Overview of Acoustic Impedance Measurement Techniques and Future Prospects. Metrology 1, 17–38. https://doi.org/10.3390/metrology1010002

Hsu, J.-C., Chao, C.-L., 2021. Acoustophoretic patterning of microparticles in a microfluidic chamber driven by standing Lamb waves. Applied Physics Letters 119, 103504. https://doi.org/10.1063/5.0056985

Huang, P.-H., Xie, Y., Ahmed, D., Rufo, J., Nama, N., Chen, Y., Yu Chan, C., Jun Huang, T., 2013. An acoustofluidic micromixer based on oscillating sidewall sharp-edges. Lab on a Chip 13, 3847–3852. https://doi.org/10.1039/C3LC50568E

Imashiro, C., Kang, B., Lee, Y., Hwang, Y.-H., Im, S., Kim, D.-E., Takemura, K., Lee, H., 2021. Propagating acoustic waves on a culture substrate regulate the directional collective cell migration. Microsyst Nanoeng 7, 90. https://doi.org/10.1038/s41378-021-00304-8

Iranmanesh, I., Barnkob, R., Bruus, H., Wiklund, M., 2013. Tunable-angle wedge transducer for improved acoustophoretic control in a microfluidic chip. J. Micromech. Microeng. 23, 105002. https://doi.org/10.1088/0960-1317/23/10/105002

Jain, V., Raj, T.P., Deshmukh, R., Patrikar, R., 2017. Design, fabrication and characterization of low cost printed circuit board based EWOD device for digital microfluidics applications. Microsyst Technol 23, 389–397. https://doi.org/10.1007/s00542-015-2680-7

Johnston, I.D., McCluskey, D.K., Tan, C.K.L., Tracey, M.C., 2014. Mechanical characterization of bulk Sylgard 184 for microfluidics and microengineering. J. Micromech. Microeng. 24, 035017. https://doi.org/10.1088/0960-1317/24/3/035017

Jolly, R.N., 1956. Investigation of shear waves. Geophysics 21, 905–938. https://doi.org/10.1190/1.1438310

Kang, B., Shin, J., Park, H.-J., Rhyou, C., Kang, D., Lee, S.-J., Yoon, Y., Cho, S.-W., Lee, H., 2018. High-resolution acoustophoretic 3D cell patterning to construct functional collateral cylindroids for ischemia therapy. Nature Communications 9, 5402. https://doi.org/10.1038/s41467-018-07823-5

Karthick, S., Pradeep, P.N., Kanchana, P., Sen, A.K., 2018. Acoustic impedance-based size-independent isolation of circulating tumour cells from blood using acoustophoresis. Lab Chip 18, 3802–3813. https://doi.org/10.1039/C8LC00921J

Keith, C.M., Crampin, S., 1977. Seismic body waves in anisotropic media: synthetic seismograms. Geophysical Journal International 49, 225–243. https://doi.org/10.1111/j.1365-246X.1977.tb03710.x

Keloth, A., Anderson, O., Risbridger, D., Paterson, L., 2018. Single Cell Isolation Using Optical Tweezers. Micromachines 9. https://doi.org/10.3390/mi9090434

Kennelly, A.E., Kurokawa, K., 1921. Acoustic Impedance and Its Measurement. Proceedings of the American Academy of Arts and Sciences 56, 3–42. https://doi.org/10.2307/20025828

Kim, S., Nam, H., Cha, B., Park, J., Sung, H.J., Jeon, J.S., 2022. Acoustofluidic Stimulation of Functional Immune Cells in a Microreactor. Advanced Science 9, 2105809. https://doi.org/10.1002/advs.202105809

Kimura, M., Ando, A., Sakabe, Y., 2010. 2 - Lead zirconate titanate-based piezo-ceramics, in: Uchino, K. (Ed.), Advanced Piezoelectric Materials, Woodhead Publishing Series in Electronic and Optical Materials. Woodhead Publishing, pp. 89–110. https://doi.org/10.1533/9781845699758.1.89

Kirschner, J., 2010. Surface Acoustic Wave Sensors (SAWS): Design for Application. Microelectromechanical systems 11.

Korecka, J.A., Verhaagen, J., Hol, E.M., 2007. Cell-replacement and gene-therapy strategies for Parkinson's and Alzheimer's disease. Regenerative Medicine 2, 425–446. https://doi.org/10.2217/17460751.2.4.425

Kuntaegowdanahalli, S.S., Bhagat, A.A.S., Kumar, G., Papautsky, I., 2009. Inertial microfluidics for continuous particle separation in spiral microchannels. Lab Chip 9, 2973–2980. https://doi.org/10.1039/B908271A

Kwon, J.-S., Oh, J.H., 2018. Microfluidic Technology for Cell Manipulation. Applied Sciences 8. https://doi.org/10.3390/app8060992

LaDou, J., 2006. Printed circuit board industry. International Journal of Hygiene and Environmental Health 209, 211–219. https://doi.org/10.1016/j.ijheh.2006.02.001

Laermer, F., 2016. Dry Etching, in: Reference Module in Materials Science and Materials Engineering. Elsevier. https://doi.org/10.1016/B978-0-12-803581-8.00526-9

Lamb, H., 1917. On waves in an elastic plate. Proceedings of the Royal Society of London. Series A, Containing papers of a mathematical and physical character 93, 114–128.

Lener, T., Gimona, M., Aigner, L., Börger, V., Buzas, E., Camussi, G., Chaput, N., Chatterjee, D., Court, F.A., Portillo, H.A. del, O'Driscoll, L., Fais, S., Falcon-Perez, J.M., Felderhoff-Mueser, U., Fraile, L., Gho, Y.S., Görgens, A., Gupta, R.C., Hendrix, A., Hermann, D.M., Hill, A.F., Hochberg, F., Horn, P.A., Kleijn, D. de, Kordelas, L., Kramer,

B.W., Krämer-Albers, E.-M., Laner-Plamberger, S., Laitinen, S., Leonardi, T., Lorenowicz, M.J., Lim, S.K., Lötvall, J., Maguire, C.A., Marcilla, A., Nazarenko, I., Ochiya, T., Patel, T., Pedersen, S., Pocsfalvi, G., Pluchino, S., Quesenberry, P., Reischl, I.G., Rivera, F.J., Sanzenbacher, R., Schallmoser, K., Slaper-Cortenbach, I., Strunk, D., Tonn, T., Vader, P., Balkom, B.W.M. van, Wauben, M., Andaloussi, S.E., Théry, C., Rohde, E., Giebel, B., 2015. Applying extracellular vesicles based therapeutics in clinical trials – an ISEV position paper. Journal of Extracellular Vesicles 4, 30087. https://doi.org/10.3402/jev.v4.30087

Li, P., Ai, Y., 2021. Label-Free Multivariate Biophysical Phenotyping-Activated Acoustic Sorting at the Single-Cell Level. Anal. Chem. https://doi.org/10.1021/acs.analchem.0c05352

Li, P., Liang, M., Lu, X., Chow, J.J.M., Ramachandra, C.J.A., Ai, Y., 2019. Sheathless Acoustic Fluorescence Activated Cell Sorting (aFACS) with High Cell Viability. Anal. Chem. 91, 15425–15435. https://doi.org/10.1021/acs.analchem.9b03021

Li, P., Mao, Z., Peng, Z., Zhou, L., Chen, Y., Huang, P.-H., Truica, C.I., Drabick, J.J., El-Deiry, W.S., Dao, M., Suresh, S., Huang, T.J., 2015. Acoustic separation of circulating tumor cells. PNAS 112, 4970–4975. https://doi.org/10.1073/pnas.1504484112

Li, S., Guo, F., Chen, Y., Ding, X., Li, P., Wang, L., Cameron, C.E., Huang, T.J., 2014. Standing Surface Acoustic Wave Based Cell Coculture. Anal. Chem. 86, 9853–9859. https://doi.org/10.1021/ac502453z

Li, S., Ren, L., Huang, P.-H., Yao, X., Cuento, R.A., McCoy, J.P., Cameron, C.E., Levine, S.J., Huang, T.J., 2016. Acoustofluidic Transfer of Inflammatory Cells from Human Sputum Samples. Anal. Chem. 88, 5655–5661. https://doi.org/10.1021/acs.analchem.5b03383

Liao, M., Du, J., Chen, L., Huang, J., Yang, R., Bao, W., Zeng, K., Wang, W., Aphan, B.C., Wu, Z., Ma, L., Lu, Q., 2024. Sono-activated materials for enhancing focused ultrasound ablation: Design and application in biomedicine. Acta Biomaterialia 173, 36–50. https://doi.org/10.1016/j.actbio.2023.11.004

Ling, S.H., Lam, Y.C., Chian, K.S., 2012. Continuous Cell Separation Using Dielectrophoresis through Asymmetric and Periodic Microelectrode Array. Anal. Chem. 84, 6463–6470. https://doi.org/10.1021/ac300079q

Liu, G., He, F., Li, Y., Zhao, H., Li, X., Tang, H., Li, Z., Yang, Z., Zhang, Y., 2019. Effects of two surface acoustic wave sorting chips on particles multi-level sorting. Biomed Microdevices 21, 59. https://doi.org/10.1007/s10544-019-0419-4

Liu, J., 2013. Induced pluripotent stem cell-derived neural stem cells: new hope for stroke? Stem Cell Research & Therapy 4, 115. https://doi.org/10.1186/scrt326

Liu, L., Edgar, J.H., 2002. Substrates for gallium nitride epitaxy. Materials Science and Engineering: R: Reports 37, 61–127. https://doi.org/10.1016/S0927-796X(02)00008-6

Liu, P., Tian, Z., Hao, N., Bachman, H., Zhang, P., Hu, J., Huang, T.J., 2020. Acoustofluidic multi-well plates for enrichment of micro/nano particles and cells. Lab Chip 20, 3399–3409. https://doi.org/10.1039/D0LC00378F

Liu, Y., Lim, K.-M., 2011. Particle separation in microfluidics using a switching ultrasonic field. Lab Chip 11, 3167–3173. https://doi.org/10.1039/C1LC20481E

Liu, Z., Huang, F., Du, J., Shu, W., Feng, H., Xu, X., Chen, Y., 2013. Rapid isolation of cancer cells using microfluidic deterministic lateral displacement structure. Biomicrofluidics 7, 011801. https://doi.org/10.1063/1.4774308

Lockwood, G.R., Turnbull, D.H., Foster, F.S., 1994. Fabrication of high frequency spherically shaped ceramic transducers. IEEE Transactions on Ultrasonics, Ferroelectrics, and Frequency Control 41, 231–235. https://doi.org/10.1109/58.279136

Long, M., 2014. 6 - Wave Acoustics, in: Long, M. (Ed.), Architectural Acoustics (Second Edition). Academic Press, Boston, pp. 221–258. https://doi.org/10.1016/B978-0-12-398258-2.00006-4

Lynch, C.S., Liao, X., Cochran, S., 2017. The Performance of Piezoelectric Materials Under Stress, in: Advanced Piezoelectric Materials. Elsevier, pp. 787–814. https://doi.org/10.1016/B978-0-08-102135-4.00019-9

Mao, Z., Li, P., Wu, M., Bachman, H., Mesyngier, N., Guo, X., Liu, S., Costanzo, F., Huang, T.J., 2017. Enriching Nanoparticles via Acoustofluidics. ACS Nano 11, 603–612. https://doi.org/10.1021/acsnano.6b06784

Mason, W.P., 1981. Piezoelectricity, its history and applications. The Journal of the Acoustical Society of America 70, 1561–1566. https://doi.org/10.1121/1.387221

Mattanovich, D., Borth, N., 2006. Applications of cell sorting in biotechnology. Microbial Cell Factories 5, 12. https://doi.org/10.1186/1475-2859-5-12

McGrath, J., Jimenez, M., Bridle, H., 2014. Deterministic lateral displacement for particle separation: a review. Lab Chip 14, 4139–4158. https://doi.org/10.1039/C4LC00939H

Messing, G.L., 2021. Calcination and Phase Transformations, in: Pomeroy, M. (Ed.), Encyclopedia of Materials: Technical Ceramics and Glasses. Elsevier, Oxford, pp. 83–92. https://doi.org/10.1016/B978-0-12-818542-1.00038-2

Mikhaylov, R., Martin, M.S., Dumcius, P., Wang, H., Wu, F., Zhang, X., Akhimien, V., Sun, C., Clayton, A., Fu, Y., Ye, L., Dong, Z., Wu, Z., Yang, X., 2021. A reconfigurable and portable acoustofluidic system based on flexible printed circuit board for the manipulation of microspheres. J. Micromech. Microeng. 31, 074003. https://doi.org/10.1088/1361-6439/ac0515

Mikhaylov, R., Wu, F., Wang, H., Clayton, A., Sun, C., Xie, Z., Liang, D., Dong, Y., Yuan, F., Moschou, D., Wu, Z., Shen, M.H., Yang, J., Fu, Y., Yang, Z., Burton, C., Errington, R.J., Wiltshire, M., Yang, X., 2020. Development and characterisation of acoustofluidic devices using detachable electrodes made from PCB. Lab Chip 20, 1807–1814. https://doi.org/10.1039/C9LC01192G

Mordor Intelligence, n.d. Printed Circuit Board Market Size, Share | 2022 - 27 | [WWW Document]. URL https://www.mordorintelligence.com/industry-reports/printed-circuit-board-market (accessed 8.11.22).

Nama, N., Barnkob, R., Mao, Z., Kähler, C.J., Costanzo, F., Huang, T.J., 2015. Numerical study of acoustophoretic motion of particles in a PDMS microchannel driven by surface acoustic waves. Lab Chip 15, 2700–2709. https://doi.org/10.1039/C5LC00231A

Naseer, S.M., Manbachi, A., Samandari, M., Walch, P., Gao, Y., Zhang, Y.S., Davoudi, F., Wang, W., Abrinia, K., Cooper, J.M., Khademhosseini, A., Shin, S.R., 2017. Surface acoustic waves induced micropatterning of cells in gelatin methacryloyl (GelMA) hydrogels. Biofabrication 9, 015020. https://doi.org/10.1088/1758-5090/aa585e

Nawaz, A.A., Urbanska, M., Herbig, M., Nötzel, M., Kräter, M., Rosendahl, P., Herold, C., Toepfner, N., Kubánková, M., Goswami, R., Abuhattum, S., Reichel, F., Müller, P., Taubenberger, A., Girardo, S., Jacobi, A., Guck, J., 2020. Intelligent image-based deformation-assisted cell sorting with molecular specificity. Nat Methods 17, 595–599. https://doi.org/10.1038/s41592-020-0831-y

Nelson, W.G., 2010. Piezoelectric Materials: Structure, Properties and Applications, Materials Science and Technologies. Nova Science Publishers, Inc, New York.

Ohlin, M., Iranmanesh, I., Christakou, A.E., Wiklund, M., 2015. Temperature-controlled MPa-pressure ultrasonic cell manipulation in a microfluidic chip. Lab Chip 15, 3341–3349. https://doi.org/10.1039/C5LC00490J

Olm, F., Urbansky, A., Dykes, J.H., Laurell, T., Scheding, S., 2019. Label-free neuroblastoma cell separation from hematopoietic progenitor cell products using acoustophoresis - towards cell processing of complex biological samples. Sci Rep 9, 8777. https://doi.org/10.1038/s41598-019-45182-3

Osaki, M., Okada, F., 2019. Exosomes and Their Role in Cancer Progression. Yonago Acta Med. 62, 182–190. https://doi.org/10.33160/yam.2019.06.002

Ozcelik, A., Rich, J., Huang, T.J., 2022. Chapter 11 - Fundamentals and applications of acoustics in microfluidics, in: Li, X. (James), Yang, C., Li, P.C.H. (Eds.), Multidisciplinary Microfluidic and Nanofluidic Lab-on-a-Chip. Elsevier, Amsterdam, pp. 297–321. https://doi.org/10.1016/B978-0-444-59432-7.00016-9

Özgür, Ü., Alivov, Ya.I., Liu, C., Teke, A., Reshchikov, M.A., Doğan, S., Avrutin, V., Cho, S.-J., Morkoç, H., 2005. A comprehensive review of ZnO materials and devices. Journal of Applied Physics 98, 041301. https://doi.org/10.1063/1.1992666

Papadakis, G., Tsortos, A., Kordas, A., Tiniakou, I., Morou, E., Vontas, J., Kardassis, D., Gizeli, E., 2013. Acoustic detection of DNA conformation in genetic assays combined with PCR. Scientific Reports 3, 2033. https://doi.org/10.1038/srep02033

Park, K., Suk, H.-J., Akin, D., Bashir, R., 2009. Dielectrophoresis-based cell manipulation using electrodes on a reusable printed circuit board. Lab Chip 9, 2224–2229. https://doi.org/10.1039/B904328D

Pedlosky, J., 1987. Geophysical Fluid Dynamics, 2nd ed. Springer New York.

Pesce, G., Jones, P.H., Maragò, O.M., Volpe, G., 2020. Optical tweezers: theory and practice. The European Physical Journal Plus 135, 949. https://doi.org/10.1140/epjp/s13360-020-00843-5

Poisson, S.-D., 1830. Mémoire sur la propagation du mouvement dans les milieux élastiques. L'Académie des sciences.

Pramanik, S., Sulistio, Y.A., Heese, K., 2017. Neurotrophin Signaling and Stem Cells—Implications for Neurodegenerative Diseases and Stem Cell Therapy. Molecular Neurobiology 54, 7401–7459. https://doi.org/10.1007/s12035-016-0214-7

Raes, L., De Smedt, S.C., Raemdonck, K., Braeckmans, K., 2021. Non-viral transfection technologies for next-generation therapeutic T cell engineering. Biotechnology Advances 49, 107760. https://doi.org/10.1016/j.biotechadv.2021.107760

Ramesan, S., Rezk, A.R., Cevaal, P.M., Cortez-Jugo, C., Symons, J., Yeo, L.Y., 2021. Acoustofection: High-Frequency Vibrational Membrane Permeabilization for Intracellular siRNA Delivery into Nonadherent Cells. ACS Appl. Bio Mater. 4, 2781–2789. https://doi.org/10.1021/acsabm.1c00003

Rasouli, R., Villegas, K.M., Tabrizian, M., 2023. Acoustofluidics – changing paradigm in tissue engineering, therapeutics development, and biosensing. Lab Chip 23, 1300–1338. https://doi.org/10.1039/D2LC00439A

Rayleigh, Lord, 1885. On Waves Propagated along the Plane Surface of an Elastic Solid. Proceedings of the London Mathematical Society s1-17, 4–11. https://doi.org/10.1112/plms/s1-17.1.4

Rezk, A.R., Friend, J.R., Yeo, L.Y., 2014. Simple, low cost MHz-order acoustomicrofluidics using aluminium foil electrodes. Lab Chip 14, 1802–1805. https://doi.org/10.1039/C4LC00182F

Robert, D., Pamme, N., Conjeaud, H., Gazeau, F., Iles, A., Wilhelm, C., 2011. Cell sorting by endocytotic capacity in a microfluidic magnetophoresis device. Lab Chip 11, 1902–1910. https://doi.org/10.1039/C0LC00656D

Rufo, J., Cai, F., Friend, J., Wiklund, M., Huang, T.J., 2022. Acoustofluidics for biomedical applications. Nature Reviews Methods Primers 2, 30. https://doi.org/10.1038/s43586-022-00109-7

Sadelain, M., Rivière, I., Riddell, S., 2017. Therapeutic T cell engineering. Nature 545, 423–431. https://doi.org/10.1038/nature22395

Saigusa, Y., 2010. 5 - Quartz-based piezoelectric materials, in: Uchino, K. (Ed.), Advanced Piezoelectric Materials. Woodhead Publishing, pp. 171–203. https://doi.org/10.1533/9781845699758.1.171

Sathyakumar, N., Prasath Balaji, K., Ganapathi, R., Pandian, S.R., 2018. A Build-Your-Own Three Axis CNC PCB Milling Machine. Materials Today: Proceedings 5, 24404–24413. https://doi.org/10.1016/j.matpr.2018.10.236

Schriebl, K., Lim, S., Choo, A., Tscheliessnig, A., Jungbauer, A., 2010. Stem cell separation: A bottleneck in stem cell therapy. Biotechnology Journal 5, 50–61. https://doi.org/10.1002/biot.200900115

Shahjalal, H.Md., Abdal Dayem, A., Lim, K.M., Jeon, T., Cho, S.-G., 2018. Generation of pancreatic β cells for treatment of diabetes: advances and challenges. Stem Cell Research & Therapy 9, 355. https://doi.org/10.1186/s13287-018-1099-3

Shen, F., Hwang, H., Hahn, Y.K., Park, J.-K., 2012. Label-Free Cell Separation Using a Tunable Magnetophoretic Repulsion Force. Anal. Chem. 84, 3075–3081. https://doi.org/10.1021/ac201505j

Shur, V.Ya., 2017. Nano- and Microdomain Engineering of Lithium Niobate and Lithium Tantalate for Piezoelectric Applications, in: Advanced Piezoelectric Materials. Elsevier, pp. 235–270. https://doi.org/10.1016/B978-0-08-102135-4.00006-0

Shur, V.Ya., 2010. 6 - Lithium niobate and lithium tantalate-based piezoelectric materials, in: Uchino, K. (Ed.), Advanced Piezoelectric Materials, Woodhead Publishing Series in Electronic and Optical Materials. Woodhead Publishing, pp. 204–238. https://doi.org/10.1533/9781845699758.1.204

Slobodnik, A.J., Carr, P.H., Budreau, A.J., 1970. Microwave Frequency Acoustic Surface-Wave Loss Mechanisms on $LiNbO_3$. Journal of Applied Physics 41, 4380–4387. https://doi.org/10.1063/1.1658471

Steinem, C., Janshoff, A., 2005. SENSORS | Piezoelectric Resonators, in: Worsfold, P., Townshend, A., Poole, C. (Eds.), Encyclopedia of Analytical Science (Second Edition). Elsevier, Oxford, pp. 269–276. https://doi.org/10.1016/B0-12-369397-7/00556-2

Stokes, G.G., 1851. On the effect of the internal friction of fluids on the motion of pendulums.

Su, P., Ren, C., Fu, Y., Guo, Jinhong, Guo, Jiuchuan, Yuan, Q., 2021. Magnetophoresis in microfluidic lab: Recent advance. Sensors and Actuators A: Physical 332, 113180. https://doi.org/10.1016/j.sna.2021.113180

Sun, C., Dong, Y., Wei, J., Cai, M., Liang, D., Fu, Y., Zhou, Y., Sui, Y., Wu, F., Mikhaylov, R., Wang, H., Fan, F., Xie, Z., Stringer, M., Yang, Z., Wu, Z., Tian, L., Yang, X., 2022. Acoustically accelerated neural differentiation of human embryonic stem cells. Acta Biomaterialia 151, 333–345. https://doi.org/10.1016/j.actbio.2022.07.041

Sun, C., Mikhaylov, R., Fu, Y., Wu, F., Wang, H., Yuan, X., Xie, Z., Liang, D., Wu, Z., Yang, X., 2021. Flexible Printed Circuit Board as Novel Electrodes for Acoustofluidic Devices. IEEE Transactions on Electron Devices 68, 393–398. https://doi.org/10.1109/TED.2020.3039760

Sun, C., Wu, F., Wallis, D.J., Shen, M.H., Yuan, F., Yang, J., Wu, J., Xie, Z., Liang, D., Wang, H., Tickle, R., Mikhaylov, R., Clayton, A., Zhou, Y., Wu, Z., Fu, Y., Xun, W., Yang, X., 2020. Gallium Nitride: A Versatile Compound Semiconductor as Novel Piezoelectric Film for Acoustic Tweezer in Manipulation of Cancer Cells. IEEE Transactions on Electron Devices 67, 3355–3361. https://doi.org/10.1109/TED.2020.3002498

Sun, S., Li, Z., Glencer, P., Cai, B., Zhang, X., Yang, J., Li, X., 2017. Bringing the age-related macular degeneration high-risk allele age-related maculopathy susceptibility 2 into focus with stem cell technology. Stem Cell Research & Therapy 8, 135. https://doi.org/10.1186/s13287-017-0584-4

Syaifudin, A.R.M., Mukhopadhyay, S.C., Yu, P.-L., Haji-Sheikh, M.J., Chuang, C.-H., Vanderford, J.D., Huang, Y.-W., 2011. Measurements and Performance Evaluation of Novel Interdigital Sensors for Different Chemicals Related to Food Poisoning. IEEE Sensors Journal 11, 2957–2965. https://doi.org/10.1109/JSEN.2011.2154327

Tahara, M., Inoue, T., Miyakura, Y., Horie, H., Yasuda, Y., Fujii, H., Kotake, K., Sugano, K., 2013. Cell diameter measurements obtained with a handheld cell counter could be used as a surrogate marker of G2/M arrest and apoptosis in colon cancer cell lines exposed to SN-38. Biochemical and Biophysical Research Communications 434, 753–759. https://doi.org/10.1016/j.bbrc.2013.03.128

Takeuchi, H., Saito, M., 1972. Seismic surface waves. Methods in computational physics 11, 217–295.

Tao, R., Wang, W.B., Luo, J.T., Ahmad Hasan, S., Torun, H., Canyelles-Pericas, P., Zhou, J., Xuan, W.P., Cooke, M.D., Gibson, D., Wu, Q., Ng, W.P., Luo, J.K., Fu, Y.Q., 2019. Thin film flexible/bendable acoustic wave devices: Evolution, hybridization and

decoupling of multiple acoustic wave modes. Surface and Coatings Technology 357, 587–594. https://doi.org/10.1016/j.surfcoat.2018.10.042

Tayebi, M., Yang, D., Collins, D.J., Ai, Y., 2021. Deterministic Sorting of Submicrometer Particles and Extracellular Vesicles Using a Combined Electric and Acoustic Field. Nano Lett. https://doi.org/10.1021/acs.nanolett.1c01827

Tian, Z., Yang, S., Huang, P.-H., Wang, Z., Zhang, P., Gu, Y., Bachman, H., Chen, C., Wu, M., Xie, Y., Huang, T.J., 2019. Wave number–spiral acoustic tweezers for dynamic and reconfigurable manipulation of particles and cells. Sci. Adv. 5, eaau6062. https://doi.org/10.1126/sciadv.aau6062

Tsougeni, K., Kaprou, G., Loukas, C.M., Papadakis, G., Hamiot, A., Eck, M., Rabus, D., Kokkoris, G., Chatzandroulis, S., Papadopoulos, V., Dupuy, B., Jobst, G., Gizeli, E., Tserepi, A., Gogolides, E., 2020. Lab-on-Chip platform and protocol for rapid foodborne pathogen detection comprising on-chip cell capture, lysis, DNA amplification and surface-acoustic-wave detection. Sensors and Actuators B: Chemical 320, 128345. https://doi.org/10.1016/j.snb.2020.128345

Uchino, K., 2017. Chapter 10 - Manufacturing Methods for Piezoelectric Ceramic Materials, in: Uchino, Kenji (Ed.), Advanced Piezoelectric Materials (Second Edition), Woodhead Publishing in Materials. Woodhead Publishing, pp. 385–421. https://doi.org/10.1016/B978-0-08-102135-4.00010-2

Uchino, K., 2010. 1 - The development of piezoelectric materials and the new perspective, in: Uchino, Kenji (Ed.), Advanced Piezoelectric Materials, Woodhead Publishing Series in Electronic and Optical Materials. Woodhead Publishing, pp. 1–85. https://doi.org/10.1533/9781845699758.1

Van Assche, D., Reithuber, E., Qiu, W., Laurell, T., Henriques-Normark, B., Mellroth, P., Ohlsson, P., Augustsson, P., 2020. Gradient acoustic focusing of sub-micron particles for separation of bacteria from blood lysate. Sci Rep 10, 3670. https://doi.org/10.1038/s41598-020-60338-2

Verma, M., Lam, T.K., Hebert, E., Divi, R.L., 2015. Extracellular vesicles: potential applications in cancer diagnosis, prognosis, and epidemiology. BMC Clin Pathol 15, 6. https://doi.org/10.1186/s12907-015-0005-5

Vladimirsky, Y., 1999. 10 - LITHOGRAPHY, in: Samson, J.A.R., Ederer, D.L. (Eds.), Vacuum Ultraviolet Spectroscopy. Academic Press, Burlington, pp. 205–223. https://doi.org/10.1016/B978-012617560-8/50032-3

Wang, X., Chen, S., Kong, M., Wang, Z., Costa, K.D., Li, R.A., Sun, D., 2011. Enhanced cell sorting and manipulation with combined optical tweezer and microfluidic chip technologies. Lab Chip 11, 3656–3662. https://doi.org/10.1039/C1LC20653B

Wang, Y., Zhang, Q., Tao, R., Xie, J., Canyelles-Pericas, P., Torun, H., Reboud, J., McHale, G., Dodd, L.E., Yang, X., Luo, J., Wu, Q., Fu, Y., 2021. Flexible/Bendable Acoustofluidics Based on Thin-Film Surface Acoustic Waves on Thin Aluminum Sheets. ACS Appl. Mater. Interfaces 13, 16978–16986. https://doi.org/10.1021/acsami.0c22576

Wang, Z., Li, F., Rufo, J., Chen, C., Yang, S., Li, L., Zhang, J., Cheng, J., Kim, Y., Wu, M., Abemayor, E., Tu, M., Chia, D., Spruce, R., Batis, N., Mehanna, H., Wong, D.T.W., Huang, T.J., 2020. Acoustofluidic Salivary Exosome Isolation: A Liquid Biopsy Compatible Approach for Human Papillomavirus–Associated Oropharyngeal Cancer Detection. The Journal of Molecular Diagnostics 22, 50–59. https://doi.org/10.1016/j.jmoldx.2019.08.004

Wang, Z., Rich, J., Hao, N., Gu, Y., Chen, C., Yang, S., Zhang, P., Huang, T.J., 2022. Acoustofluidics for simultaneous nanoparticle-based drug loading and exosome encapsulation. Microsystems & Nanoengineering 8, 45. https://doi.org/10.1038/s41378-022-00374-2

Wixforth, A., Strobl, C., Gauer, Ch., Toegl, A., Scriba, J., v. Guttenberg, Z., 2004. Acoustic manipulation of small droplets. Anal Bioanal Chem 379, 982–991. https://doi.org/10.1007/s00216-004-2693-z

Wu, H., Tang, Z., You, R., Pan, S., Liu, W., Zhang, H., Li, T., Yang, Y., Sun, C., Pang, W., Duan, X., 2022. Manipulations of micro/nanoparticles using gigahertz acoustic streaming tweezers. Nanotechnology and Precision Engineering (NPE) 5, 023001. https://doi.org/10.1063/10.0009954

Wu, M., Huang, P.-H., Zhang, R., Mao, Z., Chen, C., Kemeny, G., Li, P., Lee, A.V., Gyanchandani, R., Armstrong, A.J., Dao, M., Suresh, S., Huang, T.J., 2018. Circulating Tumor Cell Phenotyping via High-Throughput Acoustic Separation. Small 14, 1801131. https://doi.org/10.1002/smll.201801131

Wu, M., Mao, Z., Chen, K., Bachman, H., Chen, Y., Rufo, J., Ren, L., Li, P., Wang, L., Huang, T.J., 2017a. Acoustic Separation of Nanoparticles in Continuous Flow. Advanced Functional Materials 27, 1606039. https://doi.org/10.1002/adfm.201606039

Wu, M., Ouyang, Y., Wang, Z., Zhang, R., Huang, P.-H., Chen, C., Li, H., Li, P., Quinn, D., Dao, M., Suresh, S., Sadovsky, Y., Huang, T.J., 2017b. Isolation of exosomes from whole blood by integrating acoustics and microfluidics. PNAS 114, 10584–10589. https://doi.org/10.1073/pnas.1709210114

Xia, Y., Whitesides, G.M., 1998. SOFT LITHOGRAPHY. Annu. Rev. Mater. Sci. 28, 153–184. https://doi.org/10.1146/annurev.matsci.28.1.153

XiaoMing Hu, 2015. Photolithography technology in electronic fabrication, in: Proceedings of the 2015 International Power, Electronics and Materials Engineering Conference. Atlantis Press, pp. 843–850. https://doi.org/10.2991/ipemec-15.2015.156

Xu, K., Clark, C.P., Poe, B.L., Lounsbury, J.A., Nilsson, J., Laurell, T., Landers, J.P., 2019. Isolation of a Low Number of Sperm Cells from Female DNA in a Glass–PDMS–Glass Microchip via Bead-Assisted Acoustic Differential Extraction. Anal. Chem. 91, 2186–2191. https://doi.org/10.1021/acs.analchem.8b04752

Xu, X., Huang, X., Sun, J., Wang, R., Yao, J., Han, W., Wei, M., Chen, J., Guo, J., Sun, L., Yin, M., 2021. Recent progress of inertial microfluidic-based cell separation. Analyst 146, 7070–7086. https://doi.org/10.1039/D1AN01160J

Yang, T., Bragheri, F., Nava, G., Chiodi, I., Mondello, C., Osellame, R., Berg-Sørensen, K., Cristiani, I., Minzioni, P., 2016. A comprehensive strategy for the analysis of acoustic compressibility and optical deformability on single cells. Scientific Reports 6, 23946. https://doi.org/10.1038/srep23946

Zakrzewski, W., Dobrzyński, M., Szymonowicz, M., Rybak, Z., 2019. Stem cells: past, present, and future. Stem Cell Research & Therapy 10, 68. https://doi.org/10.1186/s13287-019-1165-5

Zhang, B., Zhuo, J., Beache, G., 1772. MRE Determination of the Lame Constants by Simultaneous Visualization of P-and S-waves. Presented at the Proc. Intl. Soc. Mag. Reson. Med, p. 2004.

Zhang, G., 2022. Bulk and Surface Acoustic Waves : Fundamentals, Devices, and Applications. Jenny Stanford Publishing Pte. Ltd.

Zhang, N., P. Zuniga-Hertz, J., Yan Zhang, E., Gopesh, T., J. Fannon, M., Wang, J., Wen, Y., H. Patel, H., Friend, J., 2021. Microliter ultrafast centrifuge platform for size-based particle and cell separation and extraction using novel omnidirectional spiral surface acoustic waves. Lab on a Chip 21, 904–915. https://doi.org/10.1039/D0LC01012J

Zhang, X., Fang, J., Zou, L., Zou, Y., Lang, L., Gao, F., Hu, N., Wang, P., 2016. A novel sensitive cell-based Love Wave biosensor for marine toxin detection. Biosensors and Bioelectronics 77, 573–579. https://doi.org/10.1016/j.bios.2015.07.062

Zhang, Y., Zheng, T., Wang, L., Feng, L., Wang, M., Zhang, Z., Feng, H., 2021. From passive to active sorting in microfluidics: A review. REVIEWS ON ADVANCED MATERIALS SCIENCE 60, 313–324. https://doi.org/10.1515/rams-2020-0044

Zhao, S., Huang, P.-H., Zhang, H., Rich, J., Bachman, H., Ye, J., Zhang, W., Chen, C., Xie, Z., Tian, Z., Kang, P., Fu, H., Jun Huang, T., 2021. Fabrication of tunable, high-

molecular-weight polymeric nanoparticles via ultrafast acoustofluidic micromixing. Lab on a Chip. https://doi.org/10.1039/D1LC00265A

Zhao, S., Wu, M., Yang, S., Wu, Y., Gu, Y., Chen, C., Ye, J., Xie, Z., Tian, Z., Bachman, H., Huang, P.-H., Xia, J., Zhang, P., Zhang, H., Huang, T.J., 2020. A disposable acoustofluidic chip for nano/microparticle separation using unidirectional acoustic transducers. Lab Chip 20, 1298–1308. https://doi.org/10.1039/D0LC00106F

Zhao, W., Tian, S., Huang, L., Liu, K., Dong, L., 2020. The review of Lab-on-PCB for biomedical application. ELECTROPHORESIS 41, 1433–1445. https://doi.org/10.1002/elps.201900444

Zheng, C., Mylonakis, G., Kouretzis, G., Luan, L., 2022. Kinematic seismic response of end-bearing piles to S-waves. Soil Dynamics and Earthquake Engineering 163, 107547. https://doi.org/10.1016/j.soildyn.2022.107547

Zhong, J., Li, P., Liang, M., Ai, Y., 2021. Label-Free Cell Viability Assay and Enrichment of Cryopreserved Cells Using Microfluidic Cytometry and On-Demand Sorting. Advanced Materials Technologies n/a, 2100906. https://doi.org/10.1002/admt.202100906

Zhou, Q., Lau, S., Wu, D., Kirk Shung, K., 2011. Piezoelectric films for high frequency ultrasonic transducers in biomedical applications. Progress in Materials Science 56, 139–174. https://doi.org/10.1016/j.pmatsci.2010.09.001

Zhu, B., Murthy, S.K., 2013. Stem cell separation technologies. Current Opinion in Chemical Engineering 2, 3–7. https://doi.org/10.1016/j.coche.2012.11.002